Design and mechanical integrity of friction riveted joints of thermoplastic composite

Vom Promotionsausschuss der
Technischen Universität Hamburg
zur Erlangung des akademischen Grades

Doktor-Ingenieur (Dr.-Ing.)

genehmigte Dissertation

von
Natascha Zocoller Borba

aus
Ribeirão Preto

2020

Gutachter:

Univ.-Prof. Dr.-Ing. Sergio de Traglia Amancio Filho

Prof. Dr.-Ing. habil. Bodo Fiedler

Vorsitzender des Prüfungsausschusses:

Prof. Dr.-Ing. Otto von Estorff

Tag der mündlichen Prüfung:

10. September 2020

https://doi.org/10.15480/882.2959

https://orcid.org/0000-0001-9069-6686

Acknowledgments

The successful completion of this PhD work was only possible with the contribution of several people, to whom I would like to express here my sincere gratitude:

- Univ.-Prof. Dr.-Ing. Sergio de Traglia Amancio Filho for the opportunity, valuable guidance, and trust on my abilities to conduct the work.
- Prof. Dr. Jorge Dos Santos for the constant support, for providing outstanding structure which was essential to achieve the goals of this work.
- Prof. Dr.-Ing. Nobert Huber and Stephanie Koch for the management support within the institute.
- Prof. Dr.-Ing. Bodo Fiedler for contributing scientifically to the work and allowing the usage of the Institute of Polymer and Composites facilities to perform impact and fatigue tests, as well as his research assistants Johann Körbelin and Benedikt Kötter for the valuable support during the tests.
- All colleagues from the Solid State Joining department, specially Dagmar Koschek and Menno Peters for the unconditional support and setting and work example; Luciano Bergmann and Jan Carstensen for the good times together and friendship; Dr. Martin Reimann, Dr. Jannik Entringer, and Dr. Alessandro Barbini for the cheerful company, caring, and friendship.
- The friends for life Dr. Lucian Blaga, Dr. Seyed Goushegir, Dr. Eduardo Feistauer, Rielson Falck, Mihaela Malita, and my lifemate Natalia Manente from Advance Polymer-Metal Hybrid Structures Group for the teamwork, mutual learning, and professional and personal growth.
- To several HZG colleagues, among them Kay Erdmann for the assistance with fatigue test; Ms. Ivonne Ternes for her contribution to the accelerated aging experiments; Falk Dorn for the assistance with sample preparation; Dr. Vasyl Haramus for the introduction to the μCT measurements.
- All my beloved friends from Brazil and Germany (Ci, Ju, Debby, Fer, Bia, De, Mari, and Antonella) for their presence in my life and joyful video calls during the pandemic.
- All my family for their unconditional love, support and encouragement.
- My husband André for the mutual learning, unconditional love, caring, and inspiration to bring the best of us always.
- My beloved parents Madalena and Carlos, and my beloved lifemates and sisters Maika and Raissa for the love, the belief in me and my life path, and for never leaving me alone even distant of my daily life.

Abstract

Thermoplastic composites have attracted increasing interest as alternative materials for primary and secondary structures of the next aircraft generation, owing to their fast processability and good reparability. The employment of these materials has triggered research in the fields of durability, fatigue, and damage tolerance, and prompted the development of alternative joining solutions that mitigate the dissimilarity between them and the remained metal parts in the aircraft. Among these technologies, Friction Riveting (FricRiveting) is an innovative, friction-based joining process suitable for polymers, composites and hybrid metal-composite structures. Prior to this work, the maturity of FricRiveting was limited to scientific knowledge at coupon level, including topics of heat generation, microstructure, physicochemical, and quasi-static mechanical properties. Moreover, no information on the behavior of joints under harsh environmental conditions, accidental damage scenarios or cyclic loading has been assessed, which are topics essential for the industrial transferability of this new joining technology. Therefore, this PhD work was devised to fill in the gaps in scientific and technological knowledge, with a focus on further develop and understand the fundamentals of the FricRiveting process, joint design, and mechanical integrity. Case study overlapped joints were produced using a titanium alloy Ti6Al4V rivet and woven carbon fiber reinforced polyether ether ketone (CF-PEEK) parts relevant to aviation.

By a stepwise analysis of the joining process along with X-ray micro-computed tomography and digital image correlation method, the joint formation and composite flow were assessed, showing the contribution of the squeezed material between the composite parts as an additional bonding mechanism to the mechanical interlocking of the plastically deformed rivet tip. The process temperature measured by thermography and thermometry exceeded the decomposition temperature of PEEK as well as the beta transus temperature of Ti6Al4V, leading to volumetric flaws in the rivet surrounding and morphological transformations in the plastically deformed rivet tip, which promoted local mechanical changes as confirmed by micro- and nanohardness measurements. Over the process temperature range analyzed in this work, three plastic deformation shapes of the rivet tip were detected and of these a bell-shaped rivet tip produced the strongest joints under shear loading. Through statistical analysis, a set of optimized joining parameters was obtained that produces sound joints with bell-shape rivet tip and above-average quasi-static strength. In addition, fundamental understanding of the effect of joint geometries on the joint strength was analyzed, in which by optimizing the joint design (washer size and tightening torque), 30 % increase in joint strength was achieved.

Although FricRiveting presented inferior quasi-static mechanical performance compared to reference lock bolting, the fatigue life of the joints showed an improvement up to 88 %, fulfilling aircraft industry requirements. The sensitivity of the friction riveted joints to impact damage and its propagation under quasi-static and cyclic loading was investigated through drop weight impact testing as well as microstructural characterization and post-impact single lap shear and fatigue testing. The joint strength and fatigue life were not compromised by barely-visible impact damage, which did not indicate a nucleation of critical delamination. However, visible impact damage introduced both delamination and premature failure at the metal-composite interface, leading to a 40 % decrease of quasi-static mechanical strength and the fatigue limit reached at load level of 58 % of the quasi-static joint strength. The residual quasi-static strength of those joints surviving 10^6 cycles of fatigue was evaluated revealing no critical damage accumulation at the examined load level for unimpacted and impacted joints.

The durability of the joints was assessed under hydrothermal and saline aging. With hydrothermal aging a 23 % increase of joint mechanical performance was observed after 28 days of exposure, as a result of PEEK post-crystallization. With saline aging a decrease up to 23 % of the quasi-static mechanical performance could be explained by corrosion induced in the external tightening elements, which no longer contributed to redistribution of the compression stress through the composite surface.

This PhD work succeeds in further developing the FricRiveting process by covering complex and relevant issues from scientific and engineering perspectives for the introduction of thermoplastic composites and providing a new joining solution for aircraft manufacturing.

Zusammenfassung

Thermoplastischer Verbundwerkstoffe sind aufgrund ihrer schnellen Verarbeitbarkeit und guten Reparaturfähigkeit alternative Materialien für Primär- und Sekundärstrukturen der nächsten Flugzeuggeneration. Die (industrielle) Verwendung dieser neuen Materialien hat die Erforschung der Haltbarkeit, Ermüdung und Schadenstoleranz sowie der Entwicklung alternativer Verbindungsverfahren eingeleitet. Vor allem die Auswirkungen der Artfremdheit zwischen ihnen und den verbleibenden metallischen Bauteilen im Flugzeug stehen dabei im Fokus. Reibnieten (Friction Riveting) ist ein innovatives, reibbasiertes Verbindungsverfahren, das für Kunststoff-, Verbundwerkstoff- und hybride Metall-Verbundstrukturen geeignet ist und daher für diese Art der Anwendung in Frage kommt. Bevor der vorliegenden Arbeit war die Reife des Reibnietens auf den Labormaßstab beschränkt, vor allem hinsichtlich wissenschaftlicher Erkenntnisse der Wärmeerzeugung, Mikrostruktur, physikalisch-chemische- und quasi-statische mechanische Eigenschaften. Darüber hinaus waren keine Informationen über das Verhalten der Verbindung unter kritischen Umgebungsbedingungen, Unfallschadenszenario und Ermüdungsverhalten verfügbar, die für die Übertragbarkeit auf den industriellen Maßstabunerlässlich sind. Diese Arbeit wurde durchgeführt, um die wissenschaftlichen und technologischen Wissenslücken des Reibnietens zu schließen. Dabei wurde sich vor allem auf das grundlegende Prozessverständnis, das Verbindungsdesign und die mechanische Integrität von Überlappverbindungen unter Verwendung der Titanlegierung Ti6Al4V und gewebtes kohlefasergewebes - Polyetheretherketon (CF-PEEK) fokussiert.

Durch eine schrittweise Analyse des Fügeprozesses wurden die Verbindungsbildungsmechanismen und der Materialfluss bewertet. Es konnte gezeigt werden, dass das zusammengedrückte Material zwischen den Verbundteilen als zusätzlicher Haftmechanismus maßgeblich zum mechanischen Formschluss der plastisch verformten Nietspitze beiträgt. Die Prozesstemperatur übersteigt die Zersetzungstemperatur von PEEK sowie die β-Transus-Temperatur von Ti6Al4V, was zu Volumenfehlern im Verbundwerkstoff in der Nietumgebung und zu morphologischen Umwandlungen in die plastisch verformte Nietspitze führt. Über den in dieser Arbeit untersuchten Prozesstemperaturbereich wurden drei plastische Verformungsprofile der Nietspitze festgestellt, von denen die glockenförmige Nietspitze unter Scherbelastung die stärksten Verbindungen erzeugte. Ein optimierter Prozessparametersatz wurde ermittelt, um Verbindungen mit überdurchschnittlicher quasi-statischer Festigkeit herzustellen. Durch die Optimierung des Verbindungsentwurfes (Außendurchmesser der Scheibe und Anziehdrehmoment) wurde darüber hinaus eine Steigerung der Verbindungsfestigkeit um 30% erzielt.

Obwohl die quasi-statischen mechanischen Eigenschaften reibgenieteter Verbindungen denen verschraubter Referenzverbindungen unterlegen sind, hielten die Verbindungen unter Ermüdungsbelastung mit 66 % ihrer quasi-statischen Festigkeit 10^5 Zyklen stand. Somit wurde eine Verbesserung von bis zu 88 % im Vergleich zum Ermüdungsverhalten herkömmlicher mechanischer Befestigungstechniken erreicht. Der Einfluss verschiedener Rissausbreitung auf die quasi-statischen und zyklischen mechanischen Eigenschaften sowie auf die Schadensausbreitung wurde untersucht. Die Festigkeit und die Ermüdungslebensdauer der Verbindung wurde bei kaum sichtbaren Aufprallschäden nicht beeinträchtigt, was auf keine Keimbildung kritischer Delamination hindeutet. Andererseits führten sichtbare Aufprallschäden zur Delamination und vorzeitigem Versagen der Metall-Verbund-Grenzfläche was zu einer Verringerung von etwa 40 % der quasi-statischen mechanischen Festigkeit sowie eine Ermüdungsgrenze entsprechend 58 % der quasi-statischen Festigkeit führt.

Die Dauerhaftigkeit der Verbindungen wurde unter hydrothermaler und Salz Alterung bewertet. Durch Alterung in hydrothermaler Alterungsbedingung erhöhte sich nach 28-tägiger Aussetzung die mechanische Leistungsfähigkeit der Verbindung um 23 % als Ergebnis der Nachkristallisation des PEEK. Bei der Salzalterung konnte die Verringerung der Festigkeit um etwa 23 % durch die Korrosion der äußeren Spannelemente erklärt werden, die dadurch nicht mehr zur Umverteilung der Druckspannung durch die Verbundoberfläche beitrugen.

Durch diese Arbeit gelingt es, das Reibnietverfahren weiterzuentwickeln, indem komplexe und relevante Themen aus wissenschaftlicher und technischer Sicht für die weitere Verwendung thermoplastischer Verbundwerkstoffe und dieser neuen Verbindungslösung in die Flugzeugfertigung behandelt werden.

List of Abbreviations

µCT	X-ray micro-computed tomography
ACARE	Advisory Council for Aviation Research and Innovation in Europe
ANOVA	Analysis of variance
Bcc	Body-centered cubic array
BM	Base material
BS	Bottom surface
BVID	Barely visible impact damage
CDF	Cumulative density function
CF	Consolidation force
CF-PEEK	Carbon fiber reinforced polyether ether ketone
CF-PEKK	Carbon fiber reinforced polyether ketone ketone
CF-PPS	Carbon fiber reinforced polyphenylene sulfide
CFRP	Carbon fiber reinforced polymer
CLSM	Confocal laser scanning microscope
CLTE	Coefficient of linear thermal expansion
CP	Clamping pressure
CR	Cooling rate
CSM	Continuous stiffness measurement
CSZ	Composite stir zone
CT	Consolidation time
CTMAZ	Composite thermomechanically affected zone
DCM	Dynamic contact module
DF	Displacement at friction
DIC	Digital image correlation
DoE	Design of experiments
DSC	Differential scanning calorimetry
DTG	Derivative thermogravimetric graph
EBW	Electron beam welding
EDS	X-ray spectroscopy
FEM	Finite element method
FF	Frictional force
FoF	Forging force
FoT	Forging time
FP	Failure point
FricRiveting	Friction Riveting
FSW	Friction stir welding
FT	Frictional time
FTIR	Fourier-transform infrared spectroscopy

GTAW	Gas tungsten arc welding
hcp	Close-packed hexagonal array
HR	Heating rate
IDP	Incipient damage point
IR	Infrared
JC	Johnson-Cook
LBW	Laser beam welding
LOM	Light optical microscope
MLP	Maximum load point
MTMAZ	Metal thermomechanically affected zone
NDT	Non-destructive testing
OFAT	One-factor-at-a-time
PDF	Probability density function
PEEK	Polyether ether ketone
PMMA	Poly(methyl methacrylate)
RS	Rotational speed
RT	Room temperature
SAI	Shear-after-impact
SEM	Scanning electron microscope
SIC	Solvent-induced crystallization
SLS	Single lap shear
TAPAS	Thermoplastic affordable primary aircraft structure
TC	Thermocouple
TGA	Thermogravimetric analysis
TMAM	Thermomechanically affected material
TP	Total point
TPC	Thermoplastic polymer composite
TT	Tightening torque
ULSF	Ultimate lap shear force
US	Ultrasound/ultrasonic
US	Upper surface
UT	Ultrasonic testing
UV	Ultraviolet
VID	Visible impact damage
VR	Volumetric ratio
XPS	X-ray photoelectron spectroscopy

List of Symbols

μ_e	Coefficient of friction
A_b	Bearing area
A_i	Impact area
A_r	Real area of the composite hole
A_{SM}	Area of squeezed material
C3D8H	Eight-node linear brick element
D	Original rivet diameter
D_c	Composite desirability
D_s	Stiffness degradation
D_b	Displacement at break
d_i (Y_i)	Desirability function
D_p	Anchoring depth
D_{rd}	Residual dent depth
D_w	Washer diameter
e	Edge distance
E	Modulus
E_0	Initial joint modulus
E_1, E_2	Encastre of FE model
F_{cf}	Centrifugal force
F_{cp}	Centripetal force
F_f (x)	Probability of failure
F_s (x)	Probability of survival
g	Grip length
G	Gap between the composite parts
G_{II}	Mode II fracture toughness
H	Rivet penetration depth
h_f	Final indentation displacement
h_{max}	Maximum indentation load
ILSS	Interlaminar shear strength
k	Number of responses from regression model
l	Specimen length
L_i, T_i, U_i	Lower, target, and upper values desired for a response
M_n	Mass change
M_r	Resultant momentum
M_s	Martensite starting temperature
N	Fatigue life (number of cycles)
P_c	Critical impact load
P_f	Failure load

P_i	Incipient damage load
P_m	Peak force
P_{max}	Maximum indentation load
P_t	Final load
R	Fatigue stress ratio
R^2_{adj}	Regression-adjusted coefficient of determination
R_x	Reliability
S_1	Not plastically deformed rivet tip
S_2	Bell-shaped rivet tip
S_3	Inverted bell-shaped rivet tip
SC8R	Quadrilateral continuum shell element
S_i	Stress
S_{Misses}	Von Mises stress
S_{xx}, S_{yy}, S_{xy}	In-plane, out-of-plane, and shear stresses
T	Temperature
t	Time
T_c	Temperature of crystallization
T_{cc}	Temperature of cold crystallization
T_d	Decomposition onset temperature
T_g	Glass-transition temperature
T_m	Melting temperature
T_{max}	Maximum temperature
U_f	Maximum energy
U_i	Incipient energy
U_m	Energy at maximum load
U_t	Total energy
U_y	Out-of-plane displacement
W	Rivet tip width
w	Joint width
W_0	Original weight of specimen
W_w	Weight of wet specimen
X_c	Degree of crystallinity
Y_i	Response from regression model
α	Weibull shape parameter
β	Weibull scale parameter
ΔH_m	Melting enthalpy
ΔH_m^0	Melting enthalpy of 100 % crystalline polymer

Contents

Chapter 1. Introduction

The increased demand for air transport and the needs of society for safe, affordable, more efficient, and environmentally friendly mobility have resulted in regulations and requirements that must be adopted by manufacturing industries by 2050 for the next generation of aircraft. For instance, challenging goals proposed by the European Commission through the ACARE (Advisory Council for Aviation Research and Innovation in Europe) include a reduction of 75 % in CO_2 by 2050, relative to 2000, an increase in the usage of sustainable, alternative fuels, and the manufacture of recyclable vehicles [1]. In this context, research and innovation are expected to lead to disruptive technologies across many fields, including the structural design of aircraft with new materials and manufacturing processes. The partial replacement of conventional metal structures with lighter solutions, including carbon fiber reinforced polymers (CFRPs) has proven a solution for the reduction of fuel consumption and emission of greenhouse gases [2]. Besides their inherent low density, CFRPs have high specific strength and fatigue performance, environmental stability, and outstanding corrosion resistance [3]. Traditionally, CFRP applications for aerospace structures (cabin ceilings, sidewalls and cargo compartment panels) are manufactured using thermoset resins, which require longer curing times and outgassing of products from the curing reactions [3]. Moreover, issues of recyclability [4], brittleness [5], and total manufacturing costs [6] are still limitations, which impair further application of the material.

Nowadays, the introduction of advanced thermoplastic polymers (TPCs) as matrix material for composite structures has attracted the interest of aircraft companies and suppliers as an alternative for metal parts and thermoset composites [7]. These polymers can be rapidly manufactured by applying heat and pressure, and therefore bear a great resemblance to the manufacturing processes of metal components [8]. This fact has encouraged the replacement of aluminum and titanium by TPCs in clips, brackets, trays and other simple parts [9]. For complex parts, the Airbus A380 features one of the largest structural thermoplastic components currently in service: a thermoplastic skin reinforced with welded ribs, which reportedly weighs about 20 % less than comparable aluminum structures [9]. Since the mid-1990s, Fokker Aerostructures BV has also supplied pressure and non-pressure floor panels for intercontinental luxury jets produced by the aircraft manufacturer Gulfstream Aerospace Corporation [10]. Moreover, the ability of thermoplastics to remelt has boosted innovation in composite assembly technology compared to their thermoset counterparts [11]. The drawbacks of conventional technologies, such as mechanical fastening and adhesive bonding, can be overcome, including the notch sensitivity of the thermoset at the drilling stage [12], extensive and costly cleaning of dust due to the drilling of holes [6], and long joining time owing to surface

preparation and the curing times of adhesives [13]. Demonstrators have shown the possibility to adopt welding-based technologies to produce integral TCP parts, along with unavoiding anti-peel rivets in the stringer run-outs [14]. In this way, a reduction in both the assembly weight and stress concentrations can be achieved [15].

Despite the intrinsic appeal of TPCs, their adoption for structural aircraft components has been restricted, owing to high material and manufacturing costs, and a lack of understanding of the joined/welded composite's reliability and predictability upon fatigue, accidental damage, and under different environmental conditions [16]. Classic theories of fracture mechanics and designs against fatigue are primarily described for metal structures and no longer apply for composite components, as the nature of damage and critical cyclical load cases vary for composites. For instance, compressive load cycles and accidental impact can severely damage composite structures, but do not cause any loss of structural integrity in metals [17]. Moreover, the damage caused by long-term exposure of metal structures to environmental conditions has been widely described as corrosion attacks, which over the years have triggered investments in systems of corrosion protection by companies [18–20]. However, predictions have shown that composites suffer damage at the fiber-matrix interface and by matrix softening [21–23], and therefore different strategies need to be adopted to protect them for the average 30 years of operational aircraft life.

In this context, Friction Riveting (FricRiveting) has been proposed as an alternative joining technology for TPCs, patented by and developed at Helmholtz-Zentrum Geesthacht, Germany [24]. The technology relies on the principles of mechanical fastening by friction welding and the feasibility has been demonstrated for several material combinations including carbon fiber [25,26] and glass fiber reinforced thermoplastics [27,28]. This PhD work was devised to advance the maturity of the technology for overlapped CFRP in aircraft applications, including evaluation of the fundamental scientific and technological aspects of the FricRiveting process. For this purpose, friction riveted joints were investigated to determine the impact of the joining process on the joint formation, design, and mechanical performance in a damage scenario of fatigue and environmental threats.

This thesis is arranged with the following chapters:

Chapter 2 defines the motivation and objectives of the work, based on the knowledge gaps and perspectives for new joining technologies of TPCs in the aircraft industry, as stated in this introduction.

Chapter 3 summarizes the relevant literature on the state-of-the-art of Friction Riveting, which is partially based on the results obtained in this PhD work along with previous publications on the topic. It also briefly introduces general aspects of structural design philosophies, durability of CFRP joints, including the effects of fatigue, impact, and environmental exposure on the joint's

mechanical behavior, and the definition of a joint design guideline. A brief description of the basic characteristics of the materials used in this work completes this chapter.

Chapter 4 sets out the experimental approach adopted in this work, focusing on the work packages defined to achieve the objective of the project.

Chapter 5 describes the materials, equipment, characterization methods, and simulation carried out in this work.

The results and a discussion are divided into five further chapters:

Chapter 6 deals with the general aspects of FricRiveting, including joint formation, bonding mechanisms, temperature history, microstructural transformations of the joint materials, and local properties (physicochemical changes of CFRP and microhardness and nanohardness of metal and CFRP). The main results of the process optimization are shown, from which an optimized joint condition was selected for the analyses in the subsequent chapters. Finally, a fundamental analysis of joint geometry for single spot friction riveted joints is addressed.

Chapter 7 presents the mechanical performance of friction riveted joints under quasi-static and cyclic loading. The quasi-static mechanical performance at room temperature is analyzed by mechanical testing combined with a finite element method and strain distribution acquired by digital image correlation. The dynamic behavior is analyzed by fatigue testing, residual strength, and stiffness degradation calculation. The failure analysis and fractography of the joints from different loading scenarios are elaborated.

Chapter 8 is devoted to a fundamental understanding of fatigue and impact damage threats, where basic concepts of damage tolerance are employed. The size of impact damage is categorized according to aircraft standards and the evolution of damage under quasi-static and cyclical loading is presented.

Chapter 9 describes the influence of hydrothermal and saline aging on surface features of the joint, local thermal and mechanical properties of the composite, and the quasi-static mechanical performance of single lap joints. As applicable, the corrosion topic is explained. The chapter also provides fracture surface analyses after each of the aging processes.

Chapter 10 summarizes the results obtained in this PhD work.

Chapter 11 provides recommendations for further scientific and technological work in this field.

Chapter 2. Motivation and Objectives

The adoption of thermoplastic composites in primary and secondary aircraft structures has triggered research into the fields of durability and fatigue, the damage tolerance of composite structures, and the development of alternative joining solutions that mitigate the dissimilarity between composite and metal parts of the aircraft. FricRiveting is an innovative metal-polymer joining process that was developed at Helmholtz-Zentrum Geesthacht prior to this PhD work.

The maturity of FricRiveting remains at the initial stages of development, where scientific knowledge has been acquired mainly at the coupon level. The topics already investigated and addressed in previous studies include: the feasibility of the process for a wide range of materials, mainly in a joint configuration of single polymer/composite plates, an analytical heat input model for unreinforced thermoplastics, the characterization of microstructural zones, metallurgical transformations in the plastically deformed rivet, and quasi-static tensile strength. However, no detailed investigation into the process variant Direct Friction Riveting for an overlapped joint configuration of composite materials has been carried out. Consequently, there are no studies available on the joint formation, material flow, shear strength, and fracture analysis of this process variant. Moreover, to advance the maturity of FricRiveting, the behavior of the joints under harsh environmental conditions, in accidental damage scenarios, and cyclical loading require assessment, along with a proof of concept for large scale samples.

This PhD work was therefore conducted to fill in the identified gaps in scientific and technological knowledge, with a focus on the mechanical integrity of friction riveted joints. For this purpose, a case study joint relevant for aircraft of a titanium alloy Ti6Al4V rivet and overlapped parts of woven carbon fiber reinforced polyether ether ketone (CF-PEEK) was selected and the following objectives were defined:

- Optimize the Direct FricRiveting process through an assessment of the relationship between process parameters, joint formation, and mechanical behavior of the joints.
- Provide a fundamental analysis of joint design for Direct FricRiveting.
- Investigate the fatigue life of friction riveted joints and understand the damage evolution during quasi-static and cyclic loading.
- Evaluate the influences of aging under different environmental conditions and impact damage on the mechanical performance of friction riveted joints.

Chapter 3. Literature Review

3.1 Design requirements of joined composites for aircraft applications

To design an aircraft structure, three general aspects must be considered: strength, expected load, and lifetime. As regards strength, the selection of appropriated materials and optimization of structural design, including the design of joints and composites (*i.e.* stacking sequence, type and amount of fibers) are assessed. An analysis of relevant loading and peak load cases of events that can occur during the operational life of an aircraft is used to define risks to the integrity of the structure and allowable stress and strain levels. The third aspect assesses the degradation of the materials and structures over operational life, owing to environmental, corrosion, impact, and fatigue damage. [29]

Joining by mechanical fastening (*i.e.* bolting, riveting, screwing) is a common technology for assembling structural components in aircraft, because it requires only simple machinery, is easy to disassemble, and is capable of joining dissimilar materials [30,31]. However, the process induces stress concentrations on the fastener surroundings and produces a non-continuous joint that allows diffusion of moisture and other fluids [32]. The common disadvantages become critical when the technology is applied to composite structures, owing to the intrinsic notch sensitivity of the composite, and therefore a susceptibility for crack initiation during fastener insertion. Thus, mechanical fastener joining technologies for composite structures demand more rigorous design knowledge and analysis than those currently available for the traditional methodology for metal structures [33]. Since the integrity of mechanically fastened joints can directly affect the performance and safety of structural composite components, an understanding of the behavior of joined composites under different environments and a wide loading spectrum, including quasi-static, cyclic, and impact loading, is critical for aircraft structural designs.

3.1.1 Joint design of a bolted composite

The design of bolted joints has been widely explored, owing to its influence on joint strength, preferential failure mode, and required number of fasteners throughout a structure. These parameters include: geometrical factors (ratio of width to diameter, edge distance, and clearance) [34], bolt material [35], coefficient of friction [36], joint configuration (single or double lap joint, single or multiple rows of bolts) [37], laminate lay-up, and tightening torque [35,38]. According to Cooper and

Turvey [39], larger ratios of width to diameter and sufficient edge distances favor bearing failure, while small edge distances favor shear-out or cleavage modes [40]. As demonstrated for carbon fiber reinforced epoxy laminates, although the bearing strength is proportional to tightening torque [38,41], higher torques induce out-of-plane shear stresses, which may lead to premature failure of composite joints [42]. The low interlaminar strength of composite materials often leads to delamination of the ply during installation of the fasteners. Therefore, clearance fit fasteners are generally avoided for composite structures, to avoid defects. However, some authors [43,44] have published improvements on the fatigue life of composite bolted joints using an interference fit, which may promote a better load-sharing capability of the joint.

In addition to its geometry, the parameters of the fastener also play a role in the mechanical behavior of composite joints. The fasteners commonly used in aerospace are screws, rivets, and bolts. Each type presents a wide range of dimensions and varieties. For instance, for lock bolts a higher flush head diameter increases the pull-through strength of composite joints, as reported by Boeing [45]. Enlarged footprints such as nut, washer, collar, and tail, are normally designed for fasteners, to provide a larger area over which the preload is spread. In this way, tensile strength is improved by preventing fastener pull-through failure [33,46]. Thus, enlarged footprints enable higher preloads to improve the joint performance, while minimizing the possibility of crush damage through the composite's thickness [45].

3.1.2 Damage tolerant design of composite structures

Since 1978, aviation requirements have adopted the damage tolerance philosophy, defined as *the ability of a structure to sustain anticipated loads in the presence of fatigue, corrosion or accidental damage until such damage is detected through inspections and subsequent repair* [33,47]. In contrast to damage tolerance, damage resistance assesses *the ability of the material to resist damage initiation* [48]. In this scope, critical structural locations where damage occurs and propagates must be identified and determined whether they can be inspected or not. In cases where inspection is impractical, a safe-life design philosophy must be implemented, which corresponds to *the number of flights in which the probability of strength degradation is low* [29]. Figure 3.1 illustrates the selection of design approaches, based on the recommendations for aircraft manufacturing [29].

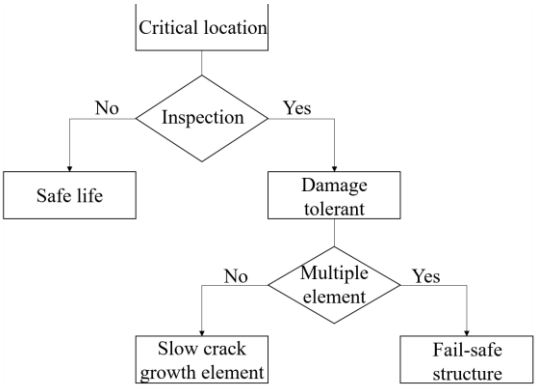

Figure 3.1 Schematic illustration of an aircraft design approach. (Adapted from [29])

According to the requirements of civil regulations for the damage tolerance of large aircraft EASA CS 25.571 and the advisory material specific for polymer composite structures (AMC 25.571), accidental impact damage is a concern for most composite structural designs, as it may go undetected and severely decrease the mechanical integrity of the composite [5,49]. In this regard, to improve the properties of through-the-thickness strength and impact resistance of composites, several approaches have been investigated, including the use of tougher thermoplastic resins [5], a tougher fiber network [50,51], and methodologies that include Z-fibers, stitched fabrics, preforms, and interlayers [52,53]. The stitching technologies have shown significant improvements to impact damage tolerance and fracture toughness, due to higher bending deformation prior to failure by internal shear [52]. Although stitching provides significant out-of-plane property improvements and drastically reduces the number of fasteners required, if used to fabricate integrated preforms it does so at a cost. This cost includes the amount of time required to provide field stitching (*i.e.* stitching not used solely for assembly or attachment) and a reduction of its in-plane properties, due to the undulating of the fiber network around the multiple penetrations of the stitching needle [50,52,54].

3.1.3 Impact behavior of aircraft composite structures

Aircraft composite structures, especially the composite fuselage, are prone to impact damage [55]. Contrary to metal structures, CFRP absorbs impact energy mainly through material damage and elastic deformation, instead of plastic deformation as with metals [56,57]. The nature of the impact damage is numerous for aircraft structures and has been classified according to the impact velocity [58,59]: tool drop during maintenance operations are classified as low velocity (4 to 10) m/s impact events with an impact energy of up to 35 J; runway debris impact has an intermediate velocity and impact energies in the order of 50 J, while bird strike and accidental damage such as the impact of

integrated parts, are classified as having medium velocities of (100 to 150) m/s with impact energies of over 100 J. In accordance with this classification, Airbus has recently reported an impact damage screening on the composite fuselage of A350XWB [47], as shown in Figure 3.2. The low-velocity impact events with an energy of up to 35 J had a higher probability of occurrence throughout the structure, being highly localized around the passenger and cargo doors.

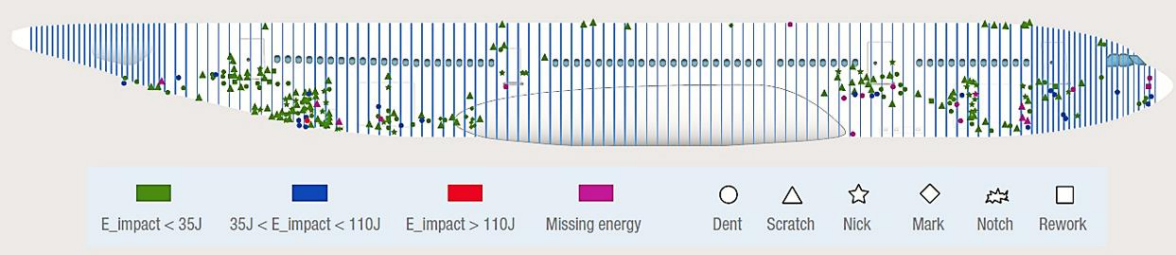

Figure 3.2 Impact damage screening of A350XWB (by permission of Airbus GmbH).

To assess the low-velocity impact damage, drop weight impact testing has been widely used to study the impact behavior of composite structures [5,56,60–63], adhesive bonded composites [64–66], and metal-composite laminates [67,68]. Some investigation has also been performed on impacted bolted composite structures [14]. Ochôa *et al.* [14] reported the detection of internal delamination in impacted stringers bolted to CF-PEKK panels of a horizontal stabilizer torsion box by an ultrasonic guided wave monitoring system. However, no investigation of impact damage evolution and residual strength was addressed.

Under drop weight impact testing, the material or joint can present a pure elastic response known as rebounding, or penetration instead, where the impact energy is totally absorbed by the material and released by the damage process, or perforation [62]. Such responses are dependent on the impact test parameters (impact velocity, indenter shape, and impact mass) [48,55,61,67], the temperature of the test [55,61], and material properties [48]. As reported by Gao *et al.* [48], CF-PEEK manufactured with a fast cooling rate presented the ability to resist damage initiation upon impact, owing to the low level of crystallinity of the PEEK matrix and consequently higher matrix ductility.

According to the EASA CS 25.571 [69] regulations for impact damage threat assessment of large aircraft, low-energy impact damage of composites is categorized as visible impact damage (VID) or barely visible impact damage (BVID). Typically, VID presents a damage area easily detected by a residual dent on the material surface, while BVID is characterized by internal damage, including matrix cracking, fiber fracture under tension and compression, and shear-driven delamination [49]. As reported by Polimeno and Meo [70], the most critical BVID is delamination, owing to its unstable crack propagation, diminished detectability by non-destructive tests, and up to 40 % decrease of the composite strength and stiffness. To define a threshold for BVID, a residual

dent depth of 0.5 mm is frequently used as the criterion, owing to the high measurement accuracy and probability of detection (90 % according to AIRBUS [47]), leading to a reasonable level of robustness for aircraft structural design [5,55,69]. Moreover, for damage tolerant designs for impacts, VID and BVID must be tested under quasi-static and cyclic loading to define their sensitivity to growth and the residual strength compared to allowable values for the composite structure [49].

Vieille, Casado, and Bouvet [5] compared the impact damage resistance and tolerance of CF-PEEK, CF-PPS, and CF-epoxy by the size of the impact damage and post-impact compression behavior. The authors reported that the BVID threshold was reached at 16 J for CF-PEEK, at 13 J for CF-PPS and at 11 J for CF-epoxy, showing a higher resistance to impact damage initiation of CF-PEEK. Additionally, as the toughness of a PEEK matrix is reported to be higher than PPS and epoxy, the propagation of the impact damage is shown to be relatively slow in CF-PEEK and the residual compressive strength 30 % higher than CF-epoxy and 12 % higher than CF-PPS, leading to better damage tolerance. Tai, Yi, and Tseng *et al.* [71] reported a decrease in the fatigue life of CF-PEEK impacted by an energy of up to 25 J and cyclic loading under a tension-tension regime. From a C-scan inspection, the authors concluded that the delamination induced by the impact did not grow during fatigue life, leading to no apparent stiffness degradation over fatigue cycles, and final failure only due to the fatigue damage.

With the presence of a metal interlayer in CFRP, additional mechanisms to release the impact energy have been reported [67,68]. Aside from delamination of fiber-matrix interface, adhesion failure of the metal-composite interface along with plastic deformation of the metal layer seems to increase the absorption of impact energy considerably in comparison to CFRP, and so represents a promising strategy for improving the impact resistance of composites [67,68].

Although a finite element model (FEM) has been used to simulate the dynamic response of impacted aircraft composite structures and hence to predict critical impact scenarios and maintenance strategies [17,72,73], there are also simple analytical models that provide valuable estimations on the occurrence of critical delamination in impacted composites. Such models are mainly used in the screening stage of aircraft design [49]. Davis and Robinson [58] have shown that a single central delamination in the mid-plane of a composite plate propagates with an in-plane shear mode (fracture mode II) upon reaching a critical force. Based on these assumptions, the authors proposed an equation for the critical impact force, which is independent of the delamination size and plate's boundary conditions, as well as which neglects bending strains upon the impact test [74,75]. The accuracy of the equation has been proven for a large number of plate geometries and CFRP [49] and is used in this PhD to predict the occurrence of delamination with impacted friction riveted joints. These results will be discussed in Appendix J.

3.1.4 Durability of aircraft composite structures

For aeronautical structures, the concept of durability is defined as the ability of a structure to withstand degradation of various kinds, including fatigue, corrosion, accidental damage, and environmental deterioration, up to an extent controllable by acceptable maintenance and inspection programs [69]. However, the term has been generally used by the scientific community to define the effects of different environmental conditions on the strength of materials, joints, and structures [21,22,76,77]. In this PhD, the latter definition is adopted.

There are many sources of potential damage to aircraft composite structures related to the operational environment, including temperature, humidity, ultraviolet light, saline atmosphere and animal interactions, as well as exposure to chemicals, such as cleaning solvents, hydraulic fluids, and fuel. To design a durable composite structure, it is of the upmost importance to understand the mechanisms of degradation caused by environmental exposure and their effects on the long-term mechanical behavior of the structure. Due to time constraints, accelerated aging is normally used to analyze isolated damage, by exposure for a shorter time under an extremely harsh environment [78].

In a hydrothermally aged composite, the water uptake by the composite promotes plasticization of the molecules and swelling stress, caused by expansion forces and the stretching of polymeric chains [78,79]. Franco *et al.* [80] reported that such effects are beneficial for the mechanical performance of thermoplastic composites under sub-zero temperatures, while at room and higher (80 °C) temperatures they are degrading factors to fatigue resistance. The plasticization of a hydrothermally aged composite is reported to induce relaxation of clamp-up torque in bolted composites, degrading the bearing fatigue performance of the joints [81]. Another reason for the reduced fatigue life of a bolted composite is degradation of the metal bolt and its interface with the composite hole [82,83]. According to Miyano, Nakada, and Sekine [82], water absorption changes the failure mechanism from microbuckling to delamination, indicating a reduction of adhesion forces at the metal/composite and fiber/matrix interfaces.

For hydrothermally aged joints of metal and CFRP, a decrease of durability under quasi-static and cyclic loading can be explained by susceptibility of the metal to corrosion. Carbon fibers and metals, such as aluminum alloys, form a galvanic coupling. When in an aggressive environment (*e.g.* water and saline solutions), this leads to galvanic corrosion of the metal, which can be followed by pitting and crevice corrosion processes [18]. Titanium and titanium alloys are less susceptible to galvanic corrosion with CFRP, owing to stable passivation by an oxide layer (Ti_2O_3) over a large potential range [84]. Although they do not require protection, the aircraft industry has adopted coating systems for titanium alloy fasteners to mitigate risks of galvanic corrosion when in contact with other

metal parts made from magnesium and aluminum alloys [85]. Anodizing and the usage of sacrificial metal coatings and parts have been used as well [84–86].

3.2 Material's survey

3.2.1 Ti6Al4V

Ti6Al4V alloy is a low-density material developed after the Second World War to attend the requirements of high corrosion resistance and strength for aviation and aerospace applications [87,88]. Traditionally, aircraft metal fasteners, engine fans, and rotorcraft propeller blades are mainly produced from Ti6Al4V [88,89]. Moreover, through superplastic forming, the material has been used to manufacture engine nacelle components applied in the Boeing 757 aircraft [90]. However, the manufacturing of complex geometries in Ti6Al4V is still limited, owing to the raw material being expensive and the drawbacks of conventional process routes, including high material waste caused by machining [91]. Recently, powder-based concepts such as metal injection molding have shown potential as methods for Ti6Al4V, owing to their near net shape property and the consequent material cost savings [92,93].

Ti6Al4V is one of the alpha-beta Ti alloys that has a low-temperature stable alpha-Ti (α) phase and a high-temperature stable beta-Ti (β) phase. The crystalline structure of α-phase is a hexagonal close-packed array (hcp), responsible for the strength of the alloy, while β-Ti phase is a body-centered cubic array (bcc), which provides good ductility [94]. The aluminum alloying element stabilizes the α-phase, while oxygen, nitrogen, iron, and vanadium enable the β-Ti phase at low temperatures [94].

The insipient melting temperature of Ti6Al4V is reported to be 1650 °C, while in thermodynamic equilibrium at 995 °C there is a phase transformation from α-Ti phase to β-Ti phase under a heating regime known as the β-*transus* temperature [95–97]. As reported by Kitamura *et al.* [87], when Ti6Al4V is exposed to severe conditions of plastic deformation, such as with Friction Stir Welding (FSW), a non-equilibrium β-*transus* temperature is established at values lower than 949 °C. Other authors have reported a β-*transus* temperature in non-thermodynamic equilibrium between 670 °C and 690 °C for cooling rates of 50 °C/min to 10 °C/min [98,99]. Moreover, titanium alloys are considered to be generally difficult to process, owing to the high dependency of its flow behavior on parameters such as temperature, strain, and strain rate during thermomechanical processing [100]. During hot forging, titanium alloys have a work-softening behavior as the strain and strain-rate increase, which is intensified by adiabatic heating and localized shear band formation [101]. The

original microstructure also has an important influence on the hot working behavior of these alloys: a higher content of beta-phase improves the Ti6Al4V forgeability [100].

The microstructure of the Ti6Al4V alloy is thermomechanically dependent. The acicular morphology resultant from the fast cooling rate of the β-Ti phase field above the Ti6Al4V *solvus* temperature (Figure 3.3-b), represents the β→α phase transformation in a non-thermodynamic equilibrium, occurring in a diffusionless process (martensitic) [95]. The result is a homogeneous transformation of the bcc phase into an hcp (α') or orthorhombic (α") crystal lattice in lamellar packets over the given volume [102]. With a low alloying element content and fast cooling rate, α' is formed preferentially. The martensite starting temperature (M_s) is a function of the impurity level (O, Fe). Below the β-*transus* (Figure 3.3-c) temperature, time and temperature-dependent phase transformations are less intense, due to the high atomic packing attributed to hcp crystal structures [95]. Thus, slow cooling from an α+β field at temperatures below β-*transus* leads to a typical equiaxed morphology, which is characterized by an α-Ti phase matrix with β-Ti phase growing in the α-grain boundaries [103]. With slow cooling in a thermodynamic equilibrium from the β-phase field (Figure 3.3-d) a so-called Widmanstätten microstructure is formed, characterized by the nucleation of individual α lamellar packets and growth of retained β grains [94,95]. Although ω-phase and its transformations are included in the diagram of Figure 3.3, this metastable phase is not usually detected in the final microstructure of Ti6Al4V welds.

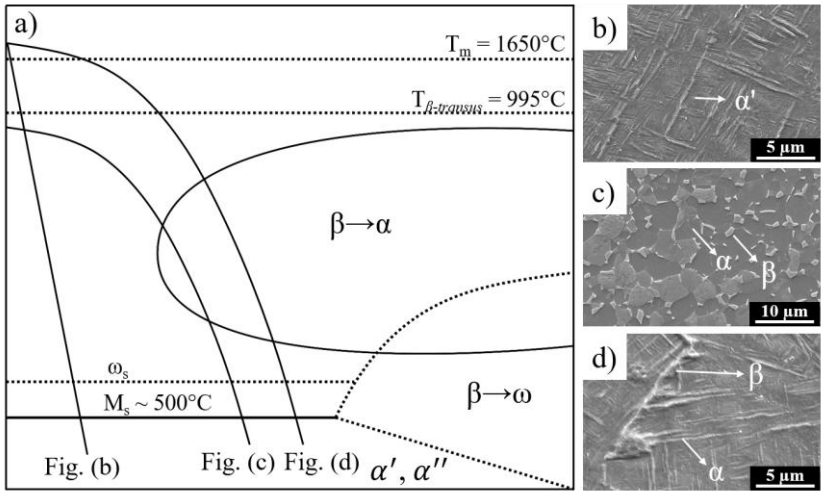

Figure 3.3 a) Continuous cooling transformation diagram of α+β titanium alloy, along with three cooling profiles: (b) fast cooling rate from a temperature above β-*transus*, resulting in a martensitic microstructure; (c) moderate cooling rate from a temperature below β-*transus*, resulting in a globular microstructure; (d) moderate cooling rate from a temperature above β-*transus*, resulting in a Widmanstätten microstructure. (Adapted from [104])

Conventional welding processes of titanium alloys such as laser beam welding (LBW) [60,105], gas tungsten arc welding (GTAW) [106], high vacuum electron beam welding (EBW)

[107,108], and solid-state welding processes such as ultrasonic welding [109] and friction stir welding (FSW) [106,110] have industrial applicability and thus have been widely investigated [60,106,109,111]. In GTAW of Ti6Al4V alloy, an increase in the arc current leads to high heat input and consequently low cooling rates, favoring α-Ti grain coarsening, formation of a Widmanstätten microstructure, and brittle intermetallic compounds [106,112]. Danielson, Wilson, and Alman [111] reported that significant oxygen contamination on the surface of Ti6Al4V alloy GTAW welds led to a predominance of acicular morphology. In the case of FSW, refinement of disoriented α-Ti acicular grains and martensitic transformation improved the tensile strength of the welds and the hardness of process-related microstructural zones [108]. Zhu, Lee, and Wang [109] demonstrated that by optimizing the welding pressure and time for ultrasonic welding of Ti6Al4V alloy and aluminum A6061, the hardness of both matrices increased, with apparent diffusion occurring across the welding interface. Kashaev *et al.* [113] joined Ti6Al4V to carbon fiber reinforced polymer using laser riveting along with surface-structured Ti6Al4V parts. Compared to the surface structured parts, conventional laser-riveted joints presented higher stiffness under quasi-static loading and lower fatigue performance which was explained by the stress concentration effect that is associated with a gradient of microstructure through the joint. Friction Riveting has been successfully used to join titanium and titanium alloys [25,26,114–116]. As reported by Borba *et al.* [114], the thermomechanical treatment upon Friction Riveting and the complex cooling regime resulted in a bimodal microstructural gradient over the plastically deformed Ti6Al4V rivet, showing a combination of equiaxed morphology, martensitic and Widmanstätten structures. Feistauer *et al.* [117] reported no microstructural transformation of Ti6Al4V metal injected parts when joined with polyetherimide parts by an ultrasonic joining process.

Ti6Al4V exhibits exceptional resistance to salt water, a marine atmosphere, and a wide range of acids, alkalis and industrial chemicals [118]. Its corrosion resistance is determined by the formation of a thin adherent titanium oxide layer (TiO_2) on the surfaces of titanium and titanium alloys [119].

3.2.2 CF-PEEK composite

CF-PEEK is a high-performance semi-crystalline engineering thermoplastic composite with application mainly in primary and secondary aircraft structures, such as the fixed leading edges of wings, ribs, and clips in Airbus and Boeing commercial aircraft as well as the rudder and elevators in the Gulfstream G650 business jet [55]. The PEEK matrix was invented and patented in 1978 by Imperial Chemical Industries [120] and its monomer structure consists of consecutive benzene rings, ether, and carbonyl groups (Figure 3.4-a). The ether improves material processability, while the aromatic backbone stiffens the monomer structure, and thus attributes high thermal and mechanical

resistance [120,121]. In addition, the material presents good mechanical properties under continuous service conditions at 260 °C [122], as well as excellent chemical and radiation resistance [123].

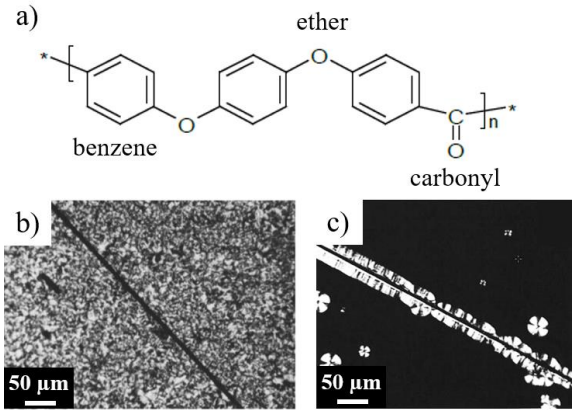

Figure 3.4 a) Polyether ether ketone monomer; b) Spherulitic crystal structure of PEEK; c) Trans-crystallinity of PEEK. Adapted from [124].

In aircraft structures with strict damage tolerance requirements, CF-PEEK overcomes the limitations of CF thermosets, particularly owing to the higher toughness of PEEK. The toughness of PEKK, however, is strongly influence by the temperature of analysis and degree of crystallinity. Garcia-Gonzalez *et al.* [61] has shown an embrittlement of PEEK impact behavior under a typical aircraft operational temperature range of -50 °C to +25 °C. Moreover, the low degree of crystallinity decreases the matrix ductility of CF-PEEK and consequently interlaminar fracture toughness [48,125].

The glass transition temperature of the amorphous phase of PEEK is 143 °C to 145 °C, while the melting temperature of the crystalline phase is in the range 340 °C to 345 °C [126–129]. Authors have reported a double melting behavior of PEEK [124,126,130,131]. This phenomenon is not fully understood and has been explained by the dual lamellar thickness of spherulites [130], simultaneous melting and recrystallization [124], and physical aging [131]. The crystal structure of PEEK has a spherulitic morphology (Figure 3.4-b) and findings in the literature [126] indicate that the crystalline unit cell is an orthorhombic crystal. The degree of crystallinity of PEEK can be increased up to 50 % by thermal annealing at 200 °C to 300 °C for 5 h to 40 h [126,130]. Additionally, authors [132–134] have published about an increase of PEEK degree of crystallinity owing to nucleation of crystals at the fiber-matrix interface, in a process known as trans-crystallization (Figure 3.4-c). This process is influenced by several factors, including a mismatch of thermal coefficients between the fiber and the matrix, surface roughness and treatment of fibers, and the processing conditions [132]. The crystalline interface has been shown to improve the mechanical performance of CF-PEEK by decreasing the discontinuity of mechanical properties between the fiber and the matrix, thereby enhancing the stress

transfer [124]. As reported in [135,136], another mechanism of PEEK crystallization can be induced by common organic liquids, such as toluene, acetone, and vapors such as CO_2, which is known as solvent-induced crystallization (SIC).

Thermal degradation of PEEK is reported to occur in two-step decomposition processes: by random chain scission of the ether and ketone bonds and by formation of stable radical intermediates from cleavage of the carbonyl bonds between 575 °C to 580 °C, and volatilization of phenols, CO, CO_2 and formation of a carbonaceous char at around 600 °C, which process continues slowly until 1000 °C [120,121,137]. The thermal stability of PEEK is shown to be higher under shielding gases than under an atmosphere of oxygen [121,137,138]. Under oxygen, the second decomposition step is mainly governed by oxidation of the carbonaceous char formed from the first decomposition step [121]. At temperatures above 600 °C and in air, the presence of carbon fibers is shown to decrease the onset-decomposition temperature of the PEEK, indicating that CF-PEEK is more susceptible to oxidize [121,137]. Crosslinking of PEEK resin is reported to occur in the presence of oxygen at temperatures commonly used for PEEK processing [139,140].

A typical range of PEEK processing temperatures is 400 °C to 485 °C [139] and PEEK can be processed by injection molding, extrusion [123,140], or selective laser sintering [127,141]. McLauchlin *et al.* [123] have reported the susceptibility of PEEK to multiple re-injection processes without compromising the mechanical properties of the material. The capacity of PEEK to retain its degree of crystallinity and therefore its strength enhances the applicability of CF-PEEK for aircraft structures over CF thermosets on thermal-based repair procedures.

3.3 Friction Riveting (FricRiveting) technique

3.3.1 General aspects

Friction Riveting is an alternative, friction-based spot joining process for multiple materials, patented by Helmholtz-Zentrum Geesthacht (HZG) in 2007 [24]. The process is based on the principles of friction welding and mechanical fastening, using frictional heat and pressure to plasticize and plastically deform a cylindrical metal rivet into a polymeric plate. The technology aims to overcome the main limitations of conventional techniques, such as adhesive bonding and mechanical fastening (riveting, bolting, clinching) that incur long joining cycles, multiple joining steps (surface preparation, drilling, cleaning, etc.), and stress concentration in the pre-drilled parts [30,142].

The flexibility of FricRiveting as it regards the joint configuration aspect is important for the structural design of joined components. Figure 3.5 illustrates the possible joint configurations. The simplest metal-inserted joint consists of a single polymeric part joined by a metal rivet. Additional demountable top layers can be further assembled into such parts prior to joining. The overlap and sandwich-like joints allow joint formation of dissimilar or similar polymeric plates or between metal and polymeric parts. For such configurations, the joining parts are almost completely inserted by the metal rivet, without previously drilling the plates of the upper joining part. This variant of the FricRiveting process is called Direct Friction Riveting (Direct FricRiveting), and is the subject of thorough investigation in this work.

Figure 3.5 Possible joint configurations of FricRiveting for multiple material types: a) metal-inserted, b) overlap, and c) sandwich-like joint.

The feasibility of the process has been demonstrated with several material combinations, mainly in the metal-inserted joint configuration, which includes unreinforced polymers [28,143,144], glass fiber [27,114,145] and carbon fiber reinforced polymers [25,115] joined with stainless steel, aluminum, and titanium alloys.

3.3.2 Principles of the process

The process allows multiple types of control, such as force control, time control, and multiple joining phases. For instance, a process with force control regulates the joining force by maintaining a pre-set level while the time is a response. Alternatively, the process can use time control, obtaining the force as a response. Moreover, the duration of each joining phase can be limited by time and displacement. For a time-limited process, the transition to the next joining phase happens as soon as a pre-set time of the previous joining phase is reached. When such a switch of joining phases depends on a pre-set axial position of the spindle, and consequently of the rivet, the limitation happens by displacement. Each combination of control and limitation is a possible process variant. The variant can be selected according to the requirements of joining cycle and knowledge maturity, regarding the material's response to heat generation during the process and geometric restrictions of the joining parts (*e.g.* accuracy of rivet penetration depth into thin polymeric plates).

The most consolidated and studied process variant is a force controlled and time-limited process comprising three phases: friction, forging and consolidation phases. The main steps of this process variant are depicted in Figure 3.6 for an overlap joint configuration. The polymeric parts are pre-assembled and fixed onto a backing plate, while the metal rivet, attached inside the chuck in the welding head, is aligned with the center of the polymeric parts (Figure 3.6-a). After the positioning step, the rivet is rotated at a pre-set rotational speed and pressed against the surface of the polymeric plate (Figure 3.6-b). The high rotation and axial force heat up the polymer part leading to softening and melting of a thin polymeric layer around the metal rivet. Due to the continuous plunging of the rivet into the polymeric part, the softened or molten polymeric layer is expelled from the joining area, forming a flash. Despite the unavoidable flash formation, such material can be removed during the joining process by using additional cutters on the welding head or be entrapped into features such as reentrances in the rivet head. Additionally, due to the low thermal conductivity of the polymer, the local temperature at the rivet tip rises and approaches the plasticizing temperature of the metal (60 % to 90 % of the melting temperature of metal alloys, such as aluminum and titanium). Thereafter, the rivet's rotation is stopped and the axial force is increased (Figure 3.6-c). The plasticized rivet tip is pushed against the cold polymeric layer beneath it, which creates the resistance required to deform the metal, anchoring it in the polymeric part. Finally, the joint is consolidated by cooling under pressure (Figure 3.6-d), the spindle retracts and the friction riveted joint is created.

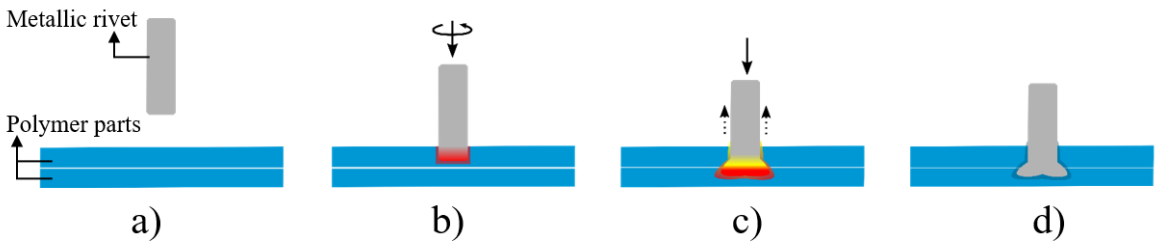

Figure 3.6 Schematic representation of Direct Friction Riveting process steps: a) positioning of the joining parts, b) friction phase (plunging of the rotating rivet through the upper part), c) forging phase (plunging of the rivet through the lower part and rivet plastic deformation), and d) joint consolidation. The flash formed during the process was not illustrated for simplification.

The plastic deformation of the rivet tip is a function of frictional heat and axial forces. However, when the heat supplied during the friction phase is sufficient to plasticize a large volume of metal and partially deform the rivet tip, the forging phase can be omitted, as reported by Proença *et al.* [145]. The authors showed that, for the combination of glass fiber reinforced polyamide 6 and aluminum alloy 6056-T6, an increase of axial force during the process did not have any significant influence on deformation of the rivet tip and likewise the mechanical performance of the joints produced. However, this behavior was only observed for samples

produced with high heat input conditions, which yielded high plasticizing levels in the metal part during the friction phase. Achievement of this can increase the energy efficiency of the process while also contribute greatly to the overall understanding of friction riveting.

Figure 3.7 illustrates the monitoring diagram of a force controlled and time-limited process with (Figure 3.7-a) and without (Figure 3.7-b) the forging phase. As shown in both cases, during the frictional phase, both rotational speed (black line) and joining force (dark gray line) increase to the defined level while the spindle moves downward (bright gray line). For the process without a forging phase, the axial displacement of the spindle decelerates whereas the force and rotational speed remain constant. In the case of a process with forging phase, the axial displacement accelerates as a response to increasing axial force while the rotational speed decreases. The final consolidation phase is similar in both cases, with no axial movement of the spindle and no rotational speed, but under some pressure, either additionally imposed or simply due to the weight of the spindle.

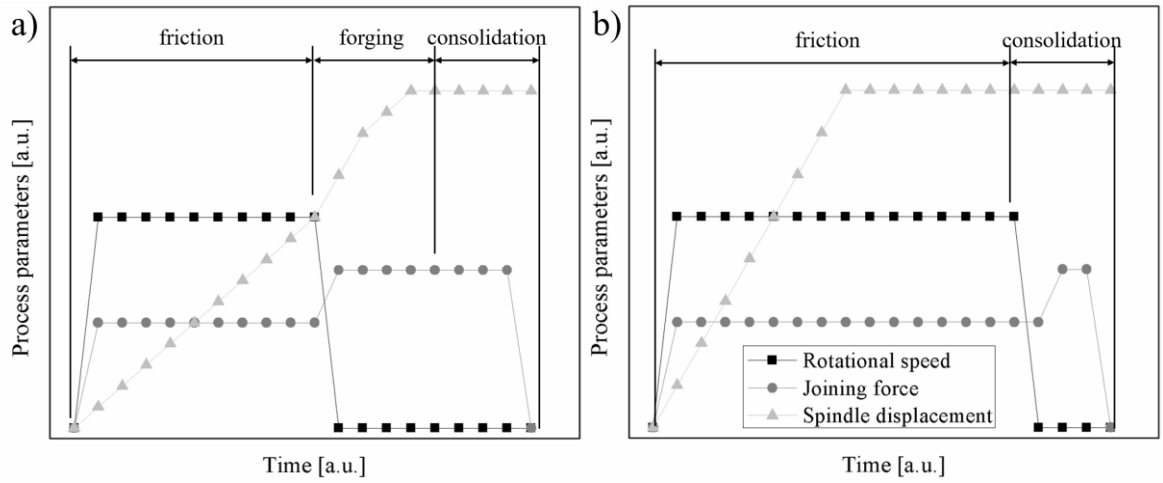

Figure 3.7 Schematic force-controlled FricRiveting diagram for a) a process with forging phase, and b) without forging phase.

The primary bonding mechanisms of friction riveted joints are mechanical interlocking, by the rivet tip widening into the polymeric part, and adhesion forces believed to be present where the molten polymer is in intimate contact with the metal. The efficiency of the rivet's mechanical anchoring has been shown to be the main contribution to the joint's mechanical performance under quasi-static loading [25,27,28]. According to Pina *et al.* [146], not only the widening of the rivet tip affects the joint strength, but also its shape, noting that overdeformation has a significant negative influence on the joint's strength. Although reported, this effect has not had any deep scientific investigation, and the topic will be covered in Section 6.3.2.

3.3.3 Heat generation

The heating regime of FricRiveting is fairly complex, described by [147] to be a combination of solid friction (a minor factor, normally less than one percent of the total generated heat) and viscous dissipation (internal shearing of macromolecules) in the molten polymer. A detailed analytical model for the heat input during FricRiveting was proposed and validated for unreinforced thermoplastic and aluminum joints [148]. In this case, viscous dissipation caused by the breakage of secondary bonds between the polymeric chains was shown to contribute most to the heating regime. Although this analytical model applies to unreinforced polymers, as it does not include a solid friction contribution of the reinforcement in composite, it must be improved for other materials.

The heat generation during FricRiveting is mainly dependent on the selection of joining parameters, materials, and geometry of the joining parts. The influence of the process parameters on the joint formation has been widely investigated for several material combinations [25,27,115,143–146,149] and will be reported later in this section. Regarding the material selection, compared to unreinforced polymers the reinforcement in polymeric composites contributes to heat generation by solid friction as well as increasing the viscosity of the molten polymeric matrix, leading to more plastic deformation of the rivet tip. Altmeyer [116] showed that, for the same joining parameters, there was more widening of a Ti grade 3 rivet tip with short carbon fiber reinforced PEEK than unreinforced PEEK, as illustrated in Figure 3.8. Additionally, the mechanical and thermal properties of the metal alloy also influence heat generation. For instance, with metal alloys that have low thermal conductivity and are susceptible to strain softening such as Ti6Al4V, adiabatic heat can be generated that can enhance plastic deformation of the rivet.

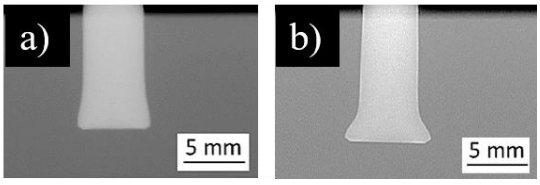

Figure 3.8 X-ray image of friction riveted joints of Ti grade 3 rivet and a) unreinforced PEEK and b) short carbon fiber reinforced PEEK. The joints were produced with the same joining condition (RS: 20000 rpm, FT: 1s, FP: 0.7 MPa, FoP: 0.9 MPa). (Adapted from [116])

Finally, the thicker the polymeric part and larger the area available for friction at the rivet tip, the more heat generated [148]. Such an area can be increased by using a larger rivet diameter

or by changing the rivet profile. Figure 3.9 illustrates a few possible geometries of the rivet. According to Borges [150], plain rivets generate more heat, owing to the larger frictional area of the rivet tip in comparison to threaded and hollow-threaded rivets, and therefore gave more plastic deformation at the rivet tip. The semi-hollowed rivets (Figure 3.9-d), despite having less initial frictional area, contribute to sideward deformation of the rivet tip, similar to the flare effect in friction self-piercing riveting [151–153].

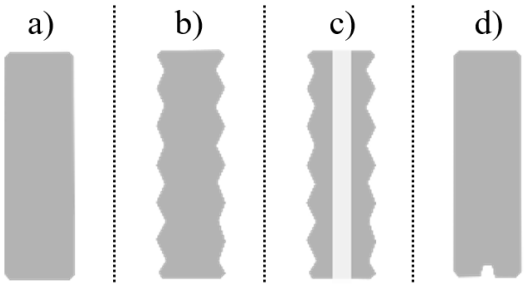

Figure 3.9 Possible rivet profiles for friction riveted joints: a) plain featureless surface, b) threaded, c) hollow-threaded, and d) semi-hollowed rivet.

3.3.4 Process parameters

The programmable process parameters depend on the selected process variable. For a conventional force controlled and time-limited process with a forging phase, there are five primary process parameters: rotational speed (RS), frictional time (FT), frictional force (FF), forging time (FoT), and forging force (FoF). In the case of a force-controlled and displacement-limited process, the joining time becomes a response, and displacement at friction (DF) is included as a process parameter. Further important parameters are: clamping pressure (CP) when the parts are clamped to avoid separation during the joining process (especially relevant for the overlap joint configuration), consolidation force (CF), and consolidation time (CT). Table 3.1 summarizes FricRiveting process parameters and their respective functions, according to statistical analysis performed for a wide range of materials.

Table 3.1 Controllable FricRiveting process parameters and their respective functions.

Joining parameter	Symbol	Function	Reference
Rotational speed	RS	Influences heat input and temperature evolution, plastic deformation of the rivet tip, molten polymer viscosity, microstructural changes in the metal and polymer/composite.	[25,27,154,155]
Frictional time	FT	Controls the joining speed, extent of heat generation, influences the rivet penetration depth and extent of polymer degradation.	[25,143,143,147]
Frictional force	FF	Influences the geometry and shape of the plastically deformed rivet tip and governs the molten polymer flow.	
Forging time	FoT	Controls the joining speed and forging regime.	
Forging force	FoF	Influences the geometry and shape of the plastically deformed rivet tip, and outward flow of molten polymer.	
Displacement at friction	DF	Controls the joining speed, extent of heat generation, and provides accurate rivet penetration depth.	[145]
Clamping pressure	CP	Hinders separation of overlapped parts, restricts squeeze flow of molten polymer, and affects the shape of the plastically deformed rivet tip.	[156]
Consolidation force	CF	Hinders geometric defects and distortion owing to the cooling regime.	[147]
Consolidation time	CT	Influences crystallinity of semi-crystalline composites, and the formation of volumetric defects.	

3.3.5 Advantages, limitations, and potential applications

The main advantages of FricRiveting in comparison to conventional mechanical fastening processes are [147]: (i) simple machinery is required, and thus the potential for transferability to a production line; (ii) no additional steps to the joining process are required; (iii) short joining cycles; (iv) clean process; (v) suitable for a wide range of materials, including thermoset composites [114]; (vi) good esthetic of joined composite components, owing to single side accessibility; (vii) comparable or improved quasi-static mechanical performance [27]. The main limitations of the process are [147]: (i) permanent joints are formed, inhibiting disassembly; (ii) a minimum thickness is required, dependent on the joint strength targets ($t_{min} > 3$ mm); (iii) recyclability and reparability

are complex owing to the loss of composite material during the process, although a thermoplastic can remelt and solidify several times; (iv) redesign of rivet and tooling may be required to avoid the use of external clamping devices for overlap joint configurations and tightening elements such washers and nuts to redistribute the stresses on the joint surface, and therefore to improve automation of the process.

The demand for disruptive technologies in the manufacturing of new aircraft generations in the near future may boost incentives in the sector for alternative joining technologies like FricRiveting that are suitable for lightweight materials, including thermoplastic composites and metal alloys. The technology can also provide cost savings, owing to the fast joining cycles and single step. Figure 3.10 illustrates two examples of potential application for FricRiveting in primary aircraft structures: composite floor structure (Figure 3.10-a and -b) and composite fuselage (Figure 3.10-c and -d). In Appendix A, a first demonstrator of a composite aircraft structure joined by FricRiveting is presented that was conceived as a result of this PhD work. The demonstrator is an integrated three-stringer CF-PEKK panel for a horizontal stabilizer produced by Fokker, Holland, as part of the Thermoplastic Affordable Primary Aircraft Structure (TAPAS) project [157]. FricRiveting successfully replaced bolts in the stringer run outs. Further mechanical tests of the panel are not within the scope of this PhD work and will be published elsewhere.

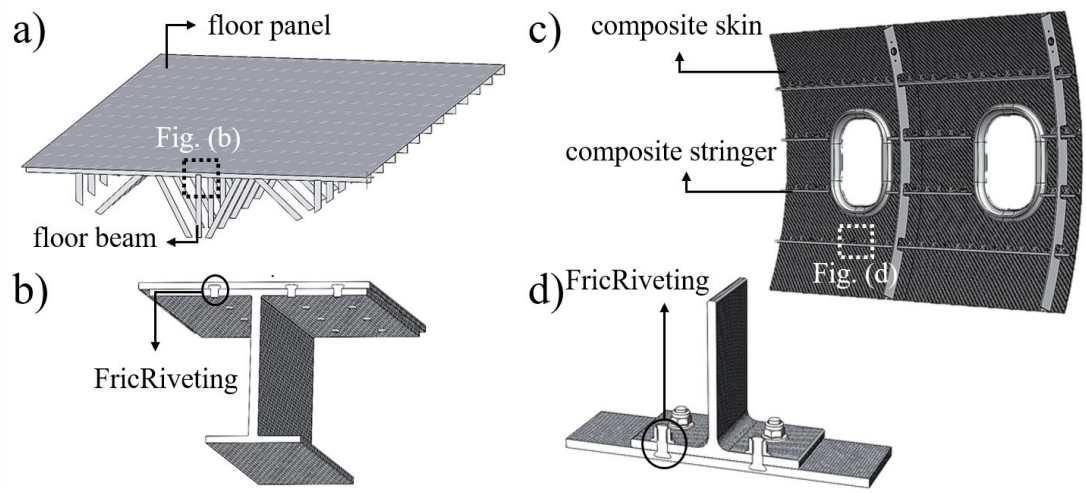

Figure 3.10 Schematic illustration of potential applications of FricRiveting in aircraft structures: a) composite floor structure, joining floor beam to floor panel, as detailed in (b); and c) composite fuselage, joining stringer to skin, as detailed in (d).

Chapter 4. Experimental Approach

This PhD thesis is structured as five work packages, as illustrated in Figure 4.1.

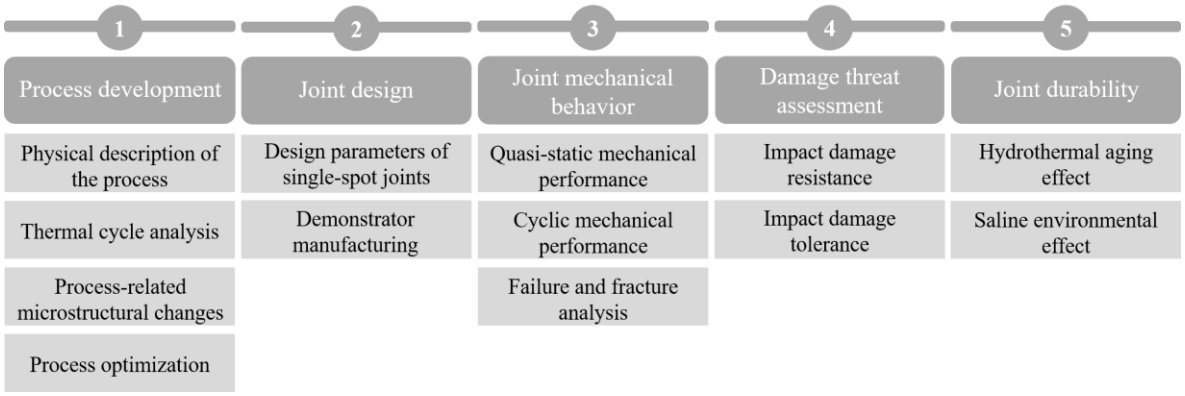

Figure 4.1 Experimental approach of this thesis.

In the first work package, the Direct Friction Riveting process was developed for an overlap configuration of CF-PEEK laminate parts joined with a Ti6Al4V rivet. After defining a range of process parameters with a one-factor-at-a-time (OFAT) approach, the joining process phases were defined. The physical and thermomechanical phenomena that occurred during these phases were thoroughly investigated by means of a thermal cycle analysis, an evaluation of the material flow and joining mechanisms, an understanding of the physicochemical changes in the composite, and a correlation of the joint microstructure with local mechanical properties. A wide range of analytical techniques were employed, including light optical microscopy (LOM), confocal laser scanning microscopy (CLSM), scanning electron microscopy (SEM), X-ray micro-computed tomography (µCT), thermal analysis by differential scanning calorimetry (DSC) and thermogravimetry analysis (TGA), microhardness and nanohardness. With a comprehensive understanding of process and joint features, Direct Friction Riveting was optimized using a full factorial design of experiments (DoE) and analysis of variance (ANOVA). The significance of individual process parameters and their influence on joint mechanical properties was analyzed, based on validated regression models. An optimized set of joining parameters that enhanced the mechanical properties of friction riveted joints while led to high levels of process reliability was obtained and used to produce further joints in the four consecutive work packages. The results of this optimization are briefly presented in Section 6.5.

In the second work package, the effect of the joint design on the joint's quasi-static strength was assessed. For single spot joints, edge distance, joint width, washer size and tightening torque

were considered as the key design parameters. The optimized joining condition for joint strength that was acquired as output of the first work package, along with the optimized joint design from the second work package provided fundamental knowledge to manufacture for the first time a Direct Friction Riveting demonstrator for the aircraft manufacturing sector. In Section 3.3.5 and Appendix A, details of the demonstrator are briefly presented as an exploratory investigation for scaling up of the process, although that is not the main focus of this thesis.

In the third work package, mechanical performance under quasi-static and cyclic loading was assessed along with failure and fracture analyses. The quasi-static mechanical testing was assisted by a digital image correlation system (DIC) to evaluate the strain fields in the joint during loading and secondary bending, and this was further correlated with the results acquired from a finite element model (FEM). The FEM also supported investigation of the fracture mechanisms carried out using SEM and ultrasonic testing (UT). A fatigue life analysis (S-N curve) of the joints was carried out using a two-parameter Weibull model. SEM and UT were also used to inspect the failure and fracture surface of friction riveted joints under fatigue.

In the fourth work package, impact damage resistance and tolerance of the friction riveted joints was evaluated. To assess impact damage resistance, the joints were impacted with different impact energies within a range of low velocity impacts and the damage size was investigated for the lower and higher impact levels. Mainly UT, CLSM and SEM were used to characterize the impact damage size. In the case of impact damage tolerance, damage initiation and propagation were assessed from the quasi-static residual strength of the joints, fatigue life, and by a joint stiffness degradation analysis.

In the fifth work package, the durability of the friction riveted joints under two different environments was investigated. The effects of hydrothermal aging and a highly saline environment were investigated on the surface features, local and global mechanical performance, and fracture surfaces using microhardness, nanohardness, DSC, CLSM, SEM and EDS.

Chapter 5. Materials and Methods

5.1 Base materials

5.1.1 Titanium alloy (Ti6Al4V)

Extruded plane rivets of Ti6Al4V with diameter of 5 mm and length of 60 mm were selected. This titanium alloy is widely used for bolts, rivets, and screws in aircraft structures and devices for the oil and gas industry due to its properties of high specific strength, good corrosion, and creep resistance [158]. Table 5.1 lists the experimentally determined chemical composition of the titanium alloy and the main properties of Ti6Al4V are summarized in Table 5.2.

Table 5.1 Chemical composition of Ti6Al4V alloy rivets.

Weight (wt. %)	**N**	**H**	**O**	**Fe**	**Al**	**V**	**Ti**
	0.002	0.003	0.107	0.217	6.2	4.5	Bal.

Table 5.2 Properties of the investigated materials.

	Ti6Al4V [158]	**CF-PEEK** [159]
Tensile/ shear strength, Ultimate [MPa]	989 ± 24* / 550	586 (warp, 0°) / 186
Tensile strength, yield [MPa]	920 ± 51*	152.0 ± 1.5 (warp, 0°)
Thermal transition [°C]	1650 (Tm) / 995 ± 15(β-*transus*)	143.0 ± 1.5 (Tg) / 343 ± 2 (Tm)*
Onset of decomposition [°C]	-	575.0 ± 0.8*
Thermal conductivity [W/m·K]	17.5	2.0
CLTE [µm/m-°C]	9.7 (20 °C to 650 °C)	30 (≤ Tg)

* Experimentally obtained

Figure 5.1-a illustrates the rivet geometry along with a microhardness map in the rivet extrusion direction, and Figure 5.1-b shows the typical globular microstructure of the titanium alloy in the same direction. Such a microstructure is comprised of two phases with an equiaxed β-Ti (body-centered cubic, bcc) phase located in the grain boundaries of an α-Ti (hexagonal close-packed, hcp) phase.

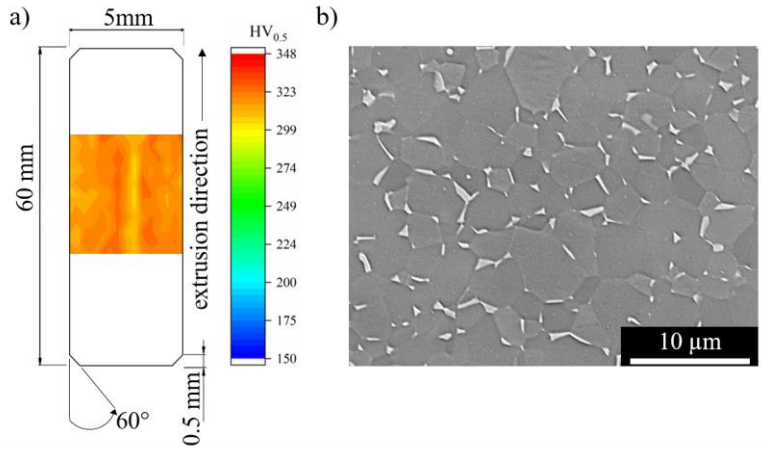

Figure 5.1 a) Geometry of the rivet along with a microhardness map of Ti6Al4V in the extrusion direction. b) Microstructure of Ti6Al4V in the extrusion direction.

5.1.2 Carbon fiber reinforced polyether ether ketone (CF-PEEK)

A woven carbon fiber reinforced polyether ether ketone (CF-PEEK) laminate 4.34 mm thick (nominal thickness) with a 58 wt. % nominal fiber content and stacking sequence of $[[(0,90)/(\pm45)]_3/(0,90)]_s$ (Toho Tenax Europe GmbH, France) was used as the composite part for overlap friction riveted joints. CF-PEEK is a high-performance semi-crystalline thermoplastic composite, which is mainly used in primary and secondary aircraft structures, because of its high strength, chemical resistance, and resistance to fatigue failure while aging [79,122]. The main properties of CF-PEEK are summarized in Table 5.2. Figure 5.2-a illustrates the microstructure of CF-PEEK in the warp direction (fibers oriented 0°). The weft fibers (fibers oriented 90°) interlaced with fibers oriented ±45° and the warp fibers can be identified, with the pattern of a 5-harness satin weave. Figure 5.2-b is an example of transmitted light optical microscopy of the PEEK matrix, showing the average size of nanometric crystals that have grown radially between the carbon fibers, as observed in Figure 5.2-c.

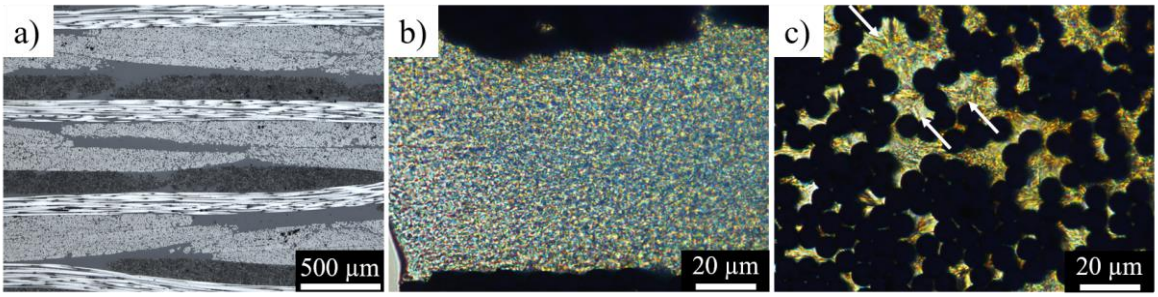

Figure 5.2 a) Microstructure of CF-PEEK in the warp direction, showing fibers oriented 0°, 90°, and ±45°; b) Transmitted light optical microscopy of PEEK matrix, showing nanometric crystals in fiber-free regions; and c) crystals between fibers, where they have grown radially. (Etchant: 1 wt. % potassium permanganate in a mixture of 5 parts by volume of concentrated sulfuric acid, 2 parts orthophosphoric acid and 2 parts distilled water. Etching time: 30 min) [160]

5.2 Methods

5.2.1 Joining procedure

Joining was performed using a FricRiveting gantry system (RNA, H. Loitz-Robotik, Germany) as depicted in Figure 5.3-a coupled with a pneumatic clamping system as illustrated in Figure 5.3-b, in which the overlapped composite parts were fixed and kept in intimate contact. The equipment has a capacity of 21000 rpm rotational speed, 24 kN axial forces and a working area up to 1 m^2 making possible the joining of a small coupon as well as a larger subcomponent and component. The gantry system allows the process to be controlled by force and position, and the duration of each process phase is limited by time and/or spindle displacement. Therefore, several process variants can be set up, combining process control and phase limitation types, which provides the flexibility to explore and tailor the process for different material combinations and joint geometries, thereby fulfilling a variety of industrial requirements. In this study, the FricRiveting process was conducted in force control mode and process phases were limited by the spindle displacement. Therefore, the joining parameters that were controlled and monitored during the process by the user interface were the rotational speed (RS), force (termed friction force, FF) and spindle displacement (termed displacement at friction, DF). The duration of the process phases is a response of such a process and so the time varies, *i.e.* it is not controllable.

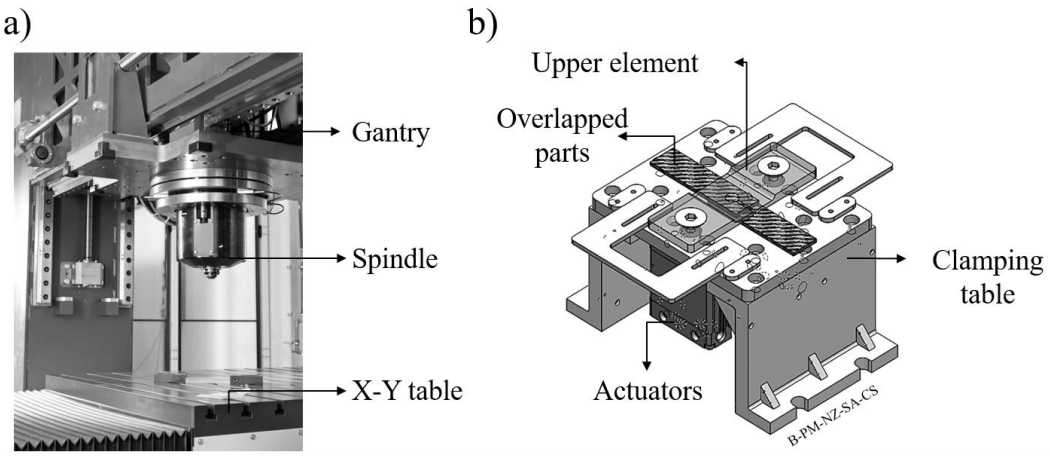

Figure 5.3 a) RNA system, showing the position of the rotation spindle and the X-Y movable table. b) Schematic illustration of the pneumatic clamping system, depicting the main elements and the position of the overlapped composite parts.

The pneumatic clamping system used was designed and conceived for this work. It was built of low carbon steel and consists of two actuators (DZF-50-25-P-A, FESTO, USA), each with a maximum capacity of 1.0 MPa, and an upper clamping element with a circular fixation diameter of 16 mm. In accordance with common practice of drilling procedures for fiber reinforced polymers [161], such a hole dimension distributes the clamping force homogeneously and reduces superficial damage of the composite by "peel-up" and "push-out". As well as ensuring intimate contact between the overlapped composite parts in the initial stages of the joining process, the clamping system also helps avoid additional separation during the cooling phase of the process, due to the differing coefficients of thermal expansion of the selected materials (see Table 5.2).

Prior to joining, the joining parts were cleaned using ethanol. The rivet was placed in a side magazine located on top the RNA movable table, from where the spindle takes it and transports it to the joining position. The composite parts were clamped between the clamping table and the upper element in the clamping system using a specific clamping pressure (CP). After positioning, the process parameters (RS, DF, FF) were set in the control unit of the RNA along with the joining position, and the process was started manually.

Figure 5.4 shows the joint geometry and sample dimensions mainly used in this work. A tightening torque of 1 N·m was applied together with an M5 stainless steel nut and washer (10 mm outer diameter) to pre-load the joints, minimizing any through-thickness failure and to increase the joint load capacity [33]. The stainless steel material for the nut and washer was selected for its low static coefficient of friction (μ_e) when in contact with Ti6Al4V ($\mu_e = 0.36$), [162], thereby increasing pre-load transferability and consequently the tightening efficiency. Changes to the geometry were proposed, to study the effects of the joint design on the joint's mechanical properties and are described in Section 5.2.11. Even so, all other characterizations were performed using the geometry depicted

in Figure 5.4, and from which regions of interest were cross-sectioned or machined according to the experimental requirements.

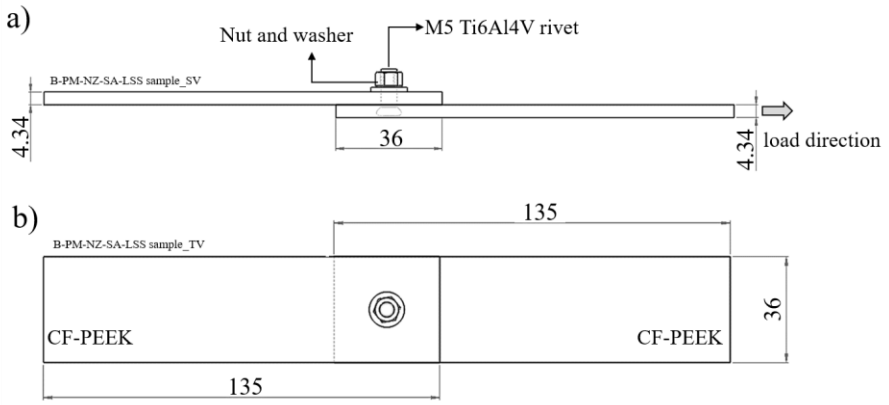

Figure 5.4 Geometry of friction riveted single lap joints: a) side and b) top views. All dimensions are in millimeters.

5.2.2 Experimental design

A 2^k factorial design of experiments (DoE) was chosen to evaluate the effect of process parameters on the joint's ultimate lap shear force (ULSF). This statistical model is particularly useful in the early stages of experimental work as it requires a small number of runs, with which the effect of the k factors can be estimated at all levels of interaction, and hence allows the drawing of valid and complete conclusions [163]. After parameter screening, using one-factor-at-a-time [115], three parameters were considered for the statistical approach: rotational speed (RS_{II}) and friction force (FF_{II}) in the second frictional phase, when the rotating rivet is plunged into the lower composite part and is plastically deformed with clamping pressure (CP). CP was included as an additional parameter to the joining process, owing to its influence on composite delamination and joint formation, as well as the shape of the plastically deformed rivet tip and separation of the overlapped composite parts [156]. In addition, the linearity assumption of the model was assured by replicating the center point of the 2^k design which also provided a better estimation of the experimental error. Three replicates of the 2^3 design and five replicates of the center point were performed in a randomized order. Moreover, the volume of metal plastically deformed in the rivet, indirectly measured by volumetric ratio (VR) (see Section 5.2.5.2.), was used as covariance due to its monotonic and almost linear relationship with joint strength, as described in Section 6.5.2. Covariance captures the degree to which the pair of responses – VR and joint strength – systematically vary around their respective means. When such a systematic covariance is detected and included in the model, a statistical model with lower error and

higher exploratory power is acquired [163]. Table 5.3 summarizes the levels of the full factorial design of experiments used in this work.

Table 5.3 Levels of the full factorial design of experiments.

Level	Factors		
	RS_{II} [krpm]	**FF_{II} [kN]**	**CP [MPa]**
-1	10	10	0.2
0	12.5	12.5	0.4
+1	15.0	15.0	0.6

A regression model for the ULSF response was obtained using Minitab software. An analysis of variance (ANOVA) was used to evaluate the significance of process parameters and their second level interactions on the ULSF response. The influence of the significance factors and interactions is described later in terms of joint formation mechanisms. A confidence interval of 95 % was selected and thus factors and interactions with p-values less than 0.05 were considered statistically significant, while those with p-values greater than 0.05 considered insignificant. By backward elimination of predictors, the insignificant factors were excluded in a stepwise manner until all predictors presented p-values smaller than 0.1. These criteria provided a regression model with a higher adjusted coefficient of determination (R^2_{adj}). Models with a high R^2_{adj} possess better explanatory power, therefore high predictability and consequently less error [164]. Validation of the reduced model was carried out using additional experiments within the parameters window of the full factorial design. The complete matrix of the experimental design and additional information of the regression model is presented in Appendix B.

To define the optimal joining condition, a composite desirability function was used in Minitab. This approach is widely applied by industry for the optimization of multiple response processes [165–167]. A desirability function ($d_i(Y_i)$) is defined based on a target (maximization, minimization, or assigned target value) for a specific response (Y_i), and this varies between zero and one, where a value of one indicates that the settings achieve favorable results for such a response [167]. The individual desirabilities are then combined by a geometric mean of k responses ($D_c = \sqrt[k]{\left(d_1(Y_1)d_2(Y_2)\dots d_k(Y_k)\right)}$), which gives the maximized overall desirability D_c – *i.e.* composite desirability – with respect to the controllable factors within the regression model. In this work, the ULSF response was set to the maximum force predictable by the reduced model along with separation between overlapped composite parts (G) varying from 0 mm to 0.3 mm. This range of gaps is actually the allowable separation of adhesively bonded parts used in aeronautic structures [168–170]. The individual desirability functions can be expressed by Equation 1.

$$d_i(Y_i) = \begin{cases} 0 & if\ Y_i < L_i \\ \left(\frac{Y_i - L_i}{T_i - L_i}\right)^s & if\ L_i < Y_i < T_i \\ 1 & if\ Y_i > T_i \end{cases} \quad (1)$$

where L_i, T_i, and U_i respectively correspond to the lower, target, and upper values desired for a response, while exponent s determines the importance to hit the target value. For maximizing a response, T_i is equal to U_i and exponent s is equal to 1.

5.2.3 Temperature measurement

The process temperature was monitored by infrared (IR) thermography and thermometry. An infrared thermographic camera (Image IR8800, InfraTec, Germany) was employed to record the temperature evolution of the expelled composite material, while nickel-chromium type K thermocouples (TC; Conatex, Germany) were employed to measure the temperature at the interface between the rivet and the composite parts. Figure 5.5 illustrates the position of the IR camera and an example of an IR thermograph, in which the area of measurement is indicated. A calibration range of 150 °C to 700 °C and a frame rate of 20 Hz were used. The sample's surfaces and the clamping components were painted black to avoid any reflective interference. From the thermometry curves, the heating and cooling rates were calculated by adopting a linear fitting of the experimental data.

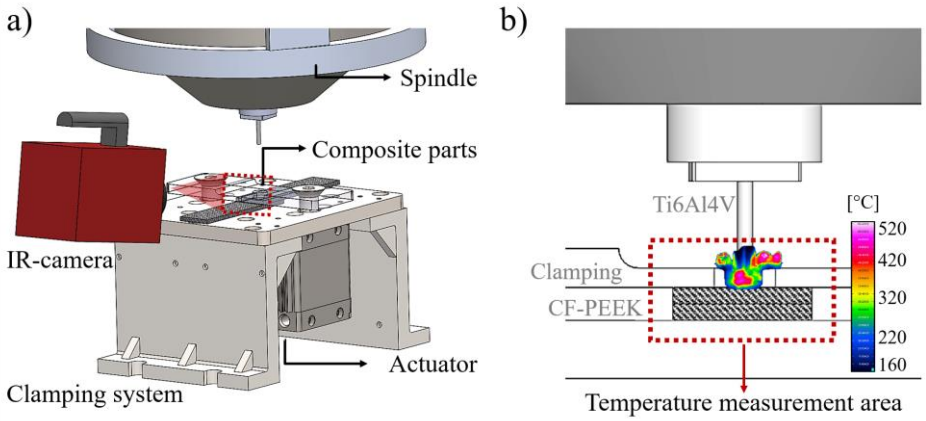

Figure 5.5 a) Joining set-up coupled with an IR camera. b) Overview of the temperature measurement area along with a typical IR thermograph on the joining parts.

Figure 5.6 shows schematically the position of two thermocouples (TC_I and TC_{II}) in the friction riveted joints, represented by the continuous black lines. Two 0.7 mm diameter TCs were placed diametrically opposite in between the overlapped composite parts, a few millimeters from the

rivet insertion path. In the figure, the white dotted lines represent the rivet penetration path and the final position of the plastically deformed rivet tip. Grooves with a depth of approximately 0.5 mm were machined in the lower composite part to accommodate the TCs and prevent their movement while joining. In fact, during the joining, after the rivet had plunged into the lower composite part, the TCs were damaged and so no longer recorded the temperature. For this reason, the temperature during the cooling phases could not be monitored by this approach.

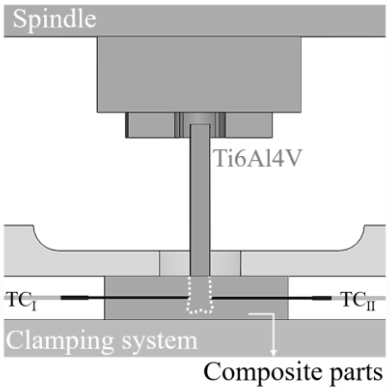

Figure 5.6 Schematic illustration of the positions of the thermocouples to measure the local temperature of the rivet tip interface.

5.2.4 Joint formation analysis

To study joint formation, the material flow, microstructural evolution and strain fields were investigated during the joining process with a stop-action approach. Such a method consists of a forced interruption of the joining process at specific stages, which provides specimens for further characterization as snapshots with arrested states of formation. Owing to the process variant adopted in this work, the stages selected were defined according to the respective times (t_I 0.25 s, t_{II} 0.55 s, t_{III} 0.70 s, t_{IV} 1.10 s) of the four levels of pre-set spindle displacement (d_I 2.2 mm, d_{II} 4.40 mm, d_{III} 6.6 mm, d_{IV} 8.0 mm), as shown in Figure 5.7. One joint was produced at each of these stages.

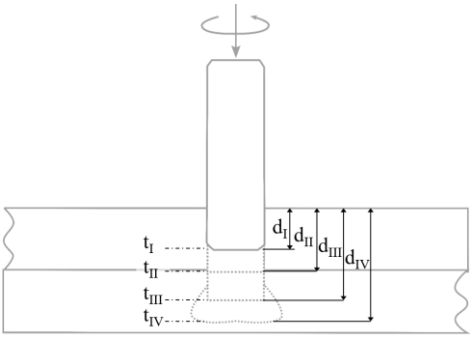

Figure 5.7 Schematic illustration of the stages selected for stop-action samples, according to spindle displacement.

To assist analysis of material flow a 5.7 mm transparent poly(methyl methacrylate) (PMMA) plate was used instead of a CF-PEEK part in the upper and lower positions of the overlapped joint configuration. This enabled better observation of the fiber breakage, the composite flow direction and evolution.

Strain fields during the Friction Riveting process that influence the joint formation were measured by a digital image correlation (DIC) system (ARAMIS-4m, GOM, Germany). The surface displacement and deformation of the clamping device and the specimen were used to indicate regions of material in different stress fields — *i.e.* under compression or tension. The stochastic speckle pattern required on the clamping device and specimen surfaces was prepared with black ink spray painted onto a white background. Figure 5.8-a depicts the DIC areas along with an example of a recorded initial frame (t = 0 s) which shows the displacement distribution in the Y-axis direction (Figure 5.8-b). An incoherent light source was used to illuminate the DIC areas. A digital camera equipped with a 50 mm focal length lens placed perpendicular to the DIC areas was used to record the images. A frame rate of 7 Hz, a facet frame of 15 pixels, and a facet step of 13 pixels, giving an overlap of 2 pixels, were set up in accordance with the image resolution required for accurate results.

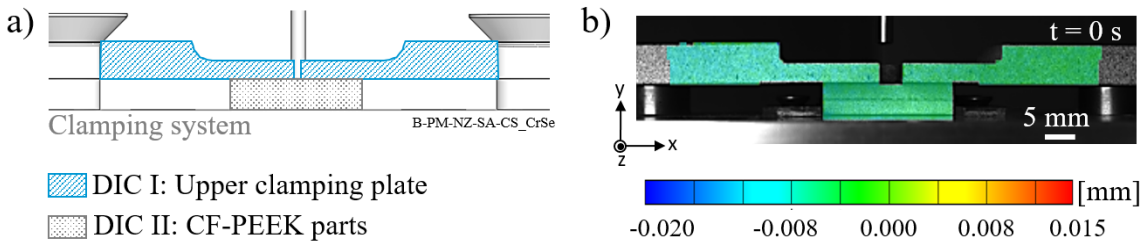

Figure 5.8 a) Overview of the clamping system showing the DIC areas analyzed, b) Example of displacement distribution through the upper clamping element and the overlapped composite parts in the Y-axis direction, at the start of joining.

5.2.5 Microstructural analysis

5.2.5.1 Materialographic procedure

To reveal the joint's microstructure, mid cross-sections were prepared following standard materialography procedures. The samples cut were embedded in a cold mounting epoxy resin, then ground and polished to obtain a smooth surface. The microstructure of the Ti6Al4V rivet was revealed by etching the samples with Kroll's reagent (96 mL H_2O, 6 mL HNO_3, and 2 mL HF), for 15 s of exposure at room temperature.

5.2.5.2 Microscopy

Light optical microscopy (LOM) (DM IR microscope, Leica Microsystems GmbH, Germany) was employed for initial inspection of the joint mid cross-sections. From these LOM images, the rivet penetration depth (H), rivet tip width (W), and anchoring depth (D_p) were measured as indicated in Figure 5.9-a. H, W, and D_p were used to calculate the volumetric ratio (VR) from Equation 2 by adopting the analytical model proposed by Pina *et al.* [143,146]. VR is the interaction volume of composite material above the plastically deformed rivet tip and this is used to assess the anchoring efficiency of the friction riveted joints.

Details of the joint microstructure and the fracture surfaces were characterized by scanning electron microscopy (SEM) (FEI Quanta^{TM} 650 FEG, FEI, USA). Voltages up to 10 kV and working distance of 10 mm were used. The SEM was equipped with an energy dispersive X-ray spectroscopic (EDS) detector (TEAM^{TM} EDS, EDAX, Germany) used to qualitatively analyze the chemical elements at the joint fracture surface. In preparation for SEM analysis, the samples were gold sputtered (Q150R ES, Quorum Technologies Ltd., England) for 30 s with a current of 65 mA. The metal coating makes the non-conductive composites conductive, suppressing the electron charging effect, which arises from interaction of the electron irradiation with the sample surface. In addition, confocal laser scanning microscopy (CLSM) was used to provide a three-dimensional analysis of the bearing area (A_b) of joint fracture surfaces and the dimensions (A_i and D_{rd}) of accidental damage introduced by impact testing (see Section 5.2.9.3). For this purpose, a 5X magnification lens was set and three replicates of each analysis were performed. Figure 5.9-b shows an example of the fracture surface measurement and Figure 5.9-c and -d highlights typical measurements of the impact area.

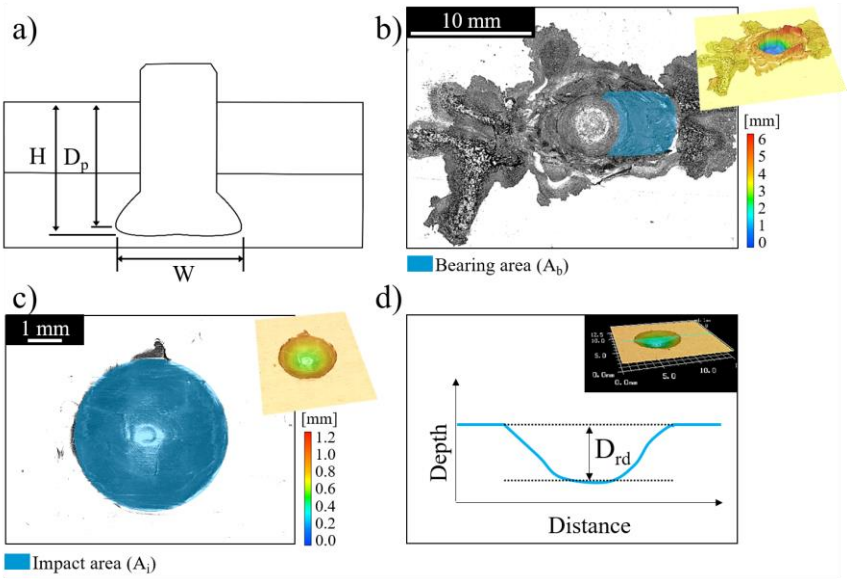

Figure 5.9 a) Schematic illustration of a single overlap friction riveted joint showing geometrical features of the anchoring zone (H, D_p, and W); b) example of the bearing area (A_b) measurement from a joint fracture surface, showing the laser intensity image along with the 3D display of the fracture; c) example of the impact area (A_i) measurement for 5 J impact energy, showing a laser intensity image along with the 3D display used to measure d) the residual dent depth (D_{rd}).

$$VR = \frac{Dp \times (W^2 - D^2)}{H \times W^2} \ [a.u] \quad (2)$$

5.2.6 Non-destructive testing of friction riveted joints

5.2.6.1 X-Ray micro-computed tomography

To evaluate the integrity of the composite and the rivet tip plastic deformation prior to mechanical testing and analysis of the fracture surfaces, non-destructive X-ray micro-computed tomography (µCT) (Y. Cougar- FineFocus X-ray system, YXLON, Germany) was carried out. VGStudio MAX 3.0 software was used to assess reconstructed three-dimensional models of failed joints and two-dimensional projections of the as-joined parts. A 3D volume segmentation was performed to analyze the distribution and size of detectable defects. An operating voltage of 60 kV current of 95 µA and no pre or post-processing filters were employed.

5.2.6.2 Ultrasonic testing

The defects introduced in the joints by the joining process, under quasi-static and cyclic loads and after impact, such as voids and composite delamination, were primarily assessed by ultrasonic (US) inspection (USPC 3040 DAC, Dr. Hilger Ingenieurbüro, Germany). The pulse-echo method was adopted, which is characterized by a single transducer working as transmitter and signal detector. The coupling medium was demineralized water. The signal detected during measurement was plotted as a function of position, providing what is known as an amplitude C-scan display. Figure 5.10-a and -b show the set-up for the US measurement. The bottom surface of the lower composite plate was scanned, while the upper composite plate was defined as a backing — *i.e.* ultrasound signals from this region were discarded. Figure 5.10-c shows a typical cross-sectional view of the as-joined friction riveted joints along with the defect's depth measurement, where the position of the rivet tip into the lower composite plate is highlighted by a circle of dashed lines.

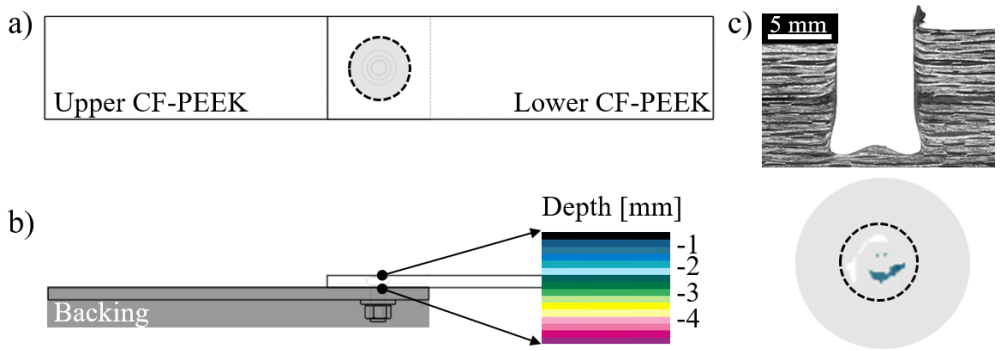

Figure 5.10 a) Schematic illustration of the bottom view of the joint, highlighting the region of US measurement; b) side view of the friction riveted joint, showing the selected backing surface and the scale of the defect depth based on the lower composite thickness; c) typical cross-sectional view of the as-joined friction riveted joint along with US measurement.

5.2.7 Physicochemical changes of the composite part (DSC and TGA)

Local physicochemical changes of the composite were evaluated using differential scanning calorimetry (DSC 200 F3 Maia, Netzsch, Germany) and thermogravimetry (TG 209 F3 Tarsus, Netzsch, Germany). Samples of approximately 6.0 mg were extracted from the base material, expelled flash, and squeezed materials for DSC analysis and placed in an aluminum crucible. Heating and cooling rates of 10 K/min were selected in the temperature range of 25 °C to 450 °C, under a

nitrogen atmosphere (flow rate of 50 mL/min). Three replicates were tested. The degree of crystallinity is determined by Equation 3 [171], adopting a melting enthalpy of 130 J/g for 100 % crystalline PEEK.

$$Xc = \frac{\Delta H_m}{\Delta H_m^0 (1-x)} \times 100 \ [\%] \qquad (3)$$

where X_c is the degree of crystallinity, ΔH_m is the melting enthalpy obtained in the peak melting area, $\Delta H°_m$ is the melting enthalpy of PEEK 100 % crystalline (130 J/g [172]), and x is the fiber weight fraction.

Samples of approximately 13 mg were extracted from the expelled flash and squeezed material for TGA and placed in an alumina crucible. A heating rate of 20 K/min from 25 °C to 800 °C under a nitrogen atmosphere (flow rate of 90 mL/min) was employed. Three replicates were tested.

5.2.8 Local mechanical properties

5.2.8.1 Microhardness

The microhardness over the cross-section of the Ti6Al4V rivet in the friction riveted joints was investigated to qualitatively identify metallurgical transformations related to the process. The measurements were performed using Vickers Zwick/Roell-ZHV indenter equipment, following the ASTM E384-17 [173] standard. A microhardness map was acquired from one half of the specimen, which suffices owing to joint symmetry, with an indentation load of 4.9 N and a holding time of 15 s. The spacing distance between indents was 300 μm.

5.2.8.2 Nanoindentation

To evaluate the local mechanical properties of the composite in the friction riveted joints, nanoindentation was carried out using a nanoindenter ® XP (MTS System Corporation, USA), equipped with a Berkovich diamond indenter. Nanoindentation was selected to minimize any data deviation due to interaction of the indenter with fibers. The hardness and stiffness were calculated as a continuous function of the indenter penetration depth, using the continuous stiffness measurement (CSM) method. This is particularly useful for polymeric materials due to its sensitivity to variations in mechanical properties between amorphous and crystal phases of the polymers [174]. A dynamic contact module (DCM) indenter head was used to minimize errors in surface detection and to improve the resolution of the measurement by measuring the harmonic contact stiffness as a continuous

function of indentation depth [175]. A maximum indentation depth (h_{max}) of 1 µm was fixed while the maximum indentation load (P_{max}) was recorded at h_{max}. A frequency target of 45 Hz, a surface approach distance of 1 µm and an allowable drift rate of 0.05 nm/s were set. Figure 5.11 illustrates the two regions of the joined CF-PEEK selected for measurement along with a typical loading and unloading curve of the CF-PEEK base material acquired from the test. P_{max} corresponds to the peak indentation load when h_{max} is reached and h_f is the final displacement after release of elastic deformation. A minimum of three indents were performed in each of the regions, which correspond to the composite thermomechanically affected zone (CTMAZ) (Area I, Figure 5.11-a) and the base material (BM) well away from the joining area (Area II, Figure 5.11-a).

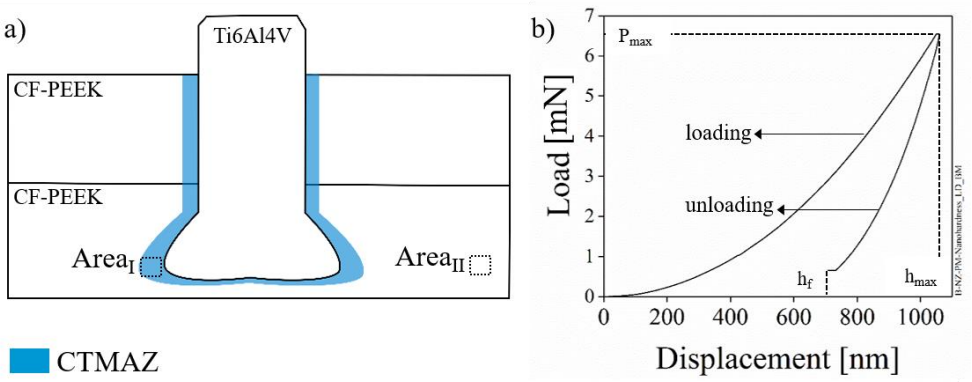

Figure 5.11 a) Schematic illustration of the areas of nanohardness measurement; b) typical loading-unloading curves of the CF-PEEK base material.

5.2.9 Global mechanical properties

5.2.9.1 Single lap shear (SLS) testing

Single lap shear testing was carried out to analyze the quasi-static mechanical performance of joints. The joint strength was evaluated in accordance with ASTM D5961-17 [176] using a universal testing machine (model 1478, Zwick Roell, Germany) with a load capacity of 100 kN. The transverse test speed was 2 mm/min and testing was carried out at room temperature (21 °C). The experiments were assisted by a digital image correlation (DIC) system (ARAMIS-4m, GOM, Germany) to record the displacement of joint surface under tensile loading. The joint surfaces were painted to create a stochastic speckle pattern that is used to monitor joint deformation by comparing the relative distance between black dots over different stages of deformation. The set-up described in Section 5.2.4 was adopted.

To determine the plastic deformation and damage accumulation in the joint under quasi-static loading, a consecutive loading and unloading approach was used. Each specimen was loaded five times at levels of 25 %, 50 %, 70 %, 85 %, and 90 % of the ULSF. Three specimens were tested at each load level, with one sample cross-section analyzed by microscopy. After each level, all the joints were qualitatively inspected by the non-destructive techniques (NDT) of the ultrasonic (US) method.

5.2.9.2 Fatigue experiments

The fatigue tests were carried out using a servo-hydraulic machine (Instron/Schenk, Germany) with ±10 kN load capacity in a tension-tension regime at R = 0.1. A constant amplitude sinusoidal loading at a frequency of 5 Hz was set. Load levels of 60 %, 65 %, 70 %, and 80 % of the ULSF were used to determine the Wöhler (S-N) curve. For post-impact fatigue tests, the load levels used were 60 %, 70 %, 80 %, and 90 % of the joint's residual strength. A minimum of three specimens for each level was tested. The single overlap joint configuration, whose geometry is depicted in Figure 5.4, was used. Complete joint failure and the joint withstanding 10^6 cycles were used as conditions to stop the test. The joints that survived 10^6 cycles without failure (termed run-out specimens) were subsequently tested under quasi-static conditions, as described in Section 5.2.9.1, and their residual strength reported.

For friction riveted joints, joint strength is expressed as a ratio of the load level in newtons to the average of the real area (A_r) of the hole, as depicted in Figure 5.12. The real area of the hole was measured from X-ray micro-computed tomography images before mechanical testing by using ImageJ software. This approach was successfully used by Blaga *et al*. in [27].

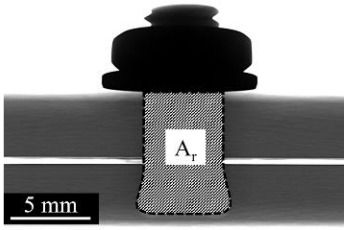

Figure 5.12 A cross-sectional view of the single lap joint obtained by X-ray micro-computed tomography that was used to measure the real bearing area (Ar).

A variation in the joint stiffness was used as an indication of damage accumulation throughout the joint fatigue life. The calculation for stiffness degradation $D_s = 1-(E/E_0)$, with E_0 as the initial joint stiffness, was applied.

Statistical analysis of the fatigue life data

A Weibull distribution was used to model fatigue life of the friction riveted joints according to the DIN 50100:2016-12 [177] standard. The two-parameter Weibull modeling approach, which considers a set of samples rather than individual results, was applied to the model and confidence estimation. This distribution has been reported in the literature as a useful tool to evaluate the broad scattered fatigue data of composite structures and their reliability [178–180].

The probability density function (PDF) of the two-parameter Weibull distribution is presented in Equation 4. An integration of the PDF results in a cumulative density function (CDF) (Equation 5) gives the probability of joint failure. Equation 6 is derived from Equation 5, with the latter corresponding to the probability of the survival, or reliability, of a set of joints [178].

$$f(x) = \frac{\beta}{\alpha}\left(\frac{x}{\alpha}\right)^{\beta-1} e^{-\left(\frac{x}{\alpha}\right)^{\beta}},\ \alpha \geq 0, \beta \geq 0 \quad (4)$$

$$F_f(x) = 1 - e^{-\left(\frac{x}{\alpha}\right)^{\beta}} \quad (5)$$

$$F_s(x) = R_x = 1 - F_f(x) \quad (6)$$

where x is the fatigue life; β is the Weibull slope; α is the characteristic life or the number of cycles in which 63.2 % of the sampling is expected to fail; $F_f(x)$ is the probability of failure; and $F_s(x)$ is the probability of survival or reliability (R_x).

Based on the above-mentioned equations, a Weibull distribution and reliability analysis were carried out. In this study, S-N plots were drawn for R_{99}, R_{90}, and R_{50}.

5.2.9.3 Drop weight impact testing

To study impact damage tolerance of the friction riveted joints, drop weight impact tests were carried out using an instrumented impact machine, following the ASTM D7136-15 [181] standard, at room temperature. Figure 5. 13 illustrates the set-up for the drop weight impact test. The specimen geometry depicted in Figure 5.4 was used. A pneumatic clamping system was employed to ensure better distribution of the impact energy and prevent movement of the specimens. A hardened steel dart impactor with a hemispherical 12.5 mm diameter tip fixed to the weight was impacted on the center of the joint's back surface. The edges of such surface were clamped between circular rings of 15 mm inner diameter. An anti-rebound system was coupled to the machine, to prevent multiple impacts during testing. The impact energies of 5 J, 10 J, 20 J, and 30 J were selected and achieved by

varying the drop weight, while the height was kept constant at 300 mm. The load over time was acquired and used to calculate the absorbed energy (U_t).

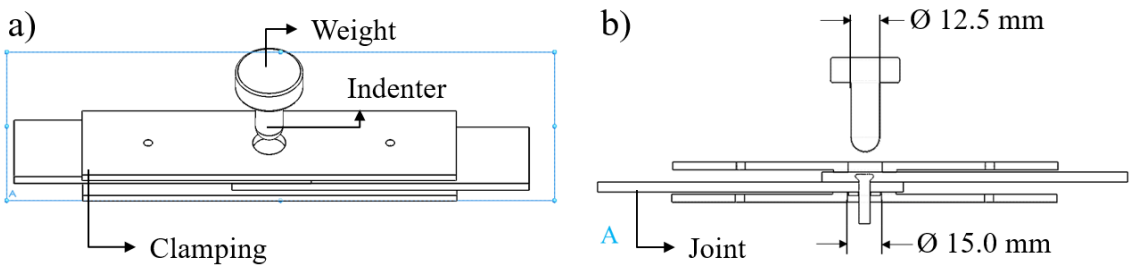

Figure 5. 13 a) Set-up of the drop weight impact test; b) neutral plane of the set-up, showing the dimensions of the indenter and the inner diameter of the ring from the clamping system.

The post-impact strength and post-impact fatigue behavior were obtained, following the testing described in Section 5.2.9.1 and Section 5.2.9.2, respectively. The impact damage was characterized by impact area (A_i) and residual dent depth (D_{rd}), using confocal laser scanning microscopy (see Section 5.2.5.2), ultrasonic inspection (see Section 5.2.6.2), and X-ray micro-computed tomography (see Section 5.2.6.1). A cross-section of the impacted joints was prepared using a standard materialography procedure and impact-induced through-thickness defects were characterized by means of light optical microscopy (LOM) and scanning electron microscopy (SEM).

5.2.10 Durability experiments

5.2.10.1 Accelerated aging

The artificially accelerated age testing was used to predict and understand the long term behavior of the friction riveted hybrid joints. Owing to the high environmental sensitivity of polymeric composites under operational conditions, such testing is widely used to certify the application of such materials in aircraft structures [21,22,182,183]. The 24 specimens and reference base materials (Ti6Al4V rivets and CF-PEEK plates) were first weighed and then placed in an artificial aging chamber (VCL 003, Vötsch Industrietechnik, Germany) for 28 days. The temperature of the chamber was set to 71 °C with a 95 % relative humidity, following the recommendations of the ASTM D3762-03 [184] standard. After 3, 14 and 28 days, 8 specimens were removed from the chamber each time, visually inspected and weighed again. Their mass change (M_n) was calculated using Equation 7 [185], where W_w is the weight of the wet (aged) specimen, and W_0 is the original weight. The influence of this hydrothermal aging on the joint mechanical performance was evaluated

from the joint's residual strength (as described in Section 5.2.9.1) and local mechanical changes in the composite (as described in Section 5.2.8.1). The failure behavior was evaluated by SEM.

$$M_n = \frac{W_w - W_0}{W_0} \times 100\ [\%] \quad (7)$$

5.2.10.2 Salt spray aging

Samples were exposed to a corrosive environment following the ASTM B117-18 [186] standard. The salt spray and fog had a chemical composition of 5 % NaCl solution (pH varying between 6.5 and 7.2). A standard salt spray cabinet (SC 450, Weiss Umwelttechnik GmbH, Germany) was used where the samples were aged continuously at 35 °C. The experiment provides a controlled and accelerated corrosive environment, which has been used to artificially assess the corrosion of the composite/metal hybrid joints in a real condition [187]. The 25 joints and reference base materials (Ti6Al4V rivets and CF-PEEK plates) were vertically hung from a polymeric wire tightened within a 16 mm diameter hole drilled in the CF-PEEK part, as schematically shown in Figure 5.14. Periodically, at increasing aging times (72 h, 168 h, 336 h, 504 h, 1008 h), five specimens were randomly removed from the cabinet, cleaned out, dried, weighed, and mechanically tested according to Section 5.2.9.1. Changes of physicochemical and local mechanical properties in the composite after exposure were assessed, following the procedures described in Section 5.2.7 and Section 5.2.8, respectively.

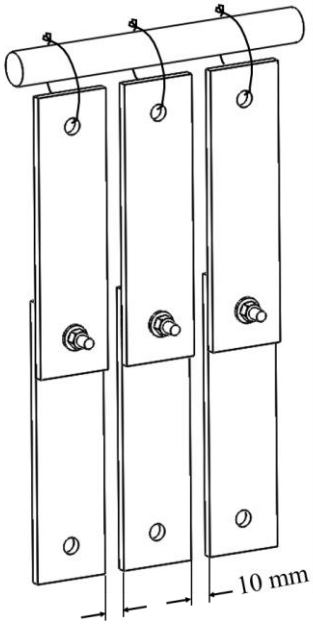

Figure 5.14 Specimen position in the salt spray cabinet..

5.2.11 Joint design

5.2.11.1 Torsion testing

A torsion test was performed to define the allowable tightening torque (TT) for friction riveted joints (known as the "break loose" torque) above which the anchored rivet loses its adhesion inside the composite base plate. The sample used is described in Section 5.2.1. A stainless steel nut and washer were tightened on the free length of threaded rivet using a torque spanner, while the composite parts were fixed in a bench vise. The tightening force applied by the washer and nut was measured using a 25 kN washer load cell with a 5 mm inner diameter hole. The load cell was placed between the nut and the washer. The tightening torque was applied and constantly increased until the break loose torque was achieved. Once the break loose torque was defined, the influence of the TT on the joint strength was investigated for three allowable torque levels (TT = 0.5 N·m, 1.0 N·m and 1.5 N·m) and joints were mechanically tested according to ASTM D5961-17 [176].

5.2.11.2 Key design parameters

To design a friction riveted joint capable of carrying high loads and that does not fail catastrophically, the effects of the edge distance (e), joint width (w), tightening torque (TT), and outer diameter of washer (D_w) on the joint strength were evaluated. The design parameters were selected by considering the main factors that influence the structural integrity and reliability of conventional bolted composite structures [33,43,188–190]. Although the composite lay-up and thickness introduce anisotropic properties and influence normal and shear interlaminar stresses, the material's features were not accounted for in this work. The specimen length (l) varied according to *e* to keep constant the joint's free length, *i.e.* the distance between the grips. Figure 5.15 illustrates the design parameters of a single spot friction riveted joint, while Table 5.4 summarizes the selected levels of each parameter.

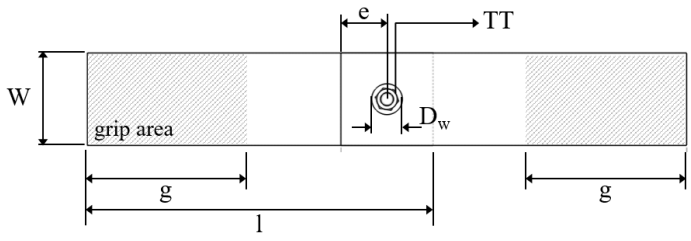

Figure 5.15 Schematic illustration of the friction riveted single lap joints, showing the design parameters selected for study of the single spot joint.

Table 5.4 Dimensions of the friction riveted single lap joints employed for the joint design study.

	Factors				
	e	**w**	**D_W**	**g [mm]**	**TT [Nm]**
Single spot joint	1.5D, 2D, 3D	3D, 5D, 7D	2D, 4D, 5D	75	1

Dimensions of e, w and D_W are multiples of the original diameter of the rivet (D = 5 mm)

5.2.12 Finite element analysis (FEA)

The finite element (FE) method was used to analyze the interlaminar stress distribution near the friction riveted joints and damage evolution during simulation of a single lap shear test. A standard explicit three-dimensional model was developed for single spot friction riveted joints using commercial software Abaqus/Standard (Version 6.14-2, Dassault Simulia, France). Figure 5.16 illustrates the model, along with detailed geometry of the parts that were defined based on the real dimensions of optimized friction riveted joints. The model comprises three parts: Ti6Al4V rivet, lower and upper CF-PEEK plates. An eight-node linear brick element (C3D8H) was used to mesh the rivet while a quadrilateral continuum shell element (SC8R) was used to mesh the composite parts. A geometrical topology function was employed to improve the mesh of the parts by integrating their faces, which minimized its complexity. Details of the mesh can be found in Appendix C.

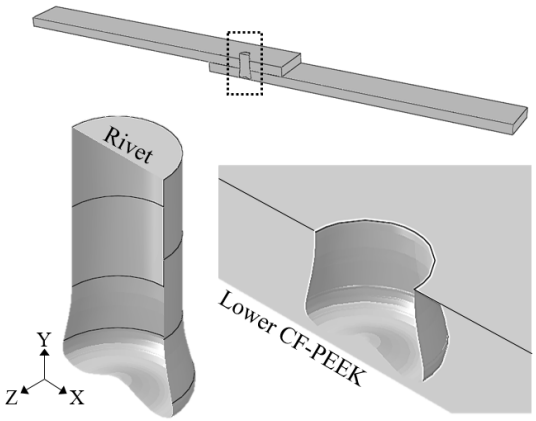

Figure 5.16 Mid-plane section on Z-axis direction of the FE model of a friction riveted single lap joint, highlighting the complex geometry of the plastically deformed rivet tip and the composite hole.

The Ti6Al4V rivet was modeled as a fully isotropic and elastic-plastic material. The ductility behavior, strain hardening and thermal softening of the metal was described using a constitutive model proposed by Johnson-Cook (JC) [191]. The JC material constants are carefully selected from the literature and shown in Appendix C. The CF-PEEK was modeled as an anisotropic material,

whose ply orientation was defined according to the laminate stacking sequence described in Section 5.1.2. To replicate interlaminar and intralaminar failure of the composite, Hashin damage criteria [192] were adopted. The material properties derived from the literature and used for computation along with the general formulation of 2D Hashin damage criteria are shown in Appendix C. For the FE computation, the material properties at each integration point were evaluated and degraded. If any failure index reached unity, the relevant material properties were automatically reduced to zero. To compute the interface between the materials, a hard pressure/overclosure relationship and tie constraint were adopted, while cohesive interaction was used to describe the contact between the composite parts. The contact properties are detailed in Appendix C.

Figure 5.17 presents the boundary conditions of the FE model. The free edge of the upper composite part was constrained, while a prescribed displacement was imposed on the free edge of the lower composite part, to simulate quasi-static loading in the experiment. The reaction force was extracted as output of the computation and used for validation purpose. The influence of the tightening torque on the joint mechanical behavior was neglected, to reduce the computational effort and simplify the FE model.

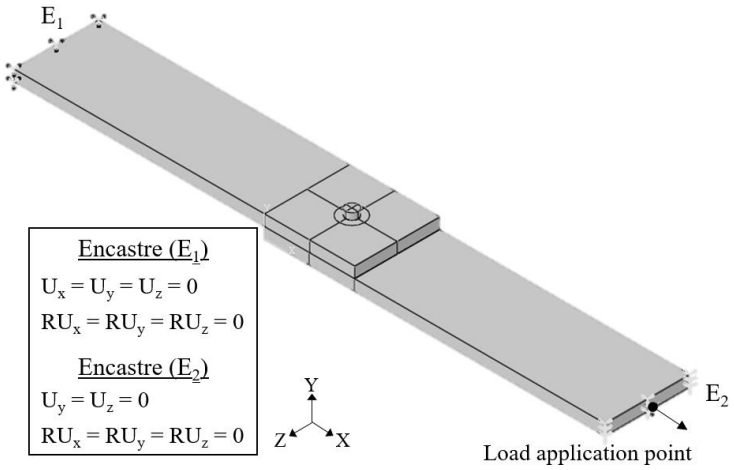

Figure 5.17 Boundary conditions of the FE model for lap shear testing of friction riveted single lap joints.

Chapter 6. Development of Direct Friction Riveting for Overlapped CFRP

The Friction Riveting process causes severe thermomechanical changes in the structure of the materials, including melting of the composite matrix, reorientation of fibers, plasticization and plastic deformation of the metal rivet. These phenomena are accompanied by a material flow, which is considerably modified by unreinforced or woven fiber reinforced polymers, and varies according to different joint and process configurations, which also affect joint formation. The sequence of phenomena is complex and gaining an understanding is made more difficult by the rapidity of the joining process. Consequently, in this chapter the process configuration of overlap joints is explored by a stepwise analysis of joint formation and temperature evolution for woven CFRP. The local changes induced by heat and deformation in the metal and composite parts are described with respect to microstructural, physicochemical and mechanical properties. To conclude this chapter, the results of the joint design, design of experiments (DoE) and analysis of variance (ANOVA), that were used to assess the effect of the process parameters on the joint's mechanical performance and to optimize the joining process, are briefly summarized.

6.1 Joint formation

Direct Friction Riveting of overlapped composite parts can be divided into four joining phases, according to the changes in process parameters, heat generation, and physical state of the joint materials. In this work, the process variant of force control and phase limitation by the spindle displacement was selected, where joining time became a response. Figure 6.1 illustrates a typical process diagram of Direct FricRiveting, plotting the monitored spindle displacement, rotational speed (RS), and joining force (JF) over the joining time. The process diagram includes temperature evolution that was recorded by IR thermography. Four stages in the temperature evolution are marked with stars and these were selected for further study of the joint formation and material flow by IR thermography (Figure 6.2-a) and the digital image correlation technique (DIC) (Figure 6.2-b).

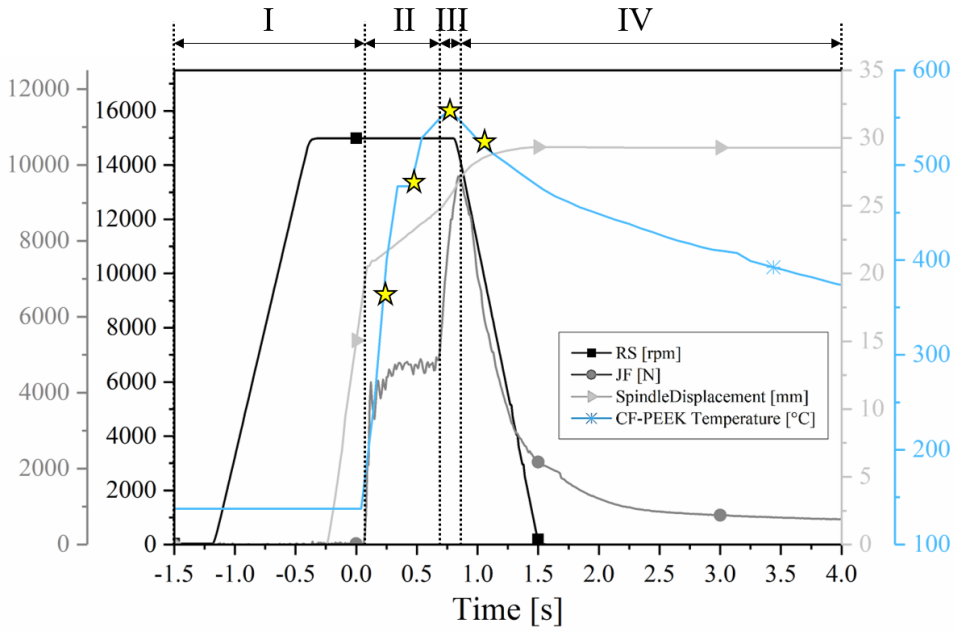

Figure 6.1 Direct Friction Riveting process diagram of overlapped composite parts, in which RS, JF, and spindle displacement were recorded by the joining system, while temperature was recorded by IR thermography.

In the first phase (Phase I, Figure 6.1), the spindle is accelerated to a pre-set RS (plateau of the black line), while the rivet mounted on the spindle approaches the surface of the upper composite part, promoting a physical contact between them. This positioning phase is followed by the first frictional phase (Phase II, Figure 6.1), which is characterized by the plunging of the rivet through the thickness of the upper composite part. In this phase, the joining force (dark gray line) increases to a pre-set JF, while the RS continues at the same level as phase I. This is accompanied by a rapid increase in temperature, which exceeds the melting point of PEEK (343 ± 2) °C after 0.25 s ($T_{0.25s}$ = 355 °C). Such an increase can be explained by a complex combination of the heat generated by solid friction and viscous dissipation. Unlike in FricRiveting of unreinforced polymers [143,147], the Coulomb friction in this case is not only ascribed to short-term friction between the rivet and solid cold polymer, but also constant friction between the rivet and the fiber network or between the fibers as the rivet plunges. As the temperature reached is too low to plasticize the fiber reinforcement (1100 °C) [193], the fibers remain in a solid state throughout the heating phase. This means the fibers are either displaced or broken by the shear and axial forces imposed by the rivet plunging. Additionally, the internal shear and breakage of secondary bonds along the polymer chains in the composite's matrix also generate heat by viscous dissipation [194]. This combination of mechanisms increases the temperature and locally melts a volume of polymer close to the rivet. Plunging of the rivet is facilitated by an outward flow of broken fibers and molten polymer as the rivet is inserted into the composite, forming a flash ($t_{0.25s}$, Figure 6.2-a). The high temperatures and shear rates

imposed by the rivet accelerate the material flow by decreasing the viscosity of the molten PEEK considerably, because it is susceptible to shear thinning even at low shear rates [127,195]. As soon as fiber breakage and polymer melting equalize with the outward material flow, the rivet penetrates at a constant rate, as observed by the linear increase of spindle displacement in phase II (light gray line in Figure 6.1).

After 0.70 s, the third frictional phase (Phase III, Figure 6.1) starts, with the insertion of the rivet through the lower composite part, which lasts until 0.9 s, when RS is decelerated. As this phase is quite short, JF is increased to facilitate the rivet's plunging – by fiber displacement and breakage – into the otherwise cold and undamaged lower composite. According to Tu and Fort [196], by increasing the axial force, the shear rate increases as well as the fluid pressure, which may push the fibers in the CF-PEEK apart, leading to less frictional resistance by the composite. However, this additional solid friction generates more heat, leading to higher temperatures ($T_{0.75s}$ = 546 °C) and additional molten polymer squeezed between the composite parts ($t_{0.75s}$, Figure 6.2-a). The higher axial force and temperature promote higher spindle displacement at a rate that decreases towards the end of phase III. As reported by Amancio-Filho and dos Santos [148], at the end of the frictional phase, the metal rivet tip plasticizes and may decelerate the spindle displacement and likewise the rivet penetration. Although the measured temperature is much lower than the onset hot working temperature of Ti6Al4V (750 °C) [197], it is expected there are higher temperatures at the rivet tip, owing to the low thermal conductivity of Ti6Al4V and its susceptibility to adiabatic heating under compression. These phenomena considerably reduce the flow stress of Ti6Al4V, softening the material. The effect of the thermal properties on the plastic deformation of the rivet tip and the Ti6Al4V microstructure will be more deeply discussed in Section 6.3.2. Additionally, according to Deignan *et al.* [195], at high axial pressures (over 156 kPa), the viscosity of the friction-affected CF-PEEK can increase even at high temperatures. In this case, contact between solid fibers is facilitated by the viscous matrix, and therefore the molten PEEK must undergo high strain rates in its small inter-fiber spaces. Thus, during the second frictional phase of Direct FricRiveting, with an axial force of 10 kN applied onto the rivet tip area (19.6 mm^2) yields a compression stress of 510 MPa, which may increase considerably the viscosity of the damaged composite underneath the rivet tip, contributing further to deceleration of rivet penetration.

Finally, in the consolidation phase (Phase IV, Figure 6.1), RS is halted as well as the JF and the joint cools down naturally. During this phase, only the weight imposed by the spindle is considered acting on the joint. As observed at $t_{1.25s}$ (Figure 6.2-a), the rivet tip plastically deforms, leading to widening of the rivet tip and more squeezed material between the composite parts. Therefore, contrary to conventional FricRiveting [147,148], no forging phase is required to plastically deform the rivet tip within the composite as the metal is highly plasticized during the frictional phases

[145]. As a consequence of the Ti6Al4V softening, the spindle continues a slow downward movement, compressing the plasticized rivet tip against a solid fiber network with high thermal resistance underneath the rivet tip, promoting its widening. The plastic deformation of the rivet tip lasts until the thermomechanical regime is no longer favorable for further deformation and at that point the spindle displacement reaches a plateau. Although Figure 6.1 shows a consolidation phase up to 4 s, this phase accounts for the complete cooling of the joint until 130 °C, which can take up to 20 s (see Section 6.2). Caution is prudent to prevent relaxation effects and geometric instability of the joint parts, due to differences in the coefficients of thermal expansion between the joint materials. As the process parameters of the second frictional phase have a significant influence on plasticization of the rivet and therefore on its plastic deformation during the consolidation phase, their influence on the joint formation and joint mechanical properties was analyzed by a design of experiments, which will be detailed in Section 6.5.

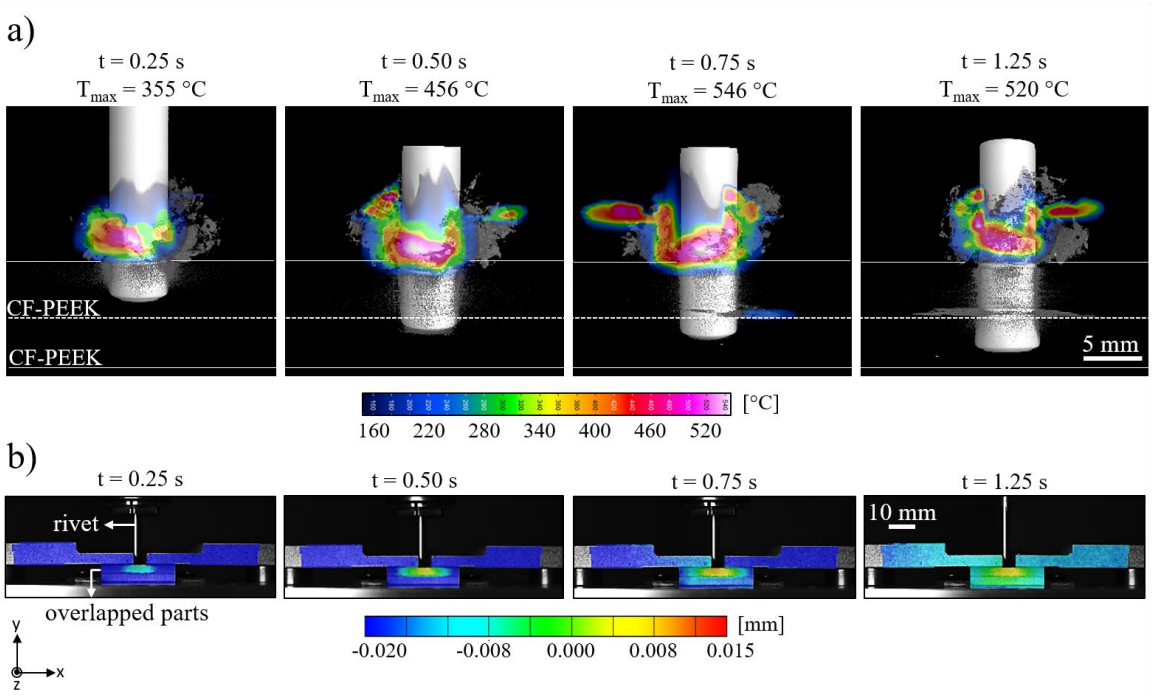

Figure 6.2 a) Maximum temperature recorded by IR thermography of the expelled material, and b) displacement of the clamping element and the composite parts obtained by DIC, over the joining time. The images correspond to the selected stages in Figure 6.1.

The flow paths taken by the process-affected composite can be analyzed as a continuous attempt of the joint to release its internal stresses. Figure 6.2-b shows how displacement of the upper clamping plate and overlapped composite parts evolve in the y-axis direction over the four selected stages analyzed by DIC. Throughout the friction phases, a localized positive displacement of the composite is formed in the rivet insertion path and this can be explained by the upward flow of the composite. Such a displacement is however impaired by the clamping system, which maintains the

joint parts under a constant negative displacement, and therefore under compression. Nonetheless, towards the end of the second frictional phase, at $t_{0.75s}$, the compression imposed by the clamping system is partially lost, owing to the squeezed material. It is believed that reaction forces to the joining force imposed by the upward flow of composite overcame the clamping force, facilitating the material flow through the composite overlap area. This effect is intensified when the rivet starts to plastically deform, because at that point a higher volume of composite is displaced from the joining area, increasing the separation between the composite parts, and therefore promoting higher positive displacement of the upper clamping plate ($t_{1.25s}$, Figure 6.2-b). Although compression losses take place throughout the consolidation phase, the clamping device still applies compressive forces to the joint, as observed by the blueish color of the upper clamping plate ($t_{1.25s}$, Figure 6.2-b), and thus it also assists the plastic deformation of rivet tip. This shows that the clamping efficiency during the joining process of overlapped joints plays an important role in the material flow and rivet plastic deformation, and thus the clamping pressure is considered an additional process parameter with an influence on joint properties, as will be discussed in Section 6.5.

To better assess the material flow path and further shear-induced phenomena in the composite during each joining phase, one of the composite parts was replaced by a transparent PMMA plate. The first frictional phase (Phase II, Figure 6.1) was evaluated with the lower composite part replaced by PMMA, as shown in Figure 6.3-a.

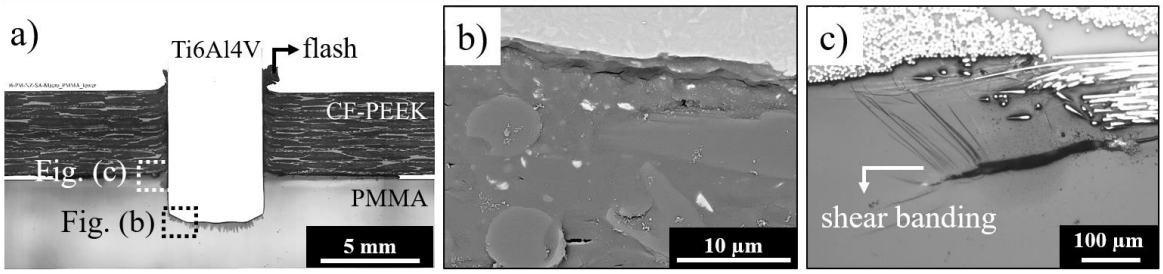

Figure 6.3 a) Cross-section of the friction riveted joint with upper CF-PEEK and lower PMMA parts; b) the metal and PMMA interface, showing broken fiber embedded in PMMA in the rivet surrounding; c) CF-PEEK and PMMA interface, showing the shear banding. (Joining parameters RS: 15000 rpm, FF_I: 5 kN, FF_{II}: 10 kN, DF: 7.5 mm, CP: 0.2 MPa)

Despite the preferential upward flow of the damaged composite in this phase, indicated by the flash expelled, broken fibers embedded in the lower PMMA part were detected underneath and around the rivet tip (Figure 6.3-b). This clearly indicates that a small amount of the damaged composite from the upper part is transported into the lower part by rivet plunging. Both translational and transversal movements of the rivet in this phase may cause additional material flow. As the low viscous composite close to the rivet assumes the rotational speed of the rivet, this effect can be understood as composite sticking on the rotating rivet surface, similar to metal that sticks onto the

rotating tool during Friction Stir Welding [198,199]. The shear stresses and axial joining force may also break and push the composite plies in the overlap area into the lower composite part. In addition, shear banding was detected at the interface between PMMA and CF-PEEK (Figure 6.3-c). As previously discussed, when the rivet leaves the upper joint part to be inserted into the lower part, it encounters material that is still cold ($T < T_m$) and which under compression plastically deforms by shear yielding, forming shear banding. This is a common phenomenon for glassy amorphous polymers such PMMA with a compressive yield stress of 103 MPa and this mechanism is explained by a stress-induced increase in the polymer free volume [200,201]. Although CF-PEEK has a semi-crystalline matrix and fibers that would lead to a different shear strain behavior, the material also undergoes shear yielding at stresses higher than 132 MPa (the compressive yield stress of PEEK is highly dependent on temperature and strain rate, decreasing to 35 MPa at 480 °C and increasing to 240 MPa at 10000/s) [195,202,203]. In this case, the relative movement between solid fibers imposes a localized shear strain to the matrix they are embedded in, forming shear bands. In the transition between the frictional phases of Direct FricRiveting, compression stresses of up to 510 MPa are expected. Therefore, similar to the shear yielding of PMMA in friction riveted joints, shear banding may occur when the rivet plunges into the second composite part.

The transition between the second frictional phase and consolidation (Phases III and IV, Figure 6.1) was evaluated by substituting the upper composite part with PMMA, as shown in Figure 6.4-a. Despite the squeezed flow in the overlap area, depicted in Figure 6.2, broken fibers were detected all over the rivet shaft in the PMMA (Figure 6.4-b). One may assume that the clamping device restricts the squeezing flow to some extent. As soon as higher volume of composite is displaced from the joint area, due to plastic deformation of the rivet, the material constrained from flowing between the composite parts is driven upward. Therefore, it is reasonable to expect that the higher the external clamping force, the thinner the squeezed layer and the more material that flows upward. Consequently, the flash formed during the process is a combination of material exposed to the frictional regime of both the first and second frictional phases of Direct FricRiveting. In addition, a reconsolidated shear layer is easily seen around the rivet shaft in the PMMA (Figure 6.4-c). This layer is a result of rotational movement of the rivet pressing against the polymer part. The thermomechanically affected material in this layer is partially expelled upwards or squeezed out, whereas the remaining material reconsolidates in the surroundings of the rivet. The formation of the shear layer can also be seen in the CF-PEEK caused by breakage and reorientation of the fibers. Figure 6.4-d shows the shear layer formed between the rivet and CF-PEEK, in a friction riveted joint with an upper CF-PEEK part. The original stacking sequence of the composite plies is visible outside the region highlighted with a white dashed-line, whereas inside the shear layer, broken fibers are reoriented radially around the rotation axis of the rivet. Although the same joining parameters were

used to produce joints with PMMA and CF-PEEK, the shape and the size of the shear layer differ, owing to differences in thermal conductivity and rheological behavior of the polymer and the composite.

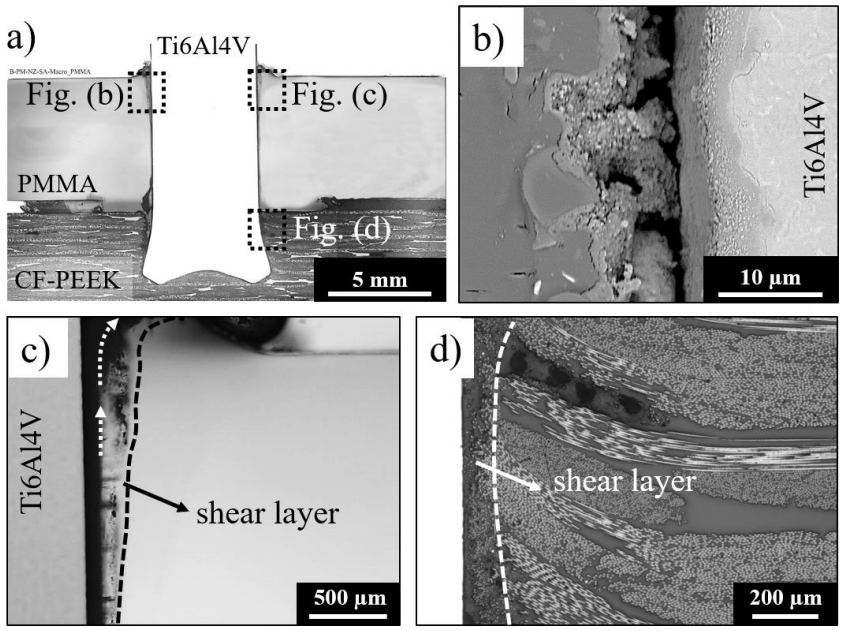

Figure 6.4 a) Cross-section of the friction riveted joint with upper PMMA and lower CF-PEEK parts; metal and PMMA interface, showing b) broken fiber embedded in PMMA close to the rivet; and c) shear layer in the PMMA; d) metal and CF-PEEK interface, showing the shear layer formed in a friction riveted joint with upper CF-PEEK part. (Joining parameters - RS: 15000 rpm, FF_I: 5 kN, FF_{II}: 10 kN, DF: 7.5 mm, CP: 0.2 MPa)

6.2 Temperature history

Knowing the process temperature is important to understand metallurgical transformations in the rivet during the joining process and the physicochemical changes in the composite, including possible degradation, and changes to its crystallinity and viscosity. Moreover, temperature provides an indication of the heat input under different joining conditions. As explained in Section 5.2.3, IR thermography was adopted to measure the temperature of the expelled composite material, while thermocouples were used to measure the temperature at the interface of the metal and composite. Figure 6.5-a shows the process temperatures of all the joining conditions evaluated in this work, as measured by thermocouples (TC) within the joint and an infrared thermographic camera (IR). The temperature varied between (413 ± 18) °C and (1064 ± 159) °C when measured by TC and between (453 ± 10) °C and (580 ± 5) °C when measured by IR. Figure 6.5-b illustrates an example of the typical temperature development over time measured by TCs and IR (Appendix D shows all the TCs

and IR curves). The temperatures measured by the TCs were approximately 68 % higher than by IR. The differences in these measurements may be explained by the fact that the thermocouples, as they are located within the rivet insertion path, were touched by the surface of the hot rivet, capturing its temperature directly. It is worth mentioning that Ti6Al4V has a low thermal conductivity (see Table 5.2) which in turn keeps the temperature localized at the rivet tip high, increasing the TCs measurement. On the other hand, for the thermographic camera, the temperature was only measured in the flash material and therefore was dependent on the amount of composite flowing out of the joining area. It is believed that when the heat input is sufficient to soften a polymeric layer, higher axial forces expel more molten polymer, which improves the acquisition of temperature data. Moreover, although the flash material has low thermal conductivity, heat is constantly lost through convection, conduction, and radiation, decreasing the measured temperature. From the results, TC was used to further explain the microstructural changes in the joint materials, while IR was used to calculate the heating and cooling rates, as the TCs were damaged by rivet insertion, compromising their measurement of the cooling phase.

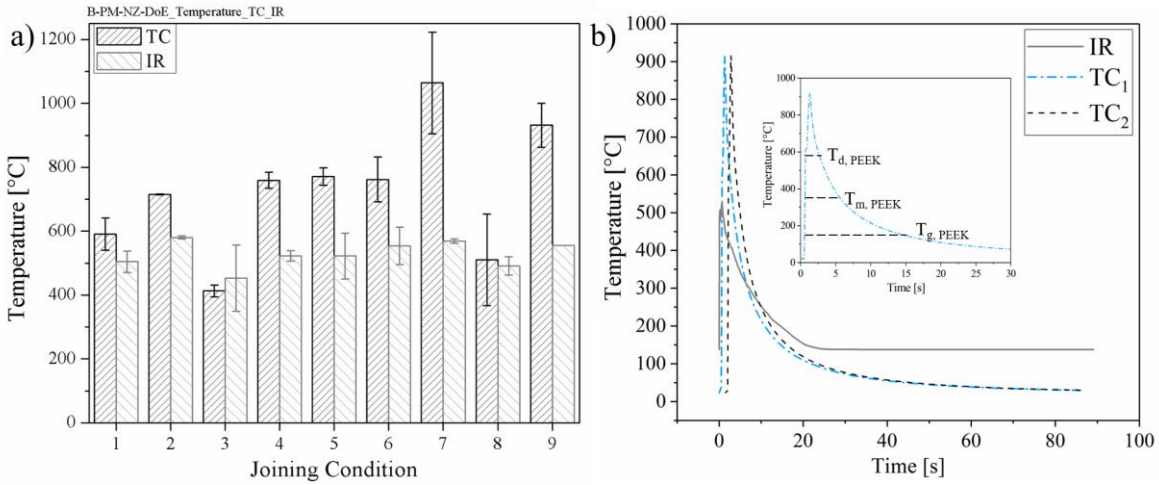

Figure 6.5 a) Average process peak temperatures for joining conditions; b) typical process temperature evolution measured by thermocouples (TC) and IR thermography (IR), the inset chart relates to TC measurement of joining condition 9.

In all conditions, the process temperature was well above the melting temperature of PEEK ($T_{m,\ PEEK}$ = 343 °C ± 2 °C) which allowed the melting of PEEK matrix close to the metal rivet. Moreover, for the majority of the joining conditions a degradation of PEEK matrix directly in contact with the rivet was expected once the decomposition onset temperature ($T_{d,\ PEEK}$ = 575 °C to 580 °C) [121] is exceeded. However, the inset graph in Figure 6.5-b shows that the polymer was exposed to temperatures above $T_{d,\ PEEK}$ for a period shorter than 5 s. Therefore, no extensive degradation is expected in the vicinity of the rivet. The highest temperatures achieved in conditions 7 (1064 ± 159) °C and 9 (932 ± 69) °C exceeded the β-*transus* temperature of Ti6Al4V, suggesting complex

process-induced microstructural transformations in the metal rivet. Such transformations, along with high temperature and strain rate, also affect the flow resistance of Ti6Al4V under hot working conditions, leading to changes in its plastic deformation [204]. The effect of the temperature on the microstructural transformation and plastic deformation of the Ti6Al4V rivet will be reported in detail in Section 6.3.2, while the physicochemical changes of PEEK will be addressed in Section 6.3.3.

Table 6.1 shows the heating rate (HR) and cooling rate (CR) of the joining conditions that developed the lowest (Condition 3, Figure 6.5-a) and the highest (Condition 7, Figure 6.5-a) process temperatures evaluated in this work. The temperature rises faster with higher heat input, represented by an increase in the process temperature, which is intensified by the low thermal conductivity of Ti6Al4V (17.5 W/m·K) and the PEEK (2.0 W/m·K). Moreover, during the plastic deformation of Ti6Al4V at high temperatures and strain rates, as observed in the FricRiveting process, adiabatic heating may also be generated, which raises the actual temperature of the sample and is not conducted away [100]. As reported by Ding, Guo, and Wilson [205], the α→β phase transformation can enhance heat accumulation even more during compressive deformation, which may explain the significant increase of process temperature and consequently HR of Condition 7 in comparison to Condition 3. Nonetheless, the heating rates calculated for FricRiveting are extremely high in comparison to other friction-based joining processes, such as friction stir welding of Ti6Al4V at 240 °C/s [206], refill friction stir spot welding of aluminum alloys (93 °C/s) [207], and friction spot joining (FSpJ) of AA2024 from (205 ± 0.3) °C/s to (355 ± 0.2) °C/s [208].

Table 6.1 Average heating and cooling rates calculated for joints produced with the lowest (Condition 3) and highest (Condition 7) heat input, *i.e.* process temperature.

	Heating rate [°C/s]	**Cooling rate [°C/s]**
Condition 3	301 ± 9	18 ± 2
Condition 7	1320 ± 22	15 ± 0.01

The measurement of cooling rate showed a moderated decrease in temperature (18 ± 2) °C/s and (15 ± 0.01) °C/s and no significant variation between Conditions 3 and 7. In contrast to the heating phase, during cooling the low thermal conductivity of Ti6Al4V and CF-PEEK tended to inhibit heat dissipation to the environment. The moderated cooling rate after FricRiveting can induce either bimodal or acicular microstructures in Ti6AlV [115] whereas can decrease the PEEK degree of crystallinity. The calculated cooling rates are much higher than the rate (0.08 °C/s [159]) that the woven composite experiences during its manufacturing, which may impair the nucleation and growth of spherulites in the PEEK matrix. These phenomena lead to changes of local mechanical properties throughout the joint, as discussed in Section 6.3.3.

6.3 Process-related changes in the materials joined by FricRiveting

6.3.1 Physicochemical changes of joined CF-PEEK

The welding and joining processes of polymers and composites rely on high temperatures, which therefore cause physicochemical changes to the materials. Such thermal effects include, in the case of semicrystalline polymers a change of degree of crystallinity, morphology of crystals, and thermal degradation, affecting their local and global mechanical properties significantly [48,125,128]. For this reason, thermal analyses (by TGA and DSC) were carried out to assess the physicochemical properties of thermomechanically affected material (TMAM) of the CF-PEEK in friction riveted joints compared to its base material (BM). Figure 6.6 shows the thermogravimetric (TG) curves and their first order derivative (DTG) curves for BM and CF-PEEK extracted from the squeezed and flash materials. The onset temperature of decomposition decreased from (575 ± 1) °C for BM, to (569 ± 2) °C for the squeezed and flash materials of TMAM. The result for the BM is in agreement with the literature for PEEK heated up at 10 °C/min [209]. As discussed in Section 6.2, the range of process temperatures measured either by IR or TC methods during FricRiveting exceed the onset decomposition temperature of the BM. Consequently, mechanisms such as chain scission and thermo-oxidation are expected to occur in the composite around the rivet during the joining process. The predominant degradation products of PEEK, such as phenol, decrease the thermal stability of the material [209], and once heated up during TGA, a decrease in the onset decomposition temperature may occur, explaining the results of the TMAM.

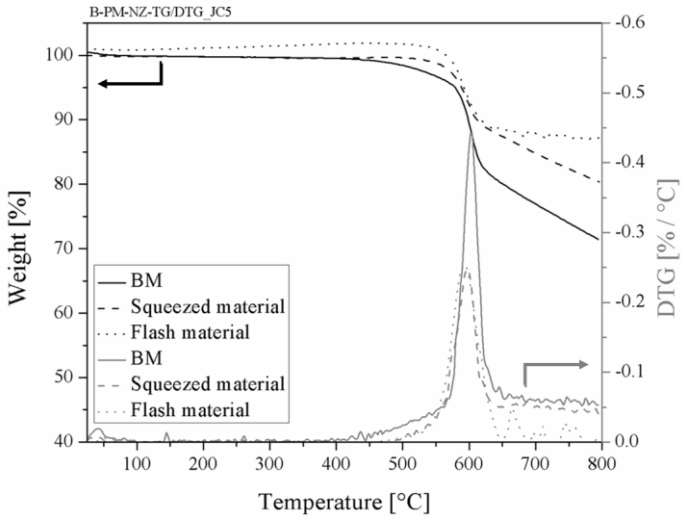

Figure 6.6 TG and DTG curves of the PEEK from BM, squeezed material, and flash material of friction riveted joints (Joining parameters RS: 15000 rpm, FF_I: 5 kN, FF_{II}: 10 kN, DF: 7.5 mm, CP: 0.2 MPa)

The TG and DTG curves showed a two-step decomposition process of BM, which complies with the decomposition mechanisms of PEEK described by Vasconcelos *et al*. [209] and Patel *et al.* [121]. The main mechanism is random chain scission of the ether and ketone bonds, forming preferentially phenol in the temperature range 500 °C to 600 °C. Between 600 °C and 800 °C, the second decomposition step is described as recombination of decomposition products by crosslinking, leading to less phenol volatilization [121]. However, the decomposition mechanisms are not only dependent on temperature, but also on heating rates and atmosphere. By increasing the heating rate, the decomposition kinetics of PEEK are impaired, requiring higher energy to trigger the mechanisms, and therefore shifting the onset decomposition temperature to higher values [209]. Moreover, in an atmosphere with oxygen, the random chain scission observed in a controlled nitrogen atmosphere is preceded by thermo-oxidation, which requires less activation energy to occur and promotes different decomposition mechanisms, including graphitization and more crosslinking [121]. Therefore, the PEEK affected by FricRiveting, although it experienced extremely fast heating rates (see Table 6.1), which would promote an increase in the onset decomposition temperature compared to the BM, may be submitted to thermo-oxidation. In this case, the thermal stability of the material may have decreased and led to the formation of char. Once heated up under a controlled nitrogen atmosphere, the differences in the TG curve of squeezed and flash materials (Figure 6.6) suggest that the decomposition behavior of such process-induced decomposition products changed. Especially the flash material, which was exposed to a longer heating phase and to an oxidizing atmosphere at high temperatures, the second step of the BM decomposition under a nitrogen atmosphere was no longer identified. In general thermo-oxidation causes cracking of the polymer and increases its moisture uptake, degrading its durability [210]. Chapter 9 is focused on the durability of the friction riveted joints, where this influence will be addressed. The details of the chemical reaction during PEEK decomposition is not the scope of this work and can be found in [121].

The crystallization and melting behavior of the thermomechanically affected material (TMAM) in the PEEK from the joints were assessed by DSC and compared with the PEEK in the BM. Figure 6.7 illustrates an example of the first thermal cycle for BM, squeezed and flash materials, highlighting the cold crystallization (T_{cc}), the melting temperature (T_m), and the crystallization temperature (T_c). The first thermal cycle evaluates the thermal history of the material, and therefore provides information about the effect of the joining process on the physicochemical properties of the composite. The transition temperatures and crystallization degrees are summarized in Table 6.2.

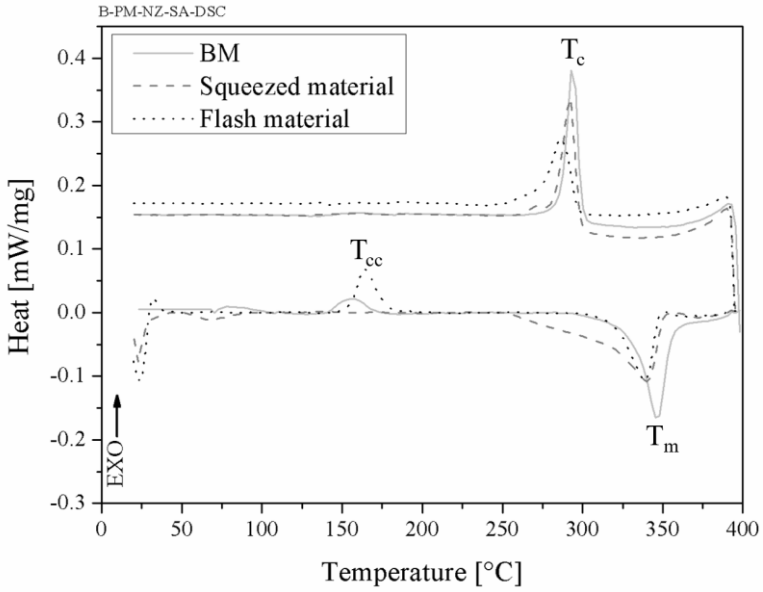

Figure 6.7 Example of DSC curves for the BM, squeezed, and flash materials, in the range of interesting heating and cooling rates of 10 °C/min in nitrogen.

Table 6.2 Main parameters obtained from DSC analysis (T_{cc} – cold crystallization temperature, T_m – melting temperature, T_c – crystallization temperature, X_c – degree of crystallization) for BM, squeezed and flash materials.

	T_{cc} [°C]	**T_m [°C]**	**T_c [°C]**	**X_c [%]**
BM	153.0 ± 1.0	345.0 ± 1.0	292.0 ± 5.0	29.0 ± 2.0
Squeezed material	-	340.0 ± 0.2	296.0 ± 1.0	24.0 ± 2.0
Flash material	168.0 ± 3.0	343.0 ± 0.2	294.0 ± 1.0	14.0 ± 7.0

The TMAM (collectively the squeezed and flash materials) presented similar trends of higher T_{cc} and T_c, with lower T_m and X_c, compared to the BM. The DSC curve of BM showed an exothermic peak of cold crystallization at (153.0 ± 1.0) °C, which indicates a matrix not fully crystallized upon manufacturing. This observation suggests a fast cooling rate during CF-PEEK manufacturing, which contradicts the controlled and slow cooling phase reported in [159]. For the flash material, T_{cc} increased to (168.0 ± 3.0) °C while for the squeezed material no T_{cc} was observed. Similar to the DSC of annealed PEEK at temperatures above T_m [211], thermal degradation of the material by crosslinking, as previously discussed, can impair the mobility of the PEEK molecules and thus hinder its crystallization. This either shifts T_{cc} to higher temperatures or leads to its dissipation in a scenario of high thermal exposure. Additionally, as the squeezed material was exposed to a higher shear rate, flow-induced crystallization may also occur at high temperatures, when distorted polymeric chains reduce the conformational entropy, leading to crystal nucleation, as reported by Nazari *et al.* [212]. Therefore, the absence of T_{cc} in the squeezed material curve may indicate a process-induced crystallization of the matrix along with degradation. The mechanism of crosslinking has also a

negative effect on the melting behavior of PEEK [139,211,213], which can partially explain the lower T_m of the squeezed (340.0 ± 0.2) °C and flash (343.0 ± 0.2) °C materials in comparison to the BM (345.0 ± 1.0) °C. Additionally, chain scission – in the first decomposition step of PEEK (see Figure 6.6) – decreases the molecular weight of polymers, plasticizing the material, and thereby decreasing T_m.

As observed in Table 6.2, the thermally affected materials presented lower degrees of crystallinity, *i.e* squeezed material = (24.0 ± 2.0) %, flash material = (14.0 ± 7.0) % compared to the BM (29.0 ± 2.0) %. According to Gao *et al.* [128], for intermediate cooling rates of 10 °C/min to 30 °C/min, a degree of crystallinity of around 30 % is expected for PEEK. Although the friction riveted joints cooled down over a similar range of rates (see Section 6.2), the degree of crystallinity of the squeezed and flash materials was under 30 %, confirming PEEK decomposition during the joining process. Both crosslinking and chain scission mechanisms can impair the crystallization, crosslinking by preventing polymer chains in a molten state from arranging into a lamellae fold [214] and chain scission by forming molecular defects such as carbonyl groups that do not fit into the crystal lattice [139,211,213]. It is believed that the flash material exposed to a longer heating phase at high temperatures, as previously discussed, was highly thermally decomposed, and as a consequence a lower degree of crystallinity was observed in this material. As a lower number of crystals requires less energy to be melted, the squeezed and flash materials had less enthalpy of melting as a result of their reduced crystallinity (Figure 6.7). Moreover, the broad melting peak of TMAM, especially the squeezed material, indicates a distribution of crystal sizes. As observed in Figure 5.2, the PEEK BM presents larger crystals between the carbon fibers, and nanometric crystals in fiber free regions. It is believed that such a difference in crystal sizes is intensified during FricRiveting. Some of the crystals may grow upon low conductivity of process-related heat, resulting in larger lamella structures, while the broken fibers in the squeezed material and flash may nucleate finer crystals, as they can work as nucleation sites for quasi-epitaxial crystallization [133] The flow-induced crystallization can also contribute to broad the melting peak by enhancing the kinetic of crystallization of PEEK, and therefore, increasing the nucleation density [212].

As a summary for this section: thermal decomposition by chain scission of the PEEK during FricRiveting was detected while decomposition by crosslinking was indirectly evidenced The changes in thermal stability and degradation behavior of the thermomechanically affected PEEK suggested a contribution of thermo-oxidation to the material decomposition. The thermomechanically affected PEEK had an inferior degree of crystallization as well as a broader melting peak compared to the BM, which may indicate crystal growth over the heating phase of FricRiveting and epitaxial crystallization on the surfaces of broken fibers.

6.3.2 Microstructure and local mechanical properties of joined Ti6Al4V rivet

The temperature effect is particularly pronounced in Ti6Al4V, because this alloy can experience phase transformations that affect the material flow, formability, and final microstructure. Figure 6.8 shows examples of three shapes of plastically deformed rivet tips in friction riveted joints that were formed using the joining conditions evaluated in this work.

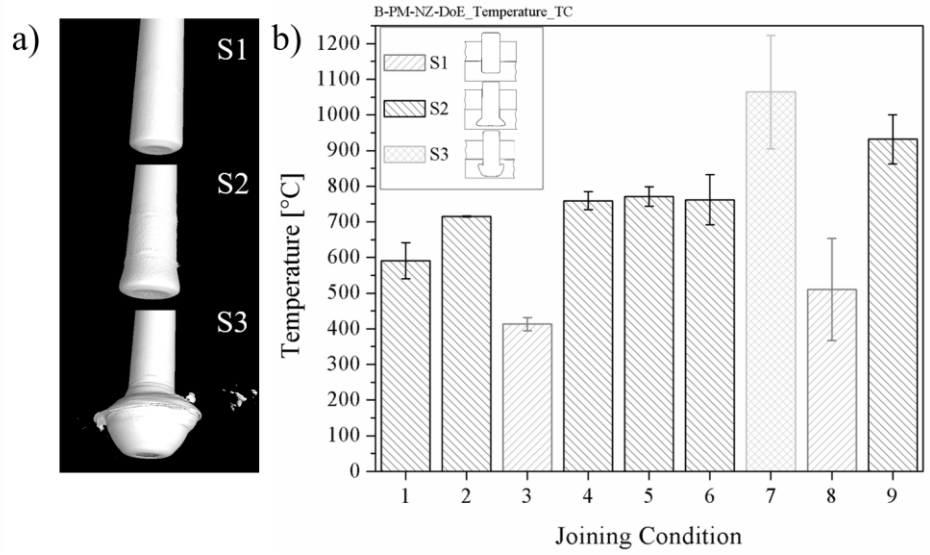

Figure 6.8 a) X-ray micro-computed tomography of three rivet tip shapes formed by the evaluated joining conditions of the FricRiveting process; b) average process peak temperatures measured by TC of the joining conditions, showing the dependency between temperature and the shape of the rivet tip.

At a lower process temperatures, as in Condition 3 (413 ± 18) °C, the heat input and strain rate of FricRiveting was insufficient to plasticize the rivet tip, and therefore no plastic deformation occurred, as shown by shape S1 in Figure 6.8-a. Conversely, when the metal rivet was processed at temperatures between 600 °C and 932 °C, the rivet tip assumed a bell shape (S2, Figure 6.8-a). According to the literature [100,204,205], in this range of temperatures, the flow stress of Ti6Al4V decreases rapidly with an increase of strain. This results from the material's susceptibility to shear banding and the adiabatic conditions generated during compressive deformation [100]. The physical barrier of the composite fiber network during FricRiveting may have gradually enhanced the deformation of plasticized rivet tip, intensifying the shear band formation and adiabatic heating. Moreover, the inhomogeneous strain distribution and low thermal conductivity of Ti6Al4V promote a localized flow in the metal [96], which may contribute to the rivet tip widening in friction riveted joints. Finally, an inverted bell shape (S3, Figure 6.8-a) was formed in friction riveted joints that were processed at a higher temperature, as in Condition 7 (1064 ± 159) °C (Figure 6.8-b). When the hot deformation is carried out near the β-*transus* temperature (995 °C), the α→β phase transformation

generates more adiabatic heat, which in turn raises the proportion of soft β-phase in the material, and this increases the softening phenomena of Ti6Al4V [97]. Thus, an excessive deformation is formed at the rivet tip in Condition 7.

The phase transformation and plastic deformation along with the fast cooling rates shown in Table 6.1 extensively modify the original globular microstructure of Ti6Al4V (refer to Figure 5.1). Figure 6.9 shows the final microstructure of a Ti6Al4V rivet joined with intermediate temperature that formed a bell-shaped rivet tip. The bell-shaped rivet tip was selected, owing to its improved mechanical performance, as will be discussed later in this chapter.

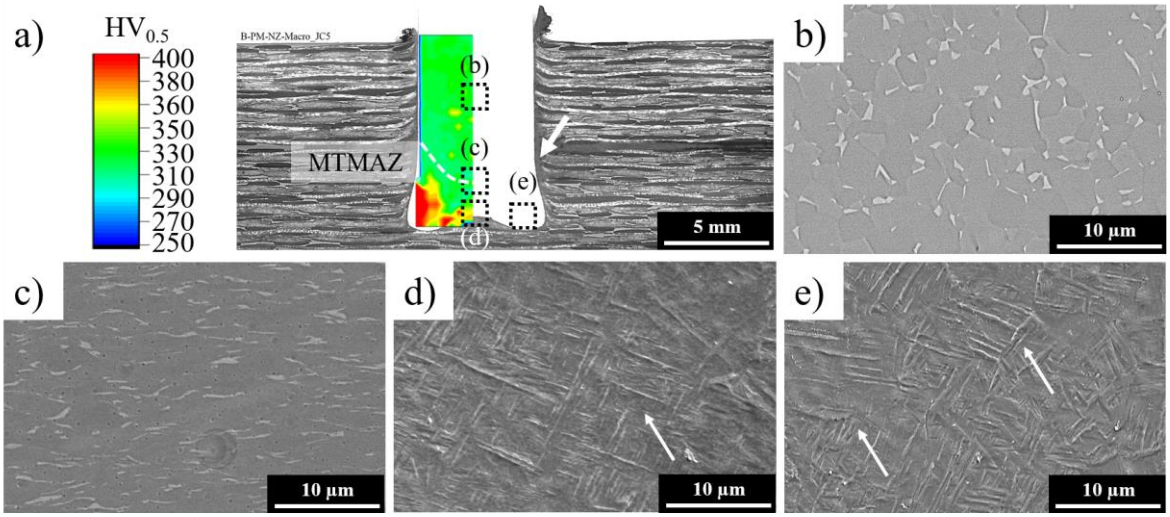

Figure 6.9 a) Typical cross-section of friction riveted Ti6Al4V and CF-PEEK, showing the microhardness map of Ti6Al4V along with four regions of microstructure interest, detailed in b) through e). (Joining parameters, RS: 15000 rpm, FF_I: 5 kN, FF_{II}: 10 kN, DF: 7.5 mm, CP: 0.2 MPa)

The gradient of microstructure through the metal rivet is similar to those reported for Friction Riveting of Ti6Al4V and glass fiber reinforced polyester [114] and is explained by the inhomogeneous local heat generation and cooling rates in the joining area. The original globular microstructure remains at the center of the rivet with no indication of any thermomechanical effect, as shown in Figure 6.9-b. The diffused microstructure in Figure 6.9-c along with some of the initial barreling (arrow in Figure 6.9-a) characterizes the threshold of the metal thermomechanically affected zone (MTMAZ). Barreling is an effect observed mainly during hot forging of metals in which differential degree of freedom to expand and/or inhomogeneous heat distribution through in the metal lead to more deformation of inner/hotter than outer/colder material upon axial force, creating a barrel shape to the part. A diffused microstructure is typically formed by a fast cooling rate from temperatures near the β-*transus* but still in the α+β phase field [205]. In this case of non-equilibrium thermodynamics, the diffusional process of portioning of alloying elements is incomplete, retaining an incompletely transformed morphology from high temperatures at room

temperature [97]. The elongated bright structures were described by Borba *et al.* [114] as vanadium-saturated regions known as β-flecks. A similar microstructure was also detected in the shear banding of hot compressed Ti6Al4V [97,100]. At the rivet tip (MTMAZ) acicular microstructures coexist, due to diffusionless α' martensite (Figure 6.9-d) and diffusional Widmanstätten (Figure 6.9-e) processes. Both of these microstructures are formed from the β-phase field and distinguished by the cooling rate to which they are exposed. Therefore, in agreement with the thermocouple measurements, the β-*transus* temperature was exceeded at the rivet tip while the fast cooling rate impaired diffusional phase transformation of β→α phase, forming a geometric pattern of acicular structures known as α' martensite. The adiabatic heating, owing to the deformation of the metal, may have impaired the fast cooling rate in regions where the plastic deformation was located, exposing the metal longer to a heating regime and consequent slow cooling rate, leading to the diffusional Widmanstätten pattern, as observed in the string shaped phase with bundles of lamellae in Figure 6.9-e. Analyses of metallic flow through microtexture and evolution of the Ti6Al4V microstructure during FricRiveting are not in the scope of this work, but can be found in [114].

Process-related microstructural changes in the Ti6Al4V rivet were further evaluated regarding their local mechanical properties, assessed by a Vickers microhardness map, as shown in Figure 6.9-a. As expected, at the center of the rivet, where no changes in the microstructure were observed compared to the base material, the microhardness was within the range 300 HV to 330 HV, the same as the base material (Figure 5.1-a). Within the rivet tip, characterized as MTMAZ, the acicular microstructures promoted a 9 % to 21 % (360 HV to 400 HV) increase in microhardness, compared to the center of the rivet. Under friction stir welding, where the material is also exposed to high temperatures and shear rates, Ti6Al4V undergoes similar behavior in the stir zone, as reported by Esmaily *et al.* [106] and Ramulu *et al.* [215]. The authors explain that the thin α-laths in acicular microstructures improve the hardness and strength of the material while decreasing its ductility compared to the globular morphology. Moreover, the elongated β-flecks identified in the threshold of the MTMAZ (Figure 6.9-c) seem to slightly decrease the hardness of the metal (290-310 HV). This phenomenon can be explained by the high amount of arrested and untransformed β-phase from the high temperature phase field. The β-phase is a body-centered cubic (bcc) crystal known to have multiple slip systems and therefore high ductility; the larger β-phase enhances local ductility and decreases the hardness [215].

6.3.3 Microstructure and local mechanical properties of joined CF-PEEK

When CF-PEEK is exposed to high temperatures and shear rate, an intense flow of broken fibers and low viscosity matrix is induced in the vicinities of the rivet shaft, which is enhanced by the

plastic deformation of the rivet tip, as discussed in Section 6.3.3. Therefore, the final microstructure of the composite is highly dependent on heat input, joining conditions, and the geometry of the rivet tip. Figure 6.10 illustrates a typical microstructure of CF-PEEK in the friction riveted joints where the rivet tip assumed a bell shape (S2, as described in Section 6.3.2).

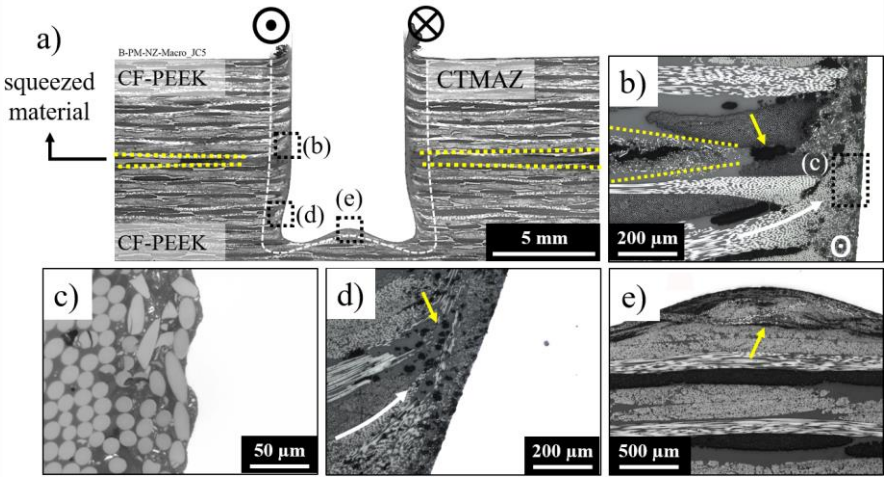

Figure 6.10 a) Typical cross-section of Ti6Al4V/ CF-PEEK friction riveted, showing the CTMAZ and the squeezed material, indicating three regions of microstructure interest as detailed in b) to d); b) and c) reoriented fiber bundles and reconsolidated composite material; d) voids; and e) fiber-matrix debonding underneath the rivet tip. (Joining parameters RS: 15000 rpm, FF_I: 5 kN, FF_{II}: 10 kN, DF: 7.5 mm, CP: 0.2 MPa)

A composite thermomechanically affected zone (CTMAZ) was identified surrounding the rivet (Figure 6.10-a) and this is characterized by reoriented fiber bundles, volumetric flaws, and reconsolidated material that was formed during the unsteady state viscous dissipation phase (II, Figure 6.1). Throughout this phase, broken fibers embedded in molten polymer flow partially outwards (forming a flash) and between the composite parts (squeezed material), as shown by the yellow dotted lines in Figure 6.10-a and -b. The circular pattern assumed by the composite flow – as reported in Section 6.1 – may realign the broken fibers in vicinity of the rivet, resulting in their near-circular appearance (Figure 6.10-c). Altmeyer *et al.* [26] defined this region as a composite stir zone (CSZ), where short fibers are stirred by the rotating rivet during FricRiveting. The rivet penetration reoriented the fiber bundles upwards in the proximity of the rivet, as indicated by the white arrow in Figure 6.10-d, which may have been enhanced by the upward flow of the composite. Internal flaws, including voids and delamination, could also be detected in the CTMAZ. The low viscosity of the molten polymer assists the entrapment of air pockets and gases evolved from the thermal degradation of the matrix, as addressed in Section 6.3.1, which remain as voids in the joint due to the fast cooling rate (voids are highlighted by yellow arrows in Figure 6.10-b and -d). Figure 6.10-e depicts matrix-fiber debonding in the composite underneath the rivet tip. Two effects could contribute to its formation: a significant difference in coefficients of thermal expansion between fiber and matrix,

which with a fast cooling rate generates residual thermal stresses, or by an extensive shear imposed by the rivet, which compromises the fiber-matrix interface leading to delamination. The first contribution would occur during the cooling phase, whereas the second would happen during the joining process.

By increasing the heat input the rivet tip over deforms, which has an influence on the composite flow and the extent of internal flaws in the friction riveted joint. Figure 6.11 shows an example of a friction riveted joint that formed an inverted bell shape (S3). Owing to greater rivet plastic deformation and the higher process temperature (1064 ± 159) °C localized in the vicinity of the rivet for a longer time, more of the composite is thermomechanically affected, thereby enlarging the CTMAZ, as outlined by the white dashed line in Figure 6.11-a. Consequently, more voids were formed (Figure 6.11-b). The overdeformation displaced more fiber bundles upwards and led to turbulence within the composite in its vicinity, shown by the formation of a vortex (dashed arrows in Figure 6.11-b). Additionally, the volume of molten polymer and broken fibers that was forced to flow outwards increased, leading to composite through-thickness delamination, where composite flowed within a fiber bundle, as shown in Figure 6.11-c. Therefore, the shape of the rivet tip compromises the integrity of the composite, which may degrade the mechanical properties of the friction riveted joints.

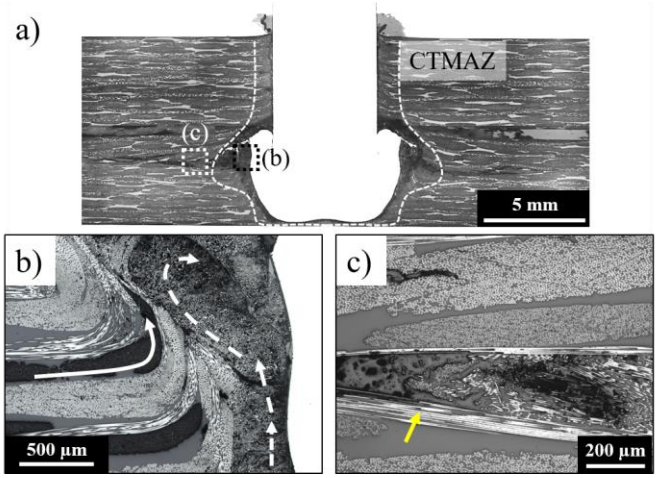

Figure 6.11 a) Cross-section of Ti6Al4V/ CF-PEEK friction riveted where the rivet tip was overdeformed, showing the CTMAZ along with two regions of microstructure interest, as detailed in b) and c); b) the reoriented fiber bundles and formation of a vortex in the reconsolidated composite material; c) composite delamination. (Joining parameters - RS: 15000 rpm, FF_I: 5 kN, FF_{II}: 15 kN, DF: 7.5 mm, CP: 0.26 MPa)

The local mechanical properties of the inner and outer regions of the CTMAZ were evaluated using nanohardness measurement, as described in Section 5.2.8.2. The nanohardness method has been widely used to describe the viscoelastic and dynamic mechanical properties of polymer composites, particularly of the matrix, where a small indentation size is required to avoid interference of the fibers with the measurement [174]. Figure 6.12 illustrates the dynamic indentation modulus

and hardness of the PEEK base material (BM) and PEEK CTMAZ. The load-displacement curves obtained from the nanohardness test are presented in Appendix E. At shallow indentation depths, up to 100 nm, any increase of the modulus and hardness is reported to be a combination of errors during the surface determination, indentation size effects, and near-to-surface modifications such as localized oxidation of the sample surface [216]. The average values of these responses are near constant, between 200 nm and 800 nm for all replicates, and therefore were used for the evaluation of properties. A 33 % decrease in elastic modulus from (5.4 ± 0.04) GPa to (3.6 ± 0.03) GPa and a 53 % decrease in hardness from (0.34 ± 0.006) GPa to (0.16 ± 0.002) GPa was observed by comparing the BM to the CTMAZ. This result complies with the physicochemical changes of the composite, as discussed in Section 6.3.1. The thermomechanical decomposition of PEEK, mainly by chain scission and possible oxidation, results in a lower molecular weight, which softens the polymer and therefore decreases its strength. In addition, any strengthening effect from the spherulites in semicrystalline polymers such as PEEK [128,130,216] is also impaired by a decrease in the degree of crystallinity caused by the thermal degradation of the friction riveted joints.

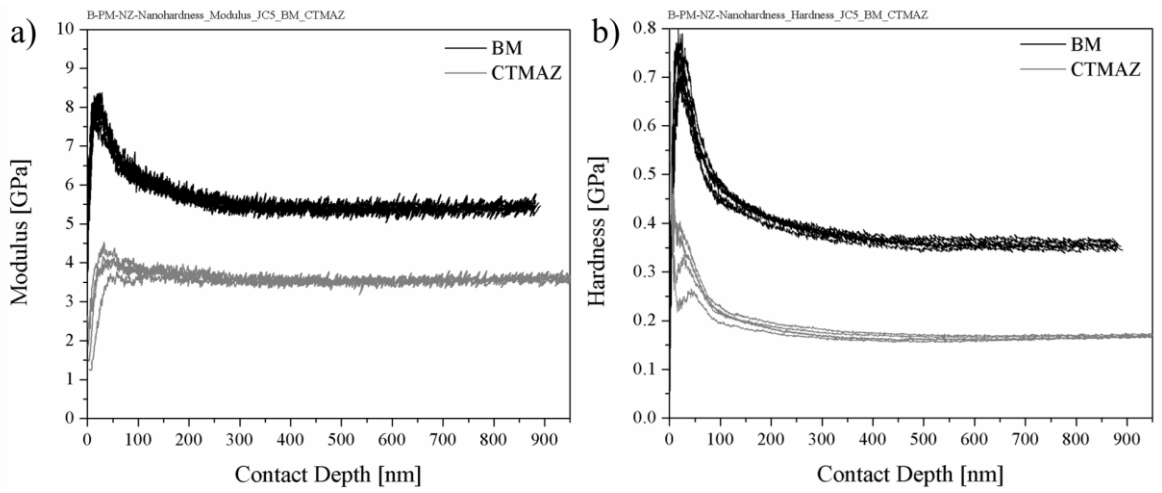

Figure 6.12 Dynamic indentation for a) modulus and b) hardness of PEEK as a function of displacement into the surface of BM and the CTMAZ of the friction riveted joint. (Joining parameters RS: 15000 rpm, FF_I: 5 kN, FF_{II}: 10 kN, DF: 7.5 mm, CP: 0.2 MPa)

6.4 Bonding mechanisms and zones

The interaction between the metal and the composite is of upmost importance as it directly influences the strength of the joint and assists understanding of the failure mechanisms. As discussed in Section 3.3, there are essentially two bonding mechanisms that promote the strength of friction riveted joints: mechanical anchoring and adhesion forces. Mechanical anchoring, also termed

macromechanical interlocking, contributes most of the joint's strength owing to the mechanical interference of the rivet tip widening [147], while reconsolidated polymer against the rivet shaft promotes additional adhesion forces. Although occurring in overlapped friction riveted joints of CFRP, other subcategories of such bonding mechanisms were explored in this work owing to the complex material flow described in Section 6.1.

Besides macromechanical interlocking (Figure 6.13-a), micromechanical interlocking occurs along the length of the rivet shaft, which is considered an adhesion mechanism [217]. Figure 6.13-b shows fiber and polymer embedding in the rough surface of the rivet. The Coulomb friction developed between the solid fiber network and the rivet at the initial stages of the joining process leads to material wear, increasing the roughness of the rivet surface. Figure 6.13-c shows irregular metal debris in the material flash probably the result of this wearing process. Moreover, the hot compressive work imposed in the rivet tip may also create additional irregularities on the rivet surface as the softened metal encounters solid fibers. The low viscosity polymer and broken fibers flow into such asperities on the metal surface, and when consolidated, promotes interlocking on a microscale.

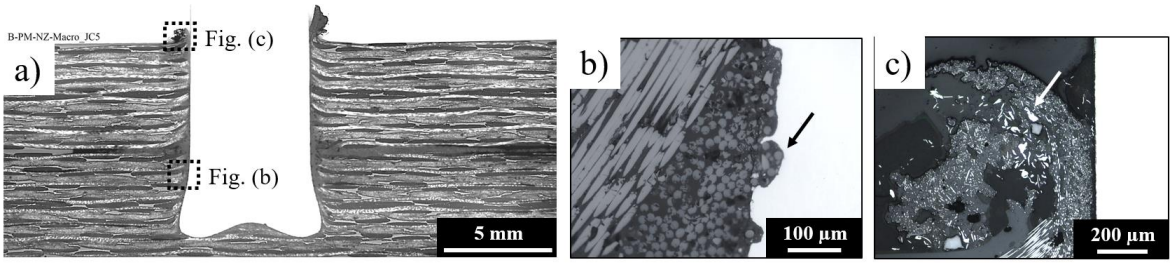

Figure 6.13 a) Overview of a friction riveted joint showing the macromechanical interlocking through the rivet tip widening; b) micromechanical interlocking by embedding of fibers and PEEK matrix; c) detail of the outward flash material showing metal debris resulting from the wearing process between fibers and rivet. (Joining parameters RS: 15000 rpm, FF_I: 5 kN, FF_{II}: 10 kN, DF: 7.5 mm, CP: 0.2 MPa)

The squeezed material consolidated between the composite parts contributes additional adhesion forces, by means of wetting and molecule interdiffusion over the composite interfaces. Figure 6.14-b shows the top view of the squeezed material obtained by µCT. During rivet insertion, a low viscosity PEEK molten layer flows through the composite plates, owing to the combined effect of centripetal forces (F_{cp}) imposed by the rotating rivet and centrifugal forces (F_{cf}) imposed by axial joining forces. However, the presence of broken fibers in the squeezed material can impair a stable flow and consequently lead to an inhomogeneous consolidation of the squeezed material. By analysing a cross-section of the squeezed material, three regions were observed, as shown in Figure 6.14-c.

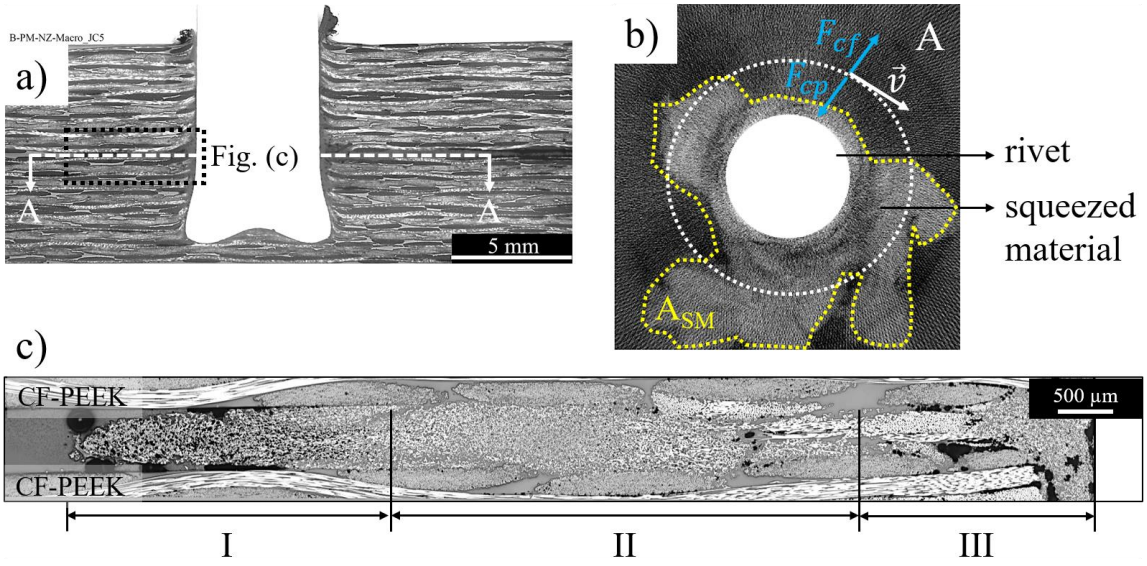

Figure 6.14 a) Overview of a friction riveted joint, showing its mid-plane where low viscous polymer and broken fiber flow, forming the squeezed material; b) top view of the squeezed material acquired by X-ray µCT; c) cross-section of the squeezed material, showing three regions of material consolidation. (Joining parameters - RS: 15000 rpm, FF_I: 5 kN, FF_{II}: 10 kN, DF: 7.5 mm, CP: 0.2 MPa)

The flow front, distant from the rivet shaft (Region I, Figure 6.14-c), incompletely wets the inner surfaces of the composites and cools down rapidly. As soon as the viscosity of the material increases, any air entrapped in the highly viscous material can no longer escape, leading to a reconsolidated material with high porosity and therefore low adhesion efficiency. Goushegir, Dos Santos, and Amancio-Filho [208] addressed a similar formation in CF-PPS/AA2024 friction spot joints. The low viscous PPS, molten during the joining process, wetted the surface of the aluminum and, owing to its fast cooling rate, entrapped air in the outer region of the joining area [208]. As the flow front cools down, the flow of still soft polymer is restricted and becomes denser, decreasing the internal flaws. Consequently, a homogeneous intermediate region is formed, without porosity (Region II, Figure 6.14-c). Additionally, the interfaces between the squeezed material and composite plates cannot be distinguished in Region II, which indicates molecule interdiffusion. When two or more polymeric plates are exposed to sufficient energy through temperature and pressure, the polymer chains gain mobility and may diffuse across interfaces to reach a favorable conformation, and thereby decrease the entropy of the system [218]. In Region III of Figure 6.14-c, which is close to the rivet, although there is polymeric interdiffusion the presence of internal flaws indicate unstable material flow and possible thermal decomposition of the composite matrix – addressed in Section 6.3.1. In this region the composite material is exposed to high temperatures for a longer time and it flows through a restricted space, which can exert shear forces on the low viscous material and consequently flow turbulences, as reported with viscous polymer systems [195].

Bearing in mind that interdiffusion of polymeric molecules promotes higher adhesion forces than incomplete wetting [219], leads one to expect that the failure mechanisms governing Region I will be adhesive failure, while in Regions II and III it will more likely be cohesive failure. The failure mechanisms of the friction riveted joints under shear loading are thoroughly investigated in the next chapter. Despite the existence of additional adhesion forces, owing to the squeezed material, it leads to inevitable separation of the composite plates, which can compromise the durability of the joints, as discussed in Chapter 9. The amount of squeezed material and extension of the adhesion regions in Figure 6.14-c is directly dependent on heat generation during the joining process and the plastic deformation of the rivet tip, and in turn these are influenced by the process parameters. With a larger widening of the rivet tip, more softened composite material is displaced from the joining area, and some of this to the composite overlap area. Figure 6.15 shows the linear dependency of the squeezed material area (A_{SM} indicated in Figure 6.14-b) with plastic deformation of the rivet, measured indirectly by volumetric ratio VR (see Section 5.2.5.2). The influence of process parameters on the joint formation, and the bonding mechanisms discussed here, were indirectly addressed in Section 6.5.2 about the DoE for optimizing mechanical performance of the joint.

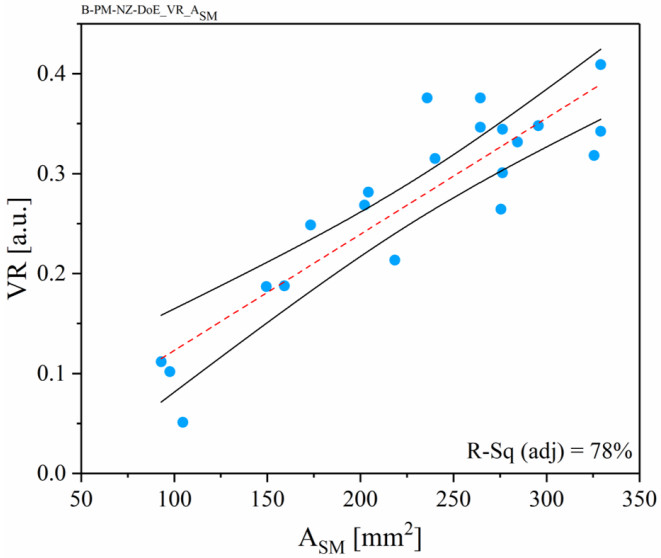

Figure 6.15 Linear correlation between volumetric ratio (VR) and area of squeezed material (A_{SM}).

6.5 Process optimization for detailed joint characterization

Earlier in this chapter, Friction Riveting was analyzed in terms of joint formation, bonding mechanisms, and the effect of process temperature on the microstructure, physicochemical, and local mechanical properties of the joint materials. This section is dedicated to further analysis of previous

observations, in order to discuss the influence of the process parameters on the lap shear strength of the joints and thereby determine an optimized joining condition for such a response. The bonding mechanisms and geometric features of the joints are used to support the discussion. A full factorial DoE and ANOVA were adopted as described in Section 5.2.2 and a new set of joining parameters was validated, while lap shear testing was performed according to Section 5.2.9.1.

6.5.1 Effect of the geometric features of friction riveted joints on the quasi-static mechanical performance

Figure 6.16 shows the average ULSF of each joining condition within the parameter window selected for the DoE, along with the categories of plastically deformed rivet tip shape described in Section 6.3.2. The joint strength varied between (2.7 ± 0.3) kN and (6.6 ± 0.4) kN (force-displacement curves are presented in Appendix F), where the bell shape (S2) of the plastically deformed rivet tip provided the strongest joints. Although the under (S1) and over (S3) plastically deformed rivet tips have similar negative impacts on the ULSF, the implications of their shapes on the bonding mechanisms and microstructure of the materials (described Section 6.3) are different, and thus were further systematically investigated. All the joints failed through a combination of composite bearing and rivet pull-through, as reported in [115]. The damage evolution was thoroughly investigated and will be presented in Section 7.1.2.

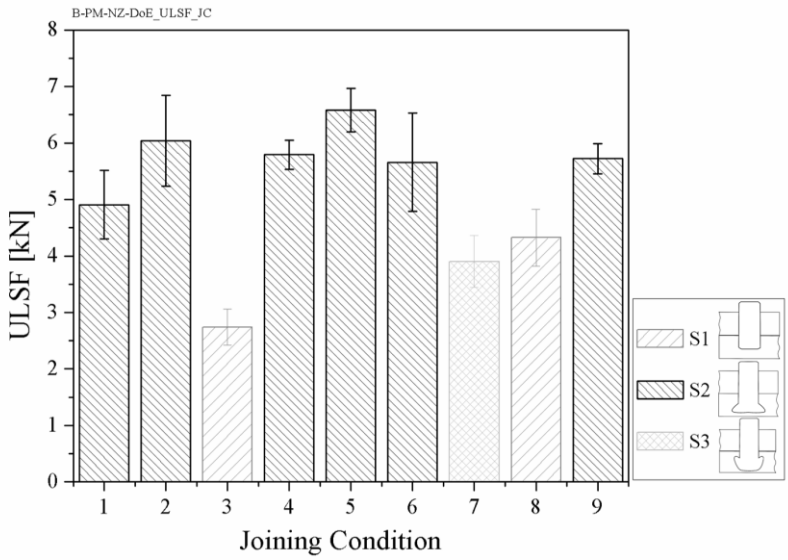

Figure 6.16 Effect of various joining conditions on the ULSF of friction riveted joints. Numbers from 1 to 8 correspond to the experiments performed as part of the DoE while 9 is the center point add to the model.

In addition to the shape of the plastically deformed rivet tip, the geometrical features of joints, including VR and A_{SM}, are also affected by the joining parameters, and these could result in changes to joint strength. VR indirectly expresses the anchoring efficiency and therefore the contribution of macromechanical interlocking to joint strength, while A_{SM} influences the adhesion forces between the composite plates. According to the results of DoE (Figure 6.17), a linear trend was observed where increasing VR increases the ULSF, with VR varying from 0.1 to 0.4 (Figure 6.17-a). This result is consistent with the relationship established between the geometry of the deformed rivet tip and the mechanical performance of friction riveted joints under tension [25,144,145,147], and shear loading [27,147]. The exploratory power (R^2_{adj} = 54 %) of such a linear model, although sufficient, is impaired by having a simplified calculation of VR that does not consider the original shape of the deformed rivet tip, only its geometrical features H, D_p and W (Equation 2). Similarly, as the A_{SM} varied between (98 ± 6) mm^2 and (280 ± 45) mm^2 and correlates to ULSF through a quadratic model with adequate fitting (R^2_{adj} = 60 %) (Figure 6.17-b). For all joining conditions, the process temperature overcame the melting temperature of PEEK (see Section 6.2), and therefore a layer of low viscous polymer was present in all joints and susceptible to flow. The intensity of the squeezed flow was then dependent on different axial forces and deformation of the metal rivet – *i.e.* VR – which imposed more or less displacement of composite material. Although VR and A_{SM} are linear dependent (see Section 6.4), their effect on ULSF does not follow the same trend, suggesting additional contributions. Selected points over the experimental range were further examined by X-ray micro-computed tomography (µCT), thus providing better visualization of the correlation mentioned, as presented in Figure 6.17-c.

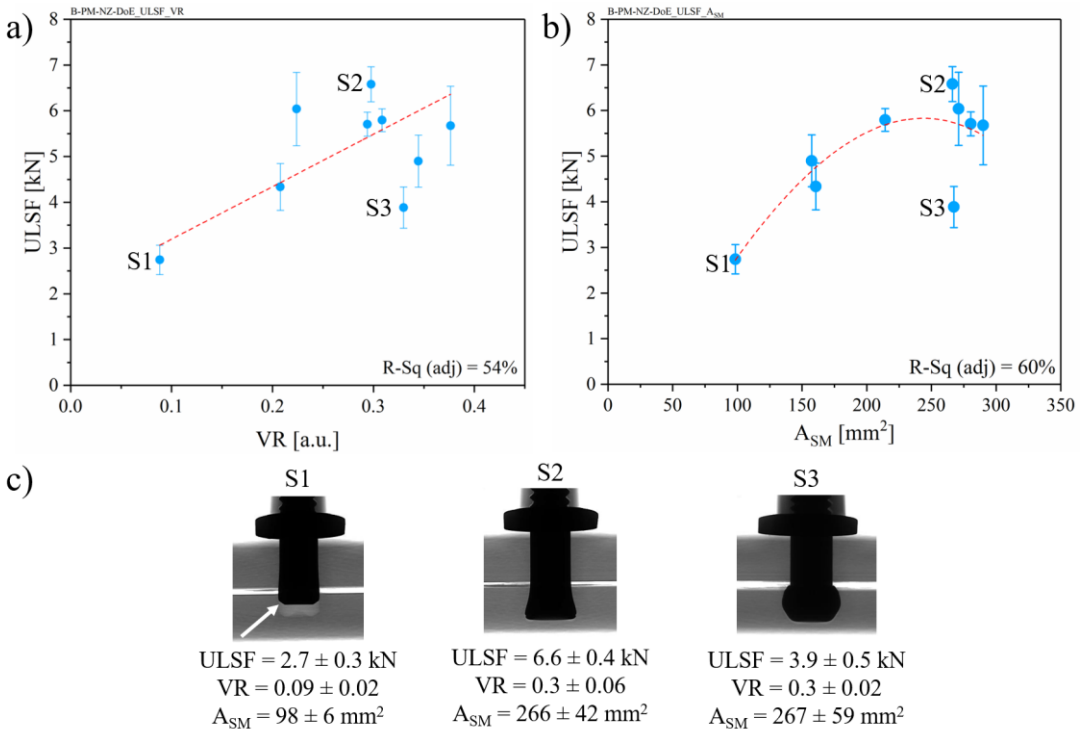

Figure 6.17 a) Linear and b) quadratic models to describe the correlations of VR and A_{SM} with ULSF, respectively; c) X-ray micro-computed tomographs of three categories of rivet plastic deformation formed over the parametric window selected.

The underdeformed rivet tip (S1) minimized the macromechanical anchoring in the composite parts, displaced the least amount of process-affected composite from the joint area, and therefore produced weaker joints. Moreover, as there was no efficient mechanical interlocking between the metal and composite, the allowable tightening torque of the joint is decreased, a concept widely known with conventional bolted joints [220]. Therefore, any additional handling after Friction Riveting, such as tightening of the nut used in this work for lap shear testing, can cause premature damage in the joining area, as highlighted by the white arrow in Figure 6.17-c, consequently compromising ULSF.

In cases where the plastically deformed rivet tip assumes a bell shape (S2) or inverted bell shape (S3), although VR and A_{SM} vary in the same range for both categories of deformed rivet tip, approximately 41 % less ULSF was observed in S3 joints compared to S2 joints. The negative effect in S3 of over deformation on the ULSF is believed to be the result of two mechanisms: an increased volume of flaws in the vicinity of the highly deformed rivet tip (see Figure 6.11) combined with larger separation between upper and lower composite plates.

The flaws in composite material surrounding the rivet is a result of incomplete wetting of the metal surface by low viscosity PEEK, owing to entrapment of volatiles from the thermal decomposition of PEEK and extensive displacement of the fiber network imposed by the upward

flow of the plasticized metal tip (see Section 6.3.3). As a consequence, micromechanical interlocking is compromised and this may lead to premature adhesive failure between the metal and composite.

The upward flow of the plasticized metal in the over deformed S3 joints would also impose more separation of the composite parts, which increases the eccentricity of the single lap joint, and thus secondary bending under lap shear testing. The negative effect of secondary bending on the quasi-static and cyclic mechanical performance of single lap joints has been widely described in the literature [221–223]. As the gap is formed one may assume that more material flows between the composite parts. However, such material is not efficiently squeezed between them, as indicated by similar A_{SM} in comparison to S2 joints (Figure 6.17-b.). Consequently, the contribution of the interface diffusion and the entanglement of polymeric molecules to the joint strength decreases.

6.5.2 Statistical analysis of the effect of process parameters on the quasi-static mechanical performance of friction riveted joints

As the process parameters affect the heat generation, and consequently the amount of squeezed material as well as the shape and geometric features of the plastically deformed rivet tip, such responses all directly influence the joint strength. Based on this, ULSF was chosen in this work to further determine the effects of process parameters on joint properties. Nonetheless, the VR statistical model is also presented in Appendix G, and the same procedures described here for ULSF were applied to VR assessment. An analysis of variance (Appendix H) provided a reduced statistical model for ULSF (Equation 8), where ULSF is the dependent variable while the process parameters (RS, FF, CP) and their interactions are the independent variables. Initial factors with p-values > 0.05 were eliminated using the stepwise backward elimination method. Figure 6.18-a shows a comparison between the experimental data and their respective predicted values obtained from Equation 8 for all of the DoE conditions (solid circles) and validation conditions (asterisks); the joining conditions selected for the validation are presented in Appendix H. The dashed red line shows the total linear relationship between the experimental and predicted values, whereas the dashed black lines are the prediction intervals, and the solid lines are 95 % confidence intervals. The R^2_{adj} value of the ULSF model was 88 % and the standard error (S) was 432 N, while the majority of the observations lie within the prediction limit interval. These results suggest that the validated model has a high explanatory power, and sufficient accuracy to predict such a response outside the selected range of joining parameters, so may be used for an understanding of their effect on the ULSF.

$$ULSF = 5114 + 541 \times RS - 419 \times CP - 825 \times RS \times FF - 417 \times RS \times FF \times CP \quad (8)$$

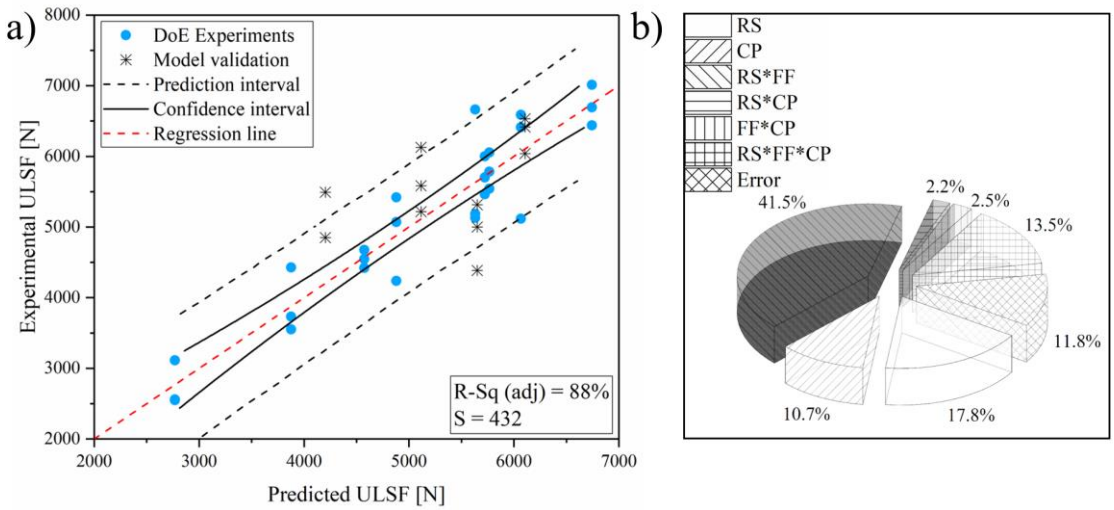

Figure 6.18 a) Validation diagram for the reduced model of ULSF; b) proportional effect of each significant factor and interaction on the ULSF.

Figure 6.18-b shows the proportional effect of each significant process parameter and interactions on ULSF. RS*FF (p-value = 0.000), RS (p-value = 0.000), RS*FF*CP (p-value = 0.001), and CP (p-value = 0.003) were the most significant contributions, and which correspond to 41.5 %, 17.8 %, 13.5 %, and 10.7 %, respectively. FF had a high p-value (p-value = 0.519), but its interaction with RS and CP appears to be significant and so this was further analyzed. Figure 6.19 illustrates the main effects of the process parameters on the ULSF response, along with an X-ray µCT analysis. In these plots, a larger slope of the lines indicates a stronger effect of the parameter on the response, whereas a slope close to zero degrees indicates insignificance of the parameter to the response. Increasing RS increases the ULSF, while increasing CP impairs the joint's mechanical performance; the effect of FF is relatively insignificant.

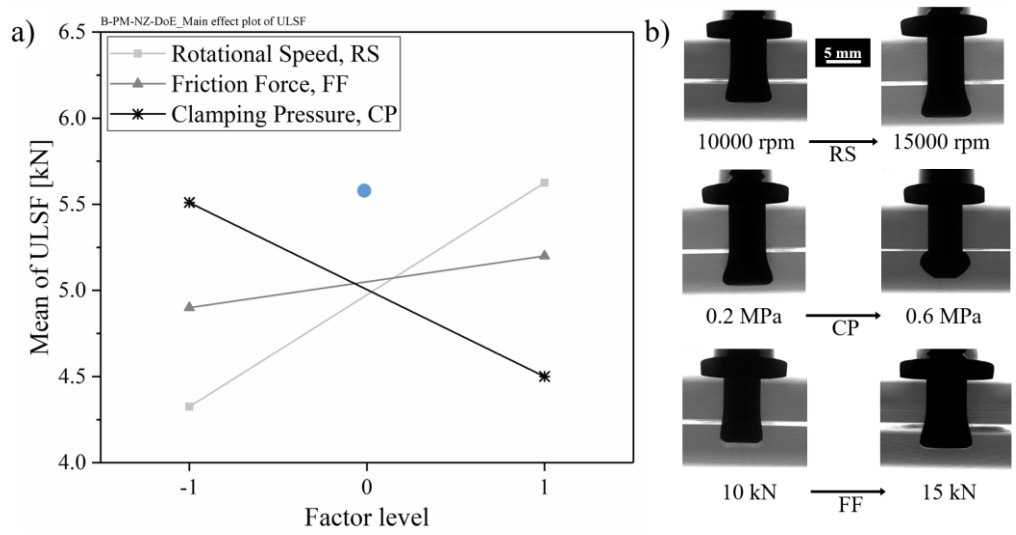

Figure 6.19 a) Main effect plots of the process parameters on the ULSF (blue dot is the center point used in the full factorial design); b) selected X-ray micro-computed tomographs of low and high limits of each individual parameter investigated within the DoE.

By increasing the rotational speed (RS), the shape of the plastically deformed rivet tip changed from under deformed (S1) to bell shaped (S2), leading to higher VR – i.e. better anchoring efficiency – and consequently improved joint mechanical performance. In this case, the VR is enhanced by increased rivet penetration depth (H) and rivet tip width (W), as shown in Figure 6.19-b. As discussed in Section 5.2.1, the joining phases in this work were limited by displacement of the spindle, and consequently H was controlled and set to be kept constant. Therefore, an increase in H can only be explained by reaction of the composite to the increase in heat generation. In accordance with [25,143,147], RS increases the energy input, melting a larger volume of composite matrix surrounding the rivet, so enabling deeper rivet penetration. The presence of continuous fibers in the woven CF-PEEK, which are not softened during the process, also contribute to an increase in heat generation with increasing RS. Similar to the drilling of composite, the fiber network increases the drilling torque, leading to fiber breakages and additional solid friction between the tool and broken fibers, which is intensified by higher RS [165,224]. Therefore, a combined effect of molten matrix and broken fibers may explain the increase of H, hence VR, with higher RS.

The clamping pressure (CP) that is applied externally to the joint during the joining process is another parameter with a large influence on the lap shear strength of the joints. The effect of the clamping system on joint formation and mechanical performance of friction riveted joints was extensively investigated by Borba *et al.* and published in [156]. By increasing the CP the bell shape (S2) of the deformed rivet tip assumes an inverted bell shape (S3) (Figure 6.19-b), which as previously explained despite sharing similar VR and ASM this increases the joint eccentricity and composite flaws close to the rivet, weakening the joint. The heat input required to deform the metal rivet into S2 and S3 shapes varies over the same range (see Section 6.2). However, for the same heat

input, the flow stress of the titanium alloy progressively decreases where the deformation first occurs, and this volume of metal continues to deform in further processing [101]. This is intensified by the α→β phase transformation, local adiabatic heating, and its low thermal conductivity which conserves the localized high temperature within the material [100,205] as explained in previous sections. Therefore, although CP does not contribute to heat generation, it is applied throughout the joining process and when it is higher more internal reactive forces arise at the rivet tip, leading to continuous deformation of the plasticized rivet tip and consequently over deformation.

The friction force (FF) was shown statistically insignificant for the ULSF, which does not comply with previous investigations into the Friction Riveting of titanium and short carbon fiber reinforced PEEK [25]. Figure 6.19-b illustrates no changes to H and a slight increase in W, resulting in a small variation in VR (up to 15 %). According to Altmeyer *et al.* [25], the frictional pressure, which can be translated as friction force, has a pronounced effect on energy input, and consequently increases the rivet penetration depth and anchoring efficiency, similar to the effect of RS. However, contrary to Altmeyer *et al.* [25], the joining phases in this work were controlled by spindle displacement (see Section 5.2.1) and therefore the joining time was a process response. Thus, one may expect that when higher axial forces are applied to the rivet it decreases the joining time, hence limiting the heat generation. Lower heat input plasticizes less metal material and composite matrix, leading to less rivet penetration. The additional rivet tip widening observed in Figure 6.19-b does not contribute to the joint strength, because it occurs close to the surface of the composite in the overlap area. The negative effect of such a deformation has already been reported by Pina *et al.* [143] in an analysis of anchoring depth (D_p) for AA2024/PEI friction riveted joints.

From the ANOVA analysis, the only second order interaction with a significant influence on the ULSF was RS*FF, as shown in Figure 6.20. From the X-ray µCT analysis (Figure 6.20-b) it is possible to see that at low RS (10000 rpm) by increasing the FF the ULSF increases, owing to widening of the rivet tip and consequently higher VR – *i.e.* anchoring efficiency. On the other hand, at high RS (15000 rpm), increasing the FF results in weaker joints with an over deformed rivet tip. In the same manner as explained for the main effect plot (Figure 6.19-a), as the low RS generates less heat and high FF shortens the joining time, there is not enough heat to further plasticize the metal and to decrease the viscosity of the polymer. Therefore, no significant changes were observed in the geometric features of joints produced with lower RS when increasing FF. However, at high RS, the formability of the rivet tip increased as a result of the higher heat input. In this situation, similar to the effect of CP, any extra axial force will more greatly compress the plasticized rivet tip against the undamaged fibers, introducing more adiabatic heating within the titanium. This contributes to the work-softening of Ti6Al4V and further deformation of the rivet tip.

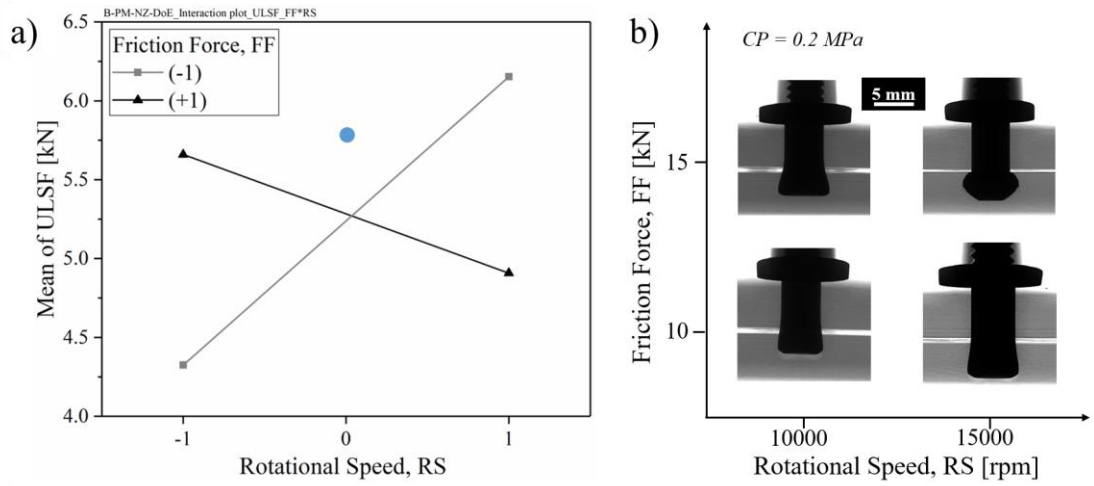

Figure 6.20 a) Interaction plot of the effect of RS*FF on the ULSF (blue dot is the center point used in the full factorial design); b) selected X-ray micro-computed tomographs of low and high limits of the combined parameters significant for the ULSF reduced model.

A third-order interaction between RS, FF, and CP was also significant for ULSF. Third-order interactions are normally excluded from reduced statistical models as their physical interpretation becomes too complex to understand and can be misleading [163]. However, in this work RS*FF*CP presented a p-value = 0.001, showing its high significance to ULSF. Although the exact reason for this result is still not well understood, a similar effect of CP and FF on the ULSF, when the latter is in combination with high RS, may help understanding this third-order interaction. As Borba *et al.* [156] have reported, clamping efficiency is a balance of internal forces in the joining area, and thus a compromise between the reactive forces arising from the joining force and the clamping force. Therefore, when enough heat is generated by high RS, changes to FF and CP may give rise to higher reactive forces at the rivet tip, leading to over deformation.

In summary, these results suggest that the highest level of RS (15000 rpm), along with the lowest level of FF (10 kN) and CP (0.2 MPa) provide an optimized set of parameters to increase the lap shear strength of friction riveted joints, over the parameter window used in this work. This set of parameters corresponds to Condition 5 of the DoE, with ULSF of (6.6 ± 0.4) kN, VR of (0.30 ± 0.06), and A_{SM} of (266 ± 42) mm^2. To confirm the optimized joining condition, a desirability function was used where maximization of ULSF and an assigned value of up to 0.3 mm of separation between the composite parts were used as the main targets of the function, as described in Section 5.2.2. For the joining conditions where an inverted bell shape (S3) of the rivet tip was formed a gap (G) could not be avoided. Therefore, to keep G at acceptable levels for aircraft applications, the response was limited to 0.3 mm, which has been published in the literature [168–170] as a common thickness of adhesives and sealants used in combination with conventional bolted joints. Three solutions for the desirability function were obtained, as shown in Table 6.3.

Table 6.3 Sets of process parameters for the optimized condition, as predicted by the desirability function

Solution	Process parameters			ULSF [kN]	Composite desirability
	RS_{II} [krpm]	FF_{II} [kN]	CP [MPa]		
1	15	10	0.2	6.7	0.94
2	15	10	0.6	6.1	0.80
3	10	15	0.6	5.8	0.72

All the optimized joining conditions predicted by the desirability function are conditions tested within the DoE and which formed a bell-shaped rivet tip with high anchoring efficiency. Solution number one, which corresponds to Condition 5 of the DoE, was selected as the optimized joining condition in this work, owing to its higher composite desirability and therefore high accuracy to fulfill all the required targets. The predictions of the desirability function for the optimized joining condition complies with the ANOVA analyses of the effects of parameters on the ULSF, leading to the same process solution.

6.6 Joint design optimization

The improvement of joint strength was further assessed by the joint design, considering the rivet parameters of tightening torque (TT), outer diameter of external washer (D_w) and the geometry of the friction riveted joint, including edge distance (e) and specimen width (W). The optimized set of joining parameters (RS: 15000 rpm, FF_I: 5 kN, FF_{II}: 10 kN, DF: 7.5 mm, CP: 0.2 MPa) was used to join the single lap specimens, which were then tested under tension. To attach a washer and nut, threads were cut along the free length of the rivet. It is worth mentioning that all the joint designs tested in this section failed by the bearing of the composite and rivet pull-through, as is reported by Borba *et al.* [115] characteristic for direct friction riveted joints of CF-PEEK and Ti6Al4V. Therefore, the aircraft requirement of a failure mode that is non-catastrophic [225] was fulfilled for all the joint geometries. The damage evolution prior to this failure mode will be described in detail in Section 7.1.2.

6.6.1 Effect of washer size

Figure 6.21-a shows the influence of washer size on the quasi-static mechanical behavior of friction riveted joints, with other variables fixed (tightening torque: 1 N·m; W/D ratio: 7; e/D ratio: 3.5). There was an increase of approximately 33 % in ULSF from untightened joints to joints assembled with a washer of any size. However, no significant change to ULSF was observed by

increasing the outer diameter of the washer. As reported in the literature [220], the washer distributes the pre-load of tightening up the joint, decreasing the stress concentration at the fastener surroundings and therefore increasing the composite's bearing capability. Moreover, the washer promotes lateral constraints to the area underneath it and may affect the secondary bending of the joints [33], as shown in Figure 6.21-b. Although no improvement in ULSF was observed, larger washers seem to affect the eccentricity of friction riveted joints, leading to higher out-of-plane displacement. Additionally, larger washers may decrease the pressure applied by the pre-tightening torque, which could impair joint stiffness and consequently also contribute to higher out-of-plane displacement. For these reasons, a washer outer diameter of 2D (10 mm) was selected as optimum, which also led to a weight saving among the geometries evaluated in this work.

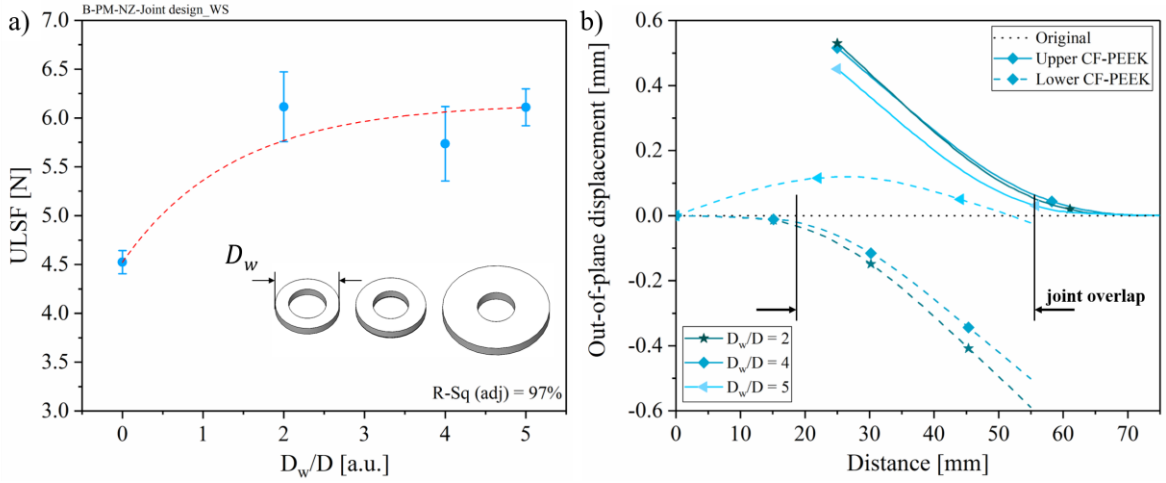

Figure 6.21 a) Ultimate lap shear force (ULSF) as a function of outer diameter of the washer (D_w); b) out-of-plane displacement of joints tightened using different sizes of washer, measured by digital image correlation (DIC).

6.6.2 Effect of tightening torque

Figure 6.22 shows the effect of tightening torque on friction riveted joint strength for both untightened and tightened joints with three levels of torque, with other variables fixed (W/D ratio: 7; e/D ratio: 3.5). As expected, by increasing the tightening torque, an improvement of approximately 30 % of joint strength was observed up to 1 N·m. Similar to bolted joints [33,189,220], changes in tightening torque promotes friction between the washer and the composite surface, which leads to an additional mechanism of load transfer during quasi-static and cyclic mechanical testing. For the untightened joints, the load is transferred mostly through the fastener in contact with the composite, while for tightened joints the load is partially transferred by friction [220]. Therefore, higher

tightening torque leads to higher friction force, which releases the stress concentration near the edge of the hole, which in turn produces stronger joints. However, after 1 N·m, a 20 % decrease of friction riveted joint strength was observed, which is explained by premature failure of the metal-composite interface at the rivet tip. Owing to excessive torsion transmitted to the rivet anchoring over the joint tightening, the adhesion between the materials was compromised, as shown in Figure 6.22-c, leading to premature debonding of the rivet from the composite hole. Therefore, a tightening torque of 1.5 N·m was considered the break loose torque, which should be avoided. For further analysis, 1 N·m was used as the optimized tightening torque for CF-PEEK/ Ti6Al4V friction riveted joints produced with the joining parameters established in this work.

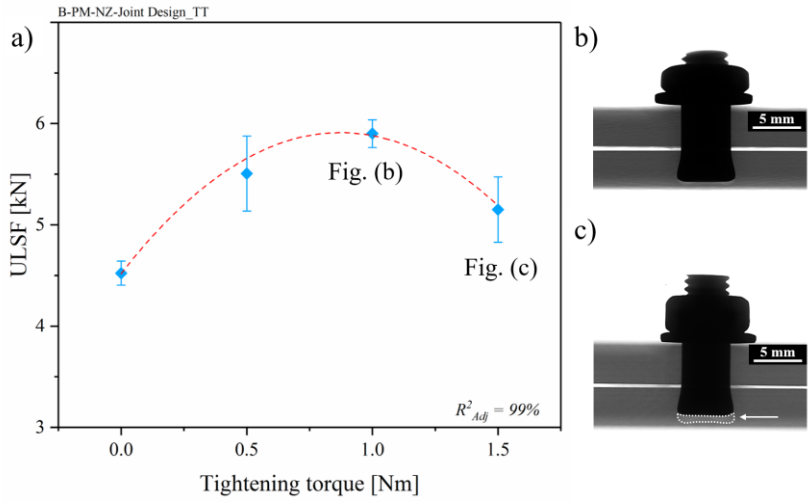

Figure 6.22 a) Ultimate lap shear force (ULSF) as a function of tightening torque; X-ray µ-computed tomographs of joints tightened with b) 1 N·m, and c) 1.5 N·m, showing the damage of the composite-metal interface when joints are tightened with a torque higher than the break loose torque.

6.6.3 Effect of joint width and edge distance

Altmeyer [116] assessed the influence of edge distance (e/D) and specimen width (W/D) on the strength and failure behavior of CF-PEEK/Ti gr.3 friction riveted joints. The author reported that joints with e = 3D and W > 4D presented higher strength and failed by progressive plastic deformation of the edges of the composite hole. Similar findings were reported by Cooper and Turvey [189] for pultruded glass fiber reinforced polyester joined with M10 steel bolts. Following these previous investigations, three levels of e and W were evaluated for CF-PEEK/Ti6Al4V friction riveted joints, including recommended levels of e = 3D and W > 4D. The other variables were kept constant (TT: 1 N·m; D_w/D: 2). Figure 6.23-a shows the average ULSF for all the joint designs. The ULSF varied between (5.3 ± 0.3) kN and (6.2 ± 0.2) kN, with no indication of dependence between joint geometry

and strength. To statistically analyze the significance of these parameters on ULSF, ANOVA was performed, and the main effect plot is shown in Figure 6.23-b. Although the increase of e and W showed a small effect on the joint strength, the flat slope of the tendency lines indicates a weak influence of the parameters on the response, and therefore they are statistically insignificant. Additionally, in contrary to the literature [116,189], CF-PEEK/Ti6Al4V friction riveted joints underwent only bearing of the composite without any change on the failure behavior. It is reasonable to assume that the W/D and e/D investigated in this work were larger enough to compensate the compressive stress concentration at the edges of the composite hole, imposed by the rivet. Thus, catastrophic tensile failure as shear-out and cleavage, commonly observed for composite bolted joints [33,189], were avoided.

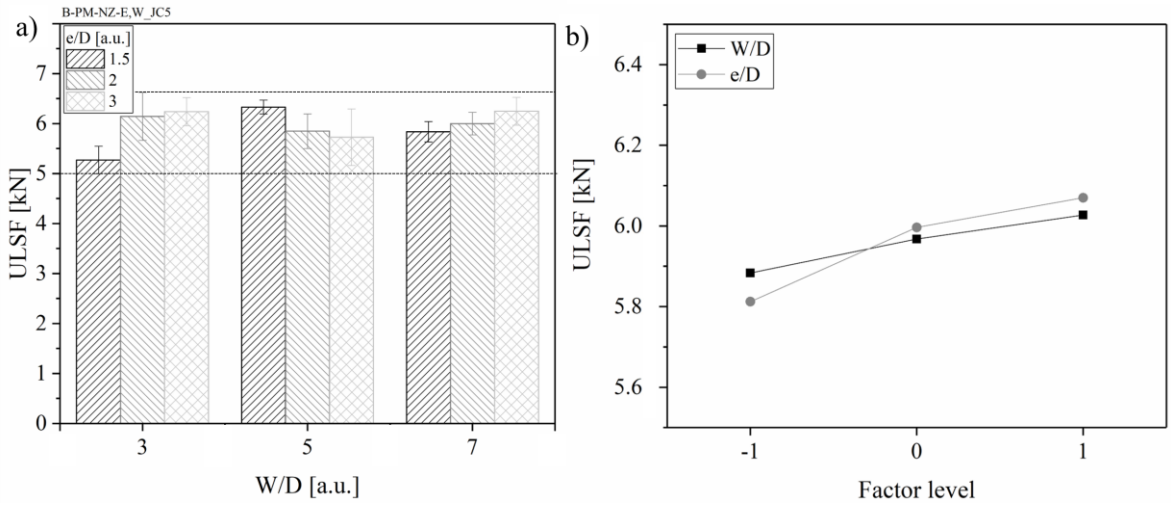

Figure 6.23 a) Effect of edge distance (e/D) and joint width (W/D) on the ultimate lap shear force (ULSF) of friction riveted joints; b) main effect plot of e/D and W/D on the ULSF, calculated from ANOVA.

As the levels of e and W investigated in this work did not influence the joint strength, and owing to better clamping of larger specimens in the clamping system (Figure 5.5-a), friction riveted joints were produced according to the recommendations of joint geometry in ASTM D5961 [176] (see Section 5.2.1).

6.7 Summary of the results

By stepwise analysis of the Direct FricRiveting process, the upward and squeezed flow of the process-affected composite were investigated as well as the formation of a shear layer and shear banding in the composite, in the vicinity of the rivet shaft. The squeezed material between the composite parts was shown to contribute an additional bonding mechanism to the mechanical interlocking of rivet tip

widening and embedding of fiber and matrix in the rough surface of the rivet. The process temperature measured by thermocouples exceed the decomposition temperature of PEEK as well as the β-*transus* temperature of Ti6Al4V. The high process temperature along with fast cooling rate decreased the mechanical properties of CF-PEEK locally, due to volumetric flaws in the thermomechanically affected zone of the composite and the low degree of crystallinity of PEEK. Such effects also increased the hardness locally of the Ti6Al4V thermomechanically affected zone owing to morphological transformation from a globular microstructure to a combination of α' martensite and Widmanstätten structures within the rivet tip. Over the process temperature range analyzed in this work, three distinct plastic deformation shapes of the rivet tip were detected: under deformed, a bell shape and an over deformed inverted bell shape. The bell-shaped rivet tip produced stronger joints under shear loading, owing to its high anchoring efficiency and low level of defects in the composite. By a DoE and ANOVA, RS, CP, RS*FF, and RS*FF*CP were found to be the significate parameters and second to third order interactions that affected the ultimate lap shear strength of the Ti6Al4V/ CF-PEEK friction riveted joints. Within the parameter window used in this work, the highest level of RS (15000 rpm), along with the lowest level of FF (10 kN) and CP (0.2 MPa) provided an optimized set of parameters to increase the lap shear strength of friction riveted joints. An improvement of joint strength was further assessed with a fundamental study of the joint design. A washer size of 10 mm ($D_w/D = 2$) and tightening torque of 1 N·m increased the ULSF of friction riveted joints by 30 % due to the better stress distribution over the rivet surroundings and additional friction between the washer and the composite surface. No correlation could be drawn between edge distance, specimen width and ULSF. The optimized joining condition and joint design (washer outer diameter of 10 mm and tightening torque of 1 Nm) were used to produce single lap joints for the analyses presented in the following chapters.

Chapter 7. Mechanical Behavior of Friction riveted Joints

This chapter describes the mechanical performance of SLS friction riveted joints under quasi-static and cyclic loading. An optimized set of joining parameters (RS: 15000 rpm, FF_I: 5 kN, FF_{II}: 10 kN, DF: 7.5 mm, CP: 0.2 MPa) was selected to join the single lap specimens. The joints were assembled with a 10 mm outer diameter washer and tightened with 1 N·m, following the fundamental investigation of joint design presented in Chapter 6. The chapter starts with an analysis of quasi-static mechanical behavior, which comprises understanding critical stress concentration sites by finite element (FE) analysis, damage evolution, and fracture mechanisms. Towards the end of the chapter, the results obtained from fatigue loading are presented, including analysis of S-N curves and fracture surfaces.

7.1 Quasi-static mechanical performance

7.1.1 Quasi-static mechanical properties

The typical force-displacement curve of a single lap friction riveted joint is shown in Figure 7.1-a. The average ultimate lap shear force (ULSF) was (6.6 ± 0.4) kN, which is less than the (8.7 ± 0.2) kN of reference lock bolted joints, owing to differences in the joint geometry, as reported by Borba *et al.* [115]. Three stages characterize the curve: a typical linear elastic behavior until the first load drop (Stage I), followed by an almost linear slope until the peak force is reached (Stage II), and a softening load drop region (Stage III). To analyze the reversibility of joint strain, which indicates the introduction of damage and plastic deformation during the mechanical test, consecutive load and unload cycles were imposed on the joint. A cross-sectional view of the joints after each cycle (see Figure 7.1-b) was evaluated to define the main failure mechanisms that govern the joint's mechanical behavior.

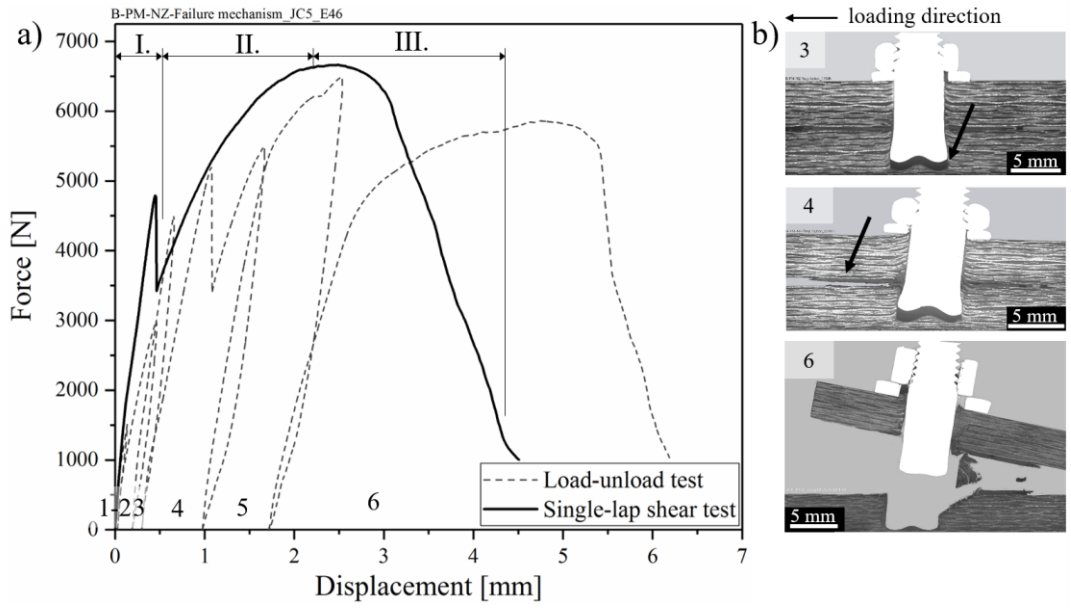

Figure 7.1 a) Typical lap shear force-displacement curve (solid line) along with six curves from the loading and unloading cycles (dashed lines); b) cross-sectional view of the samples loaded at levels of 4.5 kN, 5.5 kN, and 6.5 kN, which corresponds to cycles 3, 4 and 6.

The loading and unloading curve resulting from joints loaded with 4.5 kN (cycle 3 in Figure 7.1-a) displays a linear elastic behavior with limited unrecovered displacement and no significant change to the elastic modulus. Upon examining the specimen's cross-section in the third cycle (cycle 3 in Figure 7.1-b), a crack has nucleated and propagated throughout the interface between the rivet tip and the composite hole, leading to detachment of the rivet. At load level 5.5 kN (cycle 4 in Figure 7.1-b), which corresponds to the first load drop in the typical load-displacement curve (Stage I in Figure 7.1-a), the joint stiffness reduces significantly and a considerable plastic deformation is displayed. Such an unrecovered deformation combines adhesive/cohesive failure of the composites interface and bearing damage introduced through the composite thickness due to the bending moment to which the rivet is subjected (cycle 4 in Figure 7.1-b). The damage accumulates until the plastic-deformation capacity of CF-PEEK is reached with the peak force at load level 6.5 kN (cycle 5 in Figure 7.1-a). Although the composite is already damaged at this level, the joint still does not fail entirely and is further loaded up to 5.8 kN (cycle 6 in Figure 7.1-a). Towards the end of this cycle, the composite hole elongates concomitantly with breakage of the damaged composite and final rivet pull-through failure (cycle 6 in Figure 7.1-b).

Similar mechanical behavior has been extensively reported in the literature for hybrid joints and conventional lock bolted joints of thermoset composites [221,222,226]. Although displaying a similar behavior, Heimbs *et al.* [221] showed that for similar single lap joint geometry using Ti6Al4V bolts with a bolt diameter of 4.8 mm and a 130° countersunk head, the displacement at break of the bolted joints was 6.3 mm, which is considerably higher (approximately 44 %) than in the friction

riveted joints. A broader bolt head compared to the plastically deformed rivet tip can partially explain this difference, since it imposes more compression on the composite surface and therefore more restriction to composite bearing [220].

The state of stresses that led to the previously described typical failure of friction riveted joints was investigated using FEM simulation, as shown in Figure 7.2. The rivet was removed from the analysis for better visualization of stress concentration sites. The FE model proposed and its validation are presented in Appendix C. As can be seen in Figure 7.2-a, the FEM simulation showed a bending of the sample as a reaction of the resultant momentum M_r imposed by the force F. Furthermore, the good interface between metal and composite (see Figure 6.9) allowed the load to be efficiently transmitted to the rivet and its composite surroundings which created tension and compression stress concentration sites. Figure 7.2-b to -d shows these sites in the longitudinal, normal and shear directions. The asymmetric pressure distribution along the surrounding of the rivet shaft owing to M_r induced tensile and compressive stresses on the edges of the composite hole (Figure 7.2-b), damaging them as previously explained.

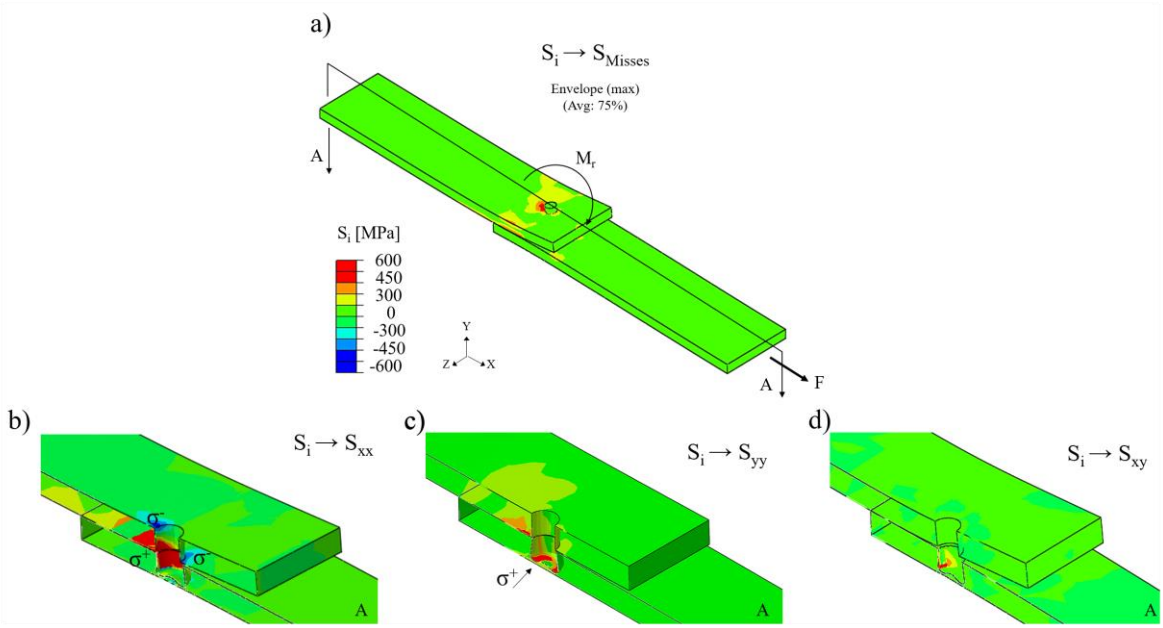

Figure 7.2 Stress analysis of friction riveted joint under lap shear testing through FEM: a) stress distribution based on Von Mises yield criterion; b) in-plane, c) out-of-plane, and d) shear stresses; showing stress concentration sites.

In terms of normal stresses (Figure 7.2-c), two concentration sites of tension stress were mainly formed: near the rivet tip and in the composite overlap area, of which the latter was less intense. Such stresses match the areas where failures by out-of-plane stress occurred during lap shear testing. At the rivet tip the tension was induced leading to rivet debonding from the composite hole, while at the composite interface the squeezed material was partially peeled up, leading to tearing of

PEEK fibrils. Moreover, the shear stresses (Figure 7.2-d) appeared to be mainly carried by the opposite hole edge to the loading direction, where a significant localized plastic deformation took place (see 6 in Figure 7.1-b).

7.1.2 Damage evolution and fracture analysis

The evolution of overall failure of the friction riveted joints, illustrated in Figure 7.3, is related to two main factors that induce several fracture micromechanisms: out-of-plane and in-plane stresses. As the geometry of single lap joints is not symmetric (Figure 7.3-a), the eccentric tensile load path induces secondary bending, which in turn leads to peeling stress [223]. The out-of-plane displacement of friction riveted joints was predicted by FEM (Figure 7.3-b) and this correlates to the out-of-plane displacement of the neutral line from the composite joint parts at different loading times ($t_{0\text{-}80}$) as recorded by DIC and shown in Figure 7.3-c. Figure 7.3-d depicts a lateral view of the deformation fields in the joint during the test. The initial stage t_0 took place prior to displacement monitoring, which starts at t_{20}. The selected loading times correspond to the end of the three stages depicted in a typical load-displacement curve for friction riveted joints, as described in the previous section (Figure 7.1).

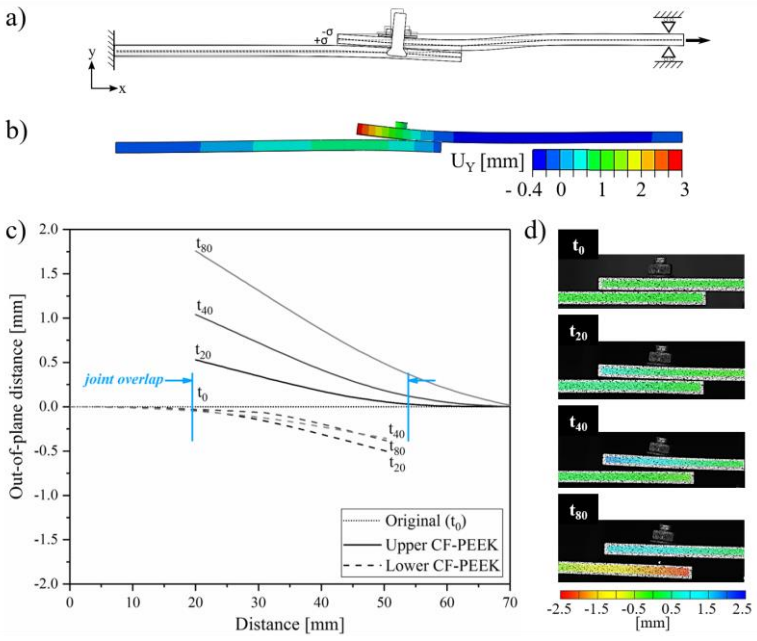

Figure 7.3 a) Schematic representation of the eccentric loading path in composite overlap friction riveted joints; b) out-of-plane displacement of friction riveted joints predicted by FEM analysis; c) out-of-plane displacement curves, and d) the respective images of the strain field at different load stages measured by digital image correlation (DIC).

The secondary bending increases with the loading due to a continuous release of the pre-tightening torque, which no longer inhibits an increment of load eccentricity, and thus contributes to compression of the composite surface and a decrease in joint stiffness. Herrington and Sabbaghian [46] reported the effect of tightening torque on the mechanical behavior of conventional composite bolted joints. The authors contend that the increase in bearing strength coming from an increased clamp-up torque is due to an out-of-plane constraint that inhibits peeling failure [46]. Additionally, the composite parts deflect asymmetrically until complete rivet removal. At t_{20} (Figure 7.3-d), such effects have led to a brittle fracture of the metal-composite interface by peel-up of the plies in the shaft of the composite hole and rivet detachment, as shown in the fracture surface of the remaining hole in Figure 7.4-a and -b. The initial separation the composite parts at t_{40} (Figure 7.3-d) appears mainly triggered by peeling stresses, which evolve into a large gap between the parts at t_{80}. In the latter step, the rivet is removed from the composite hole, increasing the out-of-plane displacement and imposing bending on the lower composite part.

A fracture analysis of the squeezed material between the composite parts (indicated by the yellow dotted area in Figure 7.4-a) illustrates three main features: a smooth adhesively failed surface (Figure 7.4-c), an elongated fibrous-like feature not oriented in the loading direction, and exposed fiber bundles oriented 90° (Figure 7.4-d). Such features indicate a combination of adhesive and cohesive failure in the composite overlap area, in accordance with the bonding mechanisms described in Section 6.4. Inside the cohesive failure area, a highly dense ductile fracture of the PEEK matrix by tearing suggests a slowdown in the crack propagation and appeared to be one of the primary fracture micromechanisms in the composite interface. Additionally, the exposure of the fibers from the composite plate suggests interlaminar cracks inside the first ply of the CF-PEEK owing to cohesive failure. No indication of shear-induced deformation in the squeezed material was identified in this region.

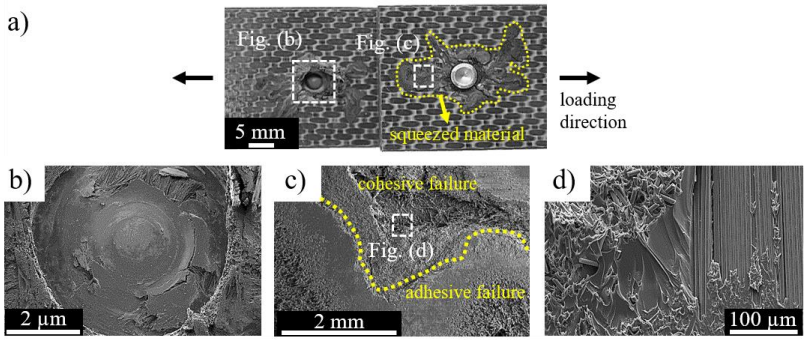

Figure 7.4 a) Overview of the fracture surface, showing the squeezed material consolidated at the interface between the composite parts; SEM micrographs of b) hole in the lower composite plate that remained after the joining process; c) squeezed material fracture surface, showing the adhesive and cohesive failure regions; and d) PEEK ductile fracture details along with exposed fiber bundles.

By increasing the eccentricity of the load path (from Stage II to Stage III in Figure 7.1), the in-plane stress became more relevant for joint integrity. Owing to the bending moment, the rotation of the rivet and the sinking of the plastically deformed rivet tip into the shaft walls of the hole imposed compression on the composite, resulting in through-thickness failure (*i.e.* bearing failure). Figure 7.5 shows the C-scan measurements of defect depth in the lower composite part for each stage of the load-displacement curve (Figure 7.1-a). The dashed lines indicate the position of the rivet, while the white regions in the diagrams correspond to the metal, for which the ultrasound signal was ignored in the current experiment. In comparison with the as-joined parts (see Figure 5.10-c), the out-of-plane stress developed in Stage I did not cause any shear-driven compressive failure in the composite. Therefore, the damaged area remained constant around the rivet. As soon as the rivet rotates in Stage II, the damage is accumulated near to the rivet tip and extends to other plies through the composite thickness (Stage III, Figure 7.5).

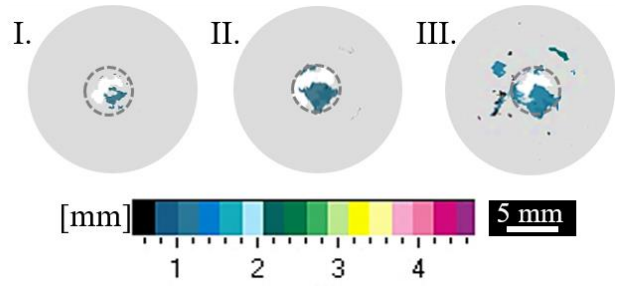

Figure 7.5 The defect depth acquired by ultrasonic inspection in the lower composite part of the overlap friction riveted joints loaded at levels of 4500 N (I), 5500 N (II), and 6500 N (III). The images highlighted with dashed circles indicate the position of the rivet.

Figure 7.6 shows the in-plane damage introduced in the joint and its micromechanisms. Critical bearing stress around the composite hole induced high local plastic deformation (*i.e.*, bearing damage), as shown in Figure 7.6-b. Moreover, the non-uniform bearing stresses across the laminate's thickness (see schematic in Figure 7.6-c) led to the shear-driven interfacial debonding of the matrix from the fiber bundle oriented 0° (Figure 7.6-d) and formation of a kink band (Figure 7.6-e). CFRP laminates are known to have poor interlaminar strength [227] and the alignment of the fibers has a significant influence on the composite's compression response [228,229]. Although the fibers oriented 0° can withstand higher compression loads [227], their higher aspect ratio assists the progress of micro-buckling leading to shear-induced fiber breakage at almost 45°, as was observed with the friction riveted joints. As the most critical ply in the stack begins to fail, the stress is redistributed to the remaining plies, which may themselves fail, thereby extending such damage — this is clearly seen in Figure 7.5. Thus, the failure of the laminate occurred progressively until no

further loading could be carried, the hole enlarged and the rivet detached from the lower composite part.

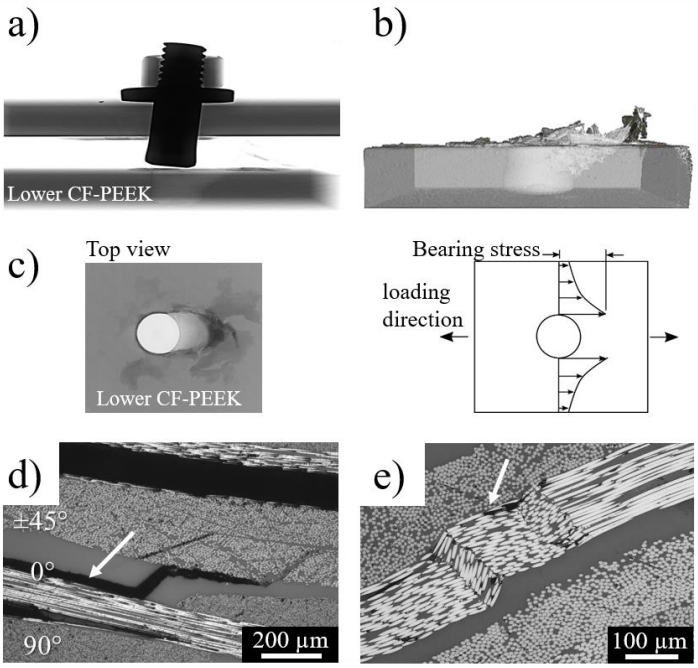

Figure 7.6 a) Selected X-ray micro-computed tomographs of the friction riveted joint after the lap-shear test; b) 3D reconstructed µCT, and c) top view of the lower composite part, highlighting the influence of the bearing stress on the plastically deformed edges of the composite hole; compression-induced failure of the composite by d) interlaminar damage, and e) kink band formation (indicated by arrows) in fiber bundles orientated 0°.

The results suggest that the overall failure of the overlap friction riveted joints under quasi-static shear loading starts with the rivet tip detachment (I, Figure 7.7-a), followed by radial crack initiation at the edges of the squeezed material. Such cracks propagate fast through an adhesive region and slow down in a cohesive failure region (II, Figure 7.7-a, and Figure 7.7-b). Furthermore, cohesive failure is transmitted through the composite thickness, owing to the compression imposed by the rivet (III, Figure 7.7-a). Figure 7.7-b illustrates the proposed failure path through the bonding zones of the overlap friction riveted joints.

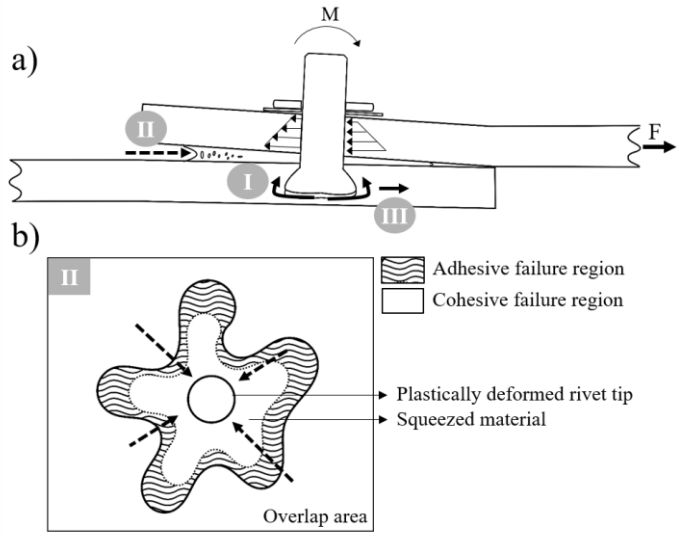

Figure 7.7 a) Schematic of the failure path in overlap friction riveted joints under shear loading; b) schematic of the fracture surface in the overlap area of friction riveted joints, indicating radial crack propagation from adhesion to cohesion failure regions.

As final failure of friction riveted joints is mainly governed by composite integrity, the damage in the lower CF-PEEK part was assessed by FEM, adopting the Hashin damage criteria, as shown in Figure 7.8. The criteria consider four fundamental failure modes that commonly take place in loaded composites, *i.e.* matrix compression failure (HSNMCCRT), matrix tensile failure (HSNMTCRT), fiber tension failure (HSNFTCRT), and fiber compression failure (HSNFCCRT) [188,226]. Blue areas represent intact material, while red is fully failed material. In agreement with the failure mechanisms described (Figure 7.7), the initial adhesive failure of the metal-composite and composite-composite interfaces (Figure 7.8-a) was governed by damage accumulation in the composite matrix, mainly by mode I fracture. The rivet detachment tensioned the composite matrix in its surrounding while underneath the rivet tip, the rivet plastic deformation encountered resistance to be pulled-out, imposing consequently compression failure to the composite matrix. At the final stages of joint failure, although the damage in the matrix was enlarged in front of the rivet, in the direction opposite to loading fiber fracture by tension and compression was identified. This led to cohesive intralaminar and interlaminar defects in the composite, including delamination, as observed in Figure 7.6. The failure processes and damage accumulation in the composite were assessed by Qing *et al.* [188] who developed a similar progressive damage model for bolted composite joints. The authors reported an accumulative bearing damage around the bolt, which was largely dependent on the layup of the composite, bolt tightening, and joint geometry. As the friction riveted joints had a similar behavior to bolted joints under lap shear testing, as discussed in Section 7.1.1, a similar

conclusion could be drawn. The joint design and its effect on strain and stress concentration sites under quasi-static mechanical testing were briefly discussed in Chapter 6.

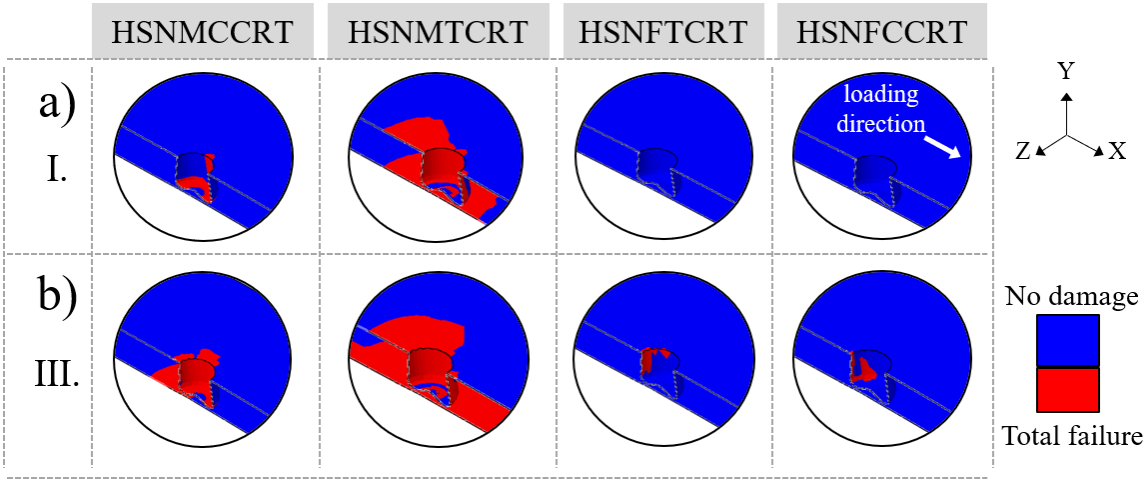

Figure 7.8 Damage accumulation in the lower composite part of the joint analyzed after a) rivet debonding and adhesive failure of the composite-composite interface (I, Figure 7.1), and b) at the final failure of the joint (III, Figure 7.1). [HSNMCCRT – matrix compression failure, HSNMTCRT – matrix tension failure, HSNFCCRT – fiber compression failure, HSNFTCRT – fiber tension failure]

One can assume that based on the fracture micromechanisms already described, out-of-plane stress triggers the crack propagation, chiefly by a tearing of the PEEK matrix in the initial stages of the quasi-static mechanical test, while the composite's shear-driven compressive failure throughout the composite thickness dictates the joint integrity, leading to a full rivet pull-out. There is no consensus on the critical fracture micromechanism, which governs the joint's mechanical behavior, and in turn provides a basis to determine the joint failure criteria for experimentally tested bolted joints of the composite [33]. According to the criteria described by Giannopoulos *et al.* [220], the maximum quasi-static loading that will be met in service by a bolted composite structure, when multiplied by a safety factor of 1.5, has to be less than or equal to the specimen's bearing strength. Furthermore, this load level is characterized by a quasi-linear and stable region in the typical load-displacement curve [164]. Considering the similarities between friction riveting and conventional bolted joints, regarding the load-displacement curve and failure mode, and thus assuming similar criteria, the allowable failure for the current joined composite material would be restricted to out-of-plane induced fracture micromechanisms at load levels up to 4.5 kN — this is shown by Figure 7.1-a.

7.2 Fatigue behavior

7.2.1 Fatigue life analysis

The S-N curves acquired from a two-parameter Weibull distribution for reliability levels (50 %, 90 % and 99 %) are shown in Figure 7.9. In the graph the arrow points to the run-out specimens and indicates the fatigue limit. The reliability curves provide the number of cycles that the joint can withstand without failure; they are a useful tool for safe structural design. Statistically, they also represent the life of the weakest member of the population, after a specified life in service [230]. For instance, in aircraft structural applications with very high safety requirements, one can assume a lower number of cycles is reasonably expected at a particular load level in a conservative design.

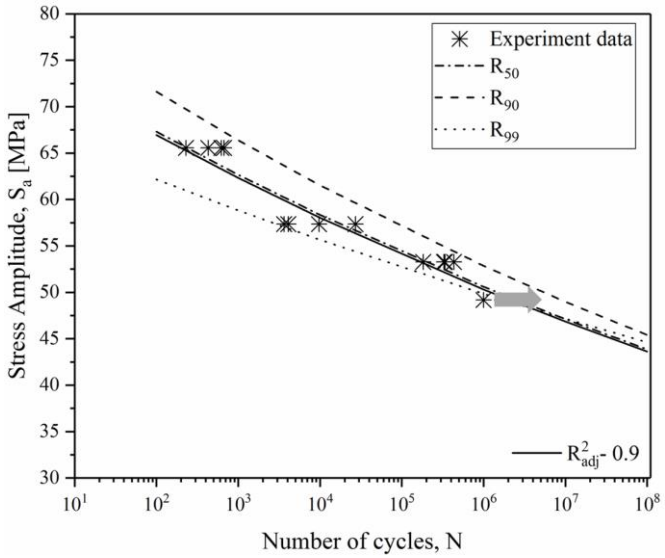

Figure 7.9. S-N curves acquired for reliabilities of 50 %, 90 %, and 99 % according to the two-parameter Weibull distribution.

A fatigue life at 10^5 cycles is commonly used in the aircraft sector to evaluate performance and to certify new designs and joining techniques [225]. For aircraft applications, bolted structures are loaded with 30 % to 35 % of their quasi-static strength and must withstand such fatigue life testing [225]. The friction riveted joints reached 10^5 cycles with a stress amplitude of 56 MPa, which corresponds to a load level of 66 % of their ultimate quasi-static lap shear force (ULSF). The result showed an improvement up to 88 % for the friction riveted joints compared with the cyclic behavior of conventional mechanical fastening techniques compliant with aircraft requirements. A similar improvement was reported by Mariam *et al.* [231] for dissimilar bolted/bonded hybrid joins of overlapping AA7075 and glass fiber reinforced epoxy parts. McCarthy, Lawlor, and Stanly. [232]

reported that the clearance in conventional bolted joints is of maximum concern when designing the limit load of aircraft. According to the authors, joints with a loose fitting hole have a shorter fatigue life than neat fitting holes, because elongation of the hole is initiated earlier when loose. The hole produced in friction riveted joints has intimate contact with the rivet, due to reconsolidation of molten material along the rivet shaft (Figure 6.10-a). This feature may provide a delay in damage initiation and accumulation in the friction riveted joints, leading to a better cyclic mechanical performance. Moreover, the squeezed material described in Section 6.4 (Figure 6.14) may also act as a failsafe mechanism and provide benefits to structural performance and durability after its failure. This finding is in agreement with the cyclic performance of bonded/bolted hybrid joints. Chowdhury *et al*. [168] and Kelly [169] have shown that hybrid joints have a higher fatigue life than bolted and bonded joints. In both studies, the presence of the fastener in a hybrid joint reduced the peel stress and arrested the crack propagation in the bond line, which increased to twice the number of cycles to final failure.

An endurance limit was considered when the joints survived one million cycles without failing, which was established at 60 % of ULSF (3.96 kN). One can assume that beyond this value, the joint would no longer be damaged by fatigue and thus the test was terminated. This hypothesis was verified from the quasi-static residual strength of the run-out specimens. The results are presented in Table 7.1. By comparing the residual strength after one million cycles (5.9 ± 0.3) kN with the quasi-static strength (6.6 ± 0.4) kN of the joints (ultimate lap shear force, ULSF), no statistically significant variation in the mechanical performance was identified. The result indicates that the loading level, which the surviving joints underwent after one million cycles, did not induce any critical fatigue damage in the joint, and did not compromise its mechanical integrity.

Table 7.1 Quasi-static residual strength of run-out friction riveted joints.

	Force [kN]
ULSF	6.2 ± 0.3
After 10^6 cycles	5.9 ± 0.3

7.2.2 Damage evolution and fracture analysis

The friction riveted joints similarly failed under cyclic testing to the way they did in the quasi-static test: failure of the squeezed material followed by bearing of the composite and rivet pull-out. The fatigue damage evolution and the fracture micromechanisms associated with the failure mode were assessed using the stiffness degradation approach [233]. Typical degradation curves for the joints loaded at different stress levels are shown in Figure 7.10. Despite the four-stage curve, the extent of each stage relative to different fracture micromechanisms is dependent on the applied load

(Figure 7.10-a). At a stress level of 80 % of the ULSF, critical damage was introduced in the joint at an earlier stage, shifting the stiffness degradation curve to lower fatigue cycles, while at lower stress levels the crack initiation and propagation were postponed to higher fatigue cycles. Moreover, the number of stages in such a stress level is reduced to three, this indicates that the load level was above the critical level that triggers the first fracture micromechanism (*i.e.* adhesive failure of squeezed material and metal-composite interface). Each stage is indicated for the joints loaded at the lower stress level of 66 % of the ULSF, as presented in Figure 7.10-b. At this level of load, all four stages of degradation are visible and are stable, and therefore this level was selected for further microstructural analysis.

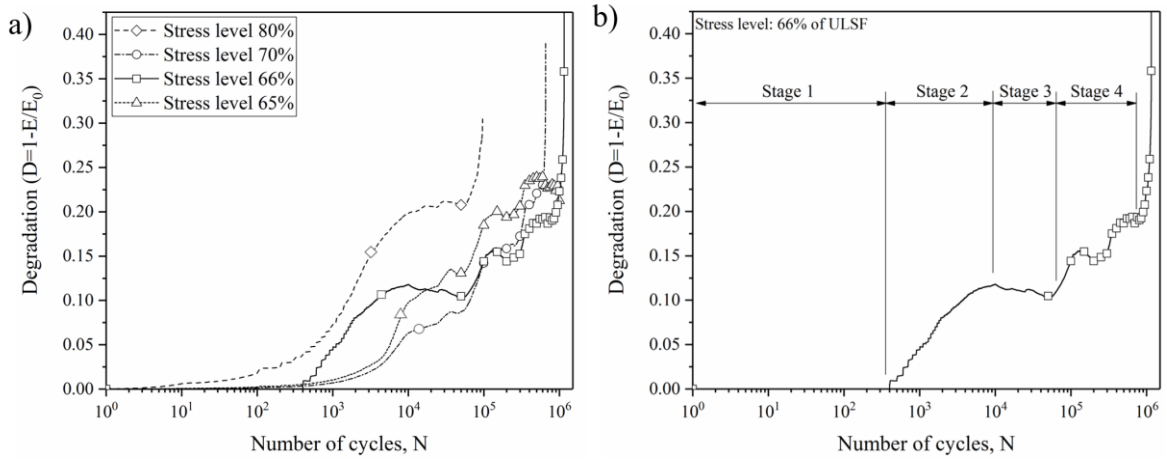

Figure 7.10 Stiffness degradation curves: a) for various stress levels, and b) for 66 % of the ULSF showing the stages of damage evolution.

The fracture analyses of friction riveted joints after each damage stage from Figure 7.10-b are presented in Figure 7.11. At the end of Stage 4 the joint failed completely, so its fracture evolution is thereafter ignored. In the first stage, up to 1.5×10^2 cycles (Figure 7.10-b), the consolidated squeezed material between the composite joining parts failed, followed by an adhesive failure of the rivet in the composite hole (Figure 7.11-a and -b). After damage initiation, the second stage shows an almost linear slope until a plateau is reached (Stage 2, Figure 7.10-b) at 10^4 cycles. At this point the cracks already developed underneath the rivet and in the squeezed material are believed to propagate towards the interface between the rivet and the composite on several fatigue crack fronts, as indicated by the solid arrows in Figure 7.11-d. The cracks are mainly oriented 45° to the loading direction and located between the reconsolidated composite material and the composite matrix. Such cracks no longer propagated after reaching the rivet shaft, which in turn arrested them and stabilized the joint stiffness until 10^5 cycles (Stage 3, Figure 7.10-b). Finally, owing to the momentum imposed on the rivet, compression-induced cracks were spread throughout the composite thickness, thereby embracing intralaminar defects in fiber bundles oriented 90° to the loading direction (Figure 7.11-e

and -f). This fiber bundle orientation carried less tension and compression, as it is significant only for transversal loads and structure stability [227].

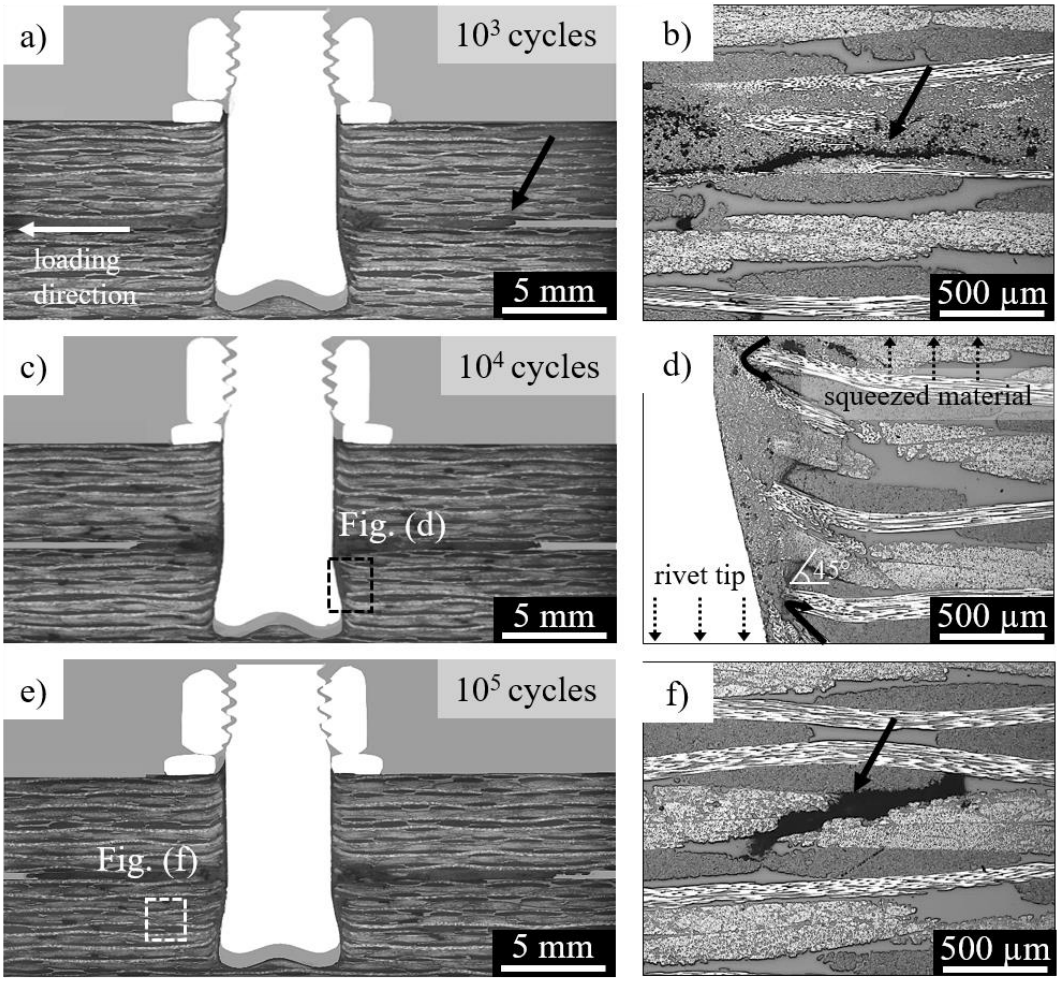

Figure 7.11 Overview of joint cross-sections after 10^3, 10^4, and 10^5 cycles (a-e) and details of the corresponding fatigue fracture mechanisms (b-f) highlighted by solid arrows; the dashed arrows in (d) illustrate the locations of squeezed material and rivet tip that are not depicted in the image. All the joints were loaded with 66 % of the ULSF.

The micromechanisms involved in the fatigue damage evolution and failure of friction riveted joints are addressed in Figure 7.12. Despite propagation of the fatigue cracks by a mixture of adhesive–cohesive failure in the squeezed material, and contrary to the joint mechanical behavior under quasi-static loading, mainly shear-induced deformation was identified in the cohesive failure region. Figure 7.12-b shows a periodic wave-like pattern of the matrix along the loading direction, which is well known in the literature as *hackles* [234]. On continued cyclic loading of ductile materials, shear-induced cracks are generally formed in the matrix between fibers. When they coalesce, they form microvoids along with highly plastically deformed waves, as in Figure 7.12-c. Simultaneously, cracks nucleated underneath the rivet tip, where the stress concentration is expected

to be higher [147], leading to adhesive failure at the interface of the rivet and composite hole (Figure 7.12-d). Although the fracture surface of the composite hole shows plastic deformation of the matrix, no out-of-plane tearing of fibrils was observed (Figure 7.12-e), indicating less influence of the out-of-plane stress.

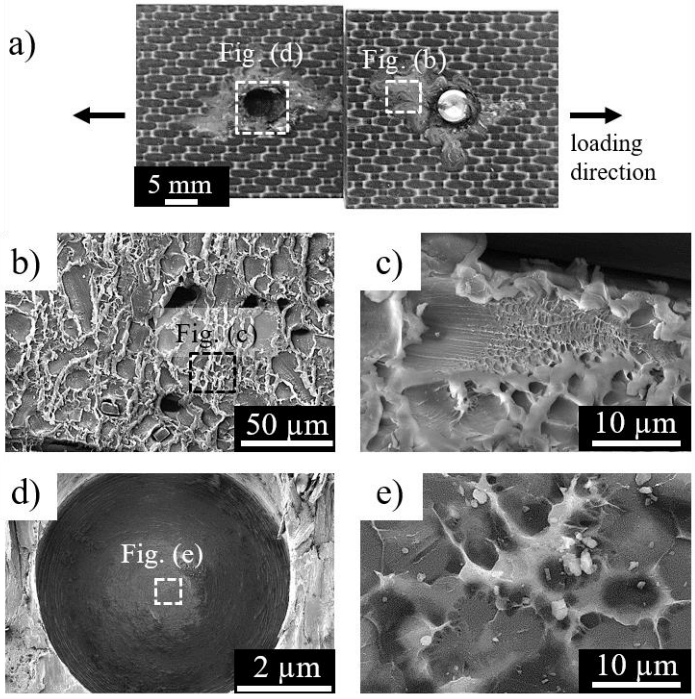

Figure 7.12 a) Overview of a high cycle fatigue fracture surface (456,824 cycles to failure); SEM micrographs of: b) squeezed material fracture surface with hackle formation; c) detail of hackles; d) the hole in the lower composite plate left after the joining process; and e) details of the plastically deformed matrix in the composite hole.

Kelly [169] published similar a failure mode and damage evolution for bolted/bonded hybrid joints. Due to their joints having a larger adhesion area between the joining parts from the adhesive applied, crack initiation was delayed until a higher fatigue life compared to the friction riveted joints.

Based on the results presented here, under cyclic loading the friction riveted joints failed by shear-induced defects while under quasi-static loading, a combination of in-plane and out-of-plane induced defects was observed. This work's description of the complex failure mode and fracture micromechanisms could be used as input to prediction models for crack initiation and propagation of composite aircraft components and therefore for defining a design that is fatigue damage tolerant for friction riveted aircraft structures. However, that task is beyond the scope of this PhD thesis.

7.3 Summary of the results

Although the friction riveted joints presented an inferior quasi-static mechanical performance (6.6 ± 0.4) kN) compared to reference lock bolted joints (8.7 ± 0.2) kN, under cyclic loading the joints withstood 10^5 cycles with 66 % of the ultimate lap shear force, showing an improvement up to 88 % when compared with the cyclic behavior of conventional mechanical fastening techniques for aircraft requirements. Moreover, the run-out specimens presented a residual strength comparable to the quasi-static behavior. The micromechanisms of failure under both loading conditions were similar and characterized by debonding of the rivet tip from the composite hole due to out-of-plane stresses, which mainly damage the composite matrix through tension. The peel stresses also promote crack initiation at the periphery of the consolidated squeezed material, which radially propagates along the interface between the composite parts by adhesive failure. The crack propagation is slowed down when the cracks reach the center of the squeezed material, where no interfaces between this layer and the composite parts can be distinguished, owing to the interdiffusion of polymer molecules. At this point cohesive failure governs the behavior of friction riveted joints. The in-plane stresses imposed by the rivet into the edges of the formed composite hole trigger shear-driven compressive failure throughout the composite thickness, which enlarges the composite hole and leads to a rivet pull-through failure of the joint. The process-induced flaws in the surroundings of the rivet also impair the joint's integrity and may enhance composite bearing over the joint loading.

Chapter 8. Damage Threat Assessment

8.1 Impact loading and energy history

Figure 8. 1 shows typical curves of contact force (impact force) and absorbed energy history as a function of time at four levels of impact energy. The incipient damage point (IDP), maximum load point (MLP), failure point (FP), and total point (TP) were detected and used to assess the impact response and resistance of the composite friction riveted specimens. The IDP is characterized by the incipient damage load (P_i) and energy (U_i) which indicate the ability of a structure to withstand the damage and deformation initiation [235]. The MLP contains the peak force (P_m) that a composite structure can tolerate before undergoing critical damage which leads to reduction of sample rigidity and failure during a particular impact event [48,236]. The energy at the maximum load (U_m) therefore can be interpreted as the required energy to induce elastic-plastic deformations through flexural deformation and interlaminar shear [235]. At the FP, characterized by maximum energy (U_f) and failure load (P_f), the sample loses its integrity through fiber breakage, matrix cracking, fiber-matrix pull-out, and delamination, bearing no more load. At the TP, the impact event ends, the load (P_t) decreases to zero, and the energy (U_t) has a constant value [235]. U_t is the total energy absorbed by the specimen and reflects the degree of induced and propagated damage [62]. The characteristic parameters were measured for three replicates and the average along with the standard deviation were reported in Table 8. 1. The additional values in Table 8. 1 are the normalized total absorbed energy (U_t/U), energy at maximum load (U_m/U), and elastic energy ($\Delta U/U$) retained in the indenter to rebound. The full results of the impact test are summarized in a table in Appendix I.

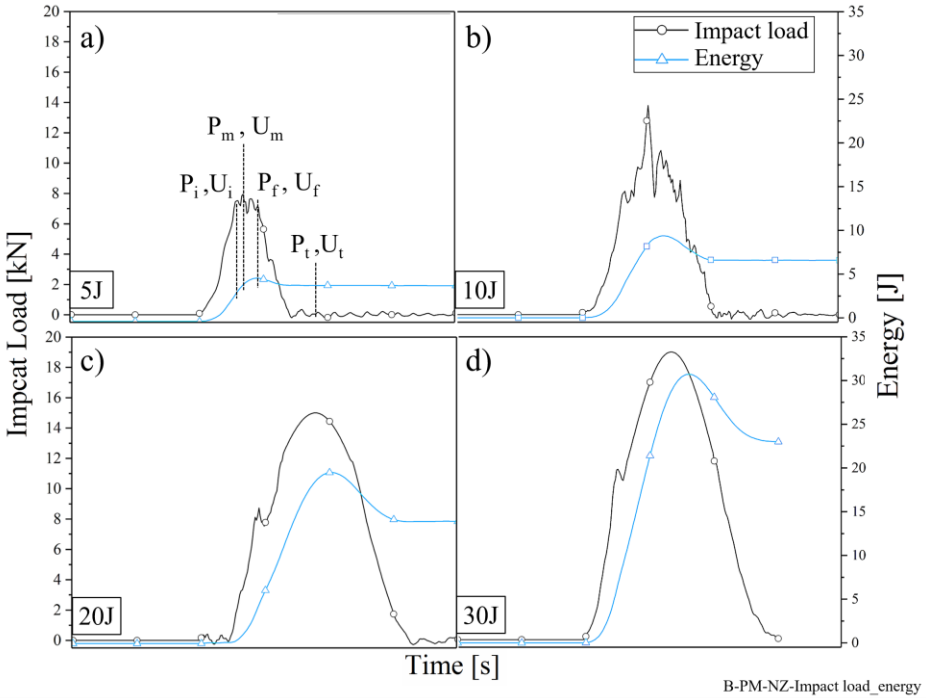

Figure 8. 1 Typical impact load and transmitted energy curves as a function of time for impact energies of a) 5 J, b) 10 J, c) 20 J, and d) 30 J.

All the characteristic parameters including the normalized energy at the maximum load (U_m/U) increased with increasing impact energy, while the normalized absorbed (U_t/U) and elastic energies ($\Delta U/U$) did not varied. According to Ghaseminejhad and Parvizi-Majidi [236], the increase of contact loads and absorbed energies over higher impact energies are expected for 4.3 mm thick and 54 % nominal fiber content CF-PEEK base material, once more potential energy of the indenter is converted into kinetic and transferred to the material through higher elastic-plastic deformation (U_m) and more internal damage (U_t). Despite the increases, typically for CF-PEEK, $\Delta U/U$ and U_m/U decrease with increasing impact energy, indicating that more energy is absorbed within the material – higher U_t/U – to initiate and propagate internal damages instead of elastic-plastic deformation [236]. For friction riveted joints however the increase of U_m/U and constant U_t/U may indicate a concealing of internal composite damage such as delamination and fiber breakage by elastic-plastic deformation of the joint materials as well as damage at the metal-composite interface, which were deeply investigated in Section 8.2.

Table 8. 1 Characteristic parameters of the dynamic response curves obtained from the drop weight impact test.

U [J]	P_i [kN]	U_i [J]	P_m[kN]	U_m [J]	P_f [kN]	U_f [J]	U_t [J]	U_t/U	U_m/U	$\Delta U/U$
5	5.4 ± 1.4	2.4 ± 0.6	7.3 ± 0.6	3.6 ± 0.2	5.8 ± 0.8	4.7 ± 0.05	4.3 ± 0.4	0.8 ± 0.008	0.7 ± 0.04	0.15 ± 0.04
10	7.5 ± 0.5	3.8 ± 0.4	14.2 ± 0.5	8.6 ± 0.2	9.5 ± 0.3	9.3 ± 0.06	7.1 ± 0.5	0.7 ± 0.05	0.8 ± 0.02	0.2 ± 0.05
20	8.8	4.7	14.4 ± 0.4	18.3 ± 0.1	14.2 ± 0.1	19.4 ± 0.0	14.6 ± 0.6	0.7 ± 0.03	0.9 ± 0.03	0.2 ± 0.03
30	11.4 ± 0.4	7.0 ± 0.5	18.7 ± 0.1	24.4 ± 4.0	16.4 ± 1.1	30.3 ± 0.01	24.0 ± 0.8	0.8 ± 0.02	0.9 ± 0.05	0.2 ± 0.02

At an impact energy of 5 J (Figure 8. 1-a) and 10 J (Figure 8. 1-b), the contact force signal presented oscillations, mainly in the descending part of the curves and P_i reached virtually similar values (approximately 7.5 kN), while at 20 J (Figure 8. 1-c) and 30 J (Figure 8. 1-d), featureless curves were observed along with higher P_i (9-11 kN). Such deviations in the behavior of the joints indicate differences in the damage mechanisms introduced by the impact load. As widely explored in the literature [48,55,56,62,71,237], discontinuities in impact force history address damage nucleation and propagation mainly by delamination and matrix cracking. In contrast, the featureless contact force signal may indicate no extensive failure of the composite by impact loading [238]. One can assume that the higher the impact energy, the larger the damaged area in the joint, especially in composites, which would result in more vibrations in the load curve. However, for hybrid friction riveted joints, similar to metal-composite laminates during an impact event [67], a featureless force-curve could indicate damage of the metal-composite interface, which in turn would lead to a different nature (elastic and/or plastic deformation) of damage, concealing the nucleation of flaws in the composite.

The relation between U and U_t determines the damage process imposed on the specimen from its contact with the indenter, which can be a rebound, penetration, or perforation [62]. On the one hand, when U_t is inferior to U the energy is partially released by elastic response, and therefore a rebound occurs. The relative elastic energy can be calculated as $\Delta U/U = (U - U_t)/U$. On the other hand, when the energies are equal the impact energy is completely released by damage to the material, inducing penetration of the indenter into the specimen. Perforation occurs when U_t no longer increases with U, meaning that the impact loading condition exceeds the load carrying capacity of the composite and the indenter passes through the thickness of the specimen. For all levels of impact

energy investigated in this work, only the rebounding behavior was identified, as shown by Table 8. 1.

The maximum load displays a nearly linear increase with low levels of impact energy (U_i < 10 J) before reaching an almost constant plateau between 10 J and 20 J at 14 kN, followed by an increase at the energy level of 30 J (Table 8. 1). The plateau indicates a range of impact energies where the joint resists damage initiation mainly in the composite. Such a behavior is in turn dependent of the ductility of the matrix resin and the ability of the composite to resist initiation and propagation of delamination induced by mode II shear loading [239]. For composites, after the plateau the stiffness of the material usually decreases, leading to less load carrying capacity [48]. Contrary to the literature [48] the friction riveted joints show an increase in load carrying capacity towards 30 J, suggesting an additional damage mechanism releasing the energy, which complies with the findings in Figure 8. 1. Therefore, above 14 kN maximum force the damage mechanism to dissipate the impact energy changes from intralaminar and interlaminar damage in the composite to defects in the metal-composite interface. This observation does not necessarily mean a higher impact damage resistance of the joint upon higher impact energy, which in turn would not affect the joint's residual strength. The mechanisms of initiation and propagation of the different damage types are explored in Section 8.2 and their influence on residual strength and fatigue life are analyzed in Section 8.3 and Section 8.4, respectively.

8.2 Impact damage

To assess the impact damage, a superficial area of damage and residual dent depth with increasing impact energy were investigated and the results are shown in Figure 8.2. It is worth to mention that the damage modes and dimensions are strongly influenced by the temperature of the impact event [55,61] and the clamping system used to fix the sample, which effects were not investigated in the current work.

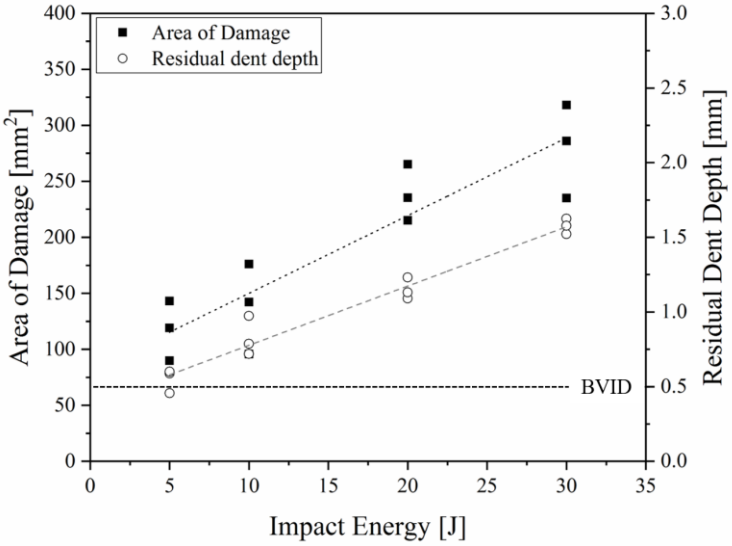

Figure 8.2 Area of damage and residual dent depth of friction riveted joints as a function of impact energy (5 J, 10 J, 20 J, and 30 J).

By increasing the impact energy, shallow and larger superficial damage was observed. Moreover, two types of damage were identified for the friction riveted joints based on the dent depth criteria applied for aircraft composite structures [240,241]: barely visible impact damage (BVID) and visible impact damage (VID). According to the literature [47,242], when the damage has over 0.5 mm of residual dent depth, it is considered VID, while below this level it is BVID. At 5J impact energy, a residual dent depth of 0.55 ± 0.06 mm was measured, and therefore considered the VID threshold for impacted friction riveted joints, below which BVID was defined. The 10 J impacted joints presented a residual dent depth of 0.8 ± 0.2 mm, which was virtually the same as for 5 J impacted joints, and consequently it was considered a transition energy level.

BVID and VID were inspected using SEM and CLSM along with the lateral view of friction riveted joints impacted with 5 J and 20 J, as shown in Figure 8.3. The 5 J and 20 J were the first impact energy levels tested to induce BVID and VID, respectively, and therefore were selected for further microstructural analysis. At 5 J BVID was introduced and few cracks were observed in the impacted surface of the joint (arrow in Figure 8.3-a). By contrast, in VID at 20 J the impacted surface exhibited a clear hemispherical indentation along with local crushing of the composite under the indenter and radial cracks (Figure 8.3-b). The increasing of impact energy also led to detachment of the composite parts as shown by the comparison between Figure 8.3-c and Figure 8.3–d. This observation suggests that as the incident impact energy increases, a higher portion of such energy was absorbed within the joint through plastic deformation of the upper composite plate, which complies with the increase of U_m as well as the U_m/U ratio, as discussed in Section 8.1. Such deformation may induce peeling stress at the overlapped area promoting partial separation of the composite parts. It can be assumed that peeling stresses induced by impact accelerate the first failure

mechanism of friction riveted joints under shear stress – *i.e.* rivet debonding from the lower composite part [243] – and hence decrease the load carrying capacity of the joints. The negative contribution of the out-of-plane stresses over an impact event on the detachment of interfaces and failure of joints through CFRP delamination was already described by Harris and Adams [244] and Machado *et al.* [245] for adhesively bonded joints. Despite the larger imprint in the impacted composite surface with higher impact energy, no global distortion of the impacted composite plate was observed, which can be considered a result of localized damage favored by the woven fabric [55,237].

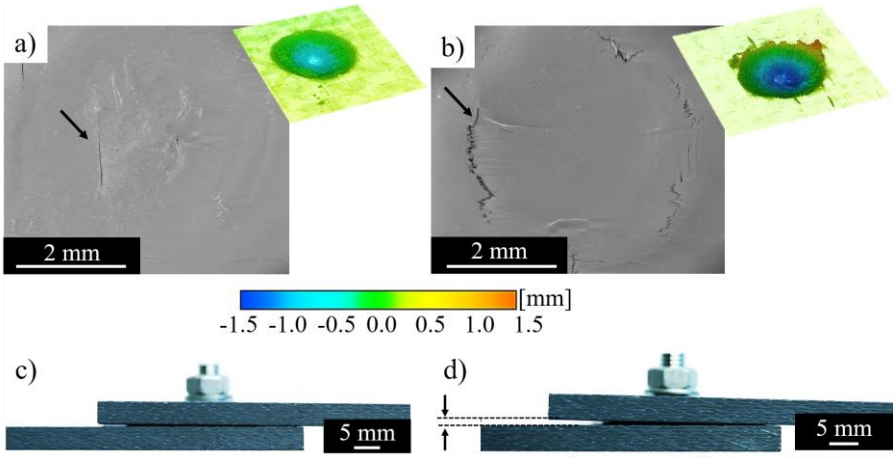

Figure 8.3 SEM images along with 3D reconstructed images by CLSM of the impacted area with a) 5 J, and b) 20 J; side view of friction riveted joints impacted with c) 5 J, and d) 20 J, showing separation of the overlapped composite parts.

Considering the energy absorbed to create a unit of elastic/plastic deformation area – *i.e.* U_m/A_i – a friction riveted joint required from 96 kJ.m^{-2} to 273 kJ.m^{-2}, in a range of 5 to 30 J of incident impact energy, while a 4.3 mm thick and 54 % nominal fiber content CF-PEEK requires between 39 kJ.m^{-2} to 62 kJ.m^{-2} in a similar incident impact energy range [236]. The result suggested that the presence of the metallic rivet in the impacted composite plate increases locally the stiffness of the composite, leading to an improvement up to four times of the required energy to further deform the composite.

The impacted composite joints also absorbs energy (see U_t in Table 1) internally to the composite leading to delamination, matrix cracks, and fiber breakage, which decrease the composite mechanical properties significantly [17]. Internal damage in the impacted friction riveted joints was assessed using the US C-Scan method. Figure 8.4 shows the normalized frequency of detected defects through the thickness of the lower composite part over different impact energies. The composite thickness consists of 14 plies (thickness per ply = 0.31 mm [159]), the orientation of which is shown in the right hand side of the graph. The position of the rivet tip in the lower composite is also depicted

in Figure 8.4 by a horizontal dashed line. For all impact energy levels, the damage was accumulated mainly in the 0° and 90° plies located near to the impacted surface (bottom surface, BS). However, by increasing the impact energy from to 10 J and 30 J, the intensity of superficial damage increased (see first bar in Figure 8.4). This can be explained by the radial propagation of cracks, as shown in Figure 8.3-b. Additionally, at such levels, the damage was extended towards the surroundings of the rivet tip and detected in the ± 45° plies at approximately 2.1 mm depth within the composite.

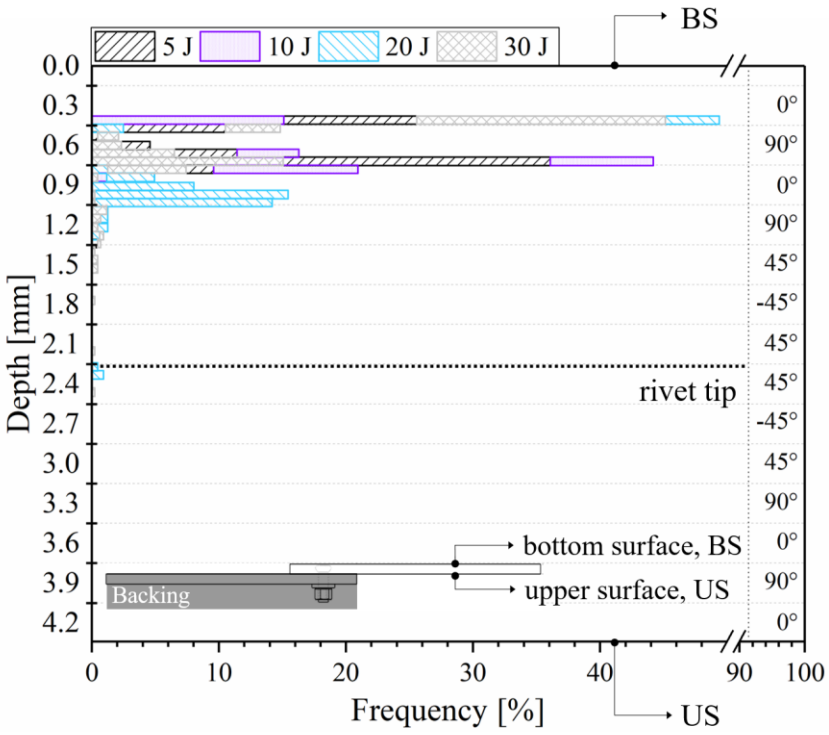

Figure 8.4 Frequency of damage through the composite thickness as a function of impact energy. The insert schematic illustrates the position of the C-scan measurement, where BS stands for bottom surface and US for upper surface.

The qualitative result of the damage location in the composite was compared to the damage mechanisms taking place under low (5 J) and high (20 J) impact energy from the cross-section fractography, as presented in Figure 8.5. At low impact energy, where a BVID was induced, cracks orientated at approximately 45° were detected in the first 0° ply and further propagated into the matrix (arrows in Figure 8.5-b). One may assume that the detected cracks resulted from pure transverse shearing stress owing to the contact between the indenter and composite. Bieniaś *et al*. [67] reported a similar behavior with CFRP and aluminum hybrid laminates.

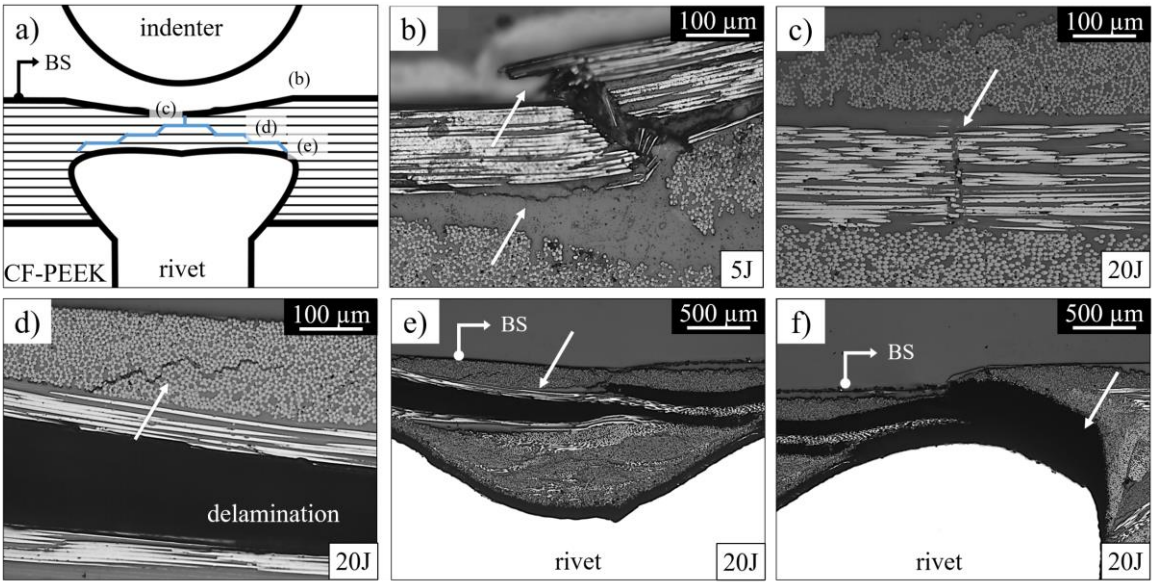

Figure 8.5 a) Schematic illustration of the impacted friction riveted joint, depicting the main damage mechanisms under impact loading, which are detailed and highlighted by arrows in images b) to f): b) fiber failure under shear; c) fiber failure under tension; d) matrix cracking; e) delamination; f) interaction of delamination with the metal-composite interface.

By examining the microstructure of 20 J impacted joints, it can be concluded that delamination is the prevailing damage mode in the VID. The failure of superficial plies were probably governed by peeling stresses, leading to vertical cracks in the 0° plies, as shown in Figure 8.5-c. In this case the normal stresses in the layer plane may have overcome the transverse tensile strength of the layer. Figure 8.5-d also shows shear-induced cracks in the 90° ply. In this case a highly deflected crack may indicate higher energy absorption reoriented the crack path, arresting and delaying the final failure of the composite [57]. Such cracks evolved into delamination mainly between 0° and 90° plies (Figure 8.5-e) and propagated towards the metal-composite interface. The stacking sequence of 0° ply followed by 90° ply is more susceptible to delamination propagation, because differences in their bending stiffness are higher [67,246]. Figure 8.5-f depicts the interaction between an elongated delamination and the metal-composite interface, leading to complete breakage of the composite, and consequently loss of joint integrity. Delamination significantly reduces the residual mechanical properties of composite joints, and therefore must be investigated in order to predict and define parameters for a damage tolerant design [57]. Although the prediction of the extent of impact and damage mechanisms was not a goal of this work, an attempt to predict these phenomena can be found in Appendix J.

8.3 Post-impact quasi-static mechanical performance

Figure 8.6-a shows residual strength under shear loading as a function of impact energy. Although compression is the critical load for composites [247], in-plane shear load is one of the most common scenario that stiffened composite panels of aircraft fuselage are submitted to during flight [17]. For this reason it is used to investigate the effects of accidental damage on the strength of such structures [248]. Therefore, shear-after-impact (SAI) testing was carried out in this work. The residual strength was calculated from the ratio between the strength of damaged friction riveted joints and ULSF. In the 5 J impacted joints damage was characterized as BVID and had only a reduction of 9 % in quasi-static strength, while impacted joints with VID decreased up to 40 %. The BVID result is way below the 19 % decrease in quasi-static strength of 2 mm CF-PEEK impacted with 3.9 J, as reported in [71], showing that the composite's impact tolerance was not compromised by the joining process. In addition, a decrease in displacement at break and a change to the mechanical behavior towards final failure of the joints were observed in the typical force-displacement curves shown in Figure 8.6-b. For the 5 J and 10 J impacted joints, the force-displacement curves display the characteristic two-peak behavior, typical for the undamaged friction riveted joints as described in Section 7.1. In such cases, the contribution of cohesive-adhesive failure of the squeezed material still provided an additional failure mechanism to arrest the energy before the crack propagation through the composite thickness is triggered by shear stresses. On the other hand, for the 20 J and 30 J impacted joints, characterized as VID, the peel stress imposed during impact (see Figure 8.3-d) already damaged the squeezed material under tension and this no longer contributed to the joint's mechanical strength. Therefore, the load carry capacity of such joints decreased drastically, leading to single-peak curves, as presented in Figure 8.6-b. Moreover, as the area of damage increased with impact energy, the stiffness of the joint decreased, promoting more secondary bending. An analysis of secondary bending was carried out using the DIC method and can be seen in Appendix K.

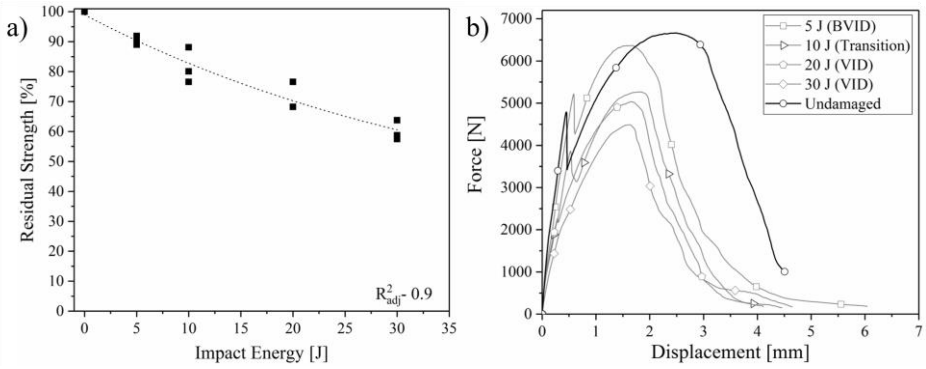

Figure 8.6 a) Residual strength as a function of impact energy; b) typical load-displacement curves of friction riveted joints impacted with 5 J, 10 J, 20 J, and 30 J, compared with undamaged specimens.

The propagation of BVID and VID during a lap shear test was assessed by comparing the normalized frequency of detected damage through the thickness of the lower composite part, before and after the lap shear test, of 5 J and 20 J impacted joints, as presented in Figure 8.7. The propagation of internal cracks introduced by 5 J impact energy essentially extended throughout the interface between the 0° and 90° plies (delamination), as well as on the composite surface and towards the surroundings of the rivet tip, where defects in the interface of ± 45° plies were also detected. In the case of 20 J, the impact damage spread across all the composite plies, especially under intralaminar failure, as observed mainly by the damage accumulation internally to ± 45° plies. It is important to emphasize that after lap shear (LS) testing, for both levels of impact energy, the impact damage interacted with the plastic deformation of the composite caused by shear loading, which makes assessment of impact damage propagation challenging. Similar to the friction riveted joints, VanderKlok, Dutta, and Tekalur [249] reported difficulty in describing the evolution of damage mechanisms on an impacted metal-composite bolted joint.

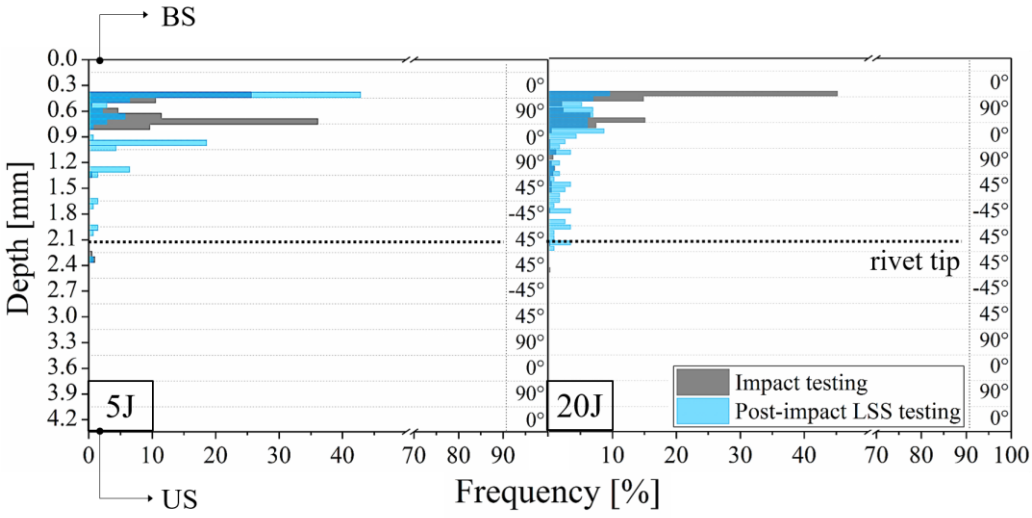

Figure 8.7 Frequency of damage through the composite thickness of friction riveted joints impacted with 5 J and 20 J. BS stands for bottom surface while US stands for upper surface. The location of rivet tip penetration in the lower composite part is shown in the histogram.

Figure 8.8 and Figure 8.9 show the indentation area along with the joint cross-section and fracture surface after LS testing for 5 J and 20 J impacted joints, respectively. An enlargement of the impacted area (Figure 8.8-a) with pronounced shear-induced cracks near the surface of the composite (Figure 8.8-b) was observed in the 5 J impacted joints, which agrees with Figure 8.7. A fully delaminated composite volume close to the composite hole is shown in Figure 8.8-d. Such defects generated an empty volume in the composite that when further compressed by the rivet may accommodate better out-of-plane displacement of fiber bundles, especially 0° plies. This would

explain the presence of a buckled 0° fiber bundle shown in Figure 8.8-e instead of a kink band formation (Figure 8.8-d).

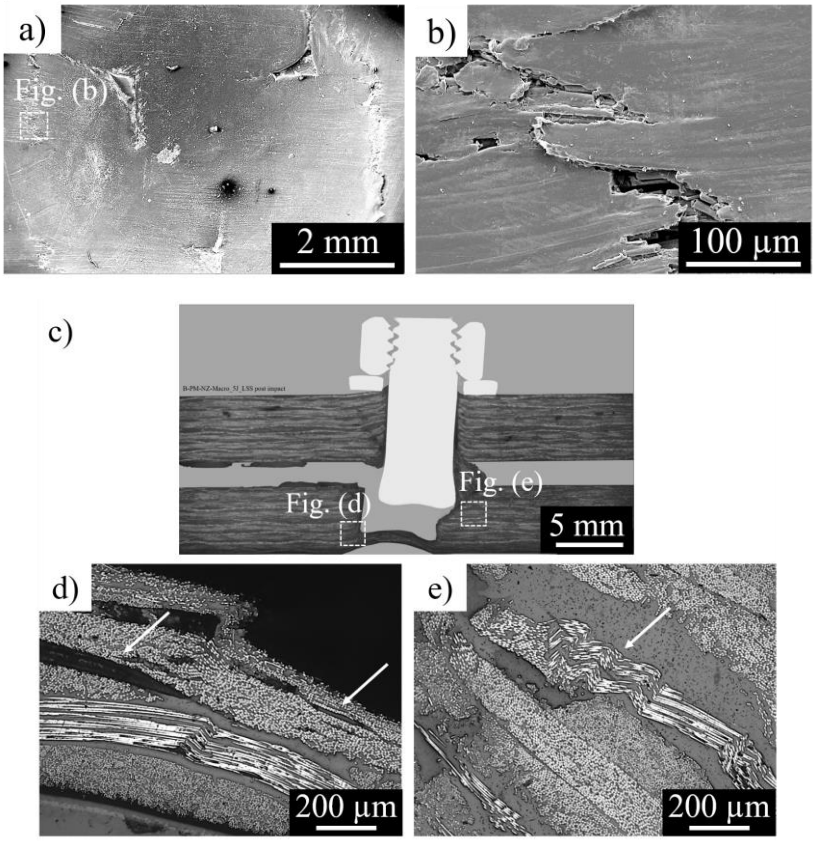

Figure 8.8 a) Overview of the 5 J impacted area after LS testing; b) superficial cracking; c) typical cross-section of 5 J impacted joint after LS testing; d) with delamination, and e) buckling of a 0° fiber bundle.

As well as enlargement of the impacted area (Figure 8.9-a), the impacted surface with 20 J revealed a tearing of the fibrils (Figure 8.9-b), which indicated the influence of secondary bending during LS testing on impact damage propagation. The fiber and matrix breakage introduced by the impact (see Figure 8.5) compromised the integrity of the composite that was under compression during LS testing and promoted extensive out-of-plane displacement of the broken fibers in a 0° ply, resulting in multiple sites with a kink band, as shown in Figure 8.9-d.

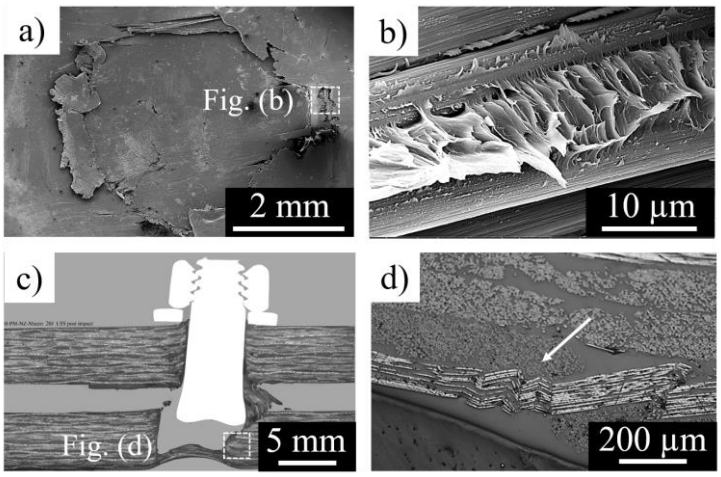

Figure 8.9 a) Overview of the 20 J impacted area after LS testing, b) highlighting tearing of superficial fibrils; c) typical cross-section of 20 J impacted joint after LS testing, d) highlighting displacement of broken fibers in a 0° fiber bundle.

8.4 Post-impact fatigue behavior

Figure 8.10-a shows the S-N curves of post-impacted friction riveted joints. The impact energies 5 J and 20 J were selected once they induced BVID and VID respectively. Post-impact fatigue testing defines the sensitivity of the structure to impact damage growth [247]. With increasing impact energy a significant decrease in fatigue resistance was observed in the friction riveted joints. This was to be expected, because the quasi-static strength of 20 J impacted joints was lower, as discussed in Section 8.3. Joints impacted with 20 J underwent higher peeling stresses, leading to the premature adhesive failure of the squeezed material, which no longer contributed to joint strength. Moreover, the slope of the S-N curve for the lower impact energy was steeper than for the higher impact energy, indicating that fatigue performance was more dependent on the stress amplitude. As reported in the literature [220], during fatigue testing peel stresses are generated at the edges of single lap joints. Therefore, it is believed that the 5 J impacted joints withstood higher peel forces, owing to the contribution of adhesion forces between the composite parts established by the undamaged squeezed material. Moreover, the stiffness degradation rate over the fatigue life indicates the initiation and propagation of different types of damage, and would help understanding the post-impact fatigue behavior of the joints [71]. For this reason, the loss of joint stiffness was monitored for 5 J and 20 J impacted friction riveted joints compared with undamaged specimens, as shown in Figure 8.10-b. The joints were loaded with 66 % of their respective ULSF, because at such a level the undamaged friction riveted joints had already withstood the 10^5 cycles that is used for certification purposes in the aircraft industry [225].

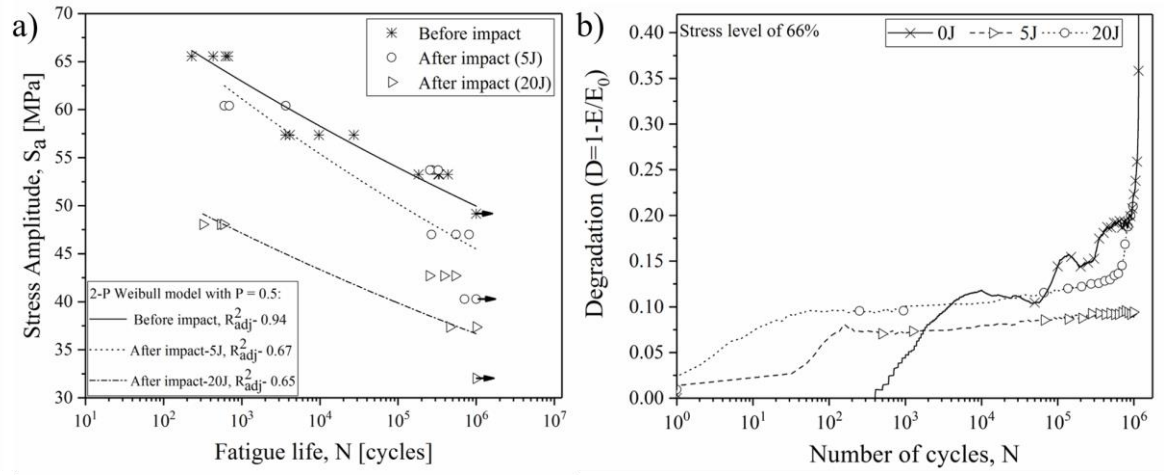

Figure 8.10 a) S-N curves and b) stiffness degradation of friction riveted joints impacted with 5 J and 20 J. The stiffness degradation was evaluated for specimens loaded with 66 % of their ULSF, to values as follows: $ULSF_{0J}$ (6.6 ± 0.4) kN, $ULSF_{5J}$ (6.0 ± 0.3) kN, $ULSF_{20J}$ (4.8 ± 0.3) kN.

As expected, the damage introduced in the composite by impact testing decreased the joint strength and impaired its fatigue resistance at low fatigue cycles. Moreover, the typical four-stage degradation curves of 0 J (undamaged) friction riveted joints became gradually increasing curves, almost a plateau with the impacted joints, leading to an unremarkable stiffness degradation towards final failure.

The joint stiffness degraded faster with 20 J impact energy in comparison to 5 J, which can be explained by the type of damage, its extent, and the effect of peel stresses induced by the impact testing. As discussed in the Section 8.2, the 20 J impacted joints presented shear-driven delamination, which extended to the metal-composite interface, along with failure of the squeezed material driven by peel stresses. According to Shahkhosravi *et al.* [250], delamination is a damage that propagates unstably and fast under fatigue testing. Therefore, it is believed that with low cycle fatigue the metal-composite interface failed entirely, compromising load transfer between the materials and hence inhibiting additional mechanisms that dissipate energy. The multiple forms of impact damage observed throughout the composite thickness in Figure 8.5 for 20 J may also work as stress concentration sites that trigger faster damage propagation during fatigue testing. On the other hand, for 5 J impacted joints in which no evidence of delamination and peeling defects were observed, it is expected that the squeezed material failed at low cycles, driven by shear stresses, followed by evolution of the matrix and fiber cracking into shear-driven delamination.

In addition, at high fatigue cycles, where a plateau-like curve was established for both impact energy scenarios, unvarying stiffness degradation might indicate the added contribution of the rivet to withstand fatigue cycles. As the squeezed material and composite were progressively and prematurely degraded at low fatigue cycles, the undamaged rivet would partially arrest the propagation of cracks in the composite and metal-composite interface. Therefore, one can assume

that the rivet plays a more important role in dissipating energy during cyclic testing in damaged joints compared to undamaged joints, where the triggering of other failure mechanisms in the composite may occur.

By inspection of the fracture analysis shown in Figure 8.11, it can be withdrawn that the final failure in BVID joints under cyclic loading was not driven by impact damage, despite it causing a reduction in their fatigue life (see Figure 8.10). As highlighted by an arrow in Figure 8.11-a, the composite underwent high plastic deformation, which enlarged the edges of the hole and assisted rivet removal from the composite part. This failure behavior is typical for undamaged friction riveted joints under quasi-static and cyclic loading, as described in Section 7.2.2. Additionally, hackles in the squeezed material confirms the plastic deformation of the squeezed material triggered by shear during fatigue testing (Figure 8.11-e) [234]. For the VID joints a more catastrophic failure of the joint was evidenced by the low plastic deformation bored by the edges of the composite hole (Figure 8.11-b) and intense cracking in the hole's surface (Figure 8.11-d), mainly around the rivet tip, where the stress concentrations are believed to be higher under shear loading [251]. Figure 8.11-f highlights the tearing of elongated fibrils in the squeezed material, confirming the influence of impact-induced peel stresses, which led to premature failure of the squeezed material prior to cyclic loading.

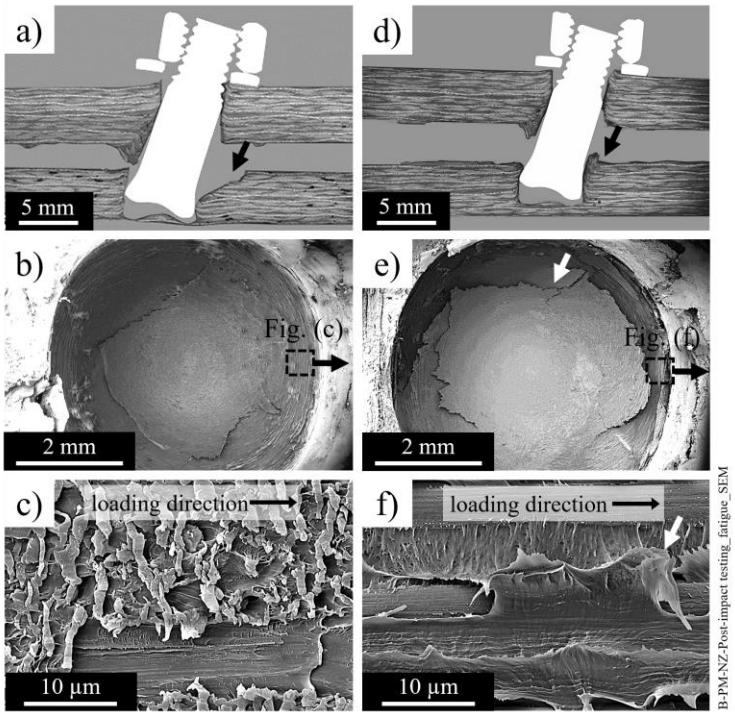

Figure 8.11 Typical cross-section of failed friction riveted joint, impacted with a) 5 J, and b) 20 J; overview of composite hole from c) 5 J, and d) 20 J impacted joints; microstructure of the squeezed material from e) 5 J, and f) 20 J impacted joints, highlighting shear-induced hackles and tearing of fibrils, respectively.

The impacted specimens that survived one million cycles were further tested under quasi-static loading to assess their residual strength. According to the recommendations proposed for the damage tolerance analysis of composite aircraft structures, by EASA [69], it is necessary to ensure that such a structure is not exposed for an excessive period, when it has a residual strength that is less than its design limit for loads. Figure 8.12 illustrates the comparison between initial quasi-static and residual strength of the impacted joints after one million cycles. For unimpacted joints, lower and higher impact energies their residual strength was lower compared to their initial strength by 9 %, 2 %, and 4 % respectively. Although the fracture analysis showed a possible extension of the impact damage upon the fatigue cycles, their narrow variations in strength and standard deviation suggest that the effects of cyclic loading on the initiation of additional damage and its propagation to the BVID and VID were not critical to the mechanical integrity of the joint.

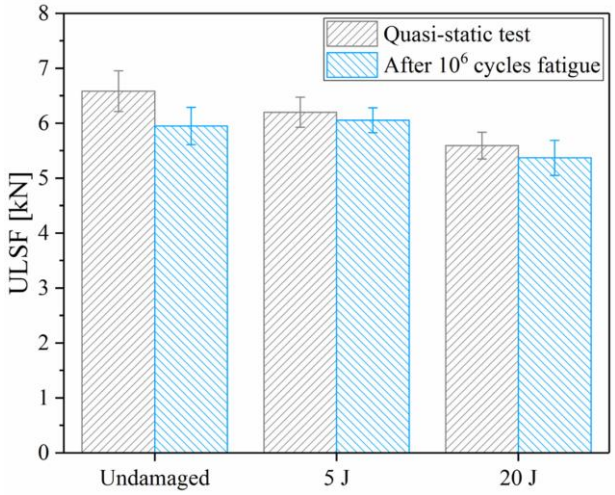

Figure 8.12 Residual strength compared with the joint strength after one million fatigue cycles of undamaged friction riveted joints and joints impacted with 5 J and 20 J.

8.5 Summary

Overall, the presence of the metallic rivet in the impacted composite plate may increase locally the stiffness of the composite, leading to an improvement up to four times of the required energy to further damage the composite by elastic/plastic deformation. The higher the impact energy, the larger was the impact damage in the composite, which was characterized in two categories – barely-visible and visible impact damage – according to their residual dent depth. The 5 J impact energy introduced barely-visible impact damage with residual dent depth up to 0.5 mm and no indication of stress-driven delamination. Consequently, quasi-static and fatigue mechanical behavior were not significantly compromised (residual strength of 91 % under quasi-static loading). For impact energies

above 5 J, visual impact damage combining delamination and failure of the metal-composite interface was identified. In addition, the higher impact energy induced peeling stresses between the composite parts, leading to premature failure under tension of the squeezed material. Consequently, the joint failure mode changed along with decrease of up to 40 % of the quasi-static joint strength. Although the fatigue resistance of the joints impacted with high energy decreased, the propagation of the impact damage under cyclic loading showed to be less dependent on the stress amplitude, once the joints were already severely damaged by the impact event. Under fatigue, similarly to the effect of low impact energy, friction riveted joints showed to be less sensible to the fatigue damage than to the impact damage, as confirmed by the high residual strength after 10^6 fatigue cycles (98% and 96% for 5 J and 20 J, respectively).

Chapter 9. Durability of Friction Riveted Joints

This chapter deals with durability of the friction riveted joints under harsh accelerated aging conditions and saline corrosive environment. The optimized set of joining parameters (RS: 15000 rpm, FF_I: 5 kN, FF_{II}: 10 kN, DF: 7.5 mm, CP: 0.2 MPa) were selected to join single lap specimens. Washers (outer diameter of 10 mm) and nuts (5M) of aeronautic semi-austenitic precipitation hardening type of stainless steel (X7CrNiAl17-7) were used to clamp-up the joints. Under a corrosive environment, the differences in electrochemical potential of stainless steel, Ti6Al4V, and CF-PEEK are critical, that can induce corrosion on the washer and nut. In this context, the external tightening elements were conceived to work as sacrificial metal, preventing the metal rivet from corroding, galvanizing and rusting [85]. The local microstructural, physicochemical and mechanical behavior changes of the joint parts were assessed by SEM, DSC and nanohardness, while the global mechanical performance of the joints was evaluated by lap shear testing. In general, the potential effects of aggressive environments must be considered to support further component design.

9.1 Hydrothermal aging effect

9.1.1 Surface features, microstructure and chemical composition

All the joints were visually inspected as soon as they were taken out of the aging chamber (hydrothermal aging testing, Section 5.2.10.1). Figure 9.1 shows the top surface of the friction riveted joints that were not exposed and those exposed to 3, 14, and 28 days. As it was expected, no visual changes in the composite or the sacrificial materials were observed, even after 28 days of aging. PEEK has high stability under hostile environments, including high humidity and temperatures [79,129,185] and precipitation hardening stainless steel is corrosion resistant [252].

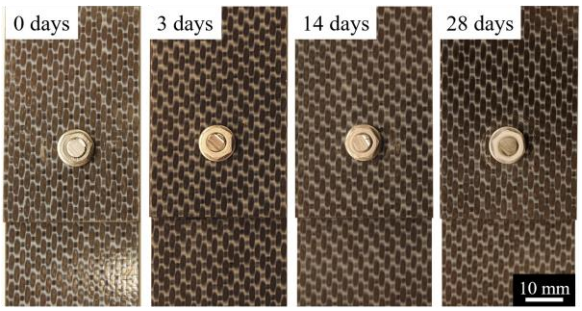

Figure 9.1 Top view of friction riveted joints after 3, 14, and 28 days of hydrothermal aging.

To further analyze the composite and metal surfaces, SEM and semi-quantitative analyses by EDS were performed using joints exposed to 28 days, maximum aging time when no visual damage was observed. The surface morphology of the metal nut (Figure 9.2-a) contains micro-sized crystallites, possibly of oxide nature (Figure 9.2-b). The EDS spectra reveal high amounts of O, Fe, Al, and Cr in the areas highlighted in Figure 9.2-b, which agrees with the presence of an oxide passive layer formed at the stainless steel surface, protecting the bulk material from corrosion [252]. According to the literature [253–255], Fe_3O_4 (magnetite), transient alumina to stable Al_2O_3, and Cr_2O_3 (eskolaite) can be formed at low temperatures, the last two oxides being thermodynamically more stable. In the presence of water vapor, oxidation kinetics may accelerate leading to a thin oxide dominated by alumina in addition to a significant amount of iron and chromium [254].

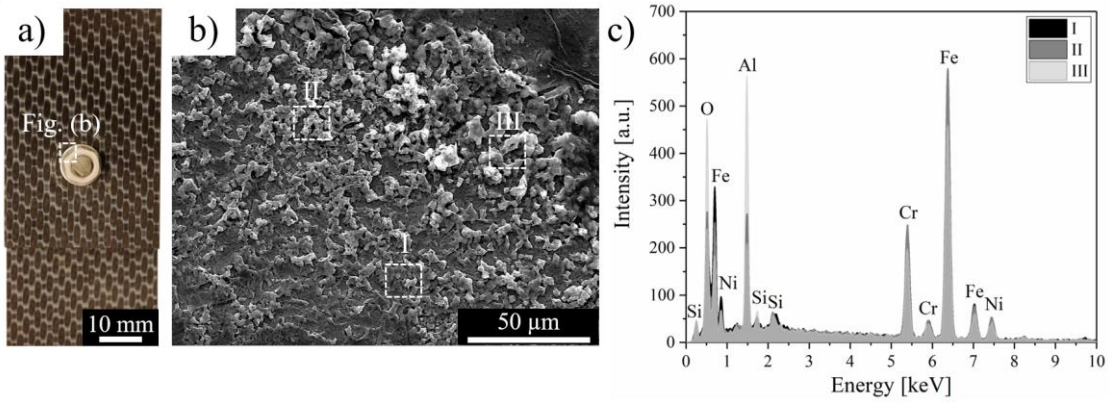

Figure 9.2 a) Top view of friction riveted joint after 28 days of aging, depicting an area of the metal nut. b) High-magnification SEM image of the stainless steel nut showing a nodular structure. c) EDS spectra of regions I-III in (b).

No corrosion by pitting and crevices typical for stainless steel was observed in the mid-section of the aged nut (Figure 9.3-b) and washer (Figure 9.3-c), showing that the aging condition was not aggressive enough to destroy the passive film and inhibited repassivation of the metal surface.

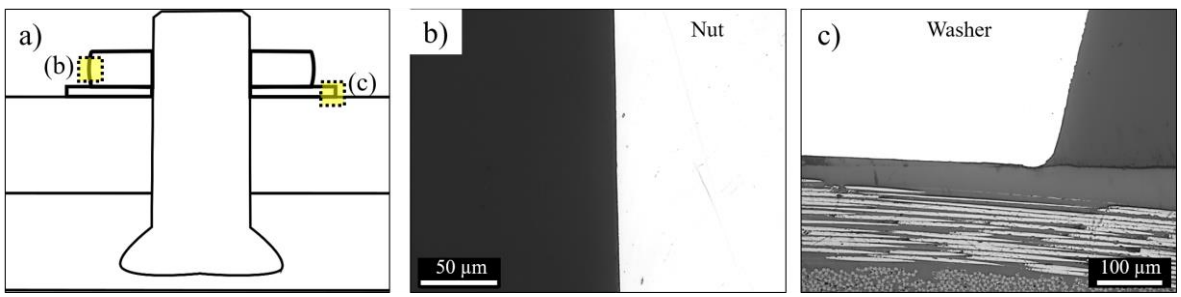

Figure 9.3 a) Schematic illustration of the mid-section of stainless steel after 28 days of aging of: b) nut, and c) washer.

Although highly resistant to high temperatures and moisture, the surface of the CF-PEEK (Figure 9.4-a) showed irregular pores in the vicinity of carbon fibers, which in turn were partially exposed after 28 days of aging. Moreover, by EDS (Figure 9.4-c) a high concentration of Al and O was observed in such a region (Region I, Figure 9.4-b) compared to the chemical composition of the PEEK matrix (Region II, Figure 9.4-b), which indicates the formation and accumulation of aluminum oxide on the composite surface. The aging at 71 °C may condense water leading to an aqueous medium that can act as an electrolyte between the stainless steel of the washer and nut and fibers exposed by accidental defects in the composite surface. Carbon fiber has a low electrochemical potential for oxidation, acting as cathode, while the stainless steel galvanically corrodes preferentially [182,256]. This would extend repassivation of the metal surface and therefore enlarge the oxide layer on the joint surface. Some resins also degrade when exposed to hydroxyl ions that are generated by the galvanic corrosion of a metal [187], which in turn exposes more surface area of carbon fiber and therefore accelerates corrosion. In particular, water molecules diffuse faster into the fiber-matrix interface in such a scenario, which can degrade by a hydrolysis reaction the unsaturated groups within the PEEK chemical structure [121,187]. Defects such as debonding and cracking may result from hydrolysis of the interface and can trigger superficial cavitation of the carbon fiber by corrosion, as reported by Gebhard *et al.* [257].

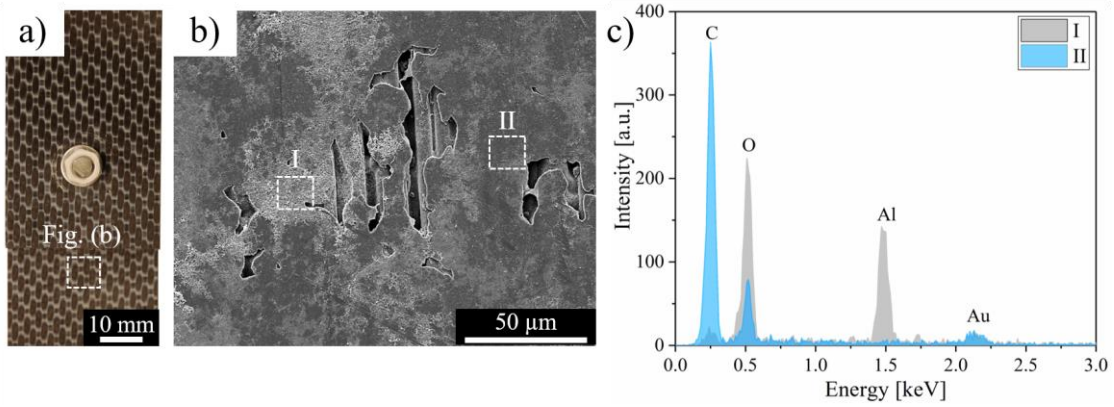

Figure 9.4 a) Top view of friction riveted joint after 28 days of aging, depicting an area of the composite surface; b) high magnification SEM image of the CF-PEEK, highlighting irregular porosities in the vicinity of superficial carbon fiber bundles; c) EDS spectra of regions I and II in (b).

9.1.2 Local physicochemical changes in CF-PEEK and mechanical performance

Temperature and moisture have been shown to have an important effect on the crystallinity and transition temperatures of semi-crystalline thermoplastics, which in turn locally and globally affect the mechanical performance of the composite [21,182,185]. This is particularly important in

the case of a friction riveted joint, because its final failure under quasi-static and cyclic loadings is mainly triggered by damage accumulation in the composite, as shown in Section 7.1.2. Therefore, DSC coupled with nanohardness testing were performed, to investigate the physicochemical change of the composite matrix after 28 days of aging and its influence on the composite's local mechanical properties. For the DSC analysis the material was extracted following the procedure described in Section 5.2.7, and for nanohardness the procedure for measurements described in Section 5.2.8.2 was adopted. It is believed that the material that consolidated in the composite against the rivet shaft (CTMAZ) was exposed to a similar thermal cycle as the flash material, due to the composite's low thermoconductivity (see Table 5.2). Therefore, the nanohardness of the CTMAZ material was further correlated with the DSC results for the flash material. The DSC results are summarized in Table 9.1. The initial heating curves of the unaged and aged samples are compiled in Appendix L.

Table 9.1 Main parameters obtained from DSC analysis (T_{cc} – cold crystallization temperature, T_m – melting temperature, T_c – crystallization temperature, X_c – degree of crystallization) for unaged and hydrothermally aged BM and TMAM materials.

		T_{cc} [°C]	T_m [°C]	T_c [°C]	X_c [%]
Before aging	**BM**	153.0 ± 1.0	345.0 ± 1.0	292.0 ± 5.0	29.0 ± 2.0
	TMAM	-	340.0 ± 0.2	296.0 ± 1.0	24.0 ± 2.0
After aging (28 days)	**BM**	152.0 ± 0.0	343.0 ± 0.6	282 ± 0.3	31.0 ± 3.0
	TMAM	160.0	343.0	281.0	34.0

The aging process had little effect on the transition temperatures of CF-PEEK compared to its effect on the degree of crystallinity, which exhibited an increase of 7 % derived from $X_{c,\ aged\ BM}$ = (31.0 ± 3.0) % and 42 % from $X_{c,\ aged\ TMAM}$ = 34 % when compared to unaged BM derived from $X_{c,\ unaged\ BM}$ = (29.0 ± 2.0) % and the TMAM from $X_{c,\ unaged\ TMAM}$ = (24.0 ± 2.0) %, respectively. Long term exposure of the joint to below T_g (71 °C) and humidity seems to induce additional mobility into the amorphous phase of PEEK, leading to macromolecular ordering and nucleation of crystals. Although PEEK has high thermal and chemical stability [21,258], Cornélis, Kander, and Martin [135] showed that the material can be swollen by solvents including acetone, which caused its plasticization and a solvent-induced crystallization (SIC) process. Even an amorphous phase can undergo a degree of reordering during annealing with a reduction of the free volume content, hence increasing the local mechanical properties of the polymer [259]. Despite the fact that water acts as a plasticizer when diffused within the polymer chains [260], it is believed that the aging temperature plays a more important role in increasing the mobility of the amorphous phase, because PEEK has a low water saturation level [185]. Moreover, post-crystallization of the exposed polymer can be maximized by the presence of fibers. Vieille, Albouy, and Taleb [261] reported the strong nucleating effect of the

fibers over a long aging period at temperatures below T_g for CF-PEEK, resulting in an increase of 3 % in the degree of crystallinity by a transcrystallinity mechanism. As reported by Gao *et al.* [128], the polar carbonyl groups of the PEEK matrix, when exposed to such environmental conditions, tend to lose conformations near the fiber surface, approximating to each other and being absorbed by functional groups of the fiber surface. This enhances fiber-matrix compatibilization by epitaxial nucleation of crystals on the fiber surface. Thus, the adhesion of PEEK to the fiber surfaces increases and this in turn leads to better local mechanical properties of the composite [134,262].

The increase in crystallinity was more pronounced in the TMAM than in the BM. One may assume that the broken fibers in the TMAM created more nucleation sites for transcrystallinity as well as presented a larger surface area that was exposed to the temperature and humidity, which in turn could accelerate crystallization kinetics [126,263].

Figure 9.5 summarizes the dynamic indentation modulus and nanohardness of BM and material in the CTMAZ before and after 28 days of aging (the detailed results of this are shown in Appendix E). The BM showed it was less sensitive to hydrothermal aging, as no significant changes in the modulus or hardness were observed. However, comparing the unaged and aged specimens of material from the CTMAZ the hardness increased by 20 % to (0.200 ± 0.009) GPa, while the dynamic modulus increased by 10 % to (3.9 ± 0.2) GPa. The surface mechanical properties of semicrystalline polymers are a function of the degree of crystallinity. The higher the crystalline content the more ordered are the molecular chains, restricting the mobility of the amorphous phase, resulting in stronger mechanical properties of the polymeric surface [216].

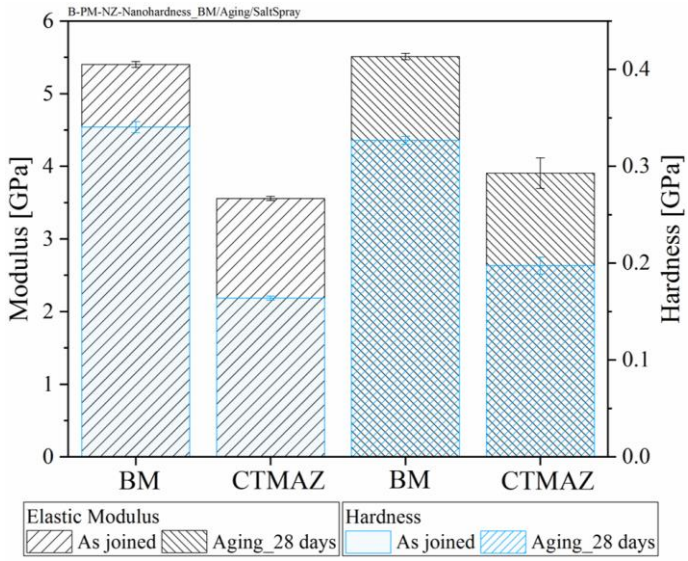

Figure 9.5 Average and standard deviation of indentation modulus and hardness of PEEK as joined and after 28 days of hydrothermal aging, obtained by CSM technique.

Contrary to the expected negative effects of corrosion-driven damage on the CF-PEEK surface after aging (Figure 9.4), the extent of galvanic corrosion seems to be restricted to the composite surface, not affecting the mechanical properties of the bulk composite material. Therefore, the local mechanical integrity of aged CF-PEEK seems more influenced by increasing transcrystallinity than the galvanic coupling effect.

A hardness map of the Ti6Al4V rivet after four weeks of aging is presented in Appendix M. The effects of hydrothermal aging on the microstructure and hence on local mechanical properties of the Ti6Al4V rivet were neglected, once no changes were detected from the typical microhardness profile of the rivet's mid-plane. Although Ti6Al4V is renowned for its outstanding resistance to corrosive media, due to formation of a stable passive oxide surface layer [84,264], environmentally assisted crack growth in titanium alloy was reported by Bache and Evans [265]. According to the authors, a fully lamellar microstructure was prone to hydrogen embrittlement of the elongated and aligned α-β interface owing to the β stabilizing effect of hydrogen, which was seen to accelerate crack growth under fatigue testing. However, mill annealed and bimodal microstructural variants of Ti6Al4V were shown largely insensitive to such effects [265]. In the case of the friction riveted joints, although the rivet tip presented lamellar structures induced by the joining process (see Figure 6.9), the entire rivet shaft in the joining area was protected by reconsolidated polymer (see Figure 6.10), which inhibited direct contact between the metal and the corrosive media, and therefore the local mechanical properties were not compromised.

9.1.3 Global mechanical performance and fracture analysis

The friction riveted joints were weighed shortly after removal of the joints from the aging chamber (within an hour) and then mechanically tested under lap shear testing. The mass change, displacement at break, and residual strength, as a function of days of exposure were compared with unaged samples, as illustrated in Figure 9.6. Up to 14 days of aging, the joint strength stayed virtually constant, but after 28 days an increase of approximately 23 % was observed. The mass change and the displacement at break both increased gradually over exposure time, reaching (2.8 ± 0.3) % and (4.1 ± 0.2) mm, respectively, after 28 days of exposure.

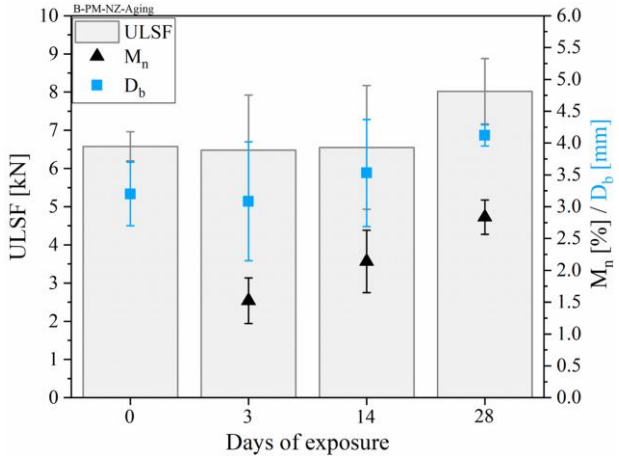

Figure 9.6 Mechanical strength along with displacement at break (D_b) and mass change (M_n) of the friction riveted joints as a function of days of aging exposure.

The water uptake in the CFRP composite can either be effected by capillary flow through volumetric defects or by diffusion, which relies on molecular arrangements, and therefore depends on the polymer's degree of crystallinity [260]. Polymer crystals are usually ordered toward secondary hydrogen bonds which when in the presence of water are partially replaced by water ions [260]. Higher crystallinity provides more potential sites for electrostatic absorption of water molecules [21]. For these reasons, after 28 days of aging the reported increase in crystallinity for the friction riveted joints (Table 9.1) may explain the reason for their increase in M_n. The process-induced defects at the metal-composite interface in the joints (Figure 6.10) may also have accelerated water uptake by capillary flow.

As is well known for polymers, water molecules in the composite work as a plasticizer, softening the composite matrix, which may explain the enhancement of D_b in the aged friction riveted joints [260]. An increase in joint ductility was also evidenced by an increase of the bearing area, as shown in Figure 9.7. After 28 days of exposure, the localized plastic deformation at the edges of the composite hole had increased by 47 %.

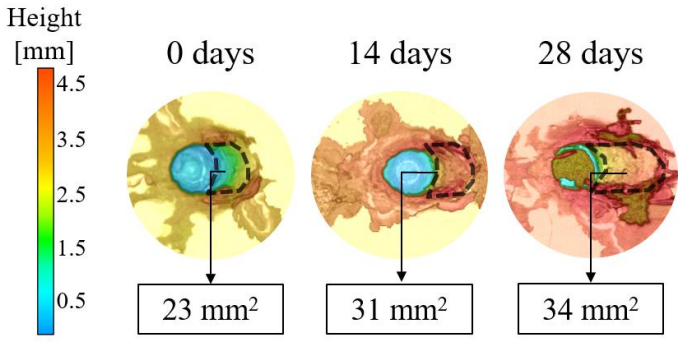

Figure 9.7 Bearing area of failed friction riveted joints loaded under shear as a function of days of hydrothermal aging exposure.

On the other hand, the water swelling caused by aging exposure can impair the composite, and consequently the joint strength, because it compromises the integrity of the fiber-matrix interface and therefore the material's load carry ability [80]. By contrast, as shown in Figure 9.6, the aged joints presented a higher strength after 28 days of exposure. As explained earlier, the hydrothermal aging enhanced the mechanical properties of the fiber-matrix interface by transcrystallinity. The nucleation of crystals on the fiber surface effectively decreases the discontinuity in moduli between the fiber and the matrix, leading to better stress transfer across the fiber-matrix interface [124]. Similar to the surface sizing of carbon fibers, transcrystallinity optimizes fiber-matrix compatibility and improves the mechanical performance of the composite [21]. As well as the crystallinity effect, thermal aging can release residual stress remained from the joining process, and may also have a positive effect on the mechanical properties, as reported by Yang *et al.* [76].

Figure 9.8-a shows a typical cross-section of a failed friction riveted joint after 28 days of hydrothermal aging. Instead of the kink band formation that is typically seem in a lap shear tested friction riveted joint, as described in Section 7.1.2 (Figure 7.6), buckling (Figure 9.8-b) and fiber debonding were identified (Figure 9.8-c) preferentially within a fiber bundle oriented 0°. Due to an increase in PEEK ductility by water uptake, it is expected that the matrix accommodate better the out-of-plane displacement of fiber bundles when under the compression imposed by the rivet in lap shear testing. Particularly for a fiber bundle oriented 0°, its high aspect ratio allowed for higher deflection when loaded under compression. As fiber deflection is accommodated within the ductile matrix, the onset of fiber breakage by transmitted shear is apparently delayed. The ductile matrix has however lower global effect on the secondary bending of the aged joints under lap shear test. Although the displacement at break increased, the out-of-plane displacement of the neutral line presented similar behavior as unaged joints, and therefore similar peel stresses are expected. The realignment of the overlap area to the neural line of aged and unaged was analyzed through digital image correlation (DIC) and the results were presented in Appendix N.

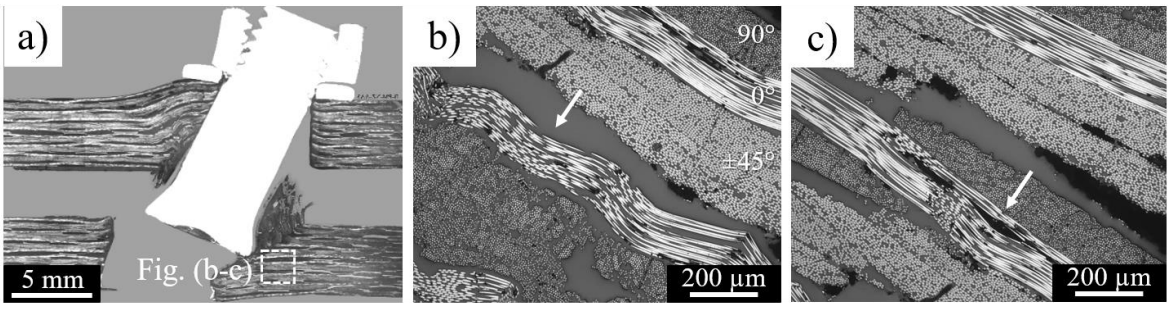

Figure 9.8 a) Typical cross-section of a friction riveted joint after 28 days of hydrothermal aging, showing high plastic deformation of the composite in rivet proximity; b) microbuckling, and c) intralaminar fiber debonding of the fiber bundles oriented 0° in the joint bearing area.

Moreover, as any transcrystalline interphase induced by hydrothermal aging is expected to enhance adhesion at the fiber-matrix interface, one may assume that load transferability between these phases increased. That would shift the fiber-matrix interface damage to within the fiber bundle during joint loading, which would explain the fiber debonding in Figure 9.8-c. Authors [22,266] proposed that moisture uptake in CFRP causes compressive strengthening by an optimized load transfer between fiber and matrix, which in turn increases shear resistance of such an interface.

Figure 9.9 shows the fracture surface of a joint after 28 days of hydrothermal aging. As explained in Section 9.1.1, the exposed surface of the composite exhibited cavitation probably induced by the galvanic coupling and hydrolysis of the PEEK. Similar defect was identified in the composite surfaces, inside the overlap area (Figure 9.9b) and close to the consolidated squeezed material (Figure 9.9-c). Despite the fact that such pit indicates lack of joint sealing, they did not affect the mechanical performance of the joints as shown in Figure 9.6. Thus, the corrosion can be neglected as detrimental effect on aged friction riveted joints. Additionally, the plastic deformed zone showed to fail mainly in a ductile manner (Figure 9.9-d), similar to the unaged joints (see Figure 7.4).

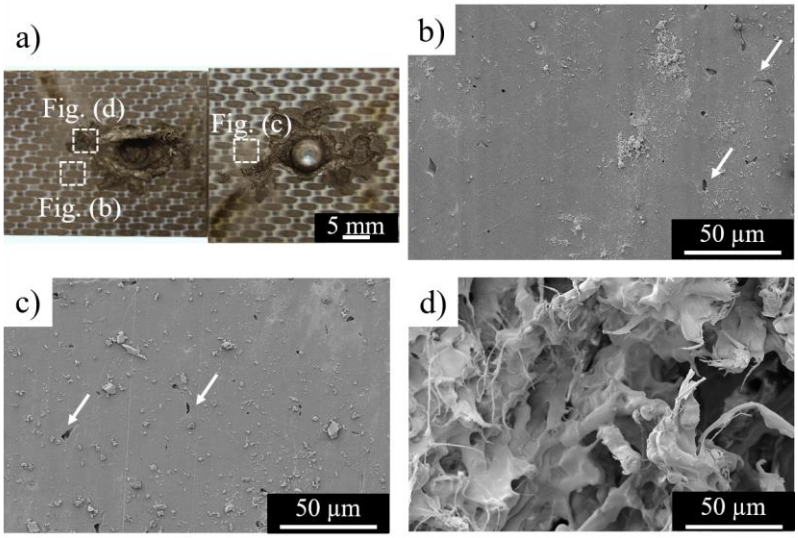

Figure 9.9 a) Typical fracture surface of the friction riveted joints after 28 days of hydrothermal aging; SEM images of the composite surfaces showing corrosion-induced cavitation from b) the lower, and c) the upper composite parts inside the overlap area; d) detailed view of the ductile failure of the squeezed material.

From a microstructural analysis of the joint fracture surface, an indication of transcrystallinity could be observed by the exposed fibers in the squeezed material, compared to the unaged sample. Figure 9.10-a shows an unfeatured fiber surface of an unaged friction riveted joint and Figure 9.10-b shows highly oriented fibrils emerging from the fiber surface of a joint hydrothermally aged for 28 days. The radial growth of crystals on the fiber and the formation of elongated fibrils familiar in several polymer composites [124,134,171,267,268] as characteristic transcrystalline morphology.

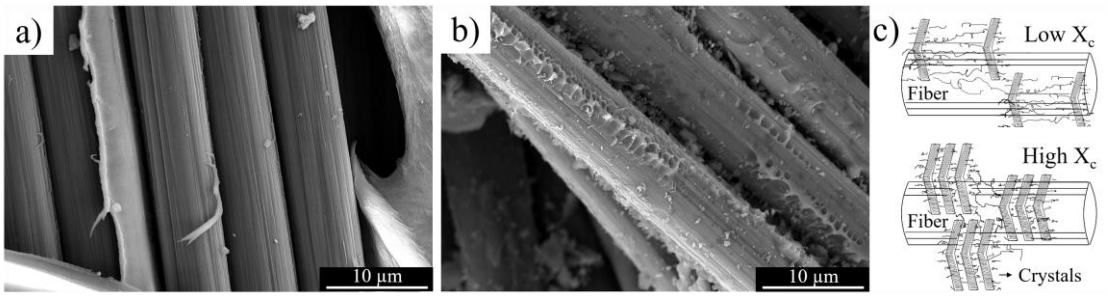

Figure 9.10 SEM images of the fiber surface of a) unaged; and b) friction riveted joints after 28 days of aging, showing an unfeatured and radial PEEK fibrils growth from the fiber surface; c) illustration of the dependence between the degree of crystallinity, transcrystallinity, and hence fiber-matrix adhesion.

The dependence of bonding mechanisms in the fiber-matrix interface on the degree of crystallinity (X_c) is schematically shown in Figure 9.10-c. Higher crystallinity creates more potential electrostatic sites for adsorption of the matrix into the fiber, which may have created the rougher fiber-matrix interface seen in Figure 9.10-b. As the strong fiber-matrix interface is loaded under shear, less adhesive failure takes place in such an interface and the bulk matrix fails cohesively instead. A deeper understanding of the transcrystallinity morphology and its nucleation and growth kinetics are beyond the scope of the work, but some literature on the topic can be found in [132].

To summarize: It can be concluded that water uptake along with the temperature led to oxidation of the metal nut and washer, as well as to cavitation of the composite surface, which did not play any role in joint performance. Moreover, transcrystallinity was induced in the composite by hydrothermal aging, preferentially in the thermomechanically affected material close to the rivet, which in turn led to better local and global mechanical properties of the friction riveted joints.

9.2 Saline environment effect

9.2.1 Surface features, microstructure and chemical composition

The effects of corrosion on the friction riveted joints were assessed by exposure to a saline atmosphere, as described in Section 5.2.10.2. In a similar manner to the hydrothermally aged samples, all joints were visually inspected as soon as they were taken out of the salt spray cabinet. Figure 9.11 shows the top surface of the friction riveted joints that were not exposed and exposed for 3, 7, 14, 21, and 42 days. The longer exposure times and more frequent analyses over time were considered necessary, to closely follow the corrosion induced in the external clamping elements and its influence on the joint mechanical properties.

Figure 9.11 Top view of the friction riveted joints after 0, 3, 7, 14, 21, and 42 days of saline fog exposure.

After three days of exposure, some changes in color of the external metallic elements were observed, and this increased gradually during the 42 days, indicating they underwent a progressive corrosion process. Due to the vertical positioning of the samples in the salt spray cabinet, the corrosion products and chlorides dripped down along with condensed water, forming the downward yellowish imprints. High magnification SEM images and EDS spectra were taken of the yellow region on the nut surface after three days of exposure (Figure 9.12-a to -e) as it was the starting point of corrosion process of the external metallic elements. The region comprises localized corrosion defects, shown as superficial cracking in Figure 9.12-c, and a continuous layer with high porosity, as shown in Figure 9.12-d. The high concentration of O and Fe in this layer indicates the formation of a passive film of iron oxide and/or hydroxide. A small amount of Cl and Na were also detected, which may relate to contamination of the surface by condensation of the saline fog during the exposure. According to the literature [269], the constituents within a passive film on Cr series stainless steels vary in depth of layer, and the outer layer is mostly composed of Fe oxides and hydroxides. Moreover, an inhomogeneous condensation of saline fog on the joint surface may have resulted in a less alkaline medium, which favors gradual decomposition of the Fe oxides (Fe_2O_3 and Fe_3O_4) into porous Fe hydroxide (FeOOH and $Fe(OH)_3$), likely the porosity shown in Figure 9.12-d, and which increases the material's susceptibility to corrosion [270].

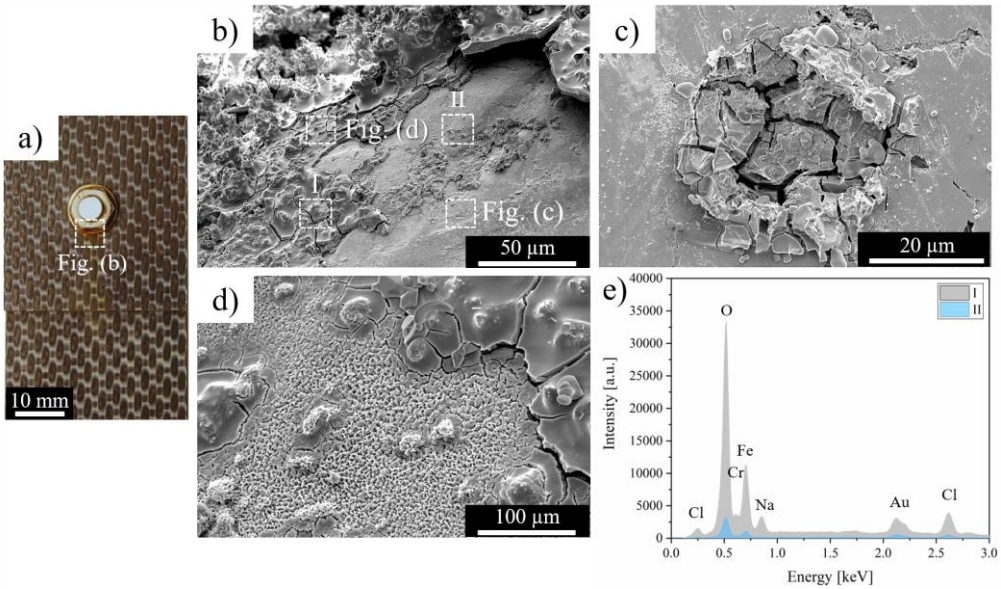

Figure 9.12 a) Top view of friction riveted joint after 3 days of salt spray testing, depicting an area of the metal nut; b) high magnification SEM image of the stainless steel nut, showing c) a localized corrosion defect, and d) a continuous film with high porosity; e) EDS spectra of regions I and II in (b).

In contrast to the hydrothermally aged joints described in Section 9.1, the corrosion observed was by pitting in the stainless steel in the mid-section of the aged nut (Figure 9.13-b) and by crevices in the washer (Figure 9.3-c). These degradation mechanisms are typical for stainless steel and occur mainly when it is exposed to aqueous solutions containing chloride. Such alkaline media chemically attack the protective oxide layer, forming irregular pits, or crevices in regions where the electrolyte stagnates such as at the interface between the washer and composite (Figure 9.13-c) [271].

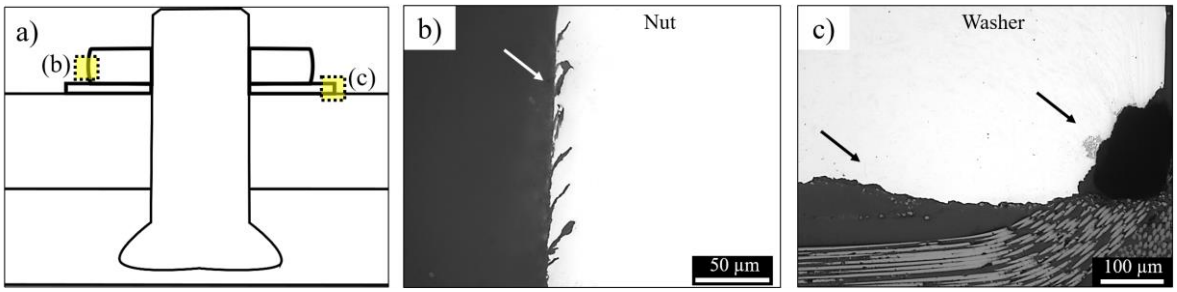

Figure 9.13 a) Schematic illustration of the mid-section of stainless steel showing corrosion defects in b) the nut, and c) the washer after 3 days of salt spray testing, by pitting and crevices, respectively.

Figure 9.14-a highlights the yellowish area on the composite surface of a joint exposed to 3 days of saline atmosphere. The continuous layer formed on the CF-PEEK (Figure 9.14-b) appears very brittle with cracks exposing the damaged composite surface (Figure 9.14-c). By EDS analysis, this layer is comprised mainly of the corrosion products (FeOOH, $Fe(OH)_3$, Fe_2O_3, Fe_3O_4) and a condensate of the saline fog (Figure 9.14-d). As explained for hydrothermal aging, it is expected that

any galvanic coupling formed between the exposed fibers and the external clamping elements would enhance the corrosion process of the metal and possibly hydrolysis of PEEK, which in turn would promote superficial cavitation of the composite.

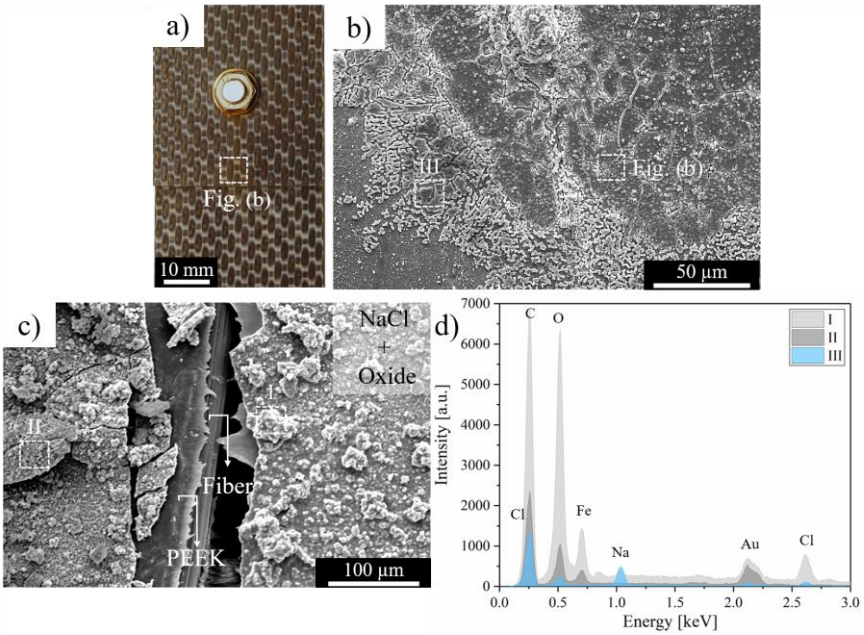

Figure 9.14 a) Top view of a friction riveted joint after 3 days of salt spray testing, depicting an area of the composite surface; high magnification SEM image of the CF-PEEK, highlighting b) the condensate layer of corrosion products and NaCl, and c) fiber exposure in failed regions of the condensate layer; c) EDS spectra of regions I and II in (c), and III in (b).

9.2.2 Local physicochemical changes in the CF-PEEK and mechanical performance

Table 9.2 compares the transition temperatures obtained by DSC analysis of the unaged and saline aged BM and TMAM materials (DSC curves shown in Appendix L). Contrary to the effects of hydrothermal aging, as described in Section 9.1, the saline aged materials did not exhibit any noticeable temperature or crystallinity changes, even after 42 days of exposure. One may assume that the lower temperature (35 °C) during salt spray testing compared to hydrothermal aging (71 °C) did not contribute post-crystallization of PEEK by transcrystallinity. Moreover, the ions present in the saline solution, once they form a condensate on the composite surface, can impair the hydrogen bonds between the polar carbonyl groups of PEEK and water molecules. This decreases water uptake and consequently PEEK chain mobility for post-crystallization. As a consequence, no changes in the local mechanical properties of the CF-PEEK were observed, as shown in Figure 9.15 (detailed results are

shown in Appendix E). Similar to hydrothermal aging, no changes to the typical microhardness profile of the rivet mid-plane were detected, as shown in Appendix M.

Table 9.2 Main parameters obtained from DSC analysis (T_{cc} – cold crystallization temperature, T_m – melting temperature, T_c – crystallization temperature, X_c – degree of crystallization) for unaged and saline aged BM and TMAM materials.

		T_{cc} [°C]	T_m [°C]	T_c [°C]	X_c [%]
Before aging	**BM**	153.0 ± 1.0	345.0 ± 1.0	292.0 ± 5.0	29.0 ± 2.0
	TMAM	-	340.0 ± 0.2	296.0 ± 1.0	24.0 ± 2.0
After SS (42 days)	**BM**	155.0 ± 1.0	343.0 ± 0.1	280 ± 0.3	27.0 ± 2.0
	TMAM	172.0 ± 2.0	338.0 ± 2.0	296.0 ± 0.5	24.0 ± 3.0

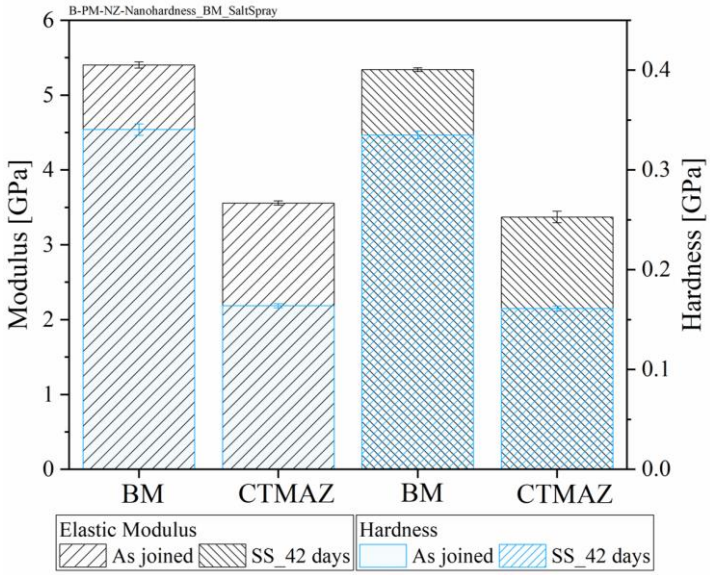

Figure 9.15 Average and standard deviation of indentation modulus and hardness of PEEK as joined and after 42 days of saline environmental exposure, obtained by the CSM technique.

9.2.3 Global mechanical performance and fracture analysis

The evolution of mechanical performance, displacement at break, and mass change, as a function of saline aging time are summarized in Figure 9.16. Until 21 days of exposure the joint strength was virtually constant, while after 42 days a decrease of approximately 23 % was observed. The mass change increased gradually over the exposure time, reaching (2.0 ± 0.3) %, while the displacement at break decreased by up to (2.25 ± 0.2) mm, indicating embrittlement of the joint.

Compared to hydrothermal aging (Figure 9.6 in Section 9.1), a relative inferior M_n and D_b towards 42 days of exposure may indicate the effect of dissolved cations and anions of NaCl in the water in inhibiting water uptake, and therefore plasticization of the PEEK. According to Alam, Robert, and Brádaigh [21], salt ions in water diffuse less readily than pure water into a polymer matrix, which results in the salinity gradient working as an osmotic counter pressure, reducing water uptake by the composite. Although the conditioning in a saline environment presented less detrimental effect on M_n, it is reported that the ions, once they are absorbed by the composite, can easily interact with polar groups in the fiber-matrix interface. This leads to physical debonding and consequently decreases the composite's load-transfer ability [187], which could help explain the degradation observed in the joint's mechanical properties.

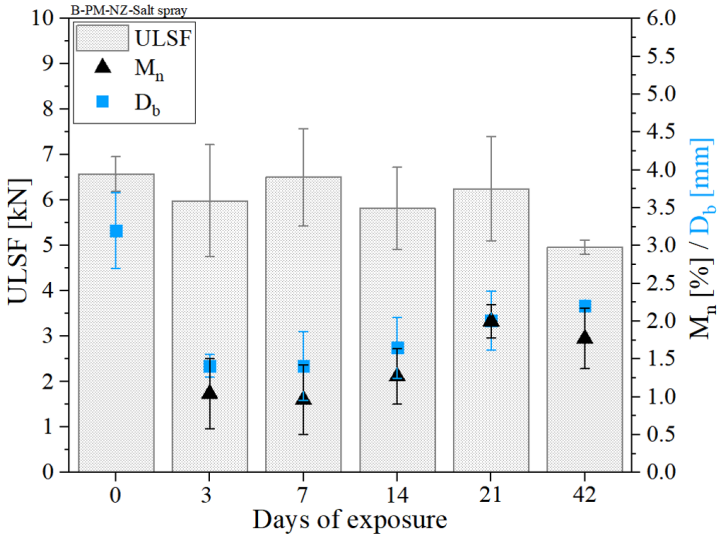

Figure 9.16 Mechanical strength along with displacement at break (D_b) and mass change (M_n) of friction riveted joints as a function of saline aging exposure days.

Besides changes of the composite properties, as observed in Figure 9.11 and Figure 9.12, the saline exposure gradually corroded the nut and washer, which might no longer contribute to tightening of the joint, consequently decreasing D_b and the bearing resistance of the joint. A decrease of tightening torque would negatively affect the friction between the tightening elements and the composite surface [272]. This would cause the compressive stresses to become poorly redistributed throughout the washer area, which in turn may have led to stress concentration sites in the edges of the composite hole, where premature failure took place prior to its extended plastic deformation. Such an effect seems to be more relevant to the global mechanical properties of the joint than the integrity of the composite, because, as discussed in the previous section, the saline atmosphere did not compromise the local mechanical properties of the composite. Additionally, and contrary to the

hydrothermal aging, because saline aging was performed at 35 °C it may be assumed that any contribution of temperature to releasing residual stress from the joining process is negligible.

The decrease in tightening torque combined with low plasticization of the composite, owing to low water uptake by the polymer after 42 days of exposure, led to a quasi-constant bearing area as highlighted by CLSM scans from the composite fracture surface as shown in Figure 9.17.

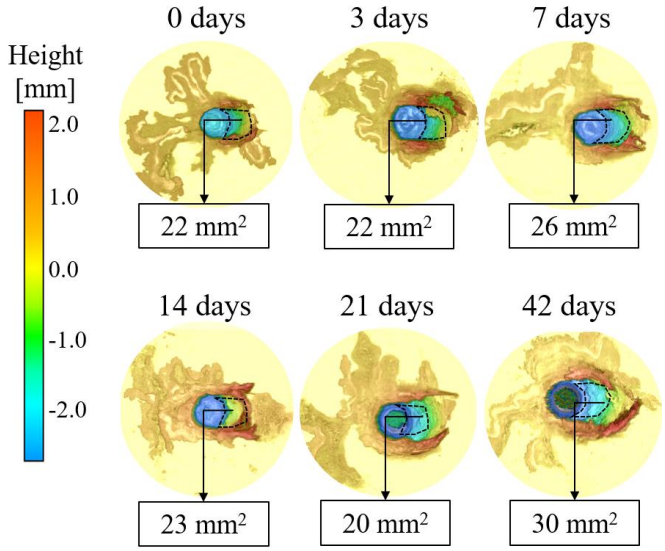

Figure 9.17 Bearing area of failed friction riveted joints loaded under shear as a function of exposure days under saline environment.

Figure 9.18 shows the fracture surface of a joint after 42 days of saline aging. All the joints failed by composite bearing and rivet pull-out, as also observed for the unaged joints and described in Section 7.1.2. The condensation of saline solution on the inner composite surface of the overlap area (Figure 9.18-b) induced cavitation in the surroundings of the consolidated squeezed material, in a similar way to the hydrothermally aged samples. As previously explained, hydrolysis of the PEEK consequently caused erosion to occur, exposing fibers from the first ply of the composite. Moreover, NaCl crystals were identified in the failed squeezed material (Figure 9.18-c) confirming a lack of joint sealing that allowed a flow of saline solution condensate into the inner regions of the composite overlap area. The presence of such a chemical may have inhibited the mobility of the polymer macromolecules in the squeezed material, resulting in its embrittlement, as is shown by brittle cracks in the inner region of the cohesively failed squeezed material (Figure 9.18-d).

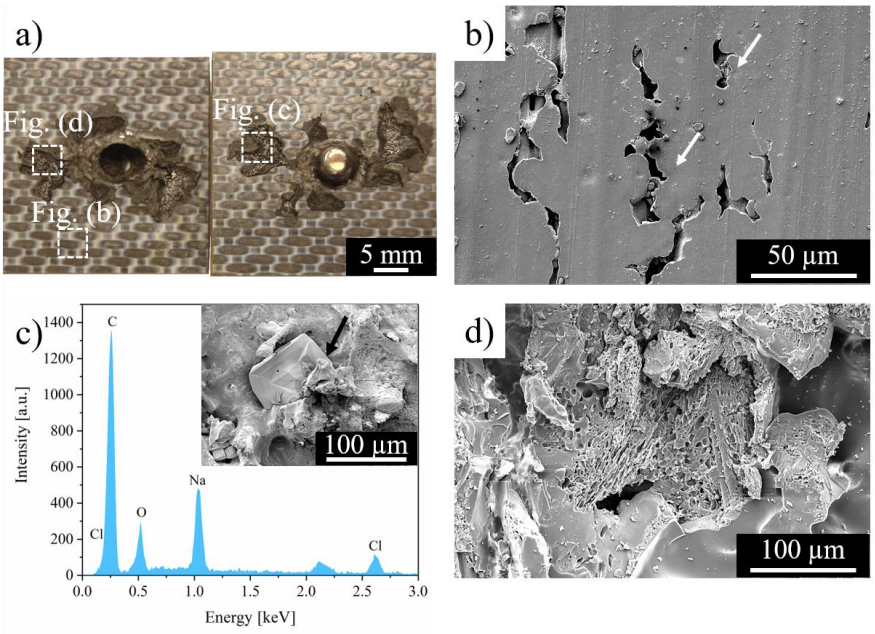

Figure 9.18 a) Typical fracture surface of friction riveted joints after 42 days of saline aging; SEM images of the composite surfaces inside the overlap area, showing b) corrosion-induced cavitation, c) contamination by NaCl crystals, and d) the brittle failure of the consolidated squeezed material.

9.2.4 Summary of the results

The capacity of the friction riveted joints to sustain mechanical performance under harsh environmental conditions and their degradation mechanisms proved complex and dependent on the testing configuration. Under controlled hydrothermal aging, a 23 % increase of joint mechanical performance was observed after 28 days of exposure, resulting from composite post-crystallization. It is believed that the temperature and water uptake may have induced additional nucleation of crystals on the surfaces of the fibers by transcrystallization. However, under controlled saline aging, a decrease of up to 23 % in quasi-static mechanical performance was explained by corrosion induced in the external tightening elements, which no longer sufficiently contributed a redistribution of the compression stress through the composite surface. No effect was observed in the physicochemical properties of the composite.

Chapter 10. Summary of the Results and Conclusions

This PhD work was conceived to explore the potential of FricRiveting for aircraft composite structures in terms of design and mechanical integrity. Another aim within the scientific approach was to gain a fundamental understanding of the correlation between joint properties of process, design and microstructure. An investigation of failure evolution by quasi-static and cyclic loading of the joints was desired to describe the failure mechanisms. The influence of damage threats, including impact and environmental aging, to joint strength and failure mechanisms was aimed to cover the mechanical integrity aspects of the work, taking an engineering approach. In this scope, the following main findings are drawn from the results obtained:

Development of Direct Friction Riveting for overlapped CFRP

By a stepwise analysis of Direct FricRiveting process, the upward and squeezed flow of the process-affected composite were investigated, as well as the formation of a shear layer and shear banding in the composite, in the vicinity of the rivet shaft. The squeezed material between the composite parts was shown to contribute as an additional bonding mechanism to the mechanical interlocking of rivet tip widening and embedding of fiber and matrix in the rough surface of the rivet. The process temperature measured by thermocouples exceeded the decomposition temperature of PEEK as well as the β-*transus* temperature of Ti6Al4V. The high process temperature and fast cooling rate locally decreased the mechanical properties of CF-PEEK, owing to volumetric flaws in the composite's thermomechanically affected zone and the low degree of crystallinity of PEEK. Such effects also locally increased the hardness of the thermomechanically affected zone of the Ti6Al4V, owing to morphological transformation from a globular microstructure to a combination of α' martensitic and Widmanstätten structures in the rivet tip. Over the process temperature range analyzed in this work, three plastic deformation shapes of rivet tip were investigated: under deformed, bell shaped and inverted bell shaped. The bell-shaped rivet tip produced stronger joints under shear loading, owing to its high anchoring efficiency and less defects in the composite. Using a DoE and ANOVA for the parameter window used in this work, the highest level of RS (15000 rpm) and the lowest level of FF (10 kN) and CP (0.2 MPa) provided the optimized set of parameters to increase the lap shear strength of the friction riveted joints. An improvement of the joint strength was further assessed by a fundamental study of the joint design. A washer size of 10 mm (D_w/D = 2) and tightening torque of 1 N·m increased the ULSF of friction riveted joints by 30 %, owing to better stress distribution to the rivet surroundings and additional friction between the washer and the

composite surface. No correlation could be drawn between edge distance, specimen width, and ULSF.

Mechanical behavior of the friction riveted Joints

Although the friction riveted joints presented an inferior quasi-static mechanical performance of (6.6 ± 0.4) kN compared to reference lock bolted joints (8.7 ± 0.2) kN, under cyclic loading the joints withstood 10^5 cycles with 66 % of the ultimate lap shear force, showing an improvement of up to 88 % in comparison with the cyclic behavior of conventional mechanical fastening techniques. Moreover, the run-out specimens presented a residual strength comparable to their quasi-static behavior. The micromechanisms of failure under both loading conditions were similar and characterized by debonding of the rivet tip from the composite hole, owing to out-of-plane stresses, which damage the composite matrix mainly by tension. The peel stresses also promoted crack initiation at the periphery of the consolidated squeezed material, which radially propagated along the interface between the composite parts by a mixture of adhesive and cohesive failure. The in-plane stresses imposed by the rivet on the edges of the composite hole triggered shear-driven compressive failure throughout the composite thickness, which enlarged the composite hole and this aided the pull-through failure of the joint.

Damage Threat Assessment

5 J impact energy was found to introduce BVID to the friction riveted joints with no indication of stress-driven defects such as delamination taking place. Therefore, quasi-static and fatigue mechanical behavior were not compromised and it the joint had a residual strength of 91 % of ULSF under quasi-static loading and of 83 % of the ULSF after 10^6 fatigue cycles. At impact energies above 5 J, VID was introduced to the friction riveted joints leading to delamination and failure of the metal-composite interface. In addition, the higher energy induced peeling stresses in the composite interface, leading to premature failure of the squeezed material. Consequently, the quasi-static mechanical strength decreased to 60 % of the ULSF. Although the fatigue resistance of the joints impacted with high energy decreased, the propagation of the impact damage under cyclic loading showed to be less dependent on the stress amplitude, once the joints were already severely damaged by the impact event. Under fatigue, friction riveted joints showed to be less sensible to the fatigue damage than to the impact damage, as confirmed by the high residual strength after 10^6 fatigue cycles (98% and 96% for 5 J and 20 J, respectively). The empirical approach adopted in this work for impact of joints, including understanding the damage mechanism, damage visual detectability, and assessment of residual strengths, can be extrapolated to validate calculation methods for other sizes of damage tolerant composite structure in the aircraft sector.

Durability of the friction riveted Joints

The capacity of the friction riveted joints to sustain mechanical performance under harsh environmental conditions proved complex and dependent on the testing configuration. Under controlled hydrothermal aging, a 23 % increase of joint mechanical performance was observed after 28 days of exposure as a result of post-crystallization. Under controlled saline aging, a decrease up to 23 % in the quasi-static mechanical performance was explained by corrosion induced in the external tightening elements, which no longer contributed as much redistribution of the compression stress across the composite surface.

The results achieved by this PhD work and proposed phenomenological descriptions have provided a better understanding of the principles of Friction Riveting for overlap joint configurations. In addition, the influence of process parameters on the microstructure and physicochemical behavior of the joints has been established and correlated with the quasi-static mechanical performance of the joints. Four aspects of joint design (tightening torque, washer size, specimen width, and edge distance) were correlated with the mechanical and failure behavior of the joints, providing a fundamental design guideline. The metal-composite bonding mechanisms (mechanical interlocking and adhesion forces) were detailed for an overlapped joint configuration and correlated with failure mechanisms and the quasi-static and fatigue mechanical behavior. Threats to the quasi-static and fatigue mechanical performance of the joints where assessed, including accidental damage (by impact) and environmental aging. Therefore, this work has successfully fulfilled the defined objectives.

Finally, this work has covered complex and relevant issues from scientific and engineering perspectives for the introduction of thermoplastic composites and a new joining solution for them in aircraft manufacturing. Therefore, these findings comply with the demands of the aeronautics sector for coming generations of sustainable and efficient aircraft. Although this work was performed on Ti6Al4V and CF-PEEK, the main principles of the technique are applicable to other combinations of lightweight metal alloys and thermoplastic composites of interest for use in aircraft.

Chapter 11. Recommendations for Future Work

Although many of the scientific and technological aspects of Direct Friction Riveting for aircraft applications have been covered in this PhD work, some topics remain open to be addressed by future investigations. The following recommendations are suggested for future work:

- The contribution of the clamping system to joint formation and mechanical strength was shown to be significant for overlapped friction riveted joints. However, to automate the joining process for an industrial application, the FricRiveting machinery should be improved by integrating a clamping function with the welding head. Therefore, a tool could be conceived to use the combined concept of C-frame and clamping ring with independent vertical movement, which has been extensively adopted for the industrial tool design of refill friction stir spot welding and friction spot joining [273,274].
- A joint design survey should address customized rivet profiles for FricRiveting. As shown in this work, the washer plays an important role in stress distribution in the rivet surroundings, similarly to the flanged lock collar [275] effect in lock bolted parts. Therefore, rivets with an integrated collar could be manufactured by various routes (*e.g.* wire drawing, cold forging, CNC machining, selective laser melting, metal injection molding, etc.). Additionally, the influences of pitch distance, number of rows, and number of rivets on quasi-static, fatigue, and impact mechanical behaviors could be investigated to assess a scaling up of the technology. Such assessments could be combined with a stress analysis by FEM, which must be improved for single spot and validated for multiple spot friction riveted joints.
- The damage introduced by fatigue in friction riveted joints should be further evaluated using the damage tolerance philosophy, including characterization and prediction of fatigue crack growth for multiple spot friction riveted parts, analysis of the strain energy release rate and residual strength. Such a methodology would supplement transferability of the technology to aircraft structures, where this philosophy is widely implemented for maintenance purposes.
- As reparability and maintenance of damaged composite structures is an issue in aircraft, a study on the topic for damaged friction riveted joints is necessary for scaling up the technology. Repair methodologies that include resin injection, chopped fiber filling, and patch repair could be used, as well as investigation of the rejoinability of a repair site using FricRiveting.

References

[1] Strategic research & innovation agenda, (n.d.). https://www.acare4europe.org/sria/exec-summary/volume-1 (accessed November 30, 2018).

[2] M. Holmes, Carbon fibre reinforced plastics market continues growth path, Reinf. Plast. 57 (2013) 24–29. https://doi.org/10.1016/S0034-3617(13)70186-3.

[3] C.A. Harper, Handbook of Plastics, Elastomers, and Composites, McGraw Hill Professional, 2002.

[4] E. Asmatulu, J. Twomey, M. Overcash, Recycling of fiber-reinforced composites and direct structural composite recycling concept, J. Compos. Mater. 48 (2014) 593–608. https://doi.org/10.1177/0021998313476325.

[5] B. Vieille, V.M. Casado, C. Bouvet, Influence of matrix toughness and ductility on the compression-after-impact behavior of woven-ply thermoplastic- and thermosetting-composites: A comparative study, Compos. Struct. 110 (2014) 207–218. https://doi.org/10.1016/j.compstruct.2013.12.008.

[6] E. Shehab, W. Ma, A. Wasim, Manufacturing Cost Modelling for Aerospace Composite Applications, in: J. Stjepandić, G. Rock, C. Bil (Eds.), Concurr. Eng. Approaches Sustain. Prod. Dev. Multi-Discip. Environ., Springer London, 2013: pp. 425–433.

[7] R. Stewart, Thermoplastic composites — recyclable and fast to process, Reinf. Plast. 55 (2011) 22–28. https://doi.org/10.1016/S0034-3617(11)70073-X.

[8] S.-S. Yao, F.-L. Jin, K.Y. Rhee, D. Hui, S.-J. Park, Recent advances in carbon-fiber-reinforced thermoplastic composites: A review, Compos. Part B Eng. 142 (2018) 241–250. https://doi.org/10.1016/j.compositesb.2017.12.007.

[9] C. Red, Thermoplastics in Aerospace Composites Outlook, 2014-2023, (n.d.). https://www.compositesworld.com/articles/the-outlook-for-thermoplastics-in-aerospace-composites-2014-2023 (accessed November 30, 2018).

[10] S. Black, Fokker Aerostructures: Hoogeveen, The Netherlands, (n.d.). https://www.compositesworld.com/articles/fokker-aerostructures-hoogeveen-the-netherlands (accessed November 30, 2018).

[11] A.P. da Costa, E.C. Botelho, M.L. Costa, N.E. Narita, J.R. Tarpani, A Review of Welding Technologies for Thermoplastic Composites in Aerospace Applications, J. Aerosp. Technol. Manag. 4 (2012) 255–265. https://doi.org/10.5028/jatm.2012.04033912.

[12] P.K. Mallick, Materials, Design and Manufacturing for Lightweight Vehicles, Elsevier, 2010.

[13] S.T. Amancio-Filho, L.-A. Blaga, Joining of Polymer-Metal Hybrid Structures: Principles and Applications, John Wiley & Sons, 2018.

[14] P. Viegas Ochoa de Carvalho, R.M. Groves, R. Benedictus, Full-scale testing of an ultrasonic guided wave based structural health monitoring system for a thermoplastic composite aircraft primary structure, EWSHM 2018 9th Eur. Workshop Struct. Health. (2018). http://resolver.tudelft.nl/uuid:98088174-5098-445f-835d-98363e193ed6 (accessed November 30, 2018).

[15] F.J.H. Ruiz, J.M.P. Lopez, P.N. Vines, A.P. Pastor, C.B.D.L. Llave, P.C. Garrofe, A.A. Hidalgo, A.G. Garcia, J.J.G. Blanco, E.A. Glowacz, A.F. Alonso, A.G. Sacristan, C.E.F. Fuentes, Optimized stringer run-out zones in aircraft components, US20130101801A1, 2013..

[16] T. Dong, N.H. Kim, Cost-Effectiveness of Structural Health Monitoring in Fuselage Maintenance of the Civil Aviation Industry †, Aerospace. 5 (2018) 87. https://doi.org/10.3390/aerospace5030087.

[17] P.E. Irving, C. Soutis, Polymer Composites in the Aerospace Industry, Elsevier, 2014. https://doi.org/10.1016/C2013-0-16303-9.

[18] S.V. Kozhukharov, Advanced Multifunctional Corrosion Protective Coating Systems for Light-Weight Aircraft Alloys—Actual Trends and Challenges, Thin Film Process. - Artifacts Surf. Phenom. Technol. Facets. (2017). https://doi.org/10.5772/67237.

[19] H. Lohner, B, Aircraft Surface Protection - Principales, Application, Future Trends, in: Corrosion Control Pract. Commer. Aircr. J., 2011: pp. 13–28.

[20] J.A. Marceau, Corrosion Control Practices on Commercial Aircraft, SAE Trans. 96 (1987) 13–28.

[21] P. Alam, C. Robert, C.M. Ó Brádaigh, Tidal turbine blade composites - A review on the effects of hygrothermal aging on the properties of CFRP, Compos. Part B Eng. 149 (2018) 248–259. https://doi.org/10.1016/j.compositesb.2018.05.003.

[22] S. Alessi, G. Pitarresi, G. Spadaro, Effect of hydrothermal ageing on the thermal and delamination fracture behaviour of CFRP composites, Compos. Part B Eng. 67 (2014) 145–153. https://doi.org/10.1016/j.compositesb.2014.06.006.

[23] U.H. Tiong, G. Clark, The structural environment as a factor affecting coating failure in aircraft joints, Procedia Eng. 2 (2010) 1393–1401. https://doi.org/10.1016/j.proeng.2010.03.151.

[24] S.T. Amancio-Filho, M. Beyer, J.F.D. Santos, Process for joining a metallic bolt to a plastic workpiece, EP 1 790 462 B1, 2011.

[25] J. Altmeyer, J.F. dos Santos, S.T. Amancio-Filho, Effect of the friction riveting process parameters on the joint formation and performance of Ti alloy/short-fibre reinforced polyether ether ketone joints, Mater. Des. 60 (2014) 164–176. https://doi.org/10.1016/j.matdes.2014.03.042.

[26] J. Altmeyer, U.F.H. Suhuddin, J.F. dos Santos, S.T. Amancio-Filho, Microstructure and mechanical performance of metal-composite hybrid joints produced by FricRiveting, Compos. Part B Eng. (2015) 130–140.

[27] L. Blaga, J.F. dos Santos, R. Bancila, S.T. Amancio-Filho, Friction Riveting (FricRiveting) as a new joining technique in GFRP lightweight bridge construction, Constr. Build. Mater. 80 (2015) 167–179. https://doi.org/10.1016/j.conbuildmat.2015.01.001.

[28] B.C. de Proença, L. Blaga, J.F. dos Santos, L.B. Canto, S.T. Amancio-Filho, Friction riveting ('FricRiveting') of 6056 T6 aluminum alloy and polyamide 6: influence of rotational speed on the formation of the anchoring zone and on mechanical performance, Weld. Int. 31 (2017) 509–518. https://doi.org/10.1080/09507116.2016.1218627.

[29] R.C. Alderliesten, Introduction to aerospace structures and materials, Delft University of Technology, Delft, The Netherlands, 2018.

[30] S.T. Amancio-Filho, J. f. dos Santos, Joining of polymers and polymer–metal hybrid structures: Recent developments and trends, Polym. Eng. Sci. 49 (2009) 1461–1476. https://doi.org/10.1002/pen.21424.

[31] R.W. Messler, Trends in key joining technologies for the twenty-first century, Assem. Autom. 20 (2000) 118–128. https://doi.org/10.1108/01445150010321733.

[32] J. Fernie, Joining of Materials and Structures: from Pragmatic Process to Enabling Technology, Assem. Autom. 25 (2005). https://doi.org/10.1108/aa.2005.03325aae.001.

[33] U.A. Khashaba, H.E.M. Sallam, A.E. Al-Shorbagy, M.A. Seif, Effect of washer size and tightening torque on the performance of bolted joints in composite structures, Compos. Struct. 73 (2006) 310–317. https://doi.org/10.1016/j.compstruct.2005.02.004.

[34] F. Sen, M. Pakdil, O. Sayman, S. Benli, Experimental failure analysis of mechanically fastened joints with clearance in composite laminates under preload, Mater. Des. 29 (2008) 1159–1169. https://doi.org/10.1016/j.matdes.2007.05.009.

[35] Y. Xiao, T. Ishikawa, Bearing strength and failure behavior of bolted composite joints (part I: Experimental investigation), Compos. Sci. Technol. 65 (2005) 1022–1031. https://doi.org/10.1016/j.compscitech.2005.02.011.

[36] W.-H. Chen, S.-S. Lee, J.-T. Yeh, Three-dimensional contact stress analysis of a composite laminate with bolted joint, Compos. Struct. 30 (1995) 287–297. https://doi.org/10.1016/0263-8223(94)00041-7.

[37] A. Riccio, L. Marciano, Effects of Geometrical and Material Features on Damage Onset and Propagation in Single-lap Bolted Composite Joints under Tensile Load: Part I – Experimental Studies, J. Compos. Mater. 39 (2005) 2071–2090. https://doi.org/10.1177/0021998305052026.

[38] S.D. Thoppul, J. Finegan, R.F. Gibson, Mechanics of mechanically fastened joints in polymer–matrix composite structures – A review, Compos. Sci. Technol. 69 (2009) 301–329. https://doi.org/10.1016/j.compscitech.2008.09.037.

[39] C. Cooper, G.J. Turvey, Effects of joint geometry and bolt torque on the structural performance of single bolt tension joints in pultruded GRP sheet material, Compos. Struct. 32 (1995) 217–226. https://doi.org/10.1016/0263-8223(95)00071-2.

[40] P.P. Camanho, M. Lambert, A design methodology for mechanically fastened joints in laminated composite materials, Compos. Sci. Technol. 66 (2006) 3004–3020. https://doi.org/10.1016/j.compscitech.2006.02.017.

[41] S. Kapti, O. Sayman, M. Ozen, S. Benli, Experimental and numerical failure analysis of carbon/epoxy laminated composite joints under different conditions, Mater. Des. 31 (2010) 4933–4942. https://doi.org/10.1016/j.matdes.2010.05.018.

[42] F. Thomas, Y. Zhao, Torque Limit for Composites Joined with Mechanical Fasteners, in: 46th AIAAASMEASCEAHSASC Struct. Struct. Dyn. Mater. Conf., American Institute of Aeronautics and Astronautics, n.d. http://arc.aiaa.org/doi/abs/10.2514/6.2005-2351 (accessed July 31, 2018).

[43] P. Camanho, L. Tong, Composite Joints and Connections | Principles, Modelling and Testing, Woodhead Publishing, 2011.

[44] L. Liu, J. Zhang, K. Chen, H. Wang, Combined and interactive effects of interference fit and preloads on composite joints, Chin. J. Aeronaut. 27 (2014) 716–729. https://doi.org/10.1016/j.cja.2014.04.014.

[45] C. Poon, Literature Review on the Design of Composite Mechanically Fastened Joints (Revue de la Documentation sur la Conception des Joints a Liaison Mecanique en Composites), (1986).

[46] P.D. Herrington, M. Sabbaghian, Effect of Radial Clearance between Bolt and Washer on the Bearing Strength of Composite Bolted Joints, J. Compos. Mater. 26 (1992) 1826–1843. https://doi.org/10.1177/002199839202601208.

[47] E. Morteau, V. Faivre, Damage tolerant composite fuselage sizing, FAST Mag. AIRBUS S.A.S. (2011) 10–16.

[48] S.-L. Gao, J.-K. Kim, Cooling rate influences in carbon fiber/PEEK composites. Part III: impact damage performance, Compos. Part Appl. Sci. Manuf. 32 (2001) 775–785. https://doi.org/10.1016/S1359-835X(00)00189-5.

[49] G. Davies, P. Irving, 9 - Impact, post-impact strength and post-impact fatigue behavior of polymer composites, in: P.E. Irving, C. Soutis (Eds.), Polym. Compos. Aerosp. Ind., Woodhead Publishing, 2015: pp. 231–259. https://doi.org/10.1016/B978-0-85709-523-7.00009-8.

[50] A. Paipetis, D. Katerelos, Post-Impact-Fatigue behavior of composite laminates: Current and novel technologies for enhanced damage tolerance, in: Compos. Laminates, Nova Science Publisher, Inc., 2010: pp. 1–82.

[51] W.A. de Morais, J.R.M. d'Almeida, L.B. Godefroid, Effect of the fiber reinforcement on the low energy impact behavior of fabric reinforced resin matrix composite materials, J. Braz. Soc. Mech. Sci. Eng. 25 (2003) 325–328. https://doi.org/10.1590/S1678-58782003000400002.

[52] A.P. Mouritz, Review of z-pinned composite laminates, Compos. Part Appl. Sci. Manuf. 38 (2007) 2383–2397. https://doi.org/10.1016/j.compositesa.2007.08.016.

[53] I.K. Partridge, M. Yasaee, G. Allegri, J.K. Lander, 6 - Damage-tolerant composite structures by Z-pinning, in: Q. Qin, J. Ye (Eds.), Toughening Mech. Compos. Mater., Woodhead Publishing, 2015: pp. 161–189. https://doi.org/10.1016/B978-1-78242-279-2.00006-8.

[54] K.L. Rugg, B.N. Cox, R. Massabò, Mixed mode delamination of polymer composite laminates reinforced through the thickness by z-fibers, Compos. Part Appl. Sci. Manuf. 33 (2002) 177–190. https://doi.org/10.1016/S1359-835X(01)00109-9.

[55] Y. Wang, J. Zhang, G. Fang, J. Zhang, Z. Zhou, S. Wang, Influence of temperature on the impact behavior of woven-ply carbon fiber reinforced thermoplastic composites, Compos. Struct. 185 (2018) 435–445. https://doi.org/10.1016/j.compstruct.2017.11.056.

[56] J. Körbelin, M. Derra, B. Fiedler, Influence of temperature and impact energy on low velocity impact damage severity in CFRP, Compos. Part Appl. Sci. Manuf. 115 (2018) 76–87. https://doi.org/10.1016/j.compositesa.2018.09.010.

[57] T.K. Tsotsis, 8 - Considerations of failure mechanisms in polymer matrix composites in the design of aerospace structures, in: Fail. Mech. Polym. Matrix Compos., Woodhead Publishing, 2012: pp. 227–278. https://doi.org/10.1533/9780857095329.2.227

[58] G.A.O. Davies, X. Zhang, Impact damage prediction in carbon composite structures, Int. J. Impact Eng. 16 (1995) 149–170. https://doi.org/10.1016/0734-743X(94)00039-Y.

[59] G. a. O. Davies, R. Olsson, Impact on composite structures, Aeronaut. J. 108 (2004) 541–563. https://doi.org/10.1017/S0001924000000385.

[60] S.H. Wang, M.D. Wei, L.W. Tsay, Tensile properties of LBW welds in Ti–6Al–4V alloy at evaluated temperatures below 450 °C, Mater. Lett. 57 (2003) 1815–1823. https://doi.org/10.1016/S0167-577X(02)01074-1.

[61] D. Garcia-Gonzalez, M. Rodriguez-Millan, A. Rusinek, A. Arias, Low temperature effect on impact energy absorption capability of PEEK composites, Compos. Struct. 134 (2015) 440–449. https://doi.org/10.1016/j.compstruct.2015.08.090.

[62] S. Boria, A. Scattina, G. Belingardi, Impact behavior of a fully thermoplastic composite, Compos. Struct. 167 (2017) 63–75. https://doi.org/10.1016/j.compstruct.2017.01.083.

[63] Z. Aslan, R. Karakuzu, B. Okutan, The response of laminated composite plates under low-velocity impact loading, Compos. Struct. 59 (2003) 119–127. https://doi.org/10.1016/S0263-8223(02)00185-X.

[64] J.J.M. Machado, P.M.-R. Gamarra, E.A.S. Marques, L.F.M. da Silva, Improvement in impact strength of composite joints for the automotive industry, Compos. Part B Eng. 138 (2018) 243–255. https://doi.org/10.1016/j.compositesb.2017.11.038.

[65] S.-S. Pang, C. Yang, Y. Zhao, Impact response of single-lap composite joints, Compos. Eng. 5 (1995) 1011–1027. https://doi.org/10.1016/0961-9526(95)00003-6.

[66] E. Ghanbari, O. Sayman, Y. Pekbey, O. Ozdemir, Experimental analysis of single-lap composite joints with two different adhesives at various conditions, J. Compos. Mater. 50 (2016) 1709–1715. https://doi.org/10.1177/0021998315595532.

[67] J. Bieniaś, P. Jakubczak, B. Surowska, K. Dragan, Low-energy impact behaviour and damage characterization of carbon fibre reinforced polymer and aluminium hybrid laminates, Arch. Civ. Mech. Eng. 15 (2015) 925–932. https://doi.org/10.1016/j.acme.2014.09.007.

[68] J. Reiner, J.P. Torres, M. Veidt, M. Heitzmann, Experimental and numerical analysis of drop-weight low-velocity impact tests on hybrid titanium composite laminates, J. Compos. Mater. 50 (2016) 3605–3617. https://doi.org/10.1177/0021998315624002.

[69] EASA: European Aviation Safety Agency, (n.d.).

[70] U. Polimeno, M. Meo, Detecting barely visible impact damage detection on aircraft composites structures, Compos. Struct. 91 (2009) 398–402. https://doi.org/10.1016/j.compstruct.2009.04.014.

[71] N.-H. Tai, M.-C. Yip, C.-M. Tseng, Influences of thermal cycling and low-energy impact on the fatigue behavior of carbon/PEEK laminates, Compos. Part B Eng. 30 (1999) 849–865. https://doi.org/10.1016/S1359-8368(99)00048-7.

[72] X. Li, D. Ma, H. Liu, W. Tan, X. Gong, C. Zhang, Y. Li, Assessment of failure criteria and damage evolution methods for composite laminates under low-velocity impact, Compos. Struct. 207 (2019) 727–739. https://doi.org/10.1016/j.compstruct.2018.09.093.

[73] K.R. Jagtap, S.Y. Ghorpade, A. Lal, B.N. Singh, Finite Element Simulation of Low Velocity Impact Damage in Composite Laminates, Mater. Today Proc. 4 (2017) 2464–2469. https://doi.org/10.1016/j.matpr.2017.02.098.

[74] G.A.O. Davies, P. Robinson, Predicting Failure by Debonding/Delamination, Imperial Coll. of Science and Technology, London (England), 1992.

[75] G.A.O. Davies D. Hitchings, J. Ankersen, Predicting delamination and debonding in modern aerospace composite structures, Compos. Sci. Technol. 66 (2006) 846–854. https://doi.org/10.1016/j.compscitech.2004.12.043.

[76] L. Yang, Y. Ohki, N. Hirai, S. Hanada, Aging of poly(ether ether ketone) by heat and gamma rays — Its degradation mechanism and effects on mechanical, dielectric and thermal properties, Polym. Degrad. Stab. 142 (2017) 117–128. https://doi.org/10.1016/j.polymdegradstab.2017.06.002.

[77] G.J. Turvey, A. Sana, Pultruded GFRP double-lap single-bolt tension joints – Temperature effects on mean and characteristic failure stresses and knock-down factors, Compos. Struct. 153 (2016) 624–631. https://doi.org/10.1016/j.compstruct.2016.06.016.

[78] N.L. Batista, M.C.M. de Faria, K. Iha, P.C. de Oliveira, E.C. Botelho, Influence of water immersion and ultraviolet weathering on mechanical and viscoelastic properties of polyphenylene sulfide–carbon fiber composites, J. Thermoplast. Compos. Mater. 28 (2015) 340–356. https://doi.org/10.1177/0892705713484747.

[79] T. Schambron, A. Lowe, H.V. McGregor, Effects of environmental ageing on the static and cyclic bending properties of braided carbon fiber/PEEK bone plates, Compos. Part B Eng. 39 (2008) 1216–1220. https://doi.org/10.1016/j.compositesb.2008.03.001.

[80] L.A.L. Franco, M.L.A. Graça, F.S. Silva, Fractography analysis and fatigue of thermoplastic composite laminates at different environmental conditions, Mater. Sci. Eng. A. 488 (2008) 505–513. https://doi.org/10.1016/j.msea.2007.11.053.

[81] H.-S. Chen, The static and fatigue strength of bolted joints in composites with hygrothermal cycling, Compos. Struct. 52 (2001) 295–306. https://doi.org/10.1016/S0263-8223(01)00022-8.

[82] Y. Miyano, M. Nakada, N. Sekine, Life Prediction of CFRP/Metal Bolted Joint Under Water Absorption Condition, J. Compos. Mater. 44 (2010) 2393–2411. https://doi.org/10.1177/0021998310372697.

[83] B. Vieille, W. Albouy, L. Taleb, Influence of stamping on the compressive behavior and the damage mechanisms of C/PEEK laminates bolted joints under severe conditions, Compos. Part B Eng. 79 (2015) 631–638. https://doi.org/10.1016/j.compositesb.2015.05.026.

[84] Y. Mueller, R. Tognini, J. Mayer, S. Virtanen, Anodized titanium and stainless steel in contact with CFRP: An electrochemical approach considering galvanic corrosion, J. Biomed. Mater. Res. A. 82A (2007) 936–946. https://doi.org/10.1002/jbm.a.31198.

[85] C.J.E. Smith, K.R. Baldwin, Advances in Protective Coatings and Their Application to Ageing Aircraft, in: RTO AVT Workshop, Corfu, Greece, 1999: p. 9.

[86] R. Narayanan, S.K. Seshadri, Phosphoric acid anodization of Ti–6Al–4V – Structural and corrosion aspects, Corros. Sci. 49 (2007) 542–558. https://doi.org/10.1016/j.corsci.2006.06.021.

[87] K. Kitamura, H. Fujii, Y. Iwata, Y.S. Sun, Y. Morisada, Flexible control of the microstructure and mechanical properties of friction stir welded Ti–6Al–4V joints, Mater. Des. 46 (2013) 348–354. https://doi.org/10.1016/j.matdes.2012.10.051.

[88] R.R. Boyer, An overview on the use of titanium in the aerospace industry, Int. Symp. Metall. Technol. Titan. Alloys. 213 (1996) 103–114. https://doi.org/10.1016/0921-5093(96)10233-1.

[89] S.V. Raj, L.J. Ghosn, B.A. Lerch, M. Hebsur, L.M. Cosgriff, J. Fedor, Mechanical properties of 17-4PH stainless steel foam panels, Mater. Sci. Eng. A. 456 (2007) 305–316. https://doi.org/10.1016/j.msea.2006.11.142.

[90] M.S.F. Lima, Laser beam welding of titanium nitrid coated titanium using pulse-shaping, Mater. Res. (2005) 323–328.

[91] A. Dehghan-Manshadi, MJ. Bermingham, M.S. Dargusch, D.H. StJohn, M. Qian, Metal injection moulding of titanium and titanium alloys: Challenges and recent development, Powder Technol. 319 (2017) 289–301. https://doi.org/10.1016/j.powtec.2017.06.053.

[92] T. Ebel, 17 - Metal injection molding (MIM) of titanium and titanium alloys, in: D.F. Heaney (Ed.), Handb. Met. Inject. Molding, Woodhead Publishing, 2012: pp. 415–445. https://doi.org/10.1533/9780857096234.4.415.

[93] G.C. Obasi, O.M. Ferri, T. Ebel, R. Bormann, Influence of processing parameters on mechanical properties of Ti–6Al–4V alloy fabricated by MIM, Mater. Sci. Eng. A. 527 (2010) 3929–3935. https://doi.org/10.1016/j.msea.2010.02.070.

[94] J. Matthew, J. Donachie, Titanium: A technical guide, 2000.

[95] C. Leyens, M. Peters, Titanium and Titanium Alloys: Fundamentals and Applications, Wiley-VCH, Weinheim, 2003.

[96] J. Peirs, W. Tirry, B. Amin-Ahmadi, F. Coghe, P. Verleysen, L. Rabet, D. Schryvers, J. Degrieck, Microstructure of adiabatic shear bands in Ti6Al4V, Mater. Charact. 75 (2013) 79–92. https://doi.org/10.1016/j.matchar.2012.10.009.

[97] K. Mutombo, C. Siyasiya, W.E. Stumpf, Dynamic Globularization of α-Phase in Ti6Al4V Alloy during Hot Compression, Mater. Sci. Forum. 783–786 (2014) 584–590. https://doi.org/10.4028/www.scientific.net/MSF.783-786.584.

[98] I. Katzarov, S. Malinov, W. Sha, Finite element modeling of the morphology of β to α phase transformation in Ti-6Al-4V alloy, Metall. Mater. Trans. A. 33 (2002) 1027–1040. https://doi.org/10.1007/s11661-002-0204-4.

[99] S. Malinov, Z. Guo, W. Sha, Modelling of beta to alpha phase transformation kinetics in Ti-6Al-4V alloy, in: United Kingdom, 2000: p. 92.

[100] Z.X. Zhang, S.J. Qu, A.H. Feng, J. Shen, D.L. Chen, Hot deformation behavior of Ti-6Al-4V alloy: Effect of initial microstructure, J. Alloys Compd. 718 (2017) 170–181. https://doi.org/10.1016/j.jallcom.2017.05.097.

[101] Takashi Choda, H. Oyama, S. Murakami, Technology for process design of titanium alloy forging, Kobelco Technol. Rev. (2015) 44–49.

[102] D.L. Moffat, D.C. Larbalestier, The competion between martensite and omega in quenched Ti-Nb alloys, Metall. Trans. A. (1988) 1677–1988.

[103] V. P.B., Effect of heat treatments on the microstructure of deformed ti-6-al-4v, Institut für Werkstoffwissenschaft und Werkstofftechnologie, Technischen Universität Wien, 2010.

[104] X. Tang, T. Ahmed, H.J. Rack, Phase transformations in Ti-Nb-Ta and Ti-Nb-Ta-Zr alloys, J. Mater. Sci. 35 (2000) 1805–1811. https://doi.org/10.1023/A:1004792922155.

[105] E. Akman, A. Demir, T. Canel, T. Sınmazçelik, Laser welding of Ti6Al4V titanium alloys, J. Mater. Process. Technol. 209 (2009) 3705–3713. https://doi.org/10.1016/j.jmatprotec.2008.08.026.

[106] M. Esmaily, S. Nooshin Mortazavi, P. Todehfalah, M. Rashidi, Microstructural characterization and formation of α′ martensite phase in Ti–6Al–4V alloy butt joints produced by friction stir and gas tungsten arc welding processes, Mater. Des. 47 (2013) 143–150. https://doi.org/10.1016/j.matdes.2012.12.024.

[107] Y.Y. Sun, P. Wang, S.L. Lu, L.Q. Li, M.L.S. Nai, J. Wei, Laser welding of electron beam melted Ti-6Al-4V to wrought Ti-6Al-4V: Effect of welding angle on microstructure and mechanical properties, J. Alloys Compd. 782 (2019) 967–972. https://doi.org/10.1016/j.jallcom.2018.12.268.

[108] S. Wang, X. Wu, Investigation on the microstructure and mechanical properties of Ti–6Al–4V alloy joints with electron beam welding, Mater. Des. 1980-2015. 36 (2012) 663–670. https://doi.org/10.1016/j.matdes.2011.11.068.

[109] Z. Zhu, K.Y. Lee, X. Wang, Ultrasonic welding of dissimilar metals, AA6061 and Ti6Al4V, Int. J. Adv. Manuf. Technol. 59 (2012) 569–574. https://doi.org/10.1007/s00170-011-3534-9.

[110] L. Zhou, H.J. Liu, Q.W. Liu, Effect of rotation speed on microstructure and mechanical properties of Ti–6Al–4V friction stir welded joints, Mater. Des. 1980-2015. 31 (2010) 2631–2636. https://doi.org/10.1016/j.matdes.2009.12.014.

[111] P. Danielson, R. Wilson, D. Alman, Microstructure of titanium welds, Adance Mater. Process. 161 (2003) 39–43.

[112] T.S. Balasubramanian, M. Balakrishnan, V. Balasubramanian, M.A.M. Manickam, Influence of welding processes on microstructure, tensile and impact properties of Ti-6Al-4V alloy joints, Trans. Nonferrous Met. Soc. China. 21 (2011) 1253–1262. https://doi.org/10.1016/S1003-6326(11)60850-9.

[113] N. Kashaev, V. Ventzke, S. Riekehr, F. Dorn, M. Horstmann, Assessment of alternative joining techniques for Ti–6Al–4V/CFRP hybrid joints regarding tensile and fatigue strength, Mater. Des. 81 (2015) 73–81. https://doi.org/10.1016/j.matdes.2015.04.051.

[114] N.Z. Borba, C.R.M. Afonso, L. Blaga, J.F. dos Santos, L.B. Canto, S.T. Amancio-Filho, On the Process-Related Rivet Microstructural Evolution, Material Flow and Mechanical Properties of

Ti-6Al-4V/GFRP Friction-Riveted Joints, Materials. 10 (2017) 184. https://doi.org/10.3390/ma10020184.

[115] N.Z. Borba, L. Blaga, J.F. dos Santos, S.T. Amancio-Filho, Direct-Friction Riveting of polymer composite laminates for aircraft applications, Mater. Lett. 215 (2018) 31–34. https://doi.org/10.1016/j.matlet.2017.12.033.

[116] J. Altmeyer, Fundamental characteristics of friction riveted multi-material joints, Doctoral Thesis, Technical University of Hamburg-TUHH, 2015.

[117] E.E. Feistauer, R.P.M. Guimarães, T. Ebel, J.F. dos Santos, S.T. Amancio-Filho, Ultrasonic joining: A novel direct-assembly technique for metal-composite hybrid structures, Mater. Lett. 170 (2016) 1–4. https://doi.org/10.1016/j.matlet.2016.01.137.

[118] A.A. Ghoneim, A.S. Mogoda, Kh. Awad, Electrochemical Studies of Titanium and its Ti-6Al-4V Alloy in Phosphoric Acid Solutions, Int. J. Electrochem. Sci. 7 (2012) 6539–6554.

[119] V.A. Alves, R.Q. Reis, I.C.B. Santos, D.G. Souza, T. de F. Gonçalves, M.A. Pereira-da-Silva, A. Rossi, L.A. da Silva, In situ impedance spectroscopy study of the electrochemical corrosion of Ti and Ti–6Al–4V in simulated body fluid at 25°C and 37°C, Corros. Sci. 51 (2009) 2473–2482. https://doi.org/10.1016/j.corsci.2009.06.035.

[120] F. Yao, J. Zheng, M. Qi, W. Wang, Z. Qi, The thermal decomposition kinetics of poly(ether-ether-ketone) (PEEK) and its carbon fiber composite, Thermochim. Acta. 183 (1991) 91–97. https://doi.org/10.1016/0040-6031(91)80448-R.

[121] P. Patel, T.R. Hull, R.W. McCabe, D. Flath, J. Grasmeder, M. Percy, Mechanism of thermal decomposition of poly(ether ether ketone) (PEEK) from a review of decomposition studies, Polym. Degrad. Stab. 95 (2010) 709–718. https://doi.org/10.1016/j.polymdegradstab.2010.01.024.

[122] A. Avanzini, G. Donzella, D. Gallina, S. Pandini, C. Petrogalli, Fatigue behavior and cyclic damage of peek short fiber reinforced composites, Compos. Part B Eng. 45 (2013) 397–406. https://doi.org/10.1016/j.compositesb.2012.06.008.

[123] A.R. McLauchlin, O.R. Ghita, L. Savage, Studies on the reprocessability of poly(ether ether ketone) (PEEK), J. Mater. Process. Technol. 214 (2014) 75–80. https://doi.org/10.1016/j.jmatprotec.2013.07.010.

[124] Y. Lee, R.S. Porter, Crystallization of poly(etheretherketone) (PEEK) in carbon fiber composites, Polym. Eng. Sci. 26 (1986) 633–639. https://doi.org/10.1002/pen.760260909.

[125] S.-L. Gao, J.-K. Kim, Cooling rate influences in carbon fibre/PEEK composites. Part II: interlaminar fracture toughness, Compos. Part Appl. Sci. Manuf. 32 (2001) 763–774. https://doi.org/10.1016/S1359-835X(00)00188-3.

[126] L. Jin, J. Ball, T. Bremner, H.-J. Sue, Crystallization behavior and morphological characterization of poly(ether ether ketone), Polymer. 55 (2014) 5255–5265. https://doi.org/10.1016/j.polymer.2014.08.045.

[127] M. Yan, X. Tian, G. Peng, D. Li, X. Zhang, High temperature rheological behavior and sintering kinetics of CF/PEEK composites during selective laser sintering, Compos. Sci. Technol. 165 (2018) 140–147. https://doi.org/10.1016/j.compscitech.2018.06.023.

[128] S.-L. Gao, J.-K. Kim, Cooling rate influences in carbon fibre/PEEK composites. Part 1. Crystallinity and interface adhesion, Compos. Part Appl. Sci. Manuf. 31 (2000) 517–530. https://doi.org/10.1016/S1359-835X(00)00009-9.

[129] V. Mylläri, T.-P. Ruoko, J. Vuorinen, H. Lemmetyinen, Characterization of thermally aged polyetheretherketone fibres – mechanical, thermal, rheological and chemical property changes, Polym. Degrad. Stab. 120 (2015) 419–426. https://doi.org/10.1016/j.polymdegradstab.2015.08.003.

[130] M. Regis, A. Bellare, T. Pascolini, P. Bracco, Characterization of thermally annealed PEEK and CFR-PEEK composites: Structure-properties relationships, Polym. Degrad. Stab. 136 (2017) 121–130. https://doi.org/10.1016/j.polymdegradstab.2016.12.005.

[131] V. Velikov, H. Marand, Studies of the enthalpy relaxation and the “multiple melting” behavior of semicrystalline poly(arylene ether ether ketone) (PEEK) | SpringerLink, J. Therm. Anal. (1997) 375–383.

[132] H. Quan, Z.-M. Li, M.-B. Yang, R. Huang, On transcrystallinity in semi-crystalline polymer composites, Compos. Sci. Technol. 65 (2005) 999–1021. https://doi.org/10.1016/j.compscitech.2004.11.015.

[133] T.Q. Li, M.Q. Zhang, H.M. Zeng, A preliminary proof of the quasi-epitaxial growth of a semicrystalline polymer in its short carbon fiber composites, J. Mater. Sci. Lett. (1999) 1861–1864.

[134] M. Zhang, J. Xu, Z. Zhang, H. Zeng, X. Xiong, Effect of transcrystallinity on tensile behaviour of discontinuous carbon fibre reinforced semicrystalline thermoplastic composites, Polymer. 37 (1996) 5151–5158. https://doi.org/10.1016/0032-3861(96)00341-2.

[135] H. Cornélis, R.G. Kander, J.P. Martin, Solvent-induced crystallization of amorphous poly(ether ether ketone) by acetone, Polymer. 37 (1996) 4573–4578. https://doi.org/10.1016/0032-3861(96)00246-7.

[136] J.L. McPeak, Solvent-Induced Crystallization of Poly(ether ether ketone), Doctoral Thesis, Virginia Tech, 1999..

[137] P. Patel, T.R. Hull, R.E. Lyon, S.I. Stoliarov, R.N. Walters, S. Crowley, N. Safronava, Investigation of the thermal decomposition and flammability of PEEK and its carbon and glass-fibre composites, Polym. Degrad. Stab. 96 (2011) 12–22. https://doi.org/10.1016/j.polymdegradstab.2010.11.009.

[138] M. Naffakh, M.A. Gómez, C. Marco, G. Ellis, Kinetic analysis of thermo-oxidative degradation of PEEK/thermotropic liquid crystalline polymer blends, Polym. Eng. Sci. 46 (2006) 129–138. https://doi.org/10.1002/pen.20439.

[139] R. Phillips, T. Glauser, J.-A.E. Månson, Thermal stability of PEEK/carbon fiber in air and its influence on consolidation, Polym. Compos. 18 (1997) 500–508. https://doi.org/10.1002/pc.10302.

[140] M. Day, D. Sally, D.M. Wiles, Thermal degradation of poly(aryl-ether-ether-ketone): Experimental evaluation of crosslinking reactions, J. Appl. Polym. Sci. 40 (1990) 1615–1625. https://doi.org/10.1002/app.1990.070400917.

[141] C. Yang, X. Tian, D. Li, Y. Cao, F. Zhao, C. Shi, Influence of thermal processing conditions in 3D printing on the crystallinity and mechanical properties of PEEK material, J. Mater. Process. Technol. 248 (2017) 1–7. https://doi.org/10.1016/j.jmatprotec.2017.04.027.

[142] E.E. Feistauer, J.F. dos Santos, S.T. Amancio-Filho, A Review on Direct Assembly of Through-the-Thickness Reinforced Metal–Polymer Composite Hybrid Structures, Polym. Eng. Sci. 0 (n.d.). https://doi.org/10.1002/pen.25022.

[143] G. Pina Cipriano, L.A. Blaga, J. F. dos Santos, P. Vilaça, S.T. Amancio-Filho, Fundamentals of Force-Controlled Friction Riveting: Part I—Joint Formation and Heat Development, Materials. 11 (2018) 2294. https://doi.org/10.3390/ma11112294.

[144] C.F. Rodrigues, L.A. Blaga, J.F. dos Santos, L.B. Canto, E. Hage, S.T. Amancio-Filho, FricRiveting of aluminum 2024-T351 and polycarbonate: Temperature evolution, microstructure and mechanical performance, J. Mater. Process. Technol. 214 (2014) 2029–2039. https://doi.org/10.1016/j.jmatprotec.2013.12.018.

[145] B. Proença, L. Blaga, L.B. Canto, J.F. Dos Santos, S.T. Amancio-Filho, Force controlled Friction Riveting of glass fiber reinforced polyamide 6 and aluminum alloy 6056 hybrid joints, in: Orlando, 2015.

[146] G. Pina Cipriano, L.A. Blaga, J.F. dos Santos, P. Vilaça, S.T. Amancio-Filho, Fundamentals of Force-Controlled Friction Riveting: Part II—Joint Global Mechanical Performance and Energy Efficiency, Materials. 11 (2018) 2489. https://doi.org/10.3390/ma11122489.

[147] S.T. Amancio-Filho, Henry Granjon Prize Competition 2009 Winner Category A: "Joining and Fabrication Technology" Friction Riveting: development and analysis of a new joining technique for polymer-metal multi-material structures, Weld. World. 55 (2011) 13–24. https://doi.org/10.1007/BF03263511.

[148] S.T. Amancio-Filho, J.F. dos Santos, Preliminary analytical modeling of heat input in Friction Riveting, in: ANTEC, Indianapolis, USA, 2016: pp. 1361–1368.

[149] N.Z. Borba, L. Blaga, J.F. Dos Santos, L.B. Canto, S. Amancio-Filho, Friction Riveting of pultruded thermoset glass fiber reinforced polyester composite and Ti6Al4V hydrid joints, in: ANTEC, Las Vegas, 2014: pp. 1768–1774.

[150] M.F. Borges, Development of new geometry of rivets for hybrid metal-composite structures joined by Friction Riveting, Master thesis, Federal University of Rio Grande do Sul, 2013.

[151] H.M. Rao, J. Kang, G. Huff, K. Avery, Impact of Specimen Configuration on Fatigue Properties of Self-Piercing Riveted Aluminum to Carbon Fiber Reinforced Polymer Composite, Int. J. Fatigue. (n.d.). https://doi.org/10.1016/j.ijfatigue.2018.03.031.

[152] R. Haque, Quality of self-piercing riveting (SPR) joints from cross-sectional perspective: A review, Arch. Civ. Mech. Eng. 18 (2018) 83–93. https://doi.org/10.1016/j.acme.2017.06.003.

[153] Y. Ma, Y. Li, W. Hu, M. Lou, Z. Lin, Modeling of Friction Self-Piercing Riveting of Aluminum to Magnesium, J. Manuf. Sci. Eng. 138 (2016) 061007-061007–9. https://doi.org/10.1115/1.4032085.

[154] S.T. Amancio-Filho, J. Roeder, S.P. Nunes, J.F. dos Santos, F. Beckmann, Thermal degradation of polyetherimide joined by friction riveting (FricRiveting). Part I: Influence of rotation speed, Polym. Degrad. Stab. 93 (2008) 1529–1538. https://doi.org/10.1016/j.polymdegradstab.2008.05.019.

[155] C.F. Rodrigues, Rebitagem por Fricção de alumínio 2024-T351 em policarbonato, Master Thesis, Federal University of São Carlos, 2014.

[156] N. Z. Borba, J.F. dos Santos, S.T. Amancio-Filho, The influence of clamping pressure on joint formation and mechanical performance of Ti6Al4V/CF-PEEK friction-riveted joint, Materials. 12 (2019) 745. https://doi.org(10.3390/ma12050745.

[157] TAPAS - Thermoplastic Affordable Primary Aircraft Structure consortium - Torsion box, (n.d.). http://www.tapasproject.nl/en/demonstrators/torsion-box (accessed January 7, 2019).

[158] G. Welsch, R. Boyer, E.W. Collings, Materials Properties Handbook: Titanium Alloys, ASM International, 1993.

[159] Toho Tenax, Teijin, Tenax®-E TPCL PEEK-HTA40 Product Data Sheet, (n.d.). http://www.tohotenax.com/pt/produtos/tenax%c2%ae-composites/tenax%c2%ae-thermoplastics/ (accessed June 20, 2017).

[160] Z. Zhang, H. Zeng, Investigation on the spherulitic morphology of poly(ether-ether-ketone), Makromol. Chem. 193 (1992) 1745–1752. https://doi.org/10.1002/macp.1992.021930718.

[161] S. Klotz, A. Lepold, F. Zanger, V. Schulze, Experimental Investigation of Clamping Systems and the Resulting Change of Cutting Conditions While Drilling Carbon Fiber Reinforced Plastics, Procedia CIRP. 62 (2017) 15–20. https://doi.org/10.1016/j.procir.2016.06.089.

[162] G.D. Lempert, A. Tsour, Reduction of static friction between surfaces of Ti-6Al-4V and between surfaces of Ti-6Al-4V and Al-7075, Surf. Coat. Technol. 52 (1992) 291–295. https://doi.org/10.1016/0257-8972(92)90029-A.

[163] D.C. Montgomery, Designed Experiments and the Generalized Linear Model, in: John Wiley & Sons, Ltd, 2012: pp. 408–463. https://doi.org/10.1002/9780470556986.ch8.

[164] S. Maksimović, Some computational and experimental aspects of optimal design process of composite structures, Compos. Struct. 16 (1990) 237–258. https://doi.org/10.1016/0263-8223(90)90074-O.

[165] E.D. Eneyew, M. Ramulu, Experimental study of surface quality and damage when drilling unidirectional CFRP composites, J. Mater. Res. Technol. 3 (2014) 354–362. https://doi.org/10.1016/j.jmrt.2014.10.003.

[166] N.R. Costa, J. Lourenço, Z.L. Pereira, Desirability function approach: A review and performance evaluation in adverse conditions, Chemom. Intell. Lab. Syst. 107 (2011) 234–244. https://doi.org/10.1016/j.chemolab.2011.04.004.

[167] D.-H. Lee, I.-J. Jeong, K.-J. Kim, A desirability function method for optimizing mean and variability of multiple responses using a posterior preference articulation approach, Qual. Reliab. Eng. Int. 34 (2018) 360–376. https://doi.org/10.1002/qre.2258.

[168] N.M. Chowdhury, J. Wang, W.K. Chiu, P. Chang, Static and fatigue testing bolted, bonded and hybrid step lap joints of thick carbon fibre/epoxy laminates used on aircraft structures, Compos. Struct. 142 (2016) 96–106. https://doi.org/10.1016/j.compstruct.2016.01.078.

[169] G. Kelly, Quasi-static strength and fatigue life of hybrid (bonded/bolted) composite single-lap joints, Compos. Struct. 72 (2006) 119–129. https://doi.org/10.1016/j.compstruct.2004.11.002.

[170] K. Bodjona, L. Lessard, Hybrid bonded-fastened joints and their application in composite structures: A general review, J. Reinf. Plast. Compos. 35 (2016) 764–781. https://doi.org/10.1177/0731684415627296.

[171] C.N. Velisaris, J.C. Seferis, Crystallization kinetics of polyetheretherketone (peek) matrices, Polym. Eng. Sci. 26 (1986) 1574–1581. https://doi.org/10.1002/pen.760262208.

[172] D.C. Bassett, R.H. Olley, I.A.M. Al Raheil, On crystallization phenomena in PEEK, Polymer. 29 (1988) 1745–1754. https://doi.org/10.1016/0032-3861(88)90386-2.

[173] ASTM International, ASTM E384-17, Test Method for Microindentation Hardness of Materials, West Conshohocken, PA, 2017. https://doi.org/10.1520/E0384-17.

[174] R.F. Gibson, A review of recent research on nanoindentation of polymer composites and their constituents, Compos. Sci. Technol. 105 (2014) 51–65. https://doi.org/10.1016/j.compscitech.2014.09.016.

[175] A.M. Díez-Pascual, M.A. Gómez-Fatou, F. Ania, A. Flores, Nanoindentation in polymer nanocomposites, Prog. Mater. Sci. 67 (2015) 1–94. https://doi.org/10.1016/j.pmatsci.2014.06.002.

[176] ASTM International, ASTM D5961, Standard Test Method for Bearing Response of Polymer Matrix Composite Laminates, West Conshohocken, PA, 2017.

[177] DIN - German Institute for Standardization, DIN 50100:2016-12, Standard Load controlled fatigue testing - Execution and evaluation of cyclic tests at constant load amplitudes on metallic specimens and components, 2016.

[178] M.H. Dirikolu, A. Aktaş, B. Birgoren, Statistical analysis of fracture strength of composite materials using Weibull distribution, Turk. J. Eng. Environ. Sci. 26 (2002) 45–48.

[179] K. Naresh, K. Shankar, R. Velmurugan, N.K. Gupta, Statistical analysis of the tensile strength of GFRP, CFRP and hybrid composites, Thin-Walled Struct. 126 (2018) 150–161. https://doi.org/10.1016/j.tws.2016.12.021.

[180] H. Jiang, T. Luo, G. Li, X. Zhang, J. Cui, Fatigue life assessment of electromagnetic riveted carbon fiber reinforce plastic/aluminum alloy lap joints using Weibull distribution, Int. J. Fatigue. 105 (2017) 180–189. https://doi.org/10.1016/j.ijfatigue.2017.08.026.

[181] ASTM International, ASTM D7136 / D7136M-15, Standard Test Method for Measuring the Damage Resistance of a Fiber-Reinforced Polymer Matrix Composite to a Drop-Weight Impact Event, West Conshohocken, PA, 2015. https://doi.org/10.1520/D7136_D7136M-15.

[182] H. Dhieb, J.G. Buijnsters, K. Elleuch, J.P. Celis, Effect of relative humidity and full immersion in water on friction, wear and debonding of unidirectional carbon fiber reinforced epoxy under reciprocating sliding, Compos. Part B Eng. 88 (2016) 240–252. https://doi.org/10.1016/j.compositesb.2015.11.011.

[183] N.R. Council, Aging of U.S. Air Force Aircraft: Final Report, 1969. https://doi.org/10.17226/5917.

[184] ASTM International, ASTM D3762-03 (2010), Standard Test Method for Adhesive-Bonded Surface Durability of Aluminum (Wedge Test), West Conshohocken, PA, 2010. https://doi.org/10.1520/D3762-03R10.

[185] R. Selzer, K. Friedrich, Inluence of water up-take on interlaminar fracture properties of carbon fibre-reinforced polymer composites, J. Mater. Sci. 30 (1995) 334–338. https://doi.org/10.1007/BF00354392.

[186] ASTM International, ASTM B117-18, Standard Practice for Operating Salt Spray (FOG) Apparatus, West Conshohocken, PA, 2011.

[187] V. Fiore, L. Calabrese, E. Proverbio, R. Passari, A. Valenza, Salt spray fog ageing of hybrid composite/metal rivet joints for automotive applications, Compos. Part B Eng. 108 (2017) 65–74. https://doi.org/10.1016/j.compositesb.2016.09.096.

[188] X. Qing, H.-T. Sun, L. Dagba, F.-K. Chang, Damage-Tolerance-Based Design of Bolted Composite Joints, Compos. Struct. Theory Pract. (2001). https://doi.org/10.1520/STP14513S.

[189] C. Cooper, G.J. Turvey, Effects of joint geometry and bolt torque on the structural performance of single bolt tension joints in pultruded GRP sheet material, Compos. Struct. 32 (1995) 217–226. https://doi.org/10.1016/0263-8223(95)00071-2.

[190] J. Li, K. Zhang, Y. Li, P. Liu, J. Xia, Influence of interference-fit size on bearing fatigue response of single-lap carbon fiber reinforced polymer/Ti alloy bolted joints, Tribol. Int. 93 (2016) 151–162. https://doi.org/10.1016/j.triboint.2015.08.044.

[191] J. Xu, M. El Mansori, Cutting Modeling of Hybrid CFRP/Ti Composite with Induced Damage Analysis, Materials. 9 (2016). https://doi.org/10.3390/ma9010022.

[192] Z. Hashin, A. Rotem, A Fatigue Failure Criterion for Fiber Reinforced Materials, J. Compos. Mater. 7 (1973) 448–464. https://doi.org/10.1177/002199837300700404.

[193] G.E. Mostovoi, L.P. Kobets, V.I. Frolov, Study of the thermal stability of the mechanical properties of carbon fibers, Mech. Compos. Mater. 15 (1979) 20–25. https://doi.org/10.1007/BF00604952.

[194] H.H. Winter, Viscous Dissipation in Shear Flows of Molten Polymers, in: J.P. Hartnett, T.F. Irvine (Eds.), Adv. Heat Transf., Elsevier, 1977: pp. 205–267. https://doi.org/10.1016/S0065-2717(08)70224-7.

[195] A. Deignan, Ł. Figiel, M.A. McCarthy, Insights into complex rheological behaviour of carbon fibre/PEEK from a novel numerical methodology incorporating fibre friction and melt viscosity, Compos. Struct. 189 (2018) 614–626. https://doi.org/10.1016/j.compstruct.2018.01.084.

[196] C.-F. Tu, T. Fort, A study of fiber–capstan friction. 1. Stribeck curves, Tribol. Int. 37 (2004) 701–710. https://doi.org/10.1016/j.triboint.2004.02.008.

[197] J.S. Jha, A. Tewari, S. Mishra, S. Toppo, Constitutive Relations for Ti-6Al-4V Hot Working, Procedia Eng. 173 (2017) 755–762. https://doi.org/10.1016/j.proeng.2016.12.089.

[198] W. Yuan, R.S. Mishra, B. Carlson, R. Verma, R.K. Mishra, Material flow and microstructural evolution during friction stir spot welding of AZ31 magnesium alloy, Mater. Sci. Eng. A. 543 (2012) 200–209. https://doi.org/10.1016/j.msea.2012.02.075.

[199] J. Schneider, R. Beshears, A.C. Nunes, Interfacial sticking and slipping in the friction stir welding process, Mater. Sci. Eng. A. 435–436 (2006) 297–304. https://doi.org/10.1016/j.msea.2006.07.082.

[200] I. Dobovšek, Some Aspects of Shear Yielding and Emergence of Shear Bands in Solid Polymers, Acta Phys. Pol. A. 128 (2015) 619–623. https://doi.org/10.12693/APhysPolA.128.619.

[201] S. Acharya, A.K. Mukhopadhyay, High strain rate compressive behavior of PMMA, Polym. Bull. 71 (2014) 133–149. https://doi.org/10.1007/s00289-013-1050-9.

[202] F. Chen, H. Ou, B. Lu, H. Long, A constitutive model of polyether-ether-ketone (PEEK), J. Mech. Behav. Biomed. Mater. 53 (2016) 427–433. https://doi.org/10.1016/j.jmbbm.2015.08.037.

[203] Z. El-Qoubaa, R. Othman, Characterization and modeling of the strain rate sensitivity of polyetheretherketone's compressive yield stress, Mater. Des. 1980-2015. 66 (2015) 336–345. https://doi.org/10.1016/j.matdes.2014.10.080.

[204] T. Choda, H. Oyama, S. Murakami, Technologies for Process Design of Titanium Alloy Forging for Aircraft Parts Titanium, Kobelco Technology Review 33 (2015)..

[205] R. Ding, Z.X. Guo, A. Wilson, Microstructural evolution of a Ti–6Al–4V alloy during thermomechanical processing, Mater. Sci. Eng. A. 327 (2002) 233–245. https://doi.org/10.1016/S0921-5093(01)01531-3.

[206] S. Mironov, Y.S. Sato, H. Kokawa, Friction-stir welding and processing of Ti-6Al-4V titanium alloy: A review, J. Mater. Sci. Technol. 34 (2018) 58–72. https://doi.org/10.1016/j.jmst.2017.10.018.

[207] M. Reimann, J. Goebel, J.F. dos Santos, Microstructure and mechanical properties of keyhole repair welds in AA 7075-T651 using refill friction stir spot welding, Mater. Des. 132 (2017) 283–294. https://doi.org/10.1016/j.matdes.2017.07.013.

[208] S.M. Goushegir, J.F. dos Santos, S.T. Amancio-Filho, Influence of process parameters on mechanical performance and bonding area of AA2024/carbon-fiber-reinforced poly(phenylene sulfide) friction spot single lap joints, Mater. Des. 83 (2015) 431–442. https://doi.org/10.1016/j.matdes.2015.06.044.

[209] G. da C. Vasconcelos, R.L. Mazur, B. Ribeiro, E.C. Botelho, M.L. Costa, Evaluation of decomposition kinetics of poly (ether-ether-ketone) by thermogravimetric analysis, Mater. Res. 17 (2014) 227–235. https://doi.org/10.1590/S1516-14392013005000202.

[210] L.H. Perng, Thermal cracking characteristics of PEEK under different environments by the TG/FTIR technique, J. Polym. Sci. Part Polym. Chem. 37 (1999) 4582–4590. https://doi.org/10.1002/(SICI)1099-0518(19991215)37:24<4582::AID-POLA15>3.0.CO;2-Q.

[211] M. Day, T. Suprunchuk, J.D. Cooney, D.M. Wiles, Thermal degradation of poly(aryl-ether–ether-ketone) (PEEK): A differential scanning calorimetry study, J. Appl. Polym. Sci. 36 (1988) 1097–1106. https://doi.org/10.1002/app.1988.070360510.

[212] B. Nazari, A.M. Rhoades, R.P. Schaake, R.H. Colby, Flow-Induced Crystallization of PEEK: Isothermal Crystallization Kinetics and Lifetime of Flow-Induced Precursors during Isothermal Annealing, ACS Macro Lett. 5 (2016) 849–853. https://doi.org/10.1021/acsmacrolett.6b00326.

[213] T. Bayerl, M. Brzeski, M. Martínez-Tafalla, R. Schledjewski, P. Mitschang, Thermal degradation analysis of short-time heated polymers, J. Thermoplast. Compos. Mater. 28 (2015) 390–414. https://doi.org/10.1177/0892705713486122.

[214] S.M. Tamboli, S.T. Mhaske, D.D. Kale, Crosslinked polyethylene, IJCT Vol116 Novemb. 2004. (2004). http://nopr.niscair.res.in/handle/123456789/9558 (accessed December 17, 2018).

[215] M. Ramulu, K. Gangwar, A. Cantrell, P. Laxminarayana, Study of Microstructural Characteristics and Mechanical Properties of Friction Stir Welded Three Titanium Alloys, Mater. Today Proc. 5 (2018) 1082–1092. https://doi.org/10.1016/j.matpr.2017.11.186.

[216] T. Iqbal, B.J. Briscoe, S. Yasin, P.F. Luckham, Nanoindentation response of poly(ether ether ketone) surfaces—A semicrystalline bimodal behavior, J. Appl. Polym. Sci. 130 (2013) 4401–4409. https://doi.org/10.1002/app.39723.

[217] K.W. Allen, Some reflections on contemporary views of theories of adhesion, Int. J. Adhes. Adhes. 13 (1993) 67–72. https://doi.org/10.1016/0143-7496(93)90015-2.

[218] S. Ebnesajjad, ed., Chapter 1 - Introduction and Adhesion Theories, in: Adhes. Technol. Handb. Second Ed., William Andrew Publishing, Norwich, NY, 2009: pp. 1–19. https://doi.org/10.1016/B978-0-8155-1533-3.50004-9.

[219] A.C. Akué Asséko, B. Cosson, É. Lafranche, F. Schmidt, Y. Le Maoult, Effect of the developed temperature field on the molecular interdiffusion at the interface in infrared welding of polycarbonate composites, Compos. Part B Eng. 97 (2016) 53–61. https://doi.org/10.1016/j.compositesb.2016.04.064.

[220] I.K. Giannopoulos, D. Doroni-Dawes, K.I. Kourousis, M. Yasaee, Effects of bolt torque tightening on the strength and fatigue life of airframe FRP laminate bolted joints, Compos. Part B Eng. 125 (2017) 19–26. https://doi.org/10.1016/j.compositesb.2017.05.059.

[221] S. Heimbs, S. Schmeer, J. Blaurock, S. Steeger, Static and dynamic failure behaviour of bolted joints in carbon fibre composites, Compos. Part Appl. Sci. Manuf. 47 (2013) 91–101. https://doi.org/10.1016/j.compositesa.2012.12.003.

[222] B. Egan, C.T. McCarthy, M.A. McCarthy, P.J. Gray, R.M. O'Higgins, Static and high-rate loading of single and multi-bolt carbon–epoxy aircraft fuselage joints, Compos. Part Appl. Sci. Manuf. 53 (2013) 97–108. https://doi.org/10.1016/j.compositesa.2013.05.006.

[223] A. Skorupa, M. Skorupa, Secondary Bending for Mechanically Fastened Joints with Eccentricities, in: Riveted Lap Jt. Aircr. Fuselage, Springer, Dordrecht, 2012: pp. 145–184. https://doi.org/10.1007/978-94-007-4282-6_6.

[224] J.L. Merino-Pérez, R. Royer, E. Merson, A. Lockwood, S. Ayvar-Soberanis, M.B. Marshall, Influence of workpiece constituents and cutting speed on the cutting forces developed in the conventional drilling of CFRP composites, Compos. Struct. 140 (2016) 621–629. https://doi.org/10.1016/j.compstruct.2016.01.008.

[225] H.S. B. Schmidt-Brandecker, Fatigue & Damage Tolerance, (2017).

[226] X.F. Hu, A. Haris, M. Ridha, V.B.C. Tan, T.E. Tay, Progressive failure of bolted single-lap joints of woven fibre-reinforced composites, Compos. Struct. 189 (2018) 443–454. https://doi.org/10.1016/j.compstruct.2018.01.104.

[227] M.C.-Y. Niu, Airframe Structural Design: Practical Design Information and Data on Aircraft Structures, Hong Kong Conmilit Press LTD., 1988.

[228] F. Nerilli, G. Vairo, Progressive damage in composite bolted joints via a computational micromechanical approach, Compos. Part B Eng. 111 (2017) 357–371. https://doi.org/10.1016/j.compositesb.2016.11.056.

[229] L.V. Awadhani, A. Bewoor, Parametric study of composite bolted joint under compressive loading, Procedia Manuf. 22 (2018) 186–195. https://doi.org/10.1016/j.promfg.2018.03.029.

[230] Determining the fatigue life of composite aircraft structures using life and Load-enhancement factores - Report, (2011).

[231] M. Mariam, M. Afendi, M.S. Abdul Majid, M.J.M. Ridzuan, A.G. Gibson, Tensile and fatigue properties of single lap joints of aluminium alloy/glass fibre reinforced composites fabricated with different joining methods, Compos. Struct. 200 (2018) 647–658. https://doi.org/10.1016/j.compstruct.2018.06.003.

[232] M.A. McCarthy, V.P. Lawlor, W.F. Stanley, An Experimental Study of Bolt-Hole Clearance Effects in Single-lap, Multibolt Composite Joints, An Experimental Study of Bolt-Hole Clearance Effects in Single-lap, Multibolt Composite Joints, J. Compos. Mater. 39 (2005) 799–825. https://doi.org/10.1177/0021998305048157.

[233] H.A. Whitworth, A stiffness degradation model for composite laminates under fatigue loading, Compos. Struct. 40 (1997) 95–101. https://doi.org/10.1016/S0263-8223(97)00142-6.

[234] A. Plumtree, L. Shi, Fatigue damage evolution in off-axis unidirectional CFRP, Int. J. Fatigue. 24 (2002) 155–159. https://doi.org/10.1016/S0142-1123(01)00068-8.

[235] M.N. Ghaseminejhad, A. Parvizi-Majidi, Impact behaviour and damage tolerance of woven carbon fibre-reinforced thermoplastic composites, Constr. Build. Mater. 4 (1990) 194–207. https://doi.org/10.1016/0950-0618(90)90040-8.

[236] M.N. Ghasemi Nejhad, A. Parvizi-Majidi, Impact behaviour and damage tolerance of woven carbon fibre-reinforced thermoplastic composites, Composites. 21 (1990) 155–168. https://doi.org/10.1016/0010-4361(90)90008-K.

[237] B. Vieille, V.M. Casado, C. Bouvet, About the impact behavior of woven-ply carbon fiber-reinforced thermoplastic- and thermosetting-composites: A comparative study, Compos. Struct. 101 (2013) 9–21. https://doi.org/10.1016/j.compstruct.2013.01.025.

[238] G. Minak, Z. Šoški, Characterization of Impact Behavior of Composite Car Components, (2011).

[239] R. Bogenfeld, J. Kreikemeier, T. Wille, Review and benchmark study on the analysis of low-velocity impact on composite laminates, Eng. Fail. Anal. 86 (2018) 72–99. https://doi.org/10.1016/j.engfailanal.2017.12.019.

[240] European Aviation Safety Agency - EASA, Certification Specifications for Large Aeroplanes (CS-25), (n.d.) 617.

[241] S. Mustapha, L. Ye, X. Dong, M.M. Alamdari, Evaluation of barely visible indentation damage (BVID) in CF/EP sandwich composites using guided wave signals, Mech. Syst. Signal Process. 76–77 (2016) 497–517. https://doi.org/10.1016/j.ymssp.2016.01.023.

[242] A. Singh, B. Davidson, D. Eisenberg, M. Czabaj, A. Zehnder, Barely Visible Impact Damage Evaluation of Composite Sandwich Structures, in: 51st AIAAASMEASCEAHSASC Struct. Struct. Dyn. Mater. Conf., American Institute of Aeronautics and Astronautics, 2010. https://doi.org/10.2514/6.2010-2770.

[243] N.Z. Borba, B. Kötter, B. Fiedler, J.F. Dos Santos, S.T. Amancio-Filho, Mechanical integrity of friction-riveted joints for aircraft applications, Submitt. Compos. Struct. (2019).

[244] J.A. Harris, R.D. Adams, An Assessment of the Impact Performance of Bonded Joints for Use in High Energy Absorbing Structures, Proc. Inst. Mech. Eng. Part C J. Mech. Eng. Sci. 199 (1985) 121–131. https://doi.org/10.1243/PIME_PROC_1985_199_102_02.

[245] J. Machado, E. Marques, L. da Silva, Mechanical behaviour of adhesively bonded composite single lap joints under quasi-static and impact conditions with variation of temperature and overlap, J. Compos. Mater. 52 (2018) 3621–3635. https://doi.org/10.1177/0021998318766641.

[246] Damage in laminates from low-velocity impacts, Dyn. Deform. Damage Fract. Compos. Mater. Struct. (2016) 35–69. https://doi.org/10.1016/B978-0-08-100080-9.00003-8.

[247] L.G. Melin, J. Schön, T. Nyman, Fatigue testing and buckling characteristics of impacted composite specimens, Int. J. Fatigue. 24 (2002) 263–272. https://doi.org/10.1016/S0142-1123(01)00081-0.

[248] Investigation on impact damage evolution under fatigue load and shear-after-impact-fatigue (SAIF) behaviors of stiffened composite panels, Int. J. Fatigue. 100 (2017) 308–321. https://doi.org/10.1016/j.ijfatigue.2017.03.046.

[249] A. VanderKlok, A. Dutta, S.A. Tekalur, Metal to composite bolted joint behavior evaluated at impact rates of loading, Compos. Struct. 106 (2013) 446–452. https://doi.org/10.1016/j.compstruct.2013.06.004.

[250] N.A. Shahkhosravi, J. Yousefi, M.A. Najafabadi, C. Burvill, G. Minak, Fatigue life reduction of GFRP composites due to delamination associated with the introduction of functional discontinuities, Compos. Part B Eng. (2019). https://doi.org/10.1016/j.compositesb.2019.01.005.

[251] M.F. Borges, S.T. Amancio-Filho, J.F. dos Santos, T.R. Strohaecker, J.A.E. Mazzaferro, Development of computational models to predict the mechanical behavior of Friction Riveting joints, Comput. Mater. Sci. 54 (2012) 7–15. https://doi.org/10.1016/j.commatsci.2011.10.031.

[252] A. Szewczyk-Nykiel, J. Kazior, Effect of Aging Temperature on Corrosion Behavior of Sintered 17-4 PH Stainless Steel in Dilute Sulfuric Acid Solution, J. Mater. Eng. Perform. 26 (2017) 3450–3456. https://doi.org/10.1007/s11665-017-2778-4.

[253] DJ. Mandrino, M. Godec, A. Kocijan, M. Lamut, M. Torkar, M. Jenko, Oxide and nitride protective layers formed on stainless steel by thermal treatment: SEM, AES, WDS and corrosion measurements, Metalurgija. 47 (2008) 119–123.

[254] H. Hooshyar, High Temperature Corrosion of Stainless Steels in Low Oxygen Activity Environments, PhD. thesis, Chalmers University of Technology, 2016. ISBN 978-91-7597-329-6.

[255] A. Sandoval-Amador, J.E. Torres-Ramirez, D.Y. Vargas-Castro, J.R. Caceres-Nuñez, H.A. Estupiñan-Duran, D.Y. Peña-Ballesteros, Electrochemical Behavior of stainless steel AISI 430 exposed to simulated food, Matér. Rio Jan. 23 (2018). https://doi.org/10.1590/s1517-707620170001.0295.

[256] Z. Peng, X. Nie, Galvanic corrosion property of contacts between carbon fiber cloth materials and typical metal alloys in an aggressive environment, Surf. Coat. Technol. 215 (2013) 85–89. https://doi.org/10.1016/j.surfcoat.2012.08.098.

[257] A. Gebhard, T. Bayerl, A.K. Schlarb, K. Friedrich, Galvanic corrosion of polyacrylnitrile (PAN) and pitch based short carbon fibres in polyetheretherketone (PEEK) composites, Corros. Sci. 51 (2009) 2524–2528. https://doi.org/10.1016/j.corsci.2009.05.051.

[258] C.-C.M. Ma, S.-W. Yur, Environmental Effect on the Water Absorption and Mechanical Properties of Carbon Fiber Reinforced PPS and PEEK Composites, J. Thermoplast. Compos. Mater. 2 (1989) 281–292. https://doi.org/10.1177/089270578900200403.

[259] O.A. Hasan, M.C. Boyce, X.S. Li, S. Berko, An investigation of the yield and postyield behavior and corresponding structure of poly(methyl methacrylate), J. Polym. Sci. Part B Polym. Phys. 31 (1993) 185–197. https://doi.org/10.1002/polb.1993.090310207.

[260] N.C.W. Judd, Absorption of water into carbon fibre composites, Br. Polym. J. 9 (1977) 36–40. https://doi.org/10.1002/pi.4980090106.

[261] B. Vieille, W. Albouy, L. Taleb, Investigations on stamping of C/PEEK laminates: Influence on meso-structure and macroscopic mechanical properties under severe environmental conditions, Compos. Part B Eng. 63 (2014) 101–110. https://doi.org/10.1016/j.compositesb.2014.03.025.

[262] G.Z. Voyiadjis, A. Samadi-Dooki, L. Malekmotiei, Nanoindentation of high performance semicrystalline polymers: A case study on PEEK, Polym. Test. 61 (2017) 57–64. https://doi.org/10.1016/j.polymertesting.2017.05.005.

[263] M.H. Theil, The crystallization of tough thermoplastic resins in the presence of carbon fibers, 1988. https://ntrs.nasa.gov/search.jsp?R=19880017080 (accessed January 10, 2019).

[264] D.W. Shoesmith, J.J. Noël, V.E. Annamalai, Corrosion of Titanium and Its Alloys, in: Ref. Module Mater. Sci. Mater. Eng., Elsevier, 2016. https://doi.org/10.1016/B978-0-12-803581-8.01637-4.

[265] M.R. Bache, W.J. Evans, The fatigue crack propagation resistance of Ti–6Al–4V under aqueous saline environments, Int. J. Fatigue. 23 (2001) 319–323. https://doi.org/10.1016/S0142-1123(01)00141-4.

[266] P.R. Stone, J.A. Nairn, Interfacial toughness and its effect on compression strength in polycarbonate/carbon fiber composites, Polym. Compos. 15 (1994) 197–205. https://doi.org/10.1002/pc.750150305.

[267] L. Vaisman, M. Fernanda González, G. Marom, Transcrystallinity in brominated UHMWPE fiber reinforced HDPE composites: morphology and dielectric properties, Polymer. 44 (2003) 1229–1235. https://doi.org/10.1016/S0032-3861(02)00848-0.

[268] H.-J. Kestenbach, J. Loos, J. Petermann, Transcrystallization at the interface of polyethylene single-polymer composites, Mater. Res. 2 (1999) 261–269. https://doi.org/10.1590/S1516-14391999000400005.

[269] Z. Ai, W. Sun, J. Jiang, D. Song, H. Ma, J. Zhang, D. Wang, Passivation Characteristics of Alloy Corrosion-Resistant Steel Cr10Mo1 in Simulating Concrete Pore Solutions: Combination Effects of pH and Chloride, Materials. 9 (2016) 749. https://doi.org/10.3390/ma9090749.

[270] A. Bautista, G. Blanco, F. Velasco, A. Gutiérrez, L. Soriano, F.J. Palomares, H. Takenouti, Changes in the passive layer of corrugated austenitic stainless steel of low nickel content due to exposure to simulated pore solutions, Corros. Sci. 51 (2009) 785–792. https://doi.org/10.1016/j.corsci.2009.01.012.

[271] M. Boniardi, A. Casaroli, Stainless steels. Gruppo Lucefin Research & Development - PDF, Lucefin S.p.A., Dipartimento di Meccanica, Politecnico di Milano, Italy, 2014. https://docplayer.net/27910676-Marco-boniardi-e-andrea-casaroli-stainless-steels-gruppo-lucefin-research-development.html (accessed January 10, 2019).

[272] J.-I. Choi, S.M. Hasheminia, H.-J. Chun, J.-C. Park, H.S. Chang, Failure load prediction of composite bolted joint with clamping force, Compos. Struct. 189 (2018) 247–255. https://doi.org/10.1016/j.compstruct.2018.01.037.

[273] Rotationsreibschweißen Roboter| Anwendungen | Kawasaki Robotics, (n.d.). https://robotics.kawasaki.com/de1/applications/friction-spot-joining/index.html (accessed November 3, 2019).

[274] Reibschweißsysteme: harms-wende, (n.d.). https://www.harms-wende.de/produkte/reibschweisssysteme/ (accessed November 3, 2019).

[275] N. Perogamvros, G. Lampeas, Experimental investigation of composite lockbolt fastened joints under in-plane low velocity impact, Compos. Part Appl. Sci. Manuf. 90 (2016) 510–521. https://doi.org/10.1016/j.compositesa.2016.08.010.

[276] M. Elia, Report: Drop weight impact test 3-stringer panel WI-18-0144 Issue date, (2018).

[277] J. Jang, H. Kim, Improvement of carbon fiber/PEEK hybrid fabric composites using plasma treatment, Polym. Compos. 18 (1997) 125–132. https://doi.org/10.1002/pc.10267.

List of Figures

List of Tables

Appendix A. Demonstrator of Direct FricRiveting for aircraft structure

A section of a horizontal stabilizer torsion box panel made of carbon fiber polyether-ketone-ketone (CF-PEKK) was used to manufacture for the first time a Direct FricRiveting demonstrator for aircraft application. The panel consists of a co-consolidated stiffened skin with multiple I-stringer in butt-joint configuration, manufactured by Fokker Aerostructure B.V, within the scope of TAPAS project (Thermoplastic Affordable Primary Aircraft Structures) (Figure A.1-a). According to Ochoa, roves, and Benedictus [14], the stringer run-out (see Figure A.1-b) is current joined using countersunk blind rivets (EN128C06) to avoid out-of-plane stresses upon impact damage events.

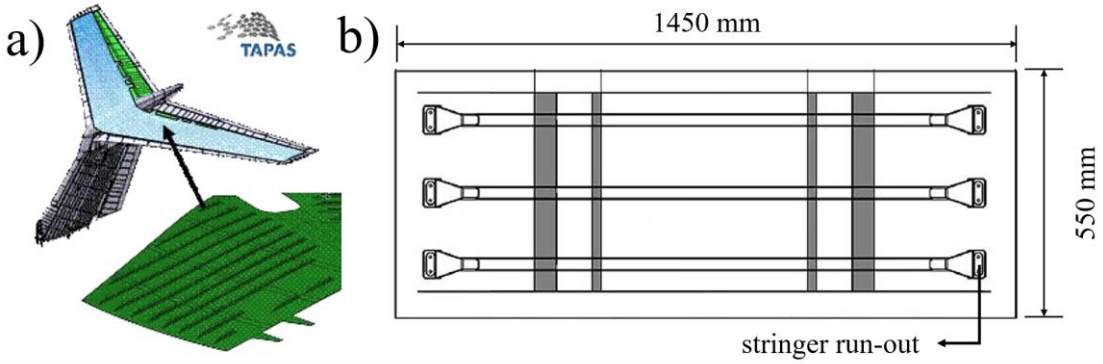

Figure A.1. Schematic illustration of the a) thermoplastic horizontal stabilizer panel conceived during TAPAS 2 project (permission from GKN Fokker) [157] and b) section of the panel used in this work and granted by Fokker (thickness of the stringer run-out region – 8.3 mm).

A section of the panel with three stringers (Figure A.1-b and Figure A.2-a) was granted by Fokker throughout a cooperation with HZG to access the feasibility of Direct FricRiveting on replacing the conventional riveting. The dimensions of the component are shown in Figure A.1-b. Additionally, preliminary investigation on the impact behavior of the friction riveted panel was proposed. Therefore, two Ti6Al4V rivets of 5 mm diameters were used in each stringer run-out, as shown in Figure A.2-b. The optimized joining condition for Ti6Al4V rivets and CF-PEEK overlapped plates (RS: 15000 rpm, FF_I: 5 kN, FF_{II}: 10 kN, DF: 7.5 mm, CP: 0.2 MPa) obtained in this work through DoE and presented in Section 6.5.2 was adopted to join the panel. The demonstrator was successfully manufactured, as shown in Figure A.2-b.

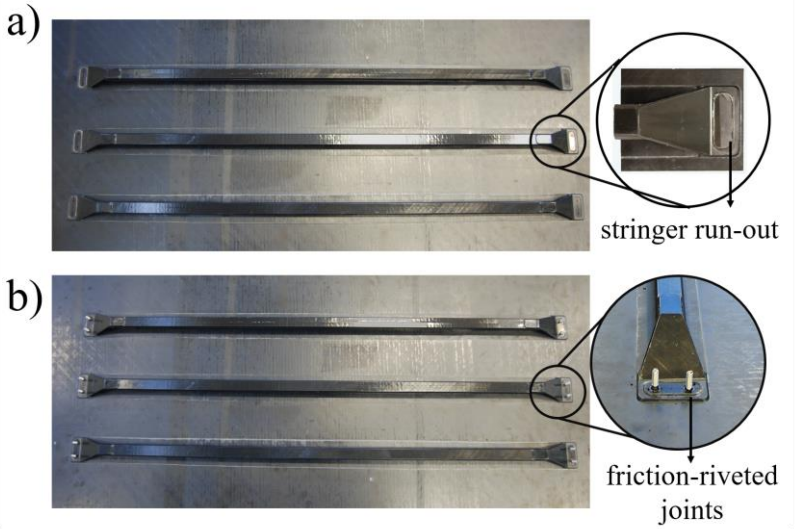

Figure A.2. Co-consolidated stiffened skin, showing the stringer run-out region a) before and b) after joining.

Exploratory investigation of the friction riveted panel behavior upon multiple impact tests was performed in Fokker facilities as a subtopic of the internship of the bachelor student Matteo Elia from Hogeschool van Arhem en Nijmegen (HAN), Holland. The main results are classified and were internally reported by Fokker in [276]. The panel was impacted with impact energies of 50 J and 100 J in multiple impact events in the locations highlighted by stars in Figure A.3. Up to four impact events the majority of the damages were classified within the BVID category, while after five consecutive impact events on the same spot, delamination could be detected. The main conclusion of the exploratory work was the potential to apply FricRiveting in aircraft components where the peeling stresses are critical, once the anchoring efficiency provided by the plastically deformed rivet tip and adhesion between composite and rivet enhance the out-of-plane resistance of the structure.

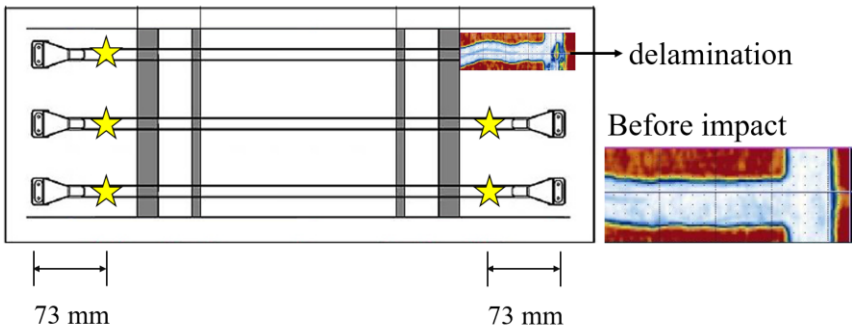

Figure A.3. Schematic illustration of the panel, highlighting the sites of the impact events and overlaid with a non-destructive ultrasonic guided wave diagram where delamination was detected after multiple impact events under 50 J and 100 J (Adapted from [276])

Appendix B. Design of experiments

The number of experiments required for 2^3 full-factorial is define by Equation B.1.

$$N = n2^k \quad \text{(B.1)}$$

where n is the number of replicates of each experiment. In this work, three replicates were produced for the experiments and five for the center point, which total 29 runs (Table B.1).

Table B.1. Matrix of experiments of 2^3 full-factorial design with center point

	Factors			**Normalized factors**			**Responses**	
Experiments	**RS_{II} [rpm]**	**FF_{II} [kN]**	**CP [MPa]**	**RS_{II}**	**FF_{II}**	**CP**	**ULSF [kN]**	**VR [a.u.]**
1	10000	10	2	-	-	-	4.42	0.19
2	15000	10	2	+	-	-	7.01	0.21
3	10000	15	2	-	+	-	4.24	0.36
4	15000	15	2	+	+	-	5.19	0.34
5	10000	10	6	-	-	+	2.56	0.11
6	15000	10	6	+	-	+	6.59	0.23
7	10000	15	6	-	+	+	5.54	0.38
8	15000	15	6	+	+	+	3.73	0.30
9	10000	10	2	-	-	-	4.54	0.25
10	15000	10	2	+	-	-	6.69	0.33
11	10000	15	2	-	+	-	5.42	0.32
12	15000	15	2	+	+	-	6.66	0.41
13	10000	10	6	-	-	+	3.11	0.10

14	15000	10	6	+	-	+	5.12	0.24
15	10000	15	6	-	+	+	6.06	0.27
16	15000	15	6	+	+	+	4.43	0.34
17	10000	10	2	-	-	-	4.68	0.19
18	15000	10	2	+	-	-	6.44	0.35
19	10000	15	2	-	+	-	5.07	0.36
20	15000	15	2	+	+	-	5.13	0.38
21	10000	10	6	-	-	+	2.55	0.05
22	15000	15	6	+	+	+	6.41	0.10
23	10000	15	6	-	+	+	5.78	0.28
24	15000	15	6	+	+	+	3.55	0.35
25	12500	12.5	4	0	0	0	6.00	0.32
26	12500	12.5	4	0	0	0	5.70	0.32
27	12500	12.5	4	0	0	0	5.46	0.26
28	12500	12.5	4	0	0	0	5.30	0.28
29	12500	12.5	4	0	0	0	5.85	0.30

The response *Y* (ULSF or VR) is estimated from a linear model (Equation B.2), where β_0 is the intercept, β_{1-3} are linear regression coefficients, $\beta_{12}, \beta_{13}, \beta_{23}, \beta_{123}$ are the interactive regression coefficient of one degree of freedom.

$$Y = \beta_0 + \beta_1 x_1 + \beta_2 x_2 + \beta_3 x_3 + \beta_{12} x_1 x_2 + \beta_{13} x_1 x_3 + \beta_{23} x_2 x_3 + \beta_{123} x_1 x_2 x_3 + \epsilon \quad \text{(B.2)}$$

Appendix C. Finite element analysis of lap shear test

Figure C. 1 shows the joint parts and the mesh elements used to simulate the stress fields over a single lap shear test of friction riveted joints.

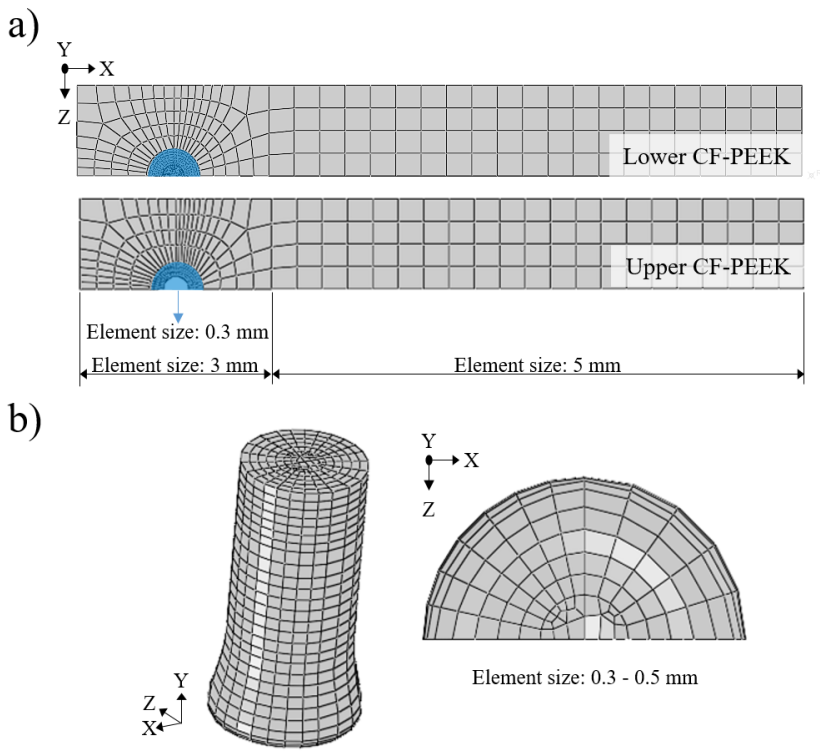

Figure C. 1 a) Half-top view of the lower and upper CF-PEEK geometries, showing the quadrilateral continuum shell element (SC8R) and its refinement used to mesh the composite parts. b) Geometry of the rivet meshed with the eight-node linear brick element (C3D8H).

The constitutive model proposed by Johnson-Cook (JC) was selected to describe the ductile behavior of Ti6Al4V which takes into account the effects of the strain hardening, strain rate sensitivity, and thermal softening behavior, according to Equation C.1.

$$\bar{\sigma} = (A + B\bar{\varepsilon}^{n}) \times \left(1 + C \ln \frac{\dot{\bar{\varepsilon}}}{\dot{\bar{\varepsilon}}_0}\right) \times \left[1 - \left(\frac{T - T_r}{T_m - T_r}\right)^{m}\right] \quad \text{(C.1)}$$

where $\bar{\sigma}$ is the flow stress, $\bar{\varepsilon}$ is the plastic strain, $\dot{\bar{\varepsilon}}$ is the plastic strain rate, $\dot{\bar{\varepsilon}}_0$ is the reference plastic strain rate, T is the process temperature, T_m is the melting temperature of Ti6Al4V, and T_r is

the room temperature. $A, B, C, m,$ and n are material constants which were selected from the literature and shown in Table C. 1.

Table C. 1 Input parameters for Johnson-Cook (JC) constitutive model [191].

A [MPa]	B [MPa]	n	m
1098	1092	0.93	1.1

The CF-PEEK material properties adopted from the literature [188] and used in the numerical computation are shown in Table C. 2.

Table C. 2 Material properties of CFRP used in the FEM analysis [188].

Longitudinal Tensile Strength, X_T [MPa]	Longitudinal Compressive Strength, X_C[MPa]	Transverse Tensile Strength, Y_T [MPa]	Transverse Compressive Strength, Y_C [MPa]	Longitudinal Shear Strength, S_L [MPa]	Transverse Shear Strength, S_T [MPa]
1500	900	27	200	80	60

2D Hashin damage criteria was adopted to account the degraded properties of the composite owing to the fiber-matrix failure over the joint loading. The material properties degradation occurs based on stiffness degradation, as shown in Table C. 3.

Table C. 3 General formulation of 2D Hashin damage criteria for CFRP [192].

Failure Criteria	Failure Mode	FE Variable
Fiber-tensile failure ($\sigma_{11} \geq 0$)	$D_{ft}^2 = \left(\frac{\sigma_{11}}{X_T}\right)^2 + \left(\frac{\sigma_{12}}{S_L}\right)^2$	HSNFTCRT
Fiber-compression failure ($\sigma_{11} < 0$)	$D_{fc}^2 = \left(\frac{\sigma_{11}}{X_C}\right)^2$	HSNFCCRT
Matrix-tensile failure ($\sigma_{22} \geq 0$)	$D_{mt}^2 = \left(\frac{\sigma_{22}}{Y_T}\right)^2 + \left(\frac{\sigma_{12}}{S_L}\right)^2$	HSNMTCRT
Matrix-compression failure ($\sigma_{22} < 0$)	$D_{mc}^2 = \left(\frac{\sigma_{22}}{2S_T}\right)^2 + \left[\left(\frac{Y_C}{2S_T}\right)^2 - 1\right]\frac{\sigma_{22}}{Y_C} + \left(\frac{\sigma_{12}}{S_L}\right)^2$	HSNMCCRT

The interaction between rivet and composite and between the composite plates were described by two contact-pairs in the FE model, as shown in Figure C. 2. Once the rivet-composite interface is governed mainly by adhesion forces, a hard pressure-overclosure relationship and tie

constraint were adopted, while a cohesive interaction was used to describe the contact between the composite parts. Between the CF-PEEK parts there is a consolidated squeezed material which is cohesively damaged over the loading, leading to the composite part separation. In the model, the area of such squeezed material was measured by μCT imaging and simplified as a circular area with D_s diameter (Figure C. 2-b). The surface-based traction-separation law with linear softening was adopted to produce the mechanical responses of such contact-pair and to simulate the damage evolution. For all the interactions, the rivet was chosen to be the master surface, while the composite was the slave surface, once is less stiff than the metal. A coefficient of friction of 0.2 was used for the metal-composite contact pair while 0.36 was selected for the composite-composite contact pair [188].

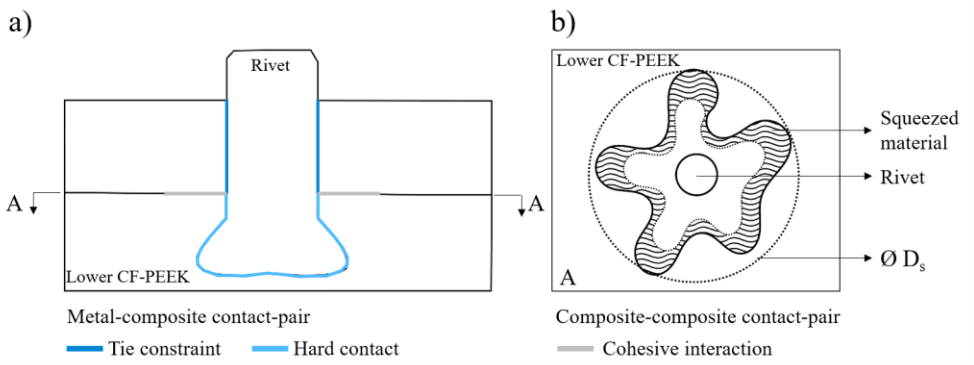

Figure C. 2 Illustration of the contact interactions used in the FE model for a) metal-composite and b) composite-composite contact-pairs.

The FE model was validated overlaying the force-displacement curve obtained by the FEM and the experimental curve, as shown in Figure C. 3. Although the joint's elastic behavior was fairly predicted, a discrepancy was observed when the first failure mode occurred. The predicted ductility of the joint was way inferior to the reality, suggesting that the adopted properties of the base materials must be refined as well as further improvements are still required to the failure description and criterion adopted.

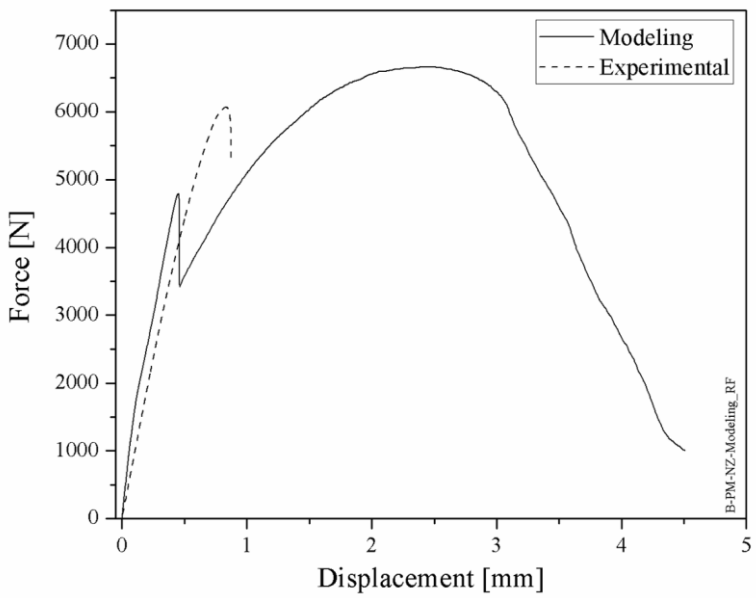

Figure C. 3 Comparison between the force-displacement curves predicted by FEM simulation and experiment.

Appendix D. Temperature measurements by thermography and thermometry

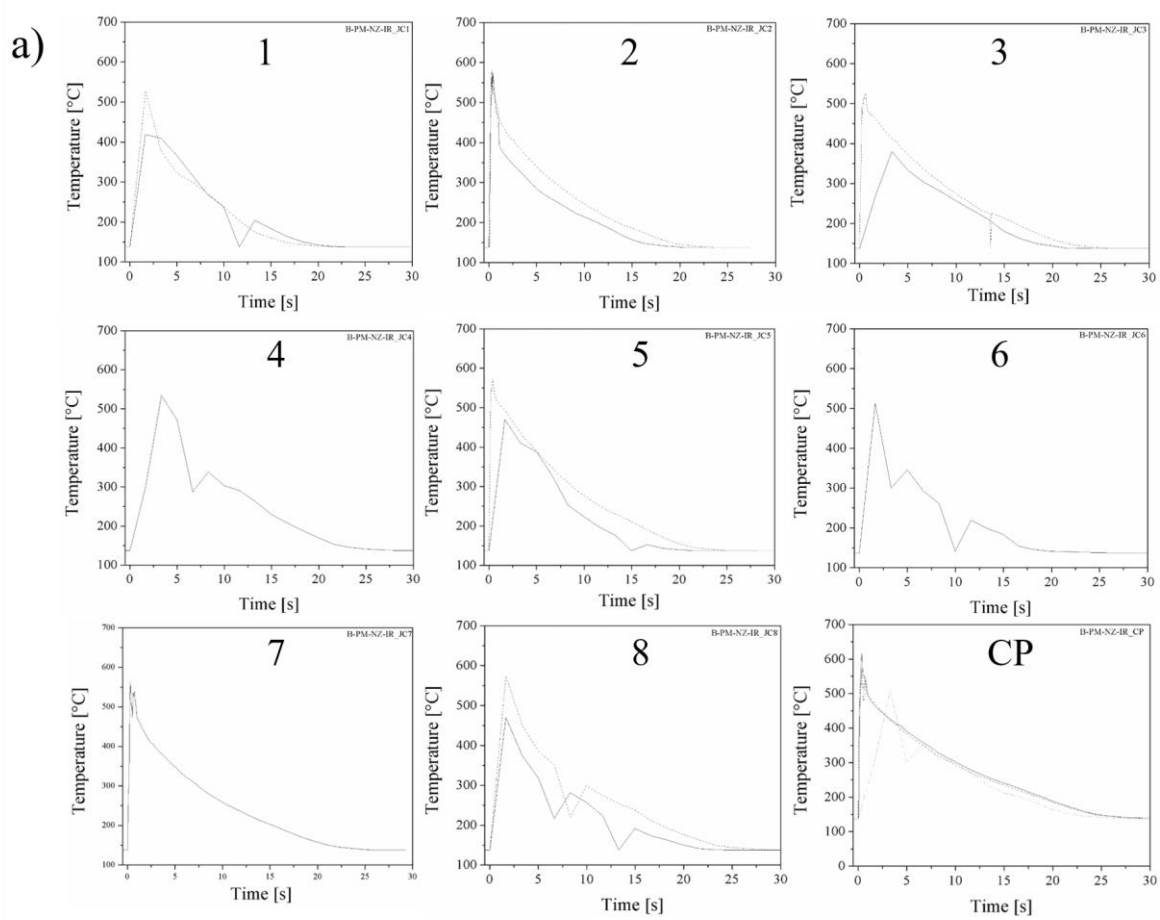

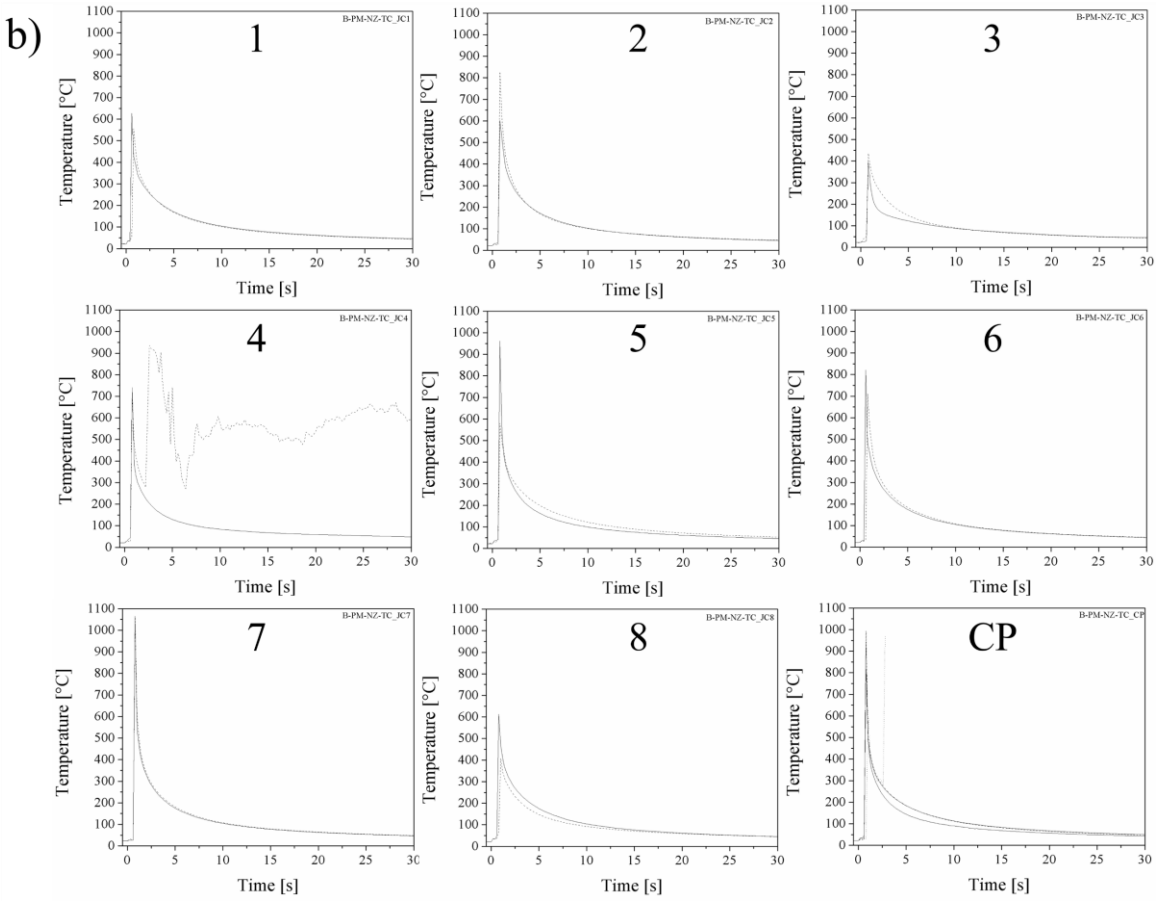

Figure D. 1 Temperature developed during FricRiveting process for all the joining conditions (1-8, center point, CP), with replicates, evaluated in this work, measured by a) thermography and b) thermometry.

Appendix E. Nanoindentation experiments on unaged and aged PEEK

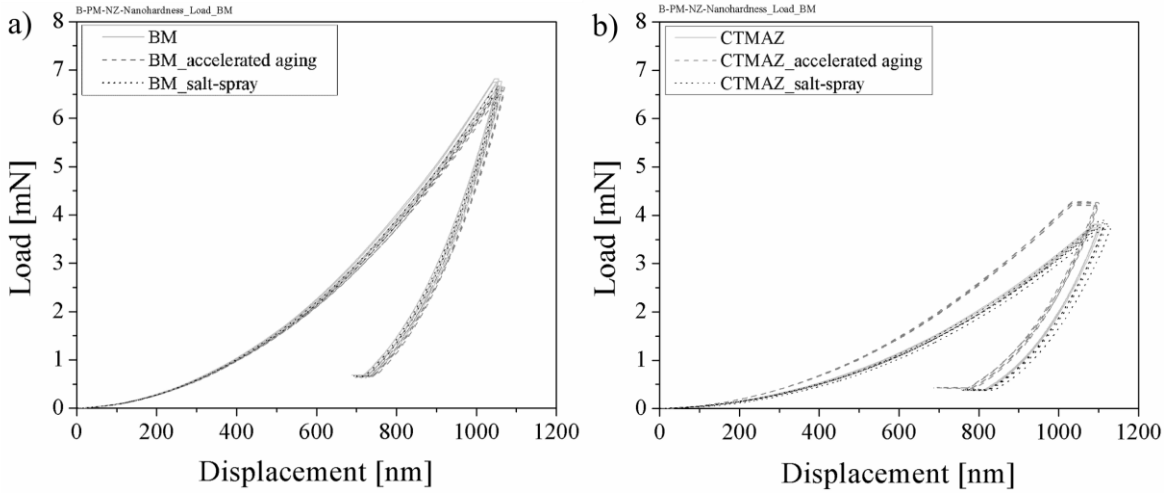

Figure E. 1 Load-displacement curves of nanoindentation on PEEK a) base material (BM) and b) from the composite thermo-mechanically affected zone (CTMAZ) before and after accelerated aging and salt-spray.

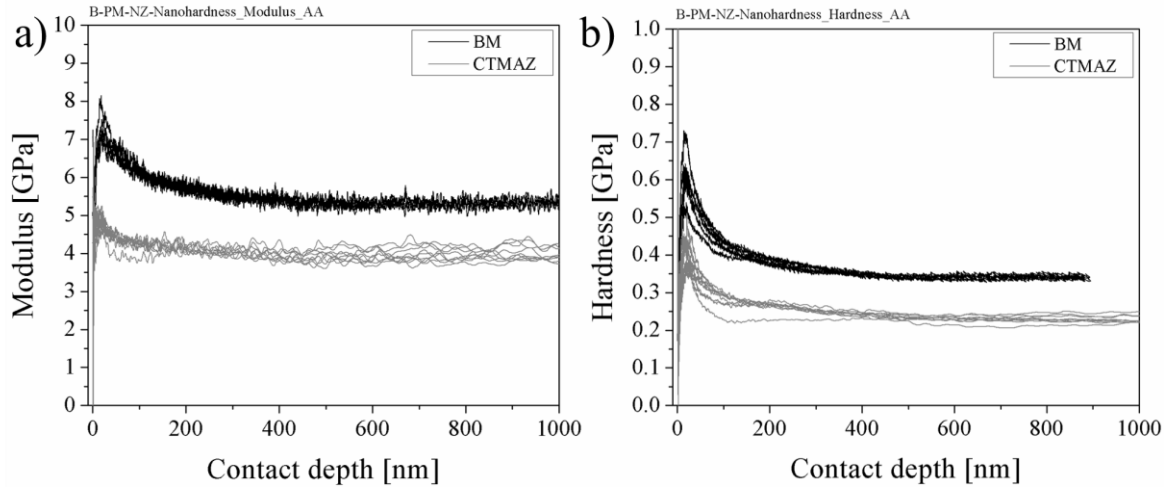

Figure E. 2 Detailed results of nanoindentation on PEEK BM and CTMAZ after 28 days of accelerated aging; a) modulus as a function of contact depth from CSM measurement, b) hardness as a function of contact depth from CSM measurement.

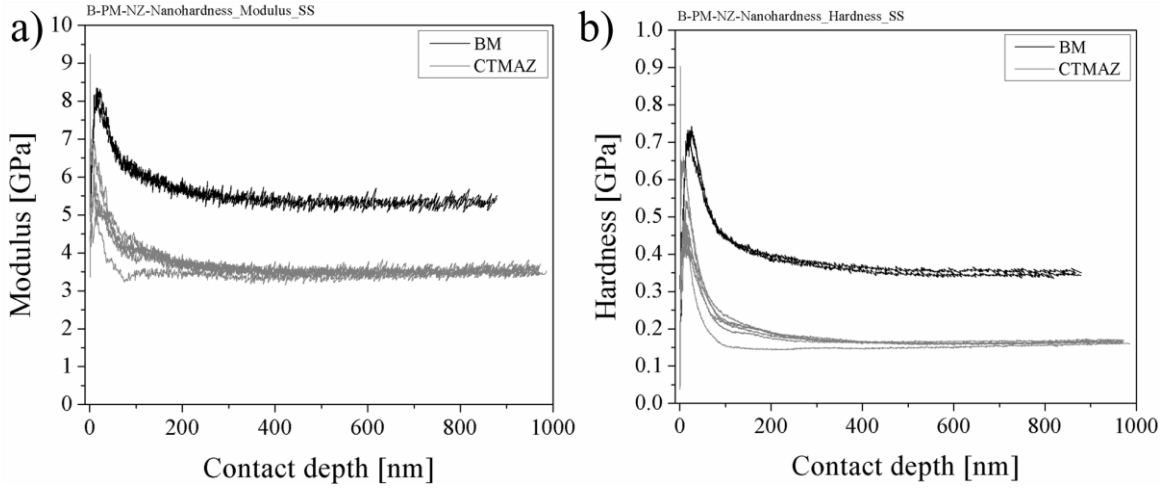

Figure E. 3 Detailed results of nanoindentation on PEEK BM and CTMAZ after 42 days of salt-spray aging; a) modulus as a function of contact depth from CSM measurement, b) hardness as a function of contact depth from CSM measurement.

Appendix F. Lap shear results from friction riveted joints of the design of experiments

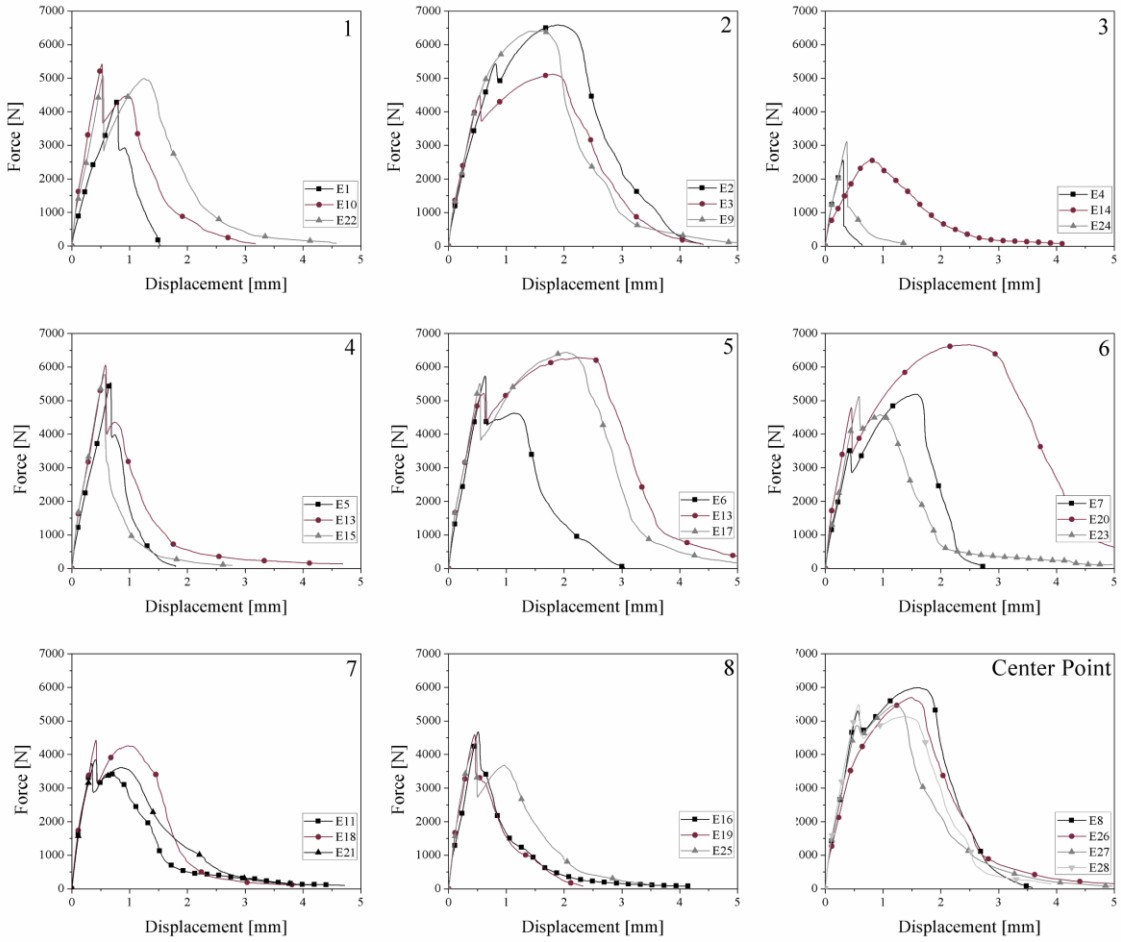

Figure F. 1. Lap shear force-displacement curves for the specimens of the design of experiments.

Appendix G. Effect of the Direct FricRiveting process parameters on the volumetric ratio

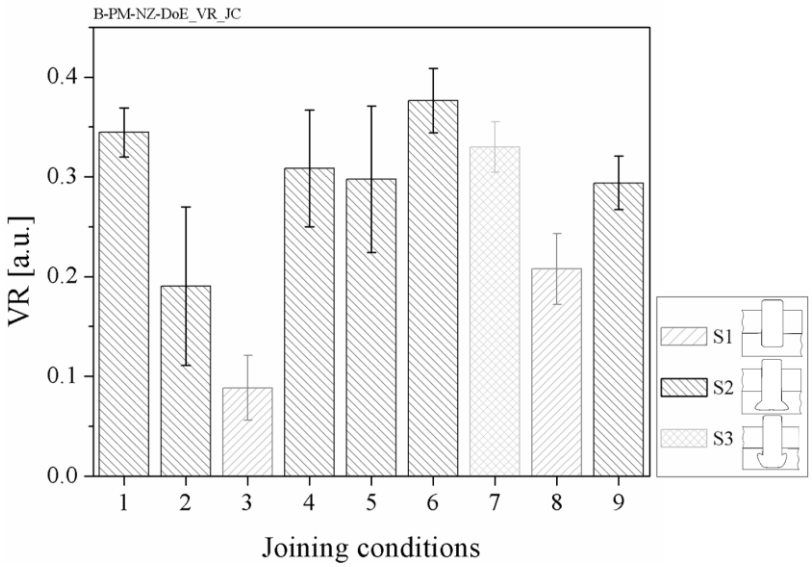

Figure G. 1 Effect of different joining conditions on the VR of friction riveted joints. Numbers from 1 to 8 correspond to the experiments performed during the DoE while 9 is the center point add to the model.

Table G. 1 ANOVA of VR model.

Source	DF	Adj SS	Adj MS	F-value	P-value
Model	3	0.200267	0.028610	11.94	0.000
Linear	3	0.1284567	0.061522	25.67	0.000
RS	1	0.021600	0.021600	9.01	0.007
FF	1	0.126150	0.126250	52.63	0.000
CP	1	0.036817	0.036817	15.36	0.001
2-way interactions	3	0.015433	0.005144	2.15	0.128
RS*FF	1	0.007350	0.007350	3.07	0.096
RS*CP	1	0.000017	0.000017	0.01	0.934
FF*CP	1	0.008067	0.008067	3.37	0.082
3-way interactions	1	0.000267	0.000267	0.11	0.742
RS*FF*CP	1	0.000267	0.00267	0.11	0.742
Error	19	0.045541	0.002397		
Curvature	1	0.002674	0.002674	1.12	0.03
Pure error	18	0.042867	0.002381		
Total	26				

Initial factors from Table G. 1. with p-values > 0.05 were eliminated by the stepwise backward elimination method resulting in the reduced statistical model of VR expressed by Equation G.1. Figure G. 2 shows the experimental plot of the reduced model, along with the contribution of the significant joining parameters to VR, and the main effect plot of these parameters on VR. Similarly to the ULSF model, RS and FF contribute positively to VR, while by increasing CP, VR decreases owing to the over-deformation of the rivet tip. Once no parameter interactions in any level were statistically significant, the interaction plots were not presented.

$$VR = -0.1623 + 0.000012 \times RS + 0.000029 \times FF - 0.01958 \times CP \quad \text{(G.1)}$$

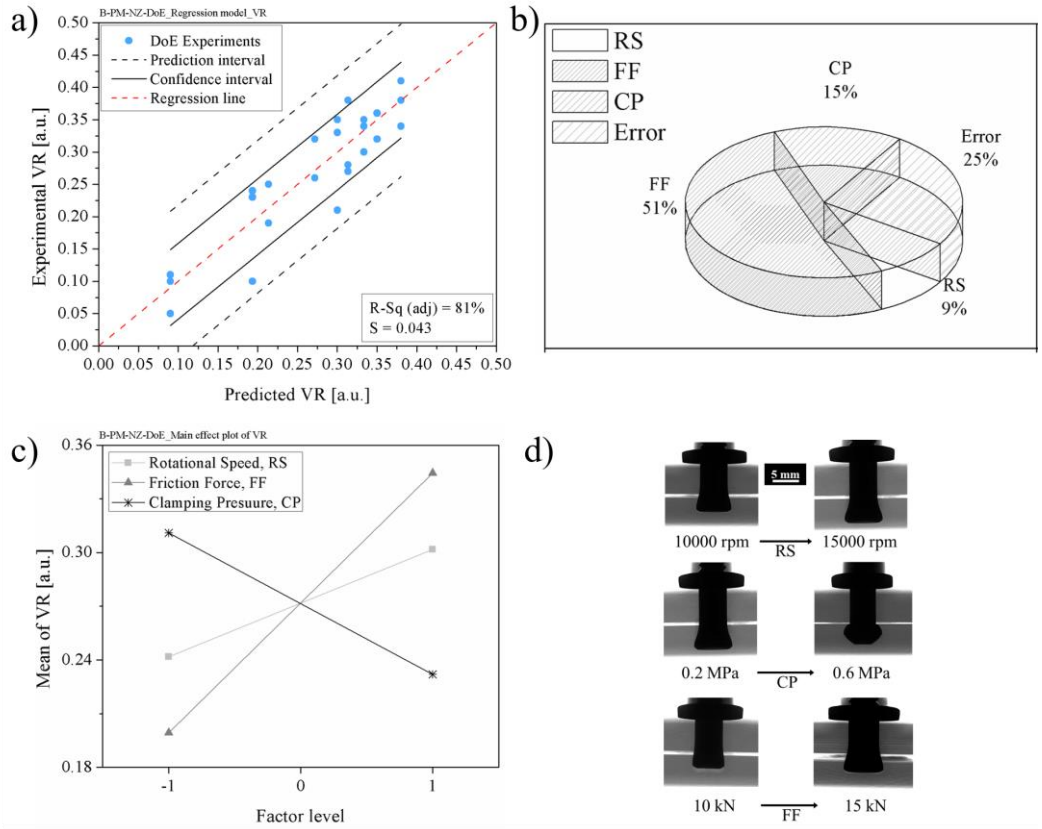

Figure G. 2 a) Experimental diagram for the reduced model of VR. b) Percentage effect of each significant factor on the VR. c) Mean effect plots of the process parameters on the VR. d) Selected X-ray µ-computed tomographies of low and high limits of each individual parameter investigated within the DoE.

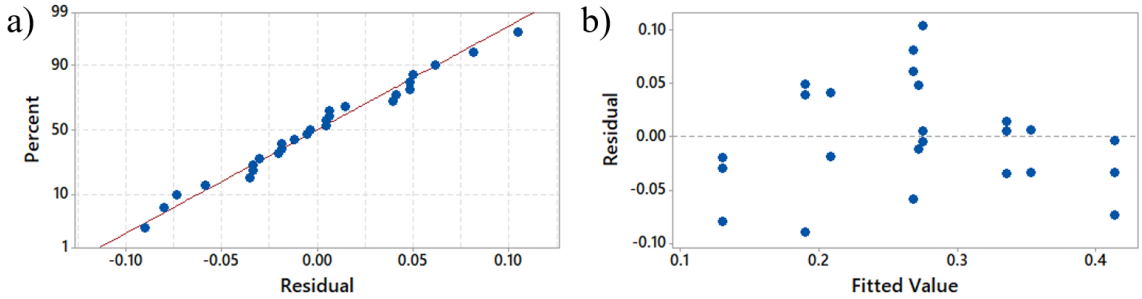

Figure G. 3 Volumetric ratio (VR) statistical model: a) normal probability plot and b) plot of residuals as a function of fitted values.

Appendix H. ANOVA of the ULSF regression model and model validation table

Table H. 1 ANOVA of ULSF model.

Source	DF	Adj SS	Adj MS	F-value	P-value
Model	7	34758854	4965551	16.02	0.000
Linear	3	11250379	3750126	12.10	0.000
RS	1	7019909	7019909	22.64	0.000
FF	1	18598	18598	0.06	0.809
CP	1	4211872	4211872	13.58	0.002
2-way interactions	3	18174961	6058320	19.54	0.000
RS*FF	1	16344736	16344736	52.72	0.000
RS*CP	1	857342	857342	2.77	0.113
FF*CP	1	972883	972883	3.14	0.093
3-way interactions	1	5333514	5333514	17.20	0.001
RS*FF*CP	1	5333514	5333514	17.20	0.001
Error	19	5891034	310054		
Curvature	1	1244289	1244289	4.81	0.041
Pure error	18	4646745	258153		
Total	26				

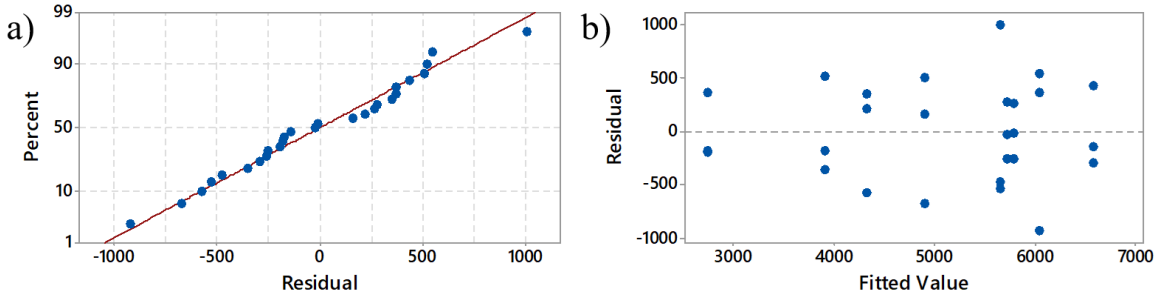

Figure H. 1 Ultimate lap shear force (ULSF) statistical model: a) normal probability plot and b) plot of residuals as a function of fitted values.

Table H. 2 Validation experiments for the ULSF model (three replicates).

Joining condition	**RS_{II} [krpm]**	**FF_{II} [kN]**	**CP [MPa]**	**Predicted ULSF [kN]**	**Actual ULSF [kN]**
LS-V_1	14	11	2	6.1 ± 0.2	6.3 ± 0.2
LS-V_2	13	10	3	5.6 ± 0.1	4.5 ± 0.6
LS-V_3	12.5	16.7	4	5.1 ± 0.1	5.6 ± 0.3
LS-V_4	8.3	12.5	4	4.2 ± 0.2	5.1 ± 0.3

Appendix I. Impact test

Table I. 1 Summary of the results for the impact test of friction riveted joints.

Impact energy, U_i [J]	5	10	20	30
Absorbed energy, U_t [J]	4.3 ± 0.3	7.2 ± 0.5	14.6 ± 0.6	24.0 ± 0.8
Insipient damage load, P_i [kN]	6.0 ± 0.8	7.6 ± 0.5	9.6 ± 0.7	11.4 ± 0.2
Maximum load, P_m [kN]	7.3 ± 0.6	14.2 ± 0.5	14.4 ± 0.4	18.7 ± 0.2
Area of damage [mm^2]	117 ± 22	138 ± 33	238 ± 20	280 ± 34
Residual dent depth [mm]	0.5 ± 0.1	0.8 ± 0.1	1.20 ± 0.06	1.60 ± 0.05
Category of damage	BVID	VID	VID	VID
Residual strength (quasi-static test) [kN]	6.2 ± 0.3	5.6 ± 0.2	5.3. ± 0.3	3.9 ± 0.2
Stress amplitude at 10^5 fatigue cycle [MPa]	53		41	
Residual strength after 10^6 fatigue cycle [kN]	6.0 ± 0.3		4.8 ± 0.2	

Appendix J. Predicting the extent of impact damage and damage mechanisms

To predict a critical impact load (P_c) above which mode II shear delamination would occur, Equation J.1, proposed by Davis and Robinson [74], was employed. The equation takes into account the energy release rate modeled on through-thickness delamination in a quasi-isotropic composite and was validated for a range of carbon fiber reinforced polymers including CF-PEEK. *E* is the elastic modulus of the composite ($E_{CF\text{-}PEEK}$ = 60 GPa, [159]), G_{II} is the mode II fracture toughness ($G_{II,\ CF\text{-}PEEK}$ = 1.75 kJ/m^2, [48]), *t* is the composite thickness (t = 4.34 mm), and ϑ is the coefficient of Poisson (ϑ = 0.4 [48]). Figure J. 1-a plots the area of damage against impact loads of the friction riveted joints, along with the threshold P_c.

$$Pc^2 = 8\pi^2 E t^3 G_{IIC}/9(1-\vartheta^2) \ldots \text{(J.1)}$$

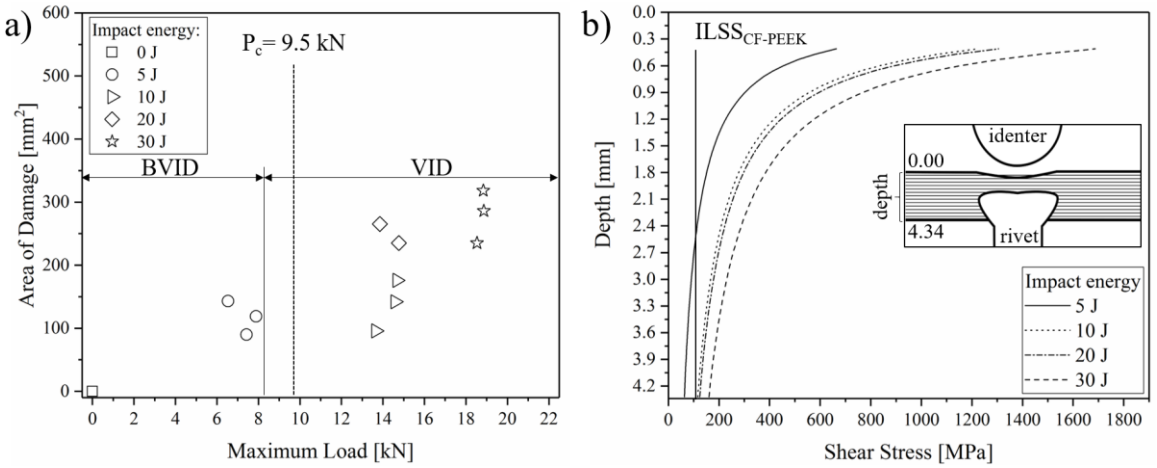

Figure J. 1 a) Area of impact damage as a function of maximum impact load; b) calculated shear stress against the lower composite plate thickness.

In agreement with the microstructural analysis of the impacted cross-section of the joint (Figure 8.5), at low impact energy in the BVID domain no delamination was expected as it is below the critical impact force of 9.5 kN. In the VID domain, two main groups of damage area were identified. For impact energies 10 J and 20 J the maximum load imposed in the joint was near to 14 kN, while for 30 J the maximum load was 19 kN. As explained in Section 8.1, the composite withstood a maximum load of 14 kN by dissipating the impact energy mainly by the initiation and propagation of delamination through the composite thickness. Above the load threshold of 14 kN the

metal-composite interface of the joints played an important role, where the delamination was extended, leading to an enlargement of the damaged area.

To predict the influence of normal and shear stresses on the fracture mechanisms depicted in Figure 8.5, shear stress (τ) was calculated from the depth into composite plies (r) using Equation J.2. This equation was proposed by Davis and Zhang [58] and assumes that impact-induced delamination is driven by shear stress in the central region of an impacted composite. Again, a simplified quasi-isotropic material and perfectly circular shape of delamination were adopted [58]. The average impact force (F) at each impact energy level was used. Figure J. 1-b shows the result, along with the interlaminar shear strength (ILSS) of the CF-PEEK base material ($ILSS_{CF\text{-}PEEK}$ = 72 MPa [277]), above which the matrix-fiber interface fails under shear loading. Except for the 5 J impacted joints, the majority of impact damage introduced in the composite was driven by shear. Bearing in mind that the equation does not consider bending of the joint on impact loading, peeling stress was neglected, although its effect is shown in Figure 8.5.

$$\tau = \frac{F}{2\pi r t} \quad \text{(J.2)}$$

The simplified models to predict delamination and its stress-trigger across a range of impact energies were successfully validated by a microstructural analysis of the impacted friction riveted joints of CF-PEEK and these can be further used for an exploratory definition of impact damage tolerant designs.

Appendix K. Digital image correlation (DIC) analysis of post-impacted friction riveted joints

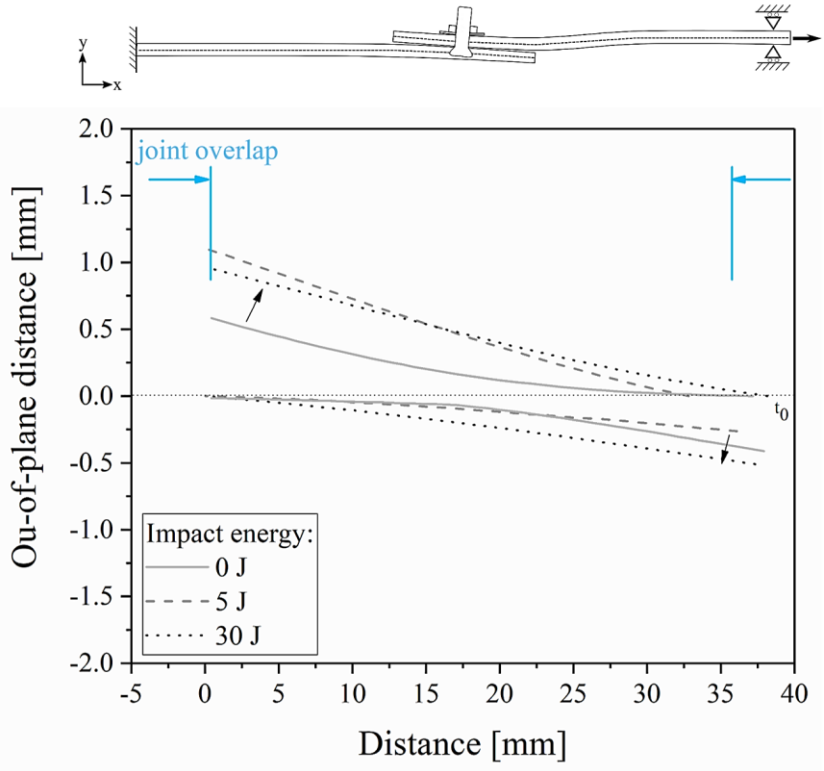

Figure K. 1 Schematic representation of the eccentric loading path in composite overlap friction riveted joint along with the out-of-plane displacement curves at the end of the loading measured by digital image correlation (DIC).

Appendix L. Thermo-analysis of aged Ti6Al4V/CF-PEEK friction riveted joints

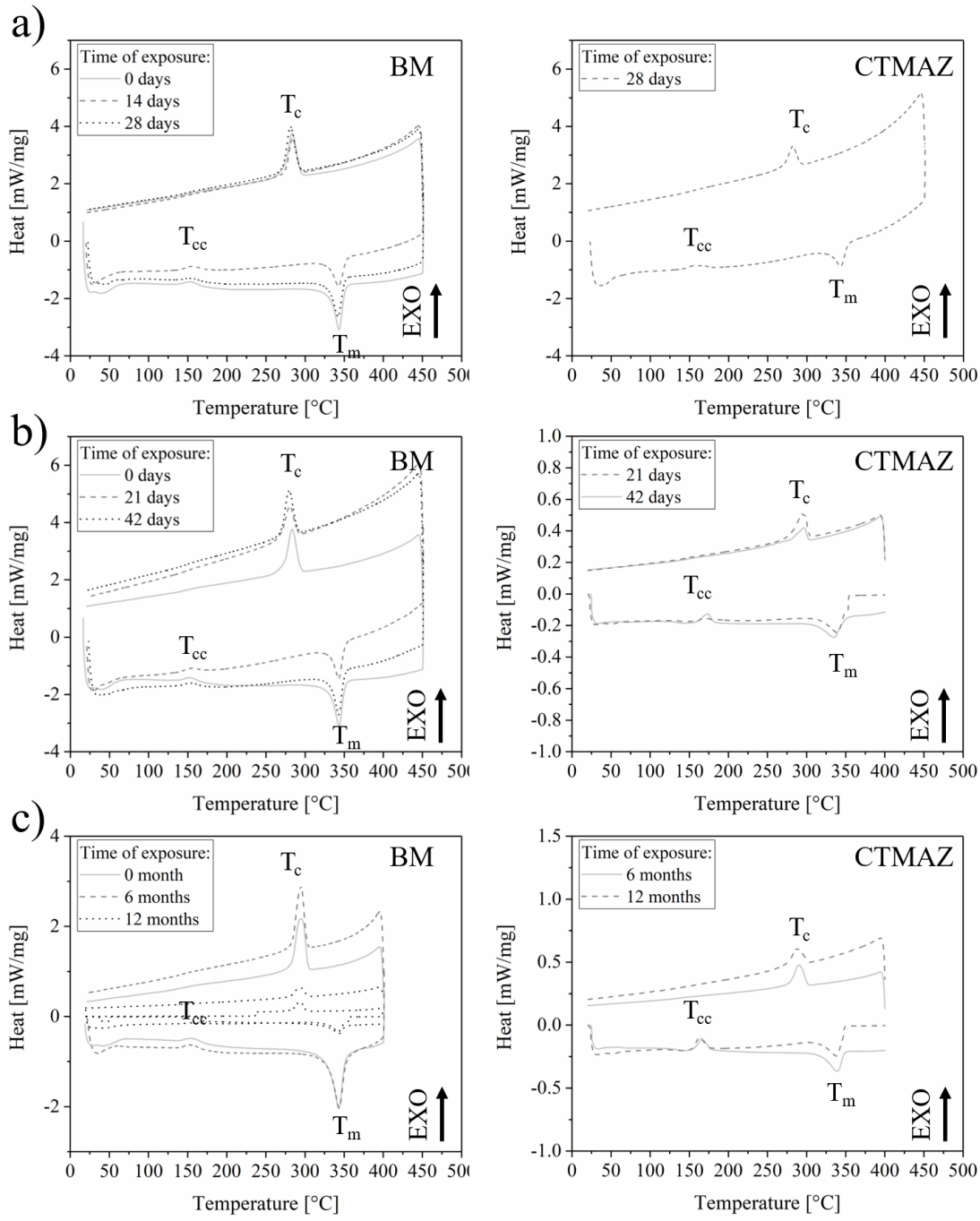

Figure L. 1 DSC curves for the base material (BM) and thermo-mechanically affected composite (CTMAZ) under a) hydrothermal, b) saline, and c) natural aging.

Appendix M. Microhardness of aged Ti6Al4V/CF-PEEK friction riveted joints

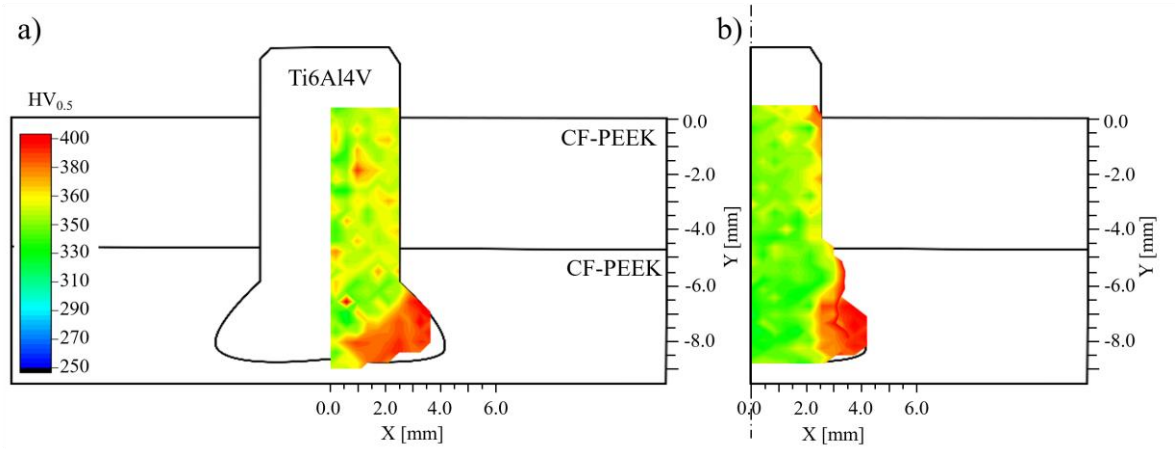

Figure M. 1 Macrohardness distribution through half of the rivet in the joining area of friction riveted joints a) hydrothermally aged during 28 days and b) exposed to saline atmosphere during 42 days.

Appendix N. Digital image correlation (DIC) analysis of hydrothermally aged friction riveted joints

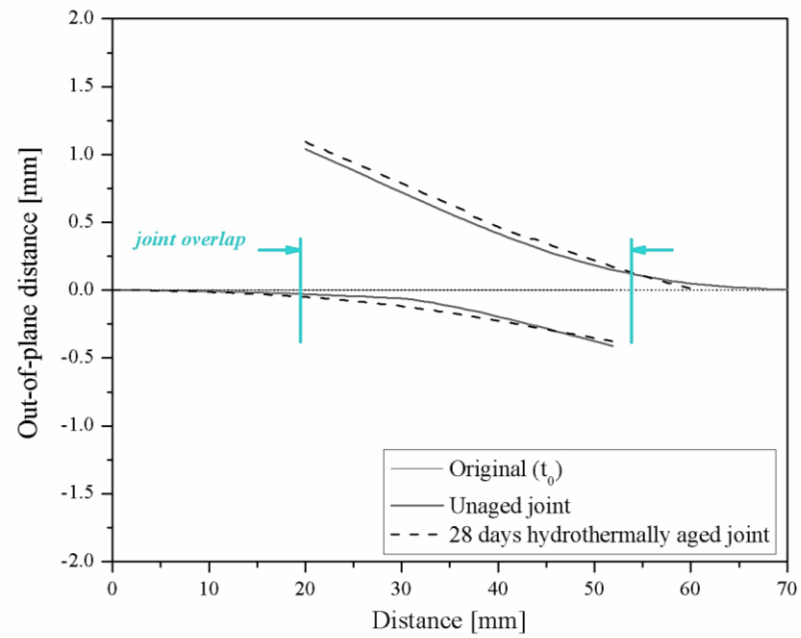

Figure N. 1 Out-of-plane displacement curves at the end of lap shear test for unaged and 28 days aged friction riveted joints measured by digital image correlation (DIC).